Advanced quantitative analysis of crack fields, observed by 2D and 3D image correlation, volume correlation and diffraction mapping

Selim Matthias Barhli

Corpus Christi College

University of Oxford

A thesis submitted for the degree of

Doctor of Philosophy

Hilary 2017

This thesis is dedicated to
Aline
for her love and support

Acknowledgements

Firstly, I would like to express my sincere gratitude to my supervisor Prof. James Marrow for his continuous support during my D.Phil project, for his energy, motivation, and immense availability. His guidance helped me in all the time of research and writing of this thesis. I could not have hoped having a better supervisor for my D.Phil study.

Beside my supervisor, I would like to thank Dr Mahmoud Mostafavi, for his insightful comments and also for his good suggestions which encouraged me to widen my research. I also thank Dr David Hollis and LaVision Gmbh for their financial support and provision of software and workstation for the project.

I sincerely thank Prof. Jean-Yves Buffière, Prof. Philip Withers and Dr Torsten Becker who provided me an opportunity to meet their team and gave me access to important data for my project. They made me meet Dr Julien Réthoré, Dr Joël Lachambre, Dr Chris Simpson and Mr Matt Molteno that I would like to thank here for their precious support.

I thank my colleagues and friends for the stimulating discussions, for the sleepless nights at DLS, and for all the fun we have had in the last four years. Thank you, in no particular order, Luis, Matthew, Yelena, Ahmet, Phil, Shixiang, Liye. Also I thank my friends from Toulouse, Leo, AlexM, Mehdi, AlexP, Franck, AlexG, Alizée, AlexR, Théo for their support and all the good times we have had. Thank you Anne, Keo, Sylvestre, Madeleine and see you soon. A big thank you to all my friends in Oxford and in particular Stéphanie, Alex, Julian, Antonio you enlightened my time in the UK.

Last but not the least, I would like to thank my family: my parents, whose support never failed, my grandma and my aunts and uncle for supporting me spiritually throughout writing this thesis and my life in general.

Thank you Aline for your positivity, your strength and altruism. You bring happiness to my life and I would not have succeeded without you.

Abstract

This thesis is concerned with the evaluation, in-situ, of the elastic strain energy release rate of cracks. This can define the criteria for crack propagation, and it is usually necessary to obtain this via calculation from the geometry and applied load. A new method is proposed, based on the conjoint use of digital image correlation to measure full-field displacements and finite element to extract the strain energy release rate of surface cracks. It has been extended to 3-D datasets with the use of digital volume correlation and tomographic imaging. A finite element model with imported full-field displacements measured by DIC/DVC acting as boundary conditions is solved and the J-integral is calculated. For linear elastic materials, modal contributions can be separated via the interaction integral.

The method has been benchmarked using synthetic datasets to assess its sensitivity to noise and experimental uncertainties. It is very robust to experimental noise and can be used without knowledge of the specimen geometry and applied loads. The application of the method in 2-D is demonstrated in an analysis of experimental data for a mode I fatigue crack, introduced to an aluminium alloy compact tension specimen. Analysis of mixed-mode cracks in 2-D is shown on a PMMA sample with the Arcan geometry. In 3-D, static loading of a fatigue crack in nodular graphite cast iron is studied and the results from the method are compared with those obtained via a field-fitting approach.

Diffraction analysis of polycrystalline materials can determine the full tensor of the elastic strains within them. Maps of elastic strains can thus be obtained typically using synchrotron X-rays or neutrons. A method is presented to calculate the elastic strain energy release rate of a crack from 2-D diffraction strain maps. The diffraction data is processed via a finite element approach to obtain the parameters required to calculate the J-integral. A validation is presented using a synthetic dataset from a finite element model. Its experimental application is demonstrated in an analysis of synchrotron X-ray diffraction strain maps of a propagating fatigue crack in a bainitic steel, before and after an overload.

Finally, a complex case study of stable fracture propagation in polygranular isotropic nuclear graphite is presented. Synchrotron X-ray tomography and strain mapping by diffraction were combined with DVC and image analysis to extract the full-field displacements and elastic crystal strains. The displacement fields have

been analysed using the developed methods to extract the critical strain energy release rate for crack propagation. Non-linear properties described the effect of microcracking on the elastic modulus in the fracture process zone. The analysis was verified by comparison of the predicted and measured elastic strain fields.

Contents

επειδ αμαρτη, κεινοσ ουκετ εστ ανηρ αβονλοσ ουδ ανολβοσ, οστισ εσ κακον πεσων ακειται μηδ ακινητοσ πελει.

All men make mistakes, But a good man yields when he knows his course is wrong, And repairs the evil. The only crime is pride.

— Sophocles's *Antigone*

1 Literature review

Contents

1.1 Introduction

The study of defect formation and crack propagation in materials has been tackled using different approaches by the scientific community in the last century. From an engineering point of view, different models have been written to predict the material response for a given loading. The main interest is to be able to ensure the soundness of structures.

However, to be able to determine such models, the fracture behavior of materials must be thoroughly studied. A goal of this work is to develop full-field based methods that can retrieve a maximum of information from experimental datasets. For instance, the analysis of results where the experimental boundary conditions might be poorly characterized due to friction effects or rig compliance, or indeed measurements of components in service, becomes possible when full-field measurements allow accurate determination of the sample loading state. The use of finite element modelling coupled with full-field measurement also allows the determination of the constitutive laws for material damage by reverse-engineering techniques. These approaches constitute a basis for both quantification of crack driving forces and crack detection methods.

The first part of this literature review will show how the failure of elastic and elastic-plastic materials can be theorized and what characterizes the crack driving forces. Emphasis will be put on the J-integral as a method to quantify a crack from its full-field data.

The second part will review the different methods used to obtain quantitative information on a crack from datasets obtained via imaging techniques. The use of Digital Image/Volume Correlation coupled with full-field calculations will be underlined due to its ease of implementation, its competitive level of error and the possibility to deal with 3-D datasets when coupled with suitable imaging methods.

In a third part, the case of diffraction methods will be tackled. Diffraction based methods allow full-field measurements of the elastic strain tensor. The analysis of those data provides additional important information on the stress field of the crack. State of the art methods using diffraction to quantify cracks will be presented.

1.2 How to characterize a crack?

1.2.1 Background theory

A crack in a material is within a thermodynamic system and its energy balance determines if the crack can propagate or not. This energy balance, widely discussed in Griffith's and Inglis' works [1, 2] for linear elastic materials, is an equilibrium between the surface energy of the material (proportional to the work required to create new surfaces) and the elastic energy supplied by the internal strains and external forces. In order for the crack to propagate, the energy balance must exceed equilibrium conditions; this observation allowed Griffith's to develop his failure stress fracture criterion for perfectly elastic materials. In the case of materials like metals that exhibit plasticity, Griffith criterion significantly underestimates the fracture strength. Work from Irwin and Orowan [3, 4] generalized this approach to account for energy dissipated by plastic deformation.

The strain energy release rate approach (or energy release rate), proposed in 1956 by Irwin [5] defines the "strain energy release rate" G, which is a measure of the energy available to propagate the crack by a unit surface area; it can also be seen as the elastic energy that will be released from the structure when the crack does propagate. A critical value of the strain energy release rate can be determined. This is equal to the energy needed to extend the crack and is denoted G_c. This quantity is considered as the fracture toughness of the material and is independent to the loading state and crack geometry.

For any crack in a linear elastic body, it was proven using analytical analysis [6–8] that the stress field in vicinity of the crack tip is proportional to $1/\sqrt{r}$, r being the distance from the crack tip. The proportionality constant K is the stress intensity factor (SIF) at the crack tip. Each mode of loading (Figure 1.1) produces a different K value (noted K_I, K_{II} and K_{III}).

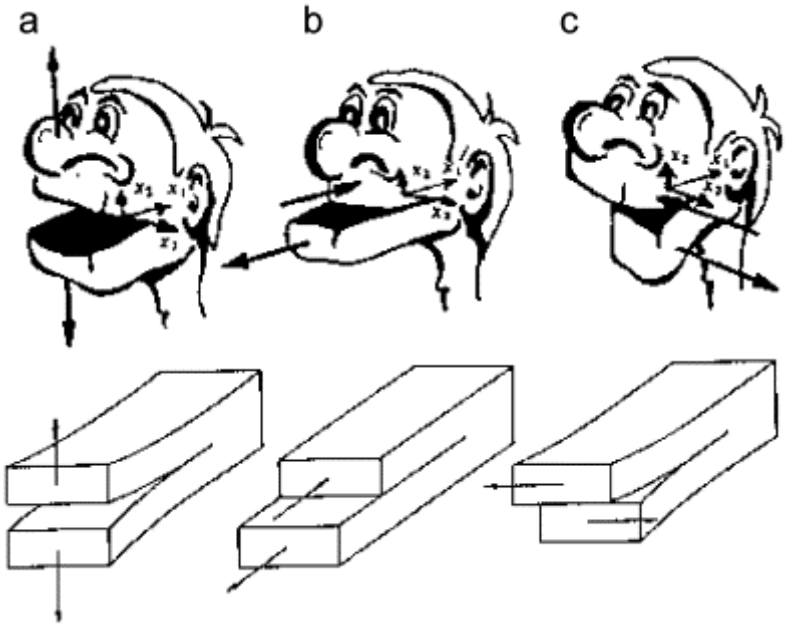

Figure 1.1: Crack loading modes (a) Mode I (b) Mode II (c) Mode III [9].

The analytical expressions of the stress, strain and displacement fields ahead of a crack tip in linear elastic, isotropic materials can be determined when the SIF and crack loading modes are known. One of the most commonly used analytic expressions for those fields ahead of the crack tip are the Williams' series [8]. The main interest of the SIF is that analytical solutions for K exist for a given loading and sample geometry.

$$G = \frac{K_I^2}{E'} + \frac{K_{II}^2}{E'} + \frac{K_{III}^2}{2\mu} \tag{1.1}$$

In linear elastic materials, the stress intensity factor K and the energy release rate G are directly linked by Equation (1.1) where $E' = E$ for plane stress and $E' = E/(1-\nu^2)$ for plane strain. Therefore, for a given mode of loading, a critical value K_c exists and is the value of SIF required to propagate the crack. Being able to determine G_c or K_c is of high interest as it will allow definition of the crack's stress and strain field and so determine the change of energy linked to an increment of crack length; both G_c or K_c are a description of the crack driving force.

In the case of mixed mode loading, the energy release rate contribution of each mode are additive (Equation (1.1)). However, the calculated energy release rate can only be used directly as a fracture initiation criterion if self-similar crack growth (i.e. the crack keeps the same shape whilst it grows) is assumed; this is rarely true under mixed-mode loading. In those cases, a Maximum Energy Release Rate criterion (MERR) can be used, which considers the energy release rate for crack propagation directions and states that fracture will happened in the direction where the value is maximal [10, 11].

In ductile materials like metals or polymers, linear elastic fracture mechanics (LEFM) does not apply in the crack tip region where a yield zone is present. The approach proposed by Irwin estimates the plastic zone size from the yield strength of the material and the SIF value using the analytical stress field formulation [6]. In the case where the plastic region is sufficiently small compared to the dimensions of the sample, the small scale yielding approximation can be considered; it can hence be assumed that the SIF is still a good description of the stress and displacement field and that it represents the crack "driving force".

If the plastic zone size is too large to allow the use of the small scale yielding approximation, an alternative is to rely on the fact the plastified material takes less stress than the part of the material that remained elastic. An effective crack length, longer than the actual crack length, can be defined and allow the use of LEFM. This approach does not reflect the physical reality of the phenomenon.

To extend LEFM to elastic-plastic materials, the elastic-plastic behaviour can be treated as nonlinear elastic. This assumption is valid if no unloading occurs (i.e. no crack propagation). The energy release rate can be defined in the same way than for elastic materials, but its meaning changes. For linear elastic materials, it represents the energy released with an increment of crack growth. However, in the case of elastic-plastic materials it represents the energy released with an increment of crack growth plus the energy absorbed by the specimen due to plastic

deformation. Work by Hutchinson, Rice and Rosengren [12, 13] (commonly referred as the HRR solution) demonstrates that for nonlinear elastic materials, the energy release rate also characterize the crack tip stress and strain field. In the case where the plastic region is too large, the HRR solution is not valid anymore but the energy release rate keeps its meaning.

One shall therefore understand the interest of determining the strain energy release rate for both linear elastic and elastic-plastic materials as it characterizes the crack "driving force". It represents the deformation field around the crack tip that is sufficient to cause crack propagation. The next sections will detail the methods that can be used in this endeavour and how they have been applied.

1.2.2 The J-integral method

The J-integral is a method to calculate the energy release rate in elastic and nonlinear elastic materials, independently developed by Cherepanov and Rice in 1967 [14, 15]. It is also applicable to elastic-plastic materials when the assumptions detailed in the previous section are met. The J-integral is defined as a path-independent contour integral that is equivalent to the energy release rate. Its value is zero over a closed contour and is independent of the path of integration; those two properties are demonstrated in the literature [15].

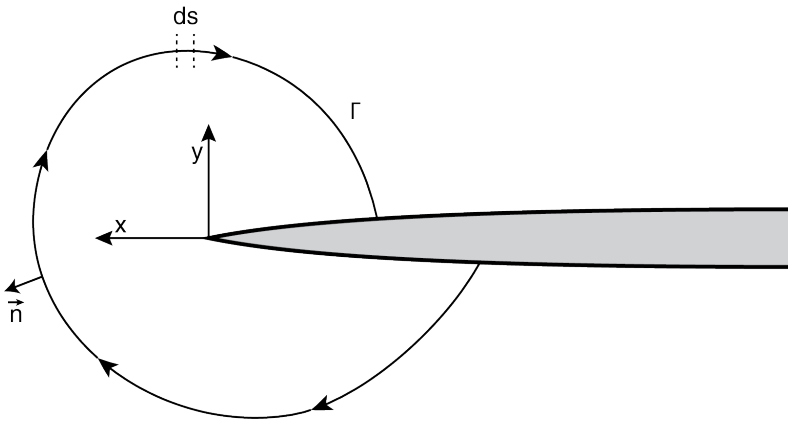

Figure 1.2: Typical J-integral integration contour.

$$J = \int_{\Gamma} \left(W \mathrm{d}y - T_i \frac{\partial u_i}{\partial x} \mathrm{d}s \right) \tag{1.2}$$

An illustration of such a contour is given on Figure 1.2 for a homogeneous body containing an opened crack. The expression of J is stated in Equation (1.2) where Γ is the contour, the strain energy density is W and T is the traction vector defined by the relation $T_i = \sigma_{ij} n_j$ where n is the normal to the path; when multiplied by the displacement vector, the traction vector gives the work associated with the surface traction. The formulation of J can also be modified to take into account a field that includes residual stresses or thermal stresses [16]. The J-integral can also be formulated as a surface or area integral using Green's theorem [17], this makes it convenient to implement in finite element analyses (area and volume integration are easier to implement numerically than contour and surface integrations). For 3-D cases, the J-integral can be defined as a volume integral [18].

The meaning of the value of strain energy release rate calculated from the J-integral should be well understood. In the case of a monotonic, quasi-static loading where an inelastic model is considered; the J-integral characterizes the crack-tip conditions thus defining both the energy available to propagate the crack and provides a single parameter defining the crack tip fields.

In the case of cyclic loading of a linear or non-linear elastic material, no problem is encountered since the range of J-integral in the cycle simply describes the change of the elastic strain field that affects very small scale plasticity at the crack tip. However, with the assumption of inelastic behaviour the material does not follow the same path at loading and unloading. This can lead to erroneous values of strain energy density if significant yield has occurred in the material and depending on the shape of the stress-strain curve.

This can be mitigated by considering each cycle separately as a monotonic loading step with full-field methods (e.g. DIC) that allows one to take the reference

step just at the beginning of the cycle. This minimises the inelastic deformation in the cycle. In the case where a crack is propagating under constant load range there would be no significant plasticity in a single cycle compared to previous cycles, so the elastic assumption is quite satisfactory. However, if the J-integral is calculated with the assumption of an elastic-plastic material, the meaning of J-integral is quite different as it includes the plastic energy dissipated during the crack growth increment plus the energy required to propagate the crack.

With more complex material models (e.g. softening with strain), it is possible to calculate a correct value of the strain energy release rate, via the J-integral, that retains its energy balance meaning even if it loses the crack tip field definition aspect.

1.3 Quantification of a crack from imaging methods

1.3.1 Analytical solutions

The strain energy release rate can be calculated from the applied loads using continuum mechanics analytical solutions or finite element (FE) methods with knowledge of the specimen geometry and applied load or displacement boundary condition [19, 20]. Analytical solutions exist for simple crack shapes whilst the FE approach can handle more complex designs. Elastic-plastic fracture mechanics also enables the extraction of SIF or energy release rate via measurement of the crack opening displacements [21, 22]. This can be done by monitoring crack length and crack mouth opening and using the relationship between crack tip opening displacement (CTOD) and energy release rate demonstrated by Shih (Equation (1.3) where δ_t is the CTOD, σ_0 is the yield stress and d_n is a function of the material's parameters) [23].

$$\delta_t = d_n \frac{J}{\sigma_0} \tag{1.3}$$

However, in some cases these solutions can be inadequate or inaccurate. For instance, residual stresses from manufacturing or crack closure following fatigue overloads, which may not be well quantified, can act against the applied loads that are the known boundary conditions; these effects are particularly important in stress corrosion [24] and fatigue [25], but may also affect fracture propagation [26]. Uncertainties in the true boundary conditions acting on a crack, such as in a real engineering component or a small-scale mechanics test of non-standard geometry where factors such as friction and misalignment can be significant, may also prevent accurate calculation of the crack field [27].

1.3.2 Field fitting approach

Consequently, there is an interest in defining the crack field by direct measurement of the deformation surrounding the crack. Typically, this deformation is measured between two successive observations that show the change in the field with a change in the applied load. Various approaches have been proposed, but such measurements are not routinely used since the analysis methods are quite complex and can be sensitive to measurement uncertainties. The most general method is the field fitting approach, which fits a theoretical field (such as the Williams field solution) to the measured displacement field in order to retrieve the SIF.

An early method by Chiang used speckle interferometry [28]; the SIF was estimated by relating the displacements at the Young's fringes to the square root of their distance from the crack tip. A similar approach is used by Barker [29] on moiré fringes analysis, he used a least square fit to the Westergaard stress function, a less general version of the Williams' series, to determine the SIF of a mode I crack; both of those techniques suffered from the fact that data was only present at the location of the fringes and thus provided a limited quantity of data to fit. Shortly afterwards, Huntley [30] determined the SIF from a full-field displacement field, obtained by double exposure laser speckle photography, via a least square fit to the Williams'

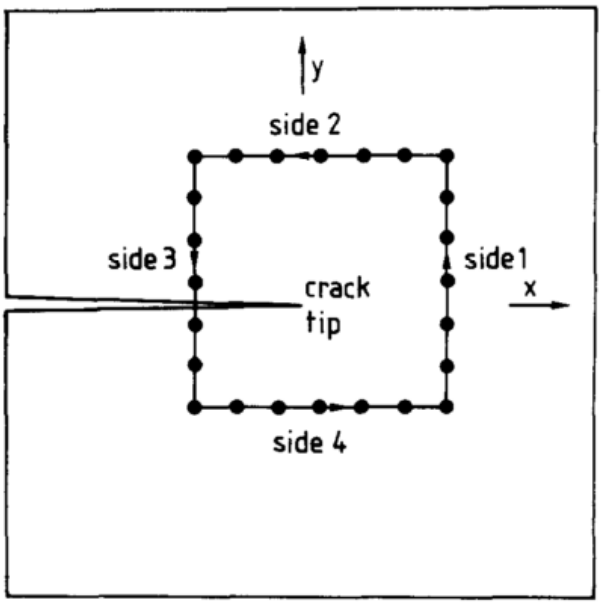

Figure 1.3: Line integral as implemented by Huntley [30], each dot represent the position of a measured displacement vector.

series; he also compared the results with those obtained with a path J-integral and concluded that the field fitting approach is superior. This is probably due to the fact the J-integral was evaluated over a line and not an area (Figure 1.3), which is not a good practice in terms of noise reduction and is probably at issue here when using it on experimental data, also the spatial resolution of the results was probably at issue.

Digital image correlation (DIC) has since been more widely used to measure the displacement field, being more readily applied than interferometry methods. The method is based on tracking of recognizable patterns between two images that allows full-field and precise measurement of displacements. Developed in 1982 by Peters and Ranson [31], the approach is based on the maximization of a correlation coefficient to determine displacements between image subsets. The correlation coefficient for each subset is optimized using rigid body displacement of the subset and the first-order displacement gradients describing the local deformation values of the subset [32]. The second-order displacement gradient can also be included in the correlation analysis and has been shown to improve DIC accuracy [33]. A number of researches were also conducted to decrease the computation time linked

to the process and optimize the solver's algorithms [34, 35]. The strength of the DIC analysis is that it can provides the displacement field values all over the sample surface, providing a trackable speckle is present in the region of interest. It therefore provides a higher data density than interferometry methods and it is also easier to automate the analysis.

The first application of DIC related to fracture mechanics can be attributed to McNeill [36]; in his paper, DIC was used to retrieve the displacement field next to the crack tip region on three ASTM standard PMMA specimens and the stress intensity factor was evaluated by fitting of the analytical linear elastic displacement field. The obtained results are compared with the analytical solution calculated from the apply load. With the use of PMMA, which can be regarded as perfectly brittle, McNeill proved the feasibility and accuracy of the method but does not tackle problems that could appear in ductile or quasi-brittle materials where the displacement field differs from the theory.

Since then, DIC has increasingly been used in fracture research. Liu and Lyons [37] studied crack tip deformation fields of Inconel 718 at high temperatures and related the growth rate of creep cracks to the stress intensity factors obtained using McNeill's method [36]. In this study, the deviation of the strain field behaviour from the analytical model was measured and the presence of plasticity was proven, however the authors judged the difference sufficiently small to be neglected. Additionally, this study demonstrated the interest of DIC as a non-contact method for probing the displacement field of a sample located in a furnace (this aspect is treated in detail in [38]). A variety of works using least-square fitting of analytical displacement fields to retrieve the SIF can also be found in the literature, applied to different materials like cements [39], energetic materials (e.g. solid propellant fuel) [40], and wood [41], etc.

The field-fitting method was also extended to mixed mode loading [42–44]. However, the least-squares technique is quite sensitive to accurate definition of the crack tip location, as highlighted by McNeill [36]. Recently, specific terms

of the Williams' series were used to provide information about the position of the crack tip [45], which improved the precision of the SIF calculation. As an example for comparison, in 1987, McNeil's [36] average error in the K_I value was 15% with a maximum of 45% compared to the ASTM standard geometry analytical solution; in 2006 and 2008, Réthoré and Roux [43, 46] both claim an average 7% error in K_I and find values different by ∼15% when working on the same dataset with different field fitting approaches.

1.3.3 *J*-integral approaches

Due to the shortcomings discussed in the previous section (i.e. sensitivity to crack tip position uncertainty, necessity to rely on a displacement field that can be correctly defined analytically, etc.), the field-fitting methods might be advantageously replaced by direct evaluation of the J-integral from the full-field measured data. This is of particular interest in cases where the displacement field cannot be described by an analytical solution due to damage, an atypical material law or a complex loading history.

This approach has been implemented by Becker et al. within the JMAN framework [47, 48], where the strain energy release rate is determined from an area J-integral applied to DIC measurements. However, DIC can fail to determine the displacement vectors satisfactorily in the vicinity of edges or discontinuities in the displacement field, such as close to a crack [36]. Several methods have been offered to alleviate this problem. Réthoré proposed an algorithm based on enrichment of finite element-based DIC subsets [49], while Poissant and Barthelat [50] offered a modification of the DIC algorithm to allow the subsets to split along the crack path. Both methods aim at producing correct DIC data next to the crack path. These solutions are quite complex and are not generally applied, however, it is quite common in DIC analysis to simply exclude those doubtful measurements in the vicinity of the crack (i.e. masking). Consequently, data are missing from the

crack tip region where the highest strains (i.e. steepest displacement gradients) occur. In the context of the J-integral evaluation, data are also missing near to the traction-free surfaces of the crack. One solution to this problem has been proposed by Molteno [51] who used linear interpolation in the crack tip and crack flank region, while Yoneyama [52] proposed a finite element method to smooth the measured DIC displacement field. One should also consider that evaluation of J-integral from experimental data requires good quality data of the displacement field for the integral to converge. This quality can be difficult to obtain due to experimental constraints. This is why an approach based on FE post-treatment of the displacement fields [52–55] is of particular interest as it provides a clean displacement field, representative of the experiment, from which the J-integral can be calculated without convergence problems.

Another issue regularly encountered is the ability to compute stresses from strains in the case of complex material behaviours. This can be done by implementing a finite-element treatment layer between the full-field measurement step and the J-integral calculation step. This is used by Caimmi [55] to compute stresses from DIC-measured strains using a hyperplastic material model. With specific materials like composites, modified formulations of the J-integral can be used. Catalanotti [56] proposes a J-integral that takes into account the ply directions and the energy dissipation acting on a cohesive zone. He applied it to DIC measurement of a CT (compact tension) composite sample.

The case of mixed-mode cracks can also be solved using J-integral-like approaches. The interaction integral (M-integral) [57] can be used to separate the different modal contributions, however it is limited to a contour going through an elastic field due to the analytical auxiliary fields it uses. An example of the use of the interaction integral on DIC displacement fields can be found in the literature [42, 43, 58]. More recently the decomposition method offered by Molteno [51] allows separation of the mode I, II and III SIFs providing the crack path is known.

Figure 1.4: Stereo-vision set-up. Two cameras and two lights. Picture from GOM website (www.gom.com).

1.3.4 Stereovision and 3-D datasets

Stereovision and 3-D DIC

A major problem with DIC measurements and other full-field methods is out-of-plane displacement. Out-of-plane displacement can be defined as displacement of the sample towards or away from the camera's imaging plane. Even if limited by an adequate experimental design, it will originate parasitic strains in a single camera DIC analysis that does not use suitable optics. Also for the study of mode III fracture, one must be able to measure out-of-plane displacements.

In stereovision systems, two cameras are looking at the same region in space (Figure 1.4) and have a given depth of field that allow them to acquire a sharp image for a range of distances from the camera. Each camera thus has a focused imaging volume. The images of samples included in the overlapped volume between the two camera focused imaging volume can be processed simultaneously (after mutual calibration of the cameras), using a 3-D DIC algorithm to retrieve both in-plane and out-of-plane displacements.

Like standard DIC, 3-D DIC has been applied to fracture mechanics; in 1994, Luo [59] measured in-plane and out-of-plane displacement next to the crack tip of a stainless steel specimen. He showed that the measured out-of-plane displacement in vicinity of the crack tip is such that it would have impacted a standard DIC

analysis. In 1995, Helm [60], from the same group, published a standard calibration procedure and experimental set-up to perform 3-D DIC analysis that is still used nowadays in most of available codes. More recently, mixed-mode stress intensity factors for modes I, II and III have been determined for elastic materials on 3-D DIC calculated displacement fields using both field-fitting and integral approaches [51, 61]. The limitation of such techniques is that the determined field concerns the surface of the sample, and this can be not representative of the full specimen thickness in ductile materials; there is therefore an interest in determining the full-field displacements within the full volume of a sample.

In this work, the determination of mode III stress intensity factors from 3-D DIC datasets will not be considered. However, 3-D DIC will be used to obtain accurate displacement fields that are not affected by the out-of-plane displacement of the sample.

Digital volume correlation

Even if quantification of cracks in 3-D bodies is now routinely performed in FE frameworks, its application to full-field data is rare in the literature. Full-field data in 3-D can be obtained by the combined use of 3-D imaging methods and Digital Volume Correlation. The 3-D datasets are obtained using techniques like computed tomography [62], magnetic resonance imaging [63] or positron emission tomography [64]. The technique must be adapted to the type of material and length scale of interest.

Digital Volume Correlation (DVC) is a method that follows the same concepts than DIC but is applied to 3-D volume images. Correlation between an original and a deformed volume allows one to retrieve 3-D displacement vectors in the volume of interest. For DIC analysis, it is common to apply a speckle to the surface. However, for tomography it is necessary that trackable features must naturally be present in the material for the analysis to work, they can be an effect of the

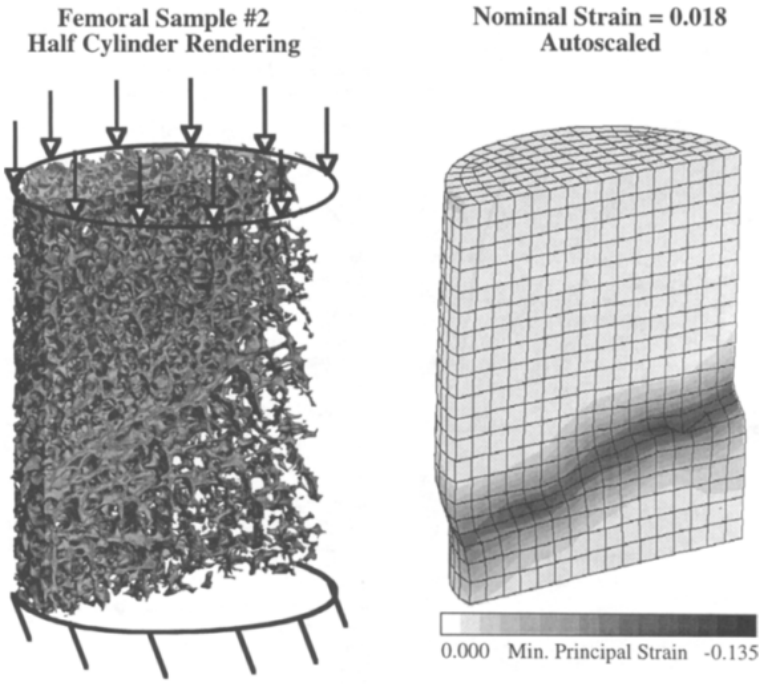

Figure 1.5: Damage in femoral bone, as shown in Bay's paper [65]. The damaged region is highlighted in the strain by a region of higher strain values. The natural microstructure of condyle bone makes DVC analysis feasible.

microstructure (Figure 1.5) [65] or of the contrast between constituents of the material. The DVC method was first used in 1999 by Bay to study damage in trabecular bone from X-ray tomographs (Figure 1.5) [65]. The original algorithm was subject to several limitations and was later progressively improved in terms of speed and accuracy by several authors [66–68].

Digital volume correlation has been used in the domain of fracture mechanics to do both quantitative and qualitative analysis of cracks. Between 2009 and 2011, Limodin and Réthoré [69–71] applied DVC analysis to tomography observations of a fatigue crack in nodular graphite cast iron; the crack length and opening displacements were observed and the SIFs were extracted by least-square field fitting of selected 2-D slices of the volume, the DVC results are also used as boundary conditions to retrieve the SIFs by FE calculation.

In 2013, Mostafavi et al. published works [72, 73] where they studied crack propagation in polygranular graphite using a stable geometry chevron notch

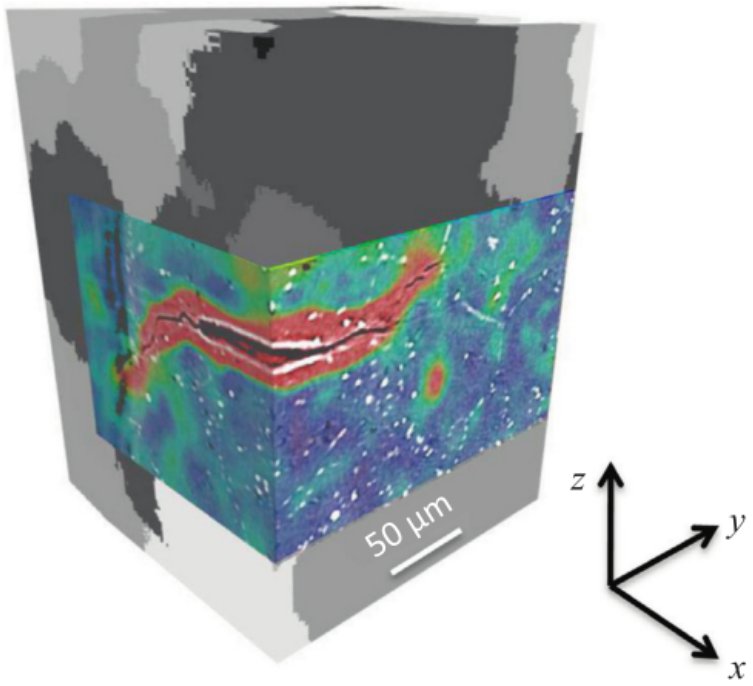

Figure 1.6: ε_{zz} strain map of a short crack in magnesium alloy as measured by Marrow et al [74]. Opening modes can be studied by looking at the U_x, U_y and U_z displacement. The underlying grain map was obtained using diffraction contrast tomography (DCT).

sample. Synchrotron tomography was used with DVC to study the crack opening displacement. The crack opening displacement was compared with cohesive FE models to highlight the presence of a fracture process zone. The SIFs were calculated from the observed crack length that was an input to the FE model. In 2014, Marrow et al [74] performed a quantitative characterization of a short fatigue crack in a magnesium alloy using micro-tomography coupled with DVC. This work showed the possibility of accurately determining the opening displacement and opening modes of three-dimensional cracks (Figure 1.6) the study was also interested in the effect of the crystal orientation on the crack propagation mechanism.

1.4 Diffraction methods for crack characterization

1.4.1 Diffraction techniques overview

In crystalline materials, elastic strains can be quantified by the analysis of diffraction patterns, obtained with monochromatic X-ray diffraction (XRD), energy-dispersive polychromatic X-ray diffraction (EDXRD) or neutron diffraction (ND) [75–77]. The periodic planes of atoms in the crystal lattice scatter the incoming radiation creating spherical waves that are not observable in most of the directions because of destructive interferences. The specific directions where constructive interference of the waves is observed are determined by Bragg's law (Equation (1.4)) where d is the spacing between the diffracting planes, θ is the incident angle, n is an integer and λ is the incident beam wavelength.

$$2d \sin\theta = n\lambda \tag{1.4}$$

X-ray diffraction methods in laboratory equipment only allow probing of a thin layer of the material due to strong attenuation; the brilliance of synchrotron high-energy X-rays can be used to look at specimens of the order of 10 mm thickness, depending of the material atomic number. Neutron diffraction presents the possibility of being able to go through much thicker samples, however as neutron cross-section does not behave linearly with increasing atomic number, its use is also limited depending on the constituting material (Figure 1.7).

The laboratory techniques will not be presented here as they have limited interest in establishing full-field strain maps, except in the case of EBSD analysis. In the XRD synchrotron technique [76], a monochromatic X-ray beam is targeted at the sample and a detector imaging plate is located a few meters away from the sample (Figure 1.8a). For a polycrystalline sample with no texture, each grain will create one or more (depending on symmetry) diffraction spot pair for each of

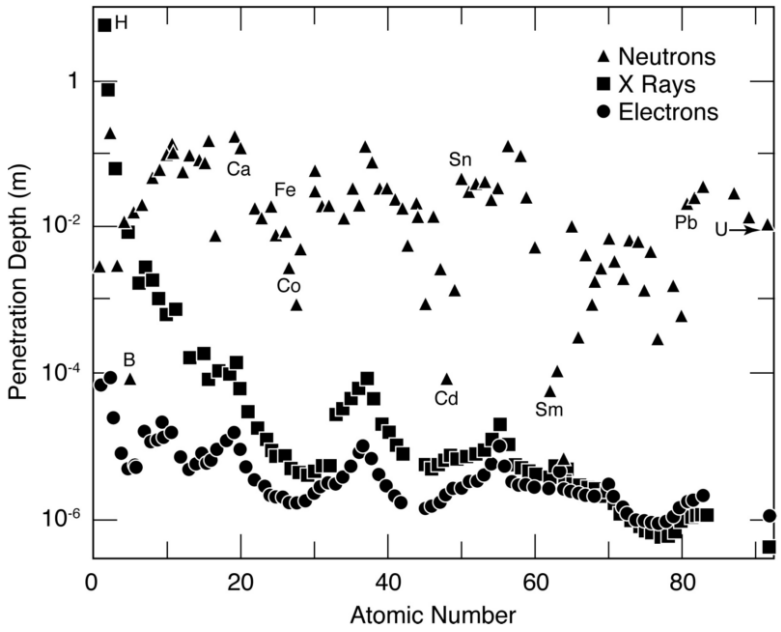

Figure 1.7: Penetration depth in an element for different incoming particles. The penetration depth is measured as the depth necessary to reduce the beam intensity by a factor $1/e$ [78].

diffracting plane family; the azimuth at which the spots are created is a function of the grain orientation. Therefore, with a sufficiently large number of grains, diffraction rings (i.e. all azimuths are "occupied") will be formed on the detector (Figure 1.8b). Following Bragg's law (Equation (1.4)) one can then determine the interplanar spacing for grains at different orientations by measuring the position of the ring at the different azimuths.

The EDXRD technique uses a polychromatic (white beam) synchrotron X-Ray beam targeted at the sample [76]. A multi-element horseshoe shaped detector (Figure 1.9) is placed a few meters away from the sample. For each element of the detector, the intensity vs. wavelength is recorded; as the fixed θ position of the detector is known, intensity peaks are observed for wavelengths that verifies Bragg's law (Equation (1.4)). From the position of those peaks, one can determine the interplanar spacing value. The d-spacing value is determined for each detector element thus providing this information at different azimuthal values (i.e. different grain orientations).

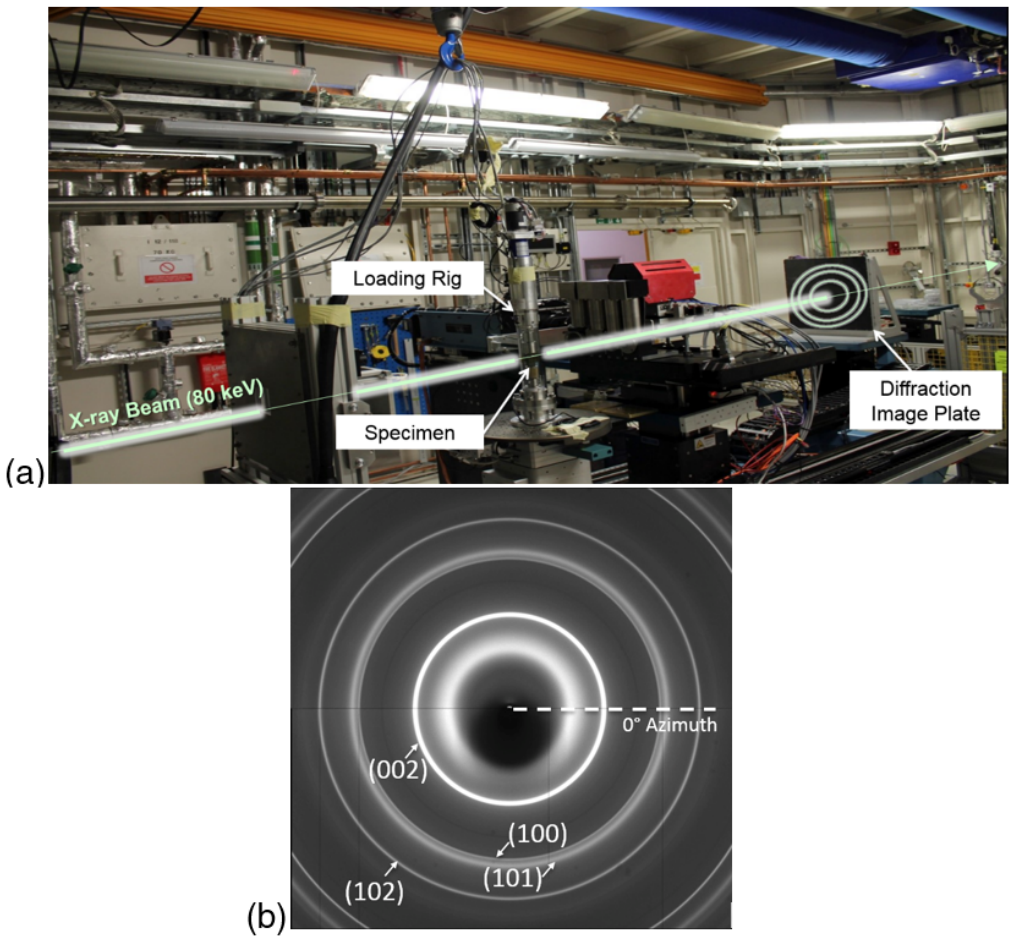

Figure 1.8: (a) Diffraction experiment set-up at Diamond Lightsource (b) Example diffraction rings from XRD with a gilsocarbon graphite sample.

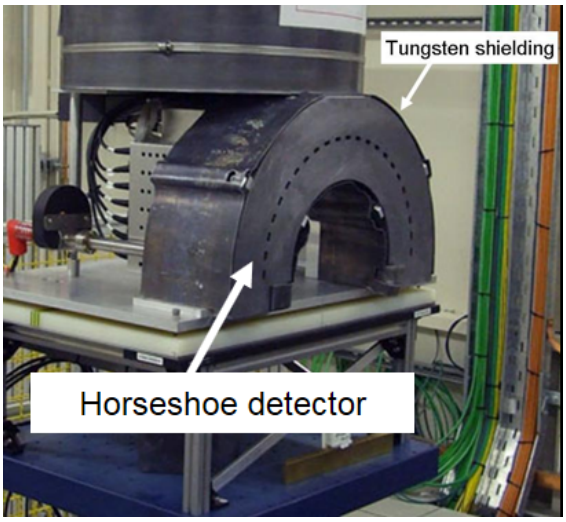

Figure 1.9: EDXRD horseshoe detector, I12 EH2 Diamond synchrotron.

With pulsed neutron sources, the principle is similar to EDXRD with the difference that the measured value is a time of flight [79]. The time of flight (i.e. particle speed) is proportional to the wavelength as defined by de Broglie's matter wave theory. It can therefore be linked to the d-spacing value. In steady-state reactor neutron sources, the scattering is measured as a function of the 2θ angle [79], similarly to what is done in synchrotron XRD, using a detector covering a large range of angles.

In all these methods, for a given position of the beam hitting the sample, a given gauge volume of grains will diffract and the interplanar spacing of the diffracting planes can be determined for this volume. As the elastic strain consists of a change in the lattice spacing, it can be calculated from a strain free value of the d-spacing and the current d-spacing using Equation (1.5). By performing the measurements at multiple azimuths the full strain tensor may be obtained using the procedure described in [76] and shown in detail in Chapter 3 of this thesis.

$$\varepsilon_{hkl} = \frac{d_{hkl} - d^0_{hkl}}{d^0_{hkl}} \tag{1.5}$$

Realization of those measurements at several positions in the sample allows creation of elastic strain maps of the specimen. Those are frequently obtained using synchrotron X-ray diffraction techniques (Figure 1.10b) thanks to the short acquisition time per point (from 0.1 to a few seconds depending on the size of the gauge area and the dead time of the acquisition system [76]). Such mapping is less common with pulsed neutron source diffraction where the exposure time is usually longer (of the order of 60 seconds with the recent improvements in detectors [76]). However they can be realised with less time constraints with steady state neutron sources (Figure 1.10a).

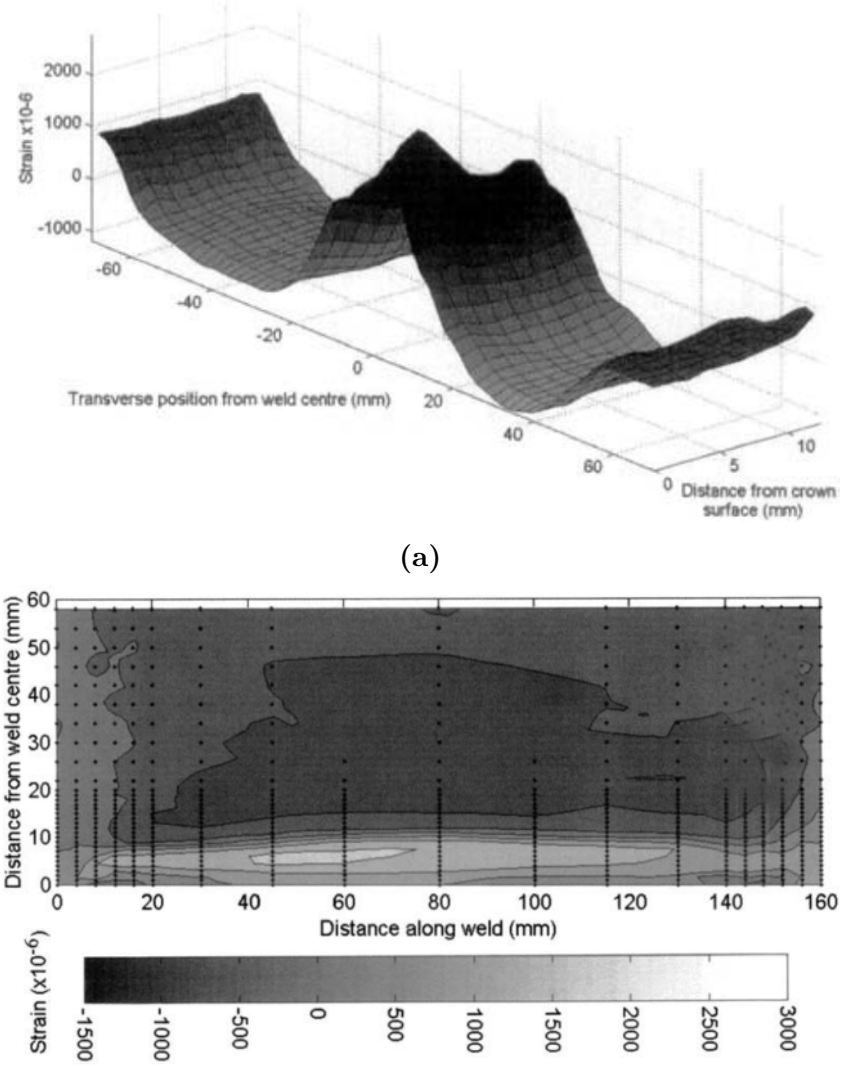

Figure 1.10: (a) Map of longitudinal strains from steady state neutron source diffraction, the sample is a 12.5 mm thick ferritic steel plate [76] (b) Synchrotron XRD map of measured longitudinal strains in a TIG welded 3 mm thick Al plate [76, 80].

1.4.2 Full-field strain mapping applied to crack characterization

Maps of elastic strains are of particular interest in the study of residual stresses. For example, neutron and X-ray diffraction have been used to study residual stresses in vicinity of weld heat affected zones in TIG welding [81] or the effect of inclusions in the strain repartition in metal matrix composites [82]. In the domain of fracture, the first applications were to study the crack-tip strain distributions of a fatigue crack

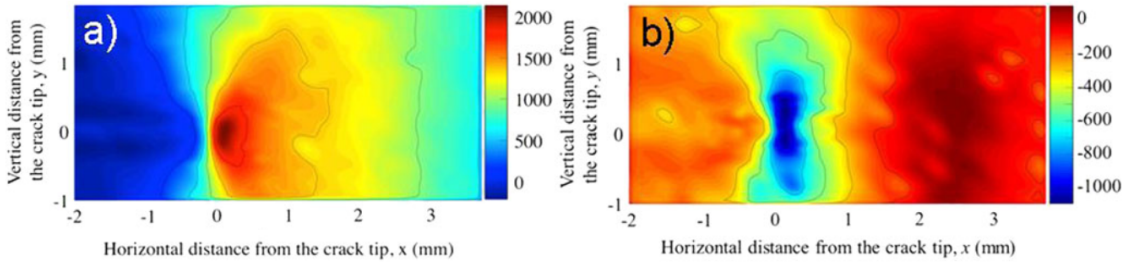

Figure 1.11: Map of the stresses (MPa) in the crack loading direction calculated from the synchrotron XRD analysis (a) at overload (b) after overload, at minimum load [84].

and the effect of overloads and closure on it [83, 84]. In Figure 1.11, the residual stresses induced by the overload are clearly observed. The mechanical shielding effect of crack bridging in stress corrosion cracking was also studied by these methods [85].

Combined diffraction strain mapping, X-ray tomography and FE modelling [86] has also been used to study the effect of overloads on fatigue cracks. Crack closure was highlighted by visual observation of the tomographs whilst the residual stress map post-overload was compared with predictions from FE modelling. Crack elastic strain field in complex geometry composite materials can also be studied and the matrix and fibre strains can be separated providing the fact those are made of different materials and thus generate different diffraction peaks (Figure 1.12). This allowed crack field quantification and development of FE models [87].

Diffraction analysis of elastic strains can also be combined with strain measurement methods such as image and volume correlation [88], allowing the link between elastic crystal strains and bulk strains to be made and the possibly to see the effect of damage from such measurements.

To support such studies, it is useful to quantify the crack field, for instance to determine the stress intensity factor of a crack. Least-square field fitting of the theoretical Williams' series to the strain maps was used to this end and applied to the study the relationship between the SIF value and the growth rate (da/dN) for a fatigue crack [89]. In this thesis, a method to apply the J-integral to elastic strain maps (i.e. only the strains are known, not the displacements)

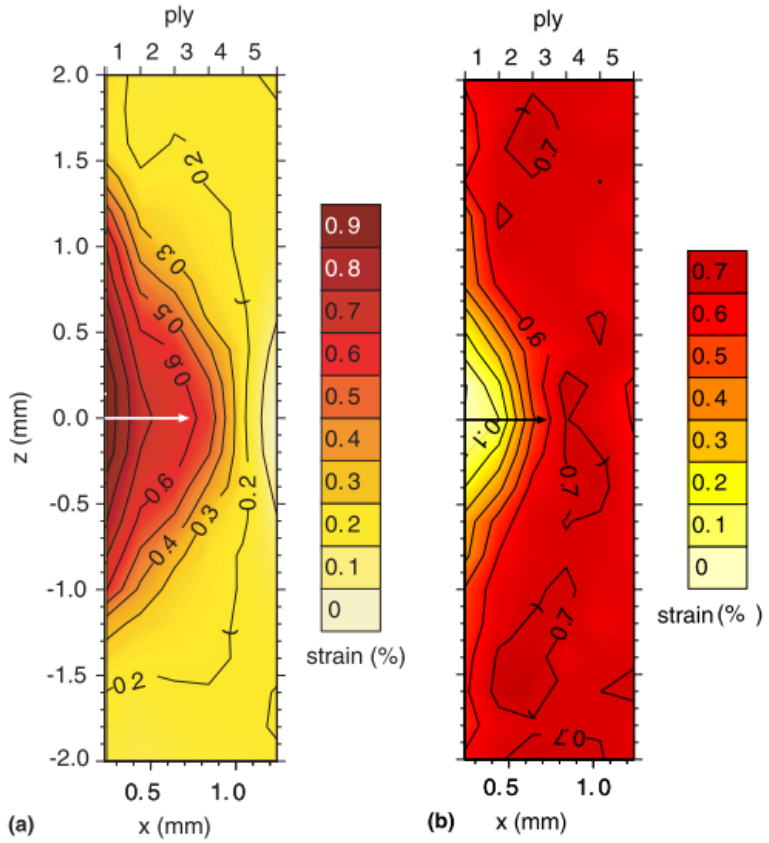

Figure 1.12: (a) fibre and (b)matrix elastic strains for the same region of a Ti-6Al-4V/SiC fibre composite sample as determined in [87]. The use of different diffraction peaks allows the separation between matrix and fibre strains.

is presented and discussed in Chapter 3; this is of particular interest when the elastic strain field shape might not follow theoretical fields due to the presence of a damaged area in the sample.

1.5 Conclusion

In this first chapter, the basic principles of fracture mechanics such as the notion of stress intensity factor and J-integral were briefly presented; their evaluation is the objective of this work. Then methods for crack quantification were presented alongside with key works and state of the art applications. The emphasis has been on works that involving use of image and volume correlation techniques as well as diffraction strain mapping techniques as they are the techniques of

choice in this thesis.

From this literature review different points of the current state of the art in crack quantification techniques were highlighted. Firstly, most of the techniques rely on the assumption of linear elasticity or on the assumption that the material displacement/strain fields follow a given analytical solution. In this work a method based on the J-integral is offered that does not make those assumptions. Additionally, the recurrent problem of J-integral contour definition and stresses calculation is offered to be addressed by the use of FE processing of measured displacement or strains. A lack of versatility in the current techniques is also observed with the development by authors of case-specific approaches or codes that often cannot deal with challenges like complex crack shape or complex material laws, this approach discussed in this thesis aims at mitigating this point. Finally, a limited number of works were found coupling several full-field measurement techniques like image/volume correlation and diffraction mapping. Those type of experiment are particularly interesting for fully characterizing a material behaviour and one example will be presented in this work.

Until they become conscious they will never rebel, and until after they have rebelled they cannot become conscious.

— George Orwell's *1984*

2

FE optimized J-integral calculation from DIC

Contents

2.1 Introduction

As presented in the literature review, the J-integral is a way to calculate the strain energy release rate from full-field displacement data. In a linear elastic body, it

describes the potential elastic energy that is available to propagate the crack and increases its surface area. In this chapter, a robust and efficient method is developed and demonstrated to obtain the crack's strain energy field, as the J-integral, by using measurements of the surface displacement field. The analysis method makes use ofa finite element approach, and is highly versatile and easy to implement, being also able to deal with noisy datasets and missing data close to the crack. The use of standardised FE software to perform the J-integral calculation alleviates the difficulties that may occur in efficient definition of integration contours. The method is benchmarked using synthetic datasets to assess the sensitivity to image resolution, uncertainty in the crack tip position, crack tip plasticity and camera noise. The possibility to separate modal components of the stress intensity factors via the application of the interaction integral is also considered.

A validation experiment is presented that compares the obtained J-integral with the conventional evaluation for a fatigue pre-crack in a standard compact tension specimen of an aluminium alloy. Finally, the decomposition of the stress intensity factors modal contributions is presented in an analysis of data from a brittle PMMA Arcan geometry specimen.

2.2 Method for analysis of DIC-measured full-field displacements

2.2.1 Digital Image Correlation (DIC) Analysis

The objective of the DIC analysis is to measure the change in the displacement field as a crack is loaded, and to identify the crack path and crack tip. An image dataset containing an original view and a deformed view of the sample surface is obtained, and this dataset is analysed by DIC using a two-step approach to provide two different results for the displacement field (Figure 2.1). The first step, A, is to retrieve the displacement vectors with optimal precision. The second

step, B, is to determine the crack tip position and the crack path, with optimal spatial resolution. In both steps a Least Square Matching (LSM) algorithm [90] has been used for the DIC; this efficient algorithm has the advantage of being insensitive to intensity changes between images. Each subset (known sometimes as an "interrogation window") provides a displacement vector. The displacement vector precision decreases, and noise increases (i.e. displacement uncertainty), with decreasing subset size, as smaller subsets contain less information [91]. In this work, the software Davis (version 8.3.0) from LaVision has been used for the DIC analyses, but other tools are available, such as Ncorr (an open-source Matlab software[1]), and could be used equivalently. In the Davis software, the subsets are equally spaced and usually square. The resulting displacement vectors lie on a regular grid with an interval that depends on the final subset size and overlap; for instance, a final subset size of 32 pixels × 32 pixels with 50% overlap results in a grid with 16 pixels interval (i.e. a step size of 16 pixels).

For the Step A analysis, the crack and its surroundings are masked (i.e. box PQRS, Figure 2.1), so its discontinuity does not perturb the accuracy of the description of the displacement field that surrounds it. The mask is obtained by excluding those displacement vectors with low correlation coefficient (typically, for a good quality image, a correlation coefficient threshold of 0.8 is used).

The subjective choice of the correlation coefficient threshold is dependent of the data and should be determined such as it removes outliers and poor quality results (e.g. next to the crack lips) but does not censor too many vectors. The correlation coefficient value can be chosen empirically by looking at the strain maps where abnormalities in the displacement field are highlighted. The correlation coefficient threshold is then adjusted by trial and error until a good compromise between number of remaining vectors and data cleanliness is obtained.

[1] http://www.ncorr.com/

The subset size in this analysis step is chosen to give a good compromise between low uncertainty in the calculated displacements and sufficient spatial resolution to map the variations in the displacement field. From a dataset of known rigid body displacement applied to the sample, the DIC error vs. subset size curve can be obtained. It is an exponential function increasing when the subset size decrease; its observation allows the choice of the smallest subset size (i.e. maximization of the spatial resolution) in the region where the error is still small. A relatively large subset size tends to be used (such as 64 × 64 pixels to 128 × 128 pixels).

The Step B analysis is performed using a small subset size, typically 8 × 8 pixels. Such a subset does not provide a good quantitative evaluation of the displacement field because of the increased uncertainty in its results, but it is a convenient method to determine the crack path and crack tip position. Subsets that overlap the discontinuity of the crack tend to abnormally high displacement gradients (i.e. strain) and/or a low correlation coefficient. These can be used to segment the results dataset, by thresholding, to identify the coordinates of the crack path with a precision of about one subset step size. The method applied here has been chosen for its simplicity, but more sophisticated methods, e.g. based on edge detection algorithms such as the phase congruency method [**Cinar2015**], may also be used.

After completing both steps, the vectors of the displacements in the plane of the surface of the sample have been determined with good precision to define the crack field (Step A). The data lie on a regular grid, which is not fully populated due to censoring (i.e. masking) of low quality DIC results in the vicinity of the crack. Other regions, remote from the crack, may also have censored vectors where the correlation quality is low, this may be due to loss of camera focus or parasitic light reflections in optical observations. The crack path has also been determined (Step B), and is described using a finer grid within the masked region.

2.2.2 Finite Element (FE) treatment

A finite element approach is used to extract the J-integral from the DIC-measured displacement fields. This is done by importing the displacement field as a set of full-field boundary conditions into a finite element model of the crack. A software tool (OUR-OMA) has been written to facilitate this; coded in Python, it runs inside the Abaqus software via its scripting capability[2]. A FE model is created that is registered with the DIC analysis results (Figure 2.1a) so that the Step A DIC dataset and the FE model share the same coordinate system. The spacing of the nodes of the FE mesh is chosen to be coincident with the Step A DIC result grid, using square elements. The FE nodes are at the same positions as the DIC grid nodes, which make the two grids inherently registered. This avoids the requirement for interpolation when subsequently applying the DIC displacement field to the FE mesh. The FE mesh is then locally refined to insert the crack within the region where the Step A displacement vectors have been censored. A rectangular bounding box is defined that contains the crack and matches the masked region. This region is remeshed separately using the Step B description of the crack path, with nodes doubled along the crack path to allow the crack to open. The mesh within the bounding box is attached to the nodes of the surrounding coarse mesh in the FE model (Figure 2.1b, c). The mesh density at the crack tip is aimed to be 3 times finer than the Step A mesh, as a good mesh quality cannot be achieved if the mesh density difference is too large between the two regions. This is done using a constraint established in the FE meshing tool that allows the mesh density to change during meshing to converge towards the finest

[2]OUR-OMA (Oxford University Reinjection-Optimized Meshing Add-on): the software is available from the author as a GUI or command line version, compatible with Abaqus version 6.10 to 6.13. The GUI version, distributable as an Abaqus plugin, can deal with common experimental cases (e.g. straight cracks). The command line version is more versatile (e.g. kinked and curved cracks).

achievable mesh density with good quality elements[3].

The results from Step A are injected onto the model by enforcing node displacements to the measured displacement vectors. These local boundary conditions are applied everywhere except in a "free" region that is free to deform in accordance with its surrounding boundary conditions and material properties (i.e. box P'Q'R'S', Figure 2.1d). This free region includes the remeshed region (PQRS) that surrounds the crack and can be extended to further censor the Step A DIC dataset. After "injecting" the displacement field data into the FE simulation using OUR-OMA, the FE software can be used to assign a material law to the model. Plane stress or plane strain elements may be used. In this work the Abaqus FE software package (version 6.13) has been used, and both linear elastic and inelastic (Ramberg-Osgood) material laws have been examined, as they are both compatible with the J-integral calculation.

The Abaqus software implements the domain integral method to calculate the J-Integral. It uses the Virtual Crack Extension method, which applies a virtual displacement field (Q-field) to increase the crack length and so evaluate the change in strain energy. To define the Q-field properly, the software requires the definition of a q-vector; this is normal to the crack front, and, if a 3D geometry is considered [92], also lies in the local plane of the crack. In the 2D model considered here, the q-vector is chosen to be collinear with the linear segment of the crack path that is closest to the crack tip. The J-integral calculation is performed over several contours to check for contour independency, and thus retrieves the potential elastic strain energy release rate of crack propagation that is due to the measured displacement field (Figure 2.1e). In the Abaqus analysis, the contours start from the crack tip and expand radially.

[3]In Abaqus, this is done by selecting the "Allow the number of elements to increase only" constraint when defining the local mesh seeds. The minimum aimed mesh side, set to 1/3 of the Step A mesh density by default, can be modified at will.

As a further step, it is possible for linear elastic materials to separate both the mode I and II stress intensity factors using the interaction integral method [61, 93, 94]; the case of mode III loading, that requires 3-D DIC techniques to extract the out-of-plane displacement is not discussed here. The interaction integral calculation is natively defined in Abaqus software and can be calculated alongside J-integral for elastic problems.

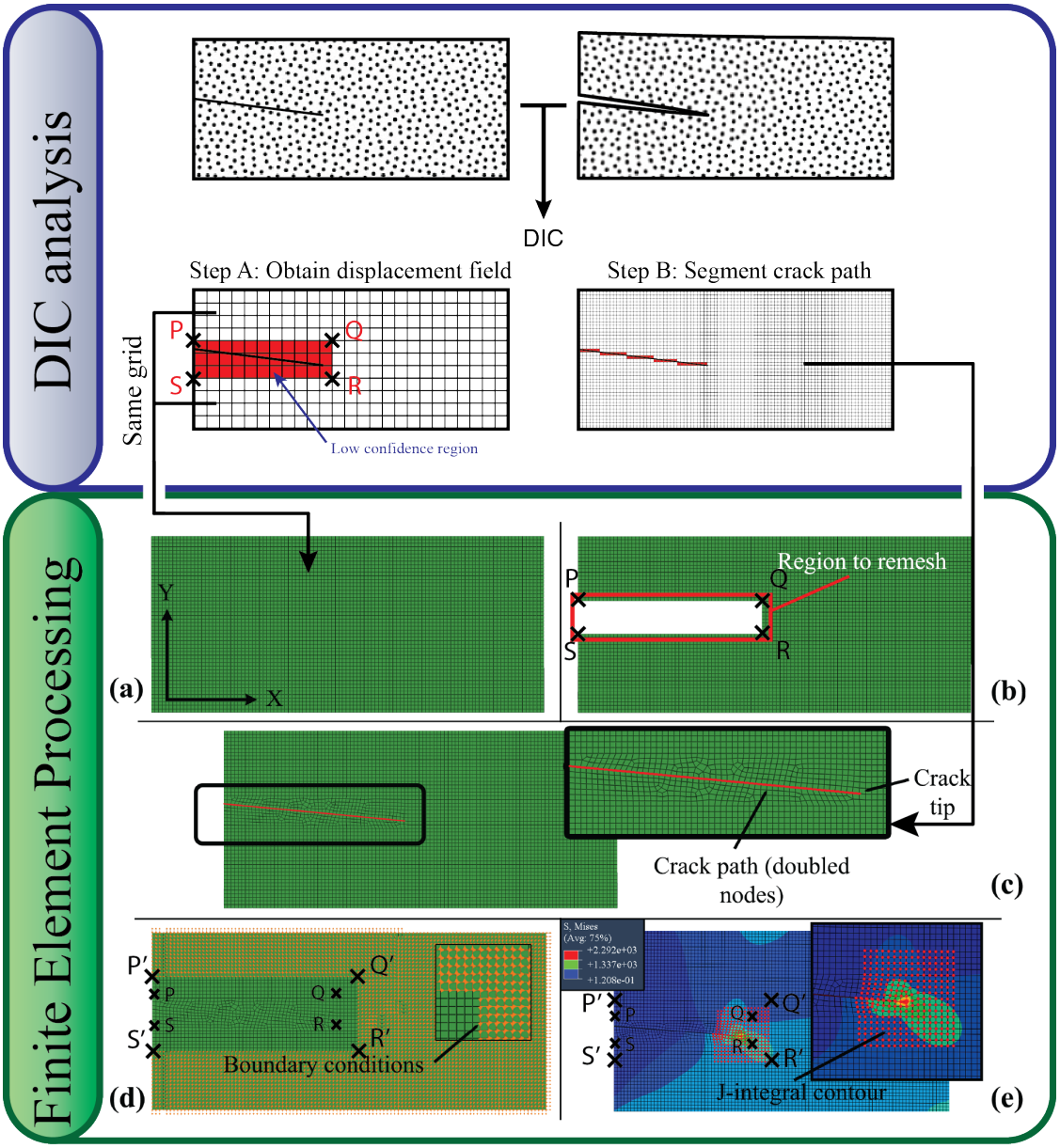

Figure 2.1: Steps of the J-integral calculation process. DIC Analysis – the displacement field is obtained in a two-step analysis with a coarse (step A) and fine (step B) subset size to map the field precisely and identify the crack path. Finite Element Processing - (a) FE mesh registered with the coarse DIC grid. (b) The region containing the crack [PQRS] is deleted for remeshing. (c) The crack is inserted in the re-meshed region, nodes are doubled on the crack path. (d) Boundary conditions are enforced on the FE nodes, except in the free region P'Q'R'S', which always includes the region PQRS. (e) The J-integral is calculated.

2.2.3 Production of synthetic image datasets

To examine the sensitivity of the J-integral calculation method to the input data quality, it is necessary to evaluate datasets with known image noise, crack geometry and deformation. Experimentally, these depend on the applied load and material properties such as elastic modulus. However, obtaining these in a controlled manner via experiments is challenging and it is of interest to be able to vary these factors independently. These constraints can be fulfilled using synthetic datasets, which allow comparison between an input J-integral and the output calculated via DIC analysis.

The objective is to produce synthetic deformed images for any displacement field. The image needs to be equivalent to that obtained experimentally by a camera viewing the surface of a deforming sample (in-plane deformation), and the image also needs to be suitable for DIC analysis. For a crack, a description of its displacement field is required that can be used to deform the image. The Williams' series [8, 95] provide an analytical solution for the displacement field around a crack in an elastic material. They are widely used to evaluate crack displacement fields [36], and could be applied to deform an image. However, the Williams' series are only relevant to linear elastic materials. The Hutchinson-Rice-Rosengren (HRR) solutions [12, 13] for crack tip strain and displacement fields in power law hardening solids are also available and can be used to simulate elastic-plastic materials. However, for both methods the assumptions made (e.g. infinitely large solid) and their limitation to certain loading conditions restrict their versatility. Finite element simulations can provide the crack displacement field for more general conditions and material properties, which may then be used to deform an image to create a synthetic dataset. A MatLab-coded tool, ODIN, was developed to produce the synthetic images, which could then be evaluated to assess the accuracy of the DIC/FE analysis method. ODIN uses an input displacement field, obtained from a FE simulation, to deform

digital images for subsequent DIC analysis. As the displacement field is obtained from a finite element model, this allows datasets to be generated with any material law for any crack geometry and boundary conditions. As new surface creation is supported in FE simulations, the progressive effects of crack propagation on the displacement field may also be simulated, but that has not been done in this work.

The actual FE output is a simulated displacement field and the connectivity of the elements. These are used together to deform an input image of a speckle pattern. The ODIN code examines each FE element in turn, identifying the pixels in the original image that are within that element. Using the element's nodal displacements, the displacement of each pixel within the element is calculated by interpolation with the element shape function; the shape function is a linear weighting function that, for each point within the element, returns the weight of each element node. The result is a cloud of points that describe how each of the pixels of the original image is translated to its new position in the deformed image. The pixel displacements are not integers of the pixel size, so interpolation is required to obtain the pixel intensities of the deformed image.

In this work a bi-cubic interpolator is used [96] as a compromise between computation time and interpolation quality. Background padding (black pixels) is added to either the original reference or deformed image, according to the displacement field to produce a dataset with reference and deformed images of the same size. It is important that the mesh density is sufficiently fine in the FE model used to generate the displacement field that is then applied within ODIN to deform an image; in testing of the ODIN code, it was found that interference was observed between the interpolators implemented in the DIC algorithm and ODIN when large FE elements were used. Such interference is characterized by stripes in the strain field subsequently obtained by DIC analysis of the deformed image (Figure 2.2). Empirically, it was found that keeping the number of pixels per element below 20×20 avoided this.

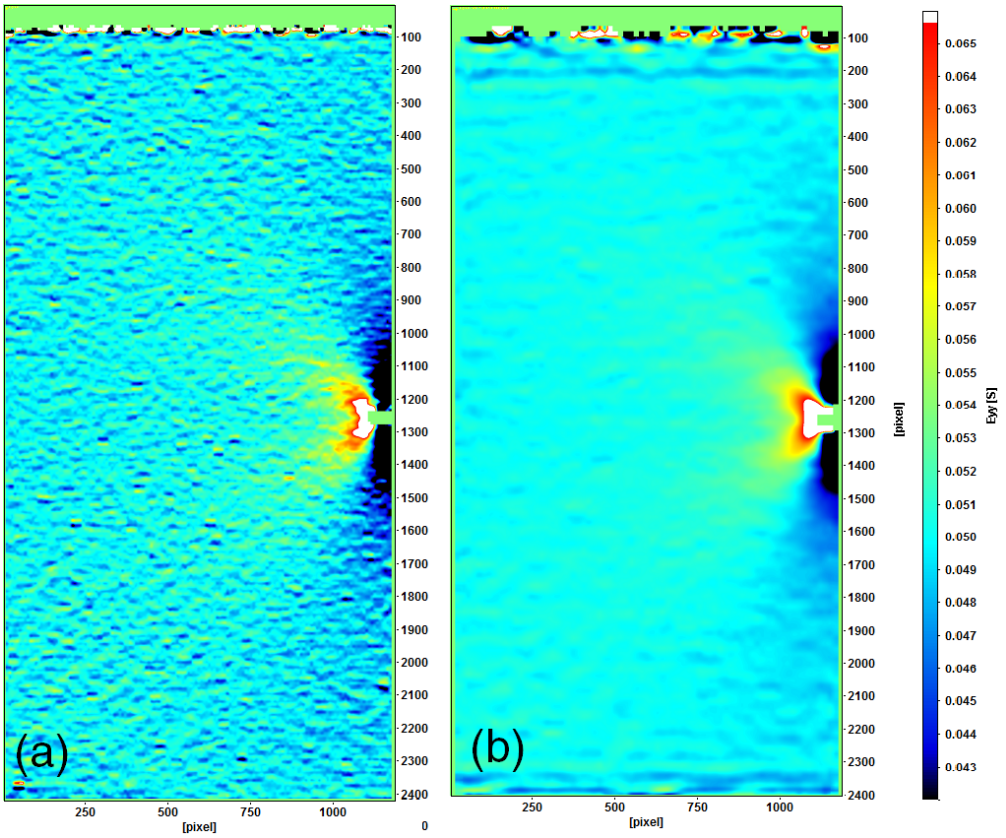

Figure 2.2: DIC analysis run on the same FE model with different mesh sizes (a) average of 36 × 36 pixels per element (b) average of 6×6 pixels per element.

In summary, the developed ODIN code can create synthetic images of a deformed sample with any material law that is implemented in the FE software. In the following section, ODIN will be used to develop image datasets for benchmarking tests to assess the accuracy of the J-integral calculation method.

2.3 Synthetic and Experimental datasets

2.3.1 Pure Mode I - Synthetic Datasets

The benchmarking tests with synthetic datasets were performed to quantify the inherent errors arising in the calculation of the J-integral. The aim was to separately investigate the effect of different parameters (image resolution, noise, etc.). The examined case simulates a straight crack, normal to the edge of a 60 × 60 mm plate; the plane stress condition was assumed. The initial crack length was 15 mm, and it

was loaded in pure mode I with tension applied to the two edges of the plate as fixed displacement boundary conditions to achieve the desired stress intensity factor. The other edges were not constrained. Two materials laws have been examined; a linear elastic model with the properties of an austenitic stainless steel (Young's modulus E=170 GPa, Poisson's ratio ν=0.33) and an inelastic, Ramberg-Osgood model optimized to fit the Al 2024-T351 stress/strain tensile curve (E=73 GPa, yield stress σ_y=350 MPa, exponent=7.5, yield offset = 1.31, ν=0.3) [97]. A mesh with a square element size of 0.1 mm side length was used; agreement (less than 0.5% difference) was obtained between the SIF obtained by the elastic FE solution and the SIF obtained from the analytical solution for this geometry [98]. The non-linear inelastic models were implemented at two applied stress intensity factors to examine the effect of crack tip plasticity. The linear elastic model needed to consider only one stress intensity factor.

The synthetic image is a 16-bit uncompressed TIFF file with a well-defined and optimal speckle pattern. This was obtained by processing of optical images; two different images of a porous concrete surface were averaged and a Gaussian blur was applied. A section of the resulting image (500 × 500 pixels) is shown in Figure 2.3a. This image contains features of different sizes, has a good occupation of the levels of grey spectrum (Figure 2.3b) and presents low periodicity, as shown by its autocorrelation map [99] (Figure 2.3c).

Experiments are typically constrained by the magnification of the digital image relative to the measured displacements, as it is usual for the speckle pattern to be optimised for the imaging system. To simulate this situation, the pattern was maintained as a constant in terms of pixels (i.e. an individual speckle is always the same size in pixels), and the effect of magnification was investigated by changing the pixel size relative to the displacement field. This was done by defining the camera pixel size, and so also determines the physical area of the displacement field that is contained in a given subset of N × N pixels (Figure 2.4). An alternative

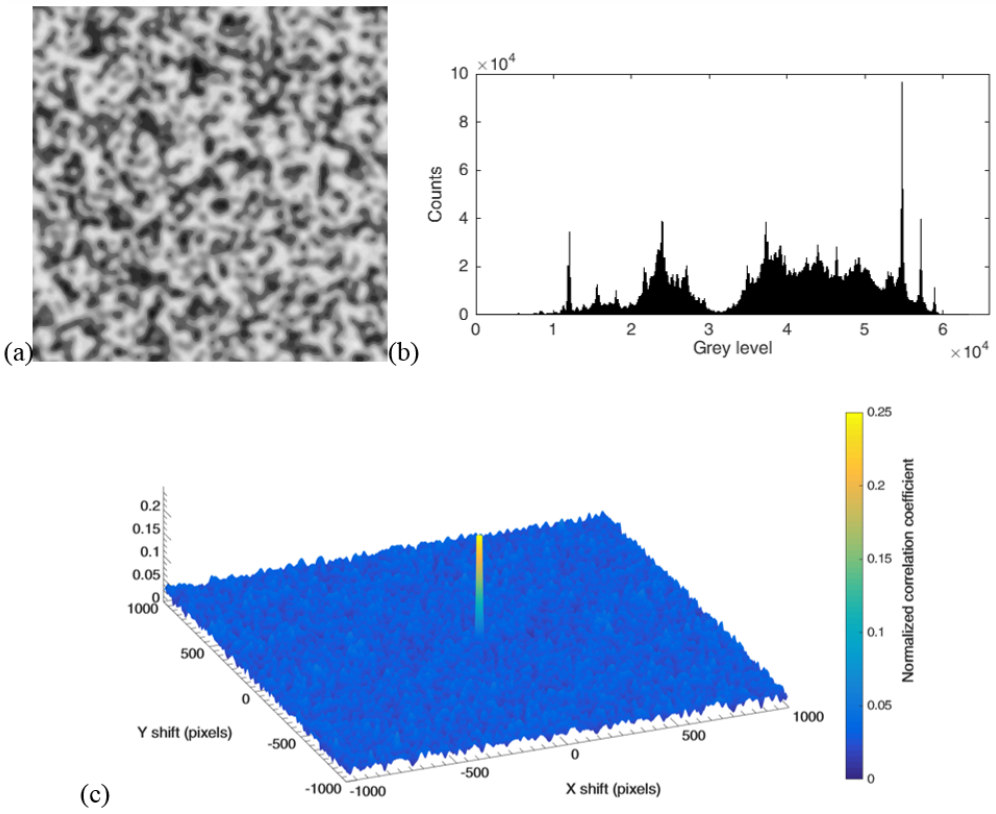

Figure 2.3: (a) Section of the optimized speckle pattern (500 × 500 pixels) used for the synthetic images. (b) Full image histogram (2048 × 2048 pixels) of the speckle pattern, the horizontal scale uses a bin size of 40 greyscale intensity levels. (c) Autocorrelation map of the full image for different shifts. The correlation coefficient is 1 when no shift is operated, and the autocorrelation peak has a full width at half height of 4 pixels. The non-periodicity of the pattern demonstrates its suitability for DIC analysis.

analysis could be done with a constant pixel size and variation of the image area (e.g. upper row of Figure 2.4), but this would increase uncertainty in the DIC measurements at high magnification as the speckle pattern would become non-optimal. To investigate the effect of image resolution on the quality of the results, datasets were created with different camera pixel size. The linear elastic model was used to produce 3 different datasets at 17, 22 and 33 μm/pixels. The inelastic datasets were at 17 μm/pixels only.

The effect of image noise was studied using the 17 μm/pixel dataset of the linear elastic crack. Additive white Gaussian noise for signal-to-noise ratios (SNR) from 45 dB to -5 dB was applied to both undeformed and deformed images; the SNR

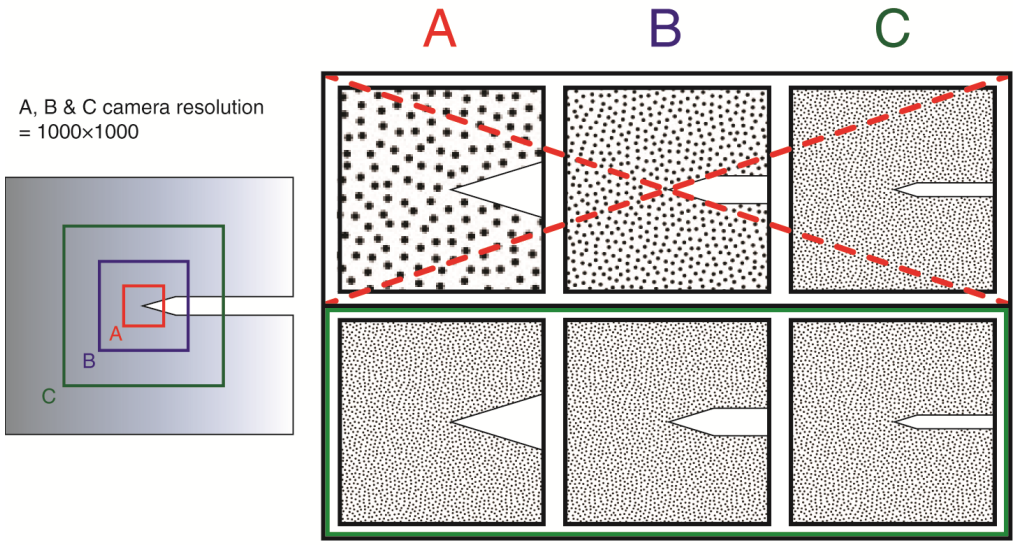

Figure 2.4: The camera pixel size is adjusted so that the speckle pattern remains constant and optimal. The upper row (dash-line cross) shows the effect of a fixed pattern size not correctly optimized to the camera pixel size. The lower row shows the case investigated in this work where the pattern speckle size is effectively optimized for the different magnifications.

was the same for both images and with different random distributions. The noise power was evaluated as its variance and the signal power as a root mean square of the pixel intensity [100]. A good image quality in an experiment would be expected to have SNR values between 40 dB and 60 dB, hence the noise levels investigated represent the range from medium image quality (45 dB) to very poor quality (-5 dB). The conditions of the obtained datasets are summarised in Table 2.1. Each dataset comprised the original image and its state after deformation using ODIN. The FE solutions used to deform the images were obtained in Abaqus using the relevant elastic or inelastic material law.

Table 2.1: Summary of parameters used to produce the synthetic datasets with different material models (linear elastic or elastic-plastic). The applied K field is calculated using FE and the indicated material model. The pixel size, image dimensions and amount of noise (signal to noise ratio, SNR) that were used in ODIN to produce the synthetic deformed images are shown.

Material model	Applied K_I (MPa.m$^{0.5}$)	Pixel size (μm/pixel)	Image size (pixels)	SNR (dB)
Linear Elastic	112.7	17	3600×3600	-5, 0, 5, 10, 15, 45, ∞
		22	2700×2700	∞
		33	1800×1800	∞
Ramberg-Osgood	37.2 47.7	17	3600×3600	∞

2.3.2 Mixed mode - synthetic datasets

The interaction integral is an additional layer that one can use above the J-integral calculation to separate modal contributions [61]. This was not the core of this thesis work and so was not benchmarked against FE-simulation data. However, a feasibility study of the method is presented in the experimental section, and a similar benchmark to the one presented for the pure Mode I method could be performed.

2.3.3 Mode I Fatigue crack experimental dataset

An experimental dataset was obtained using a fatigue pre-cracked Compact Tension (CT) specimen of an aluminium (Al2024) alloy. The sample machining and pre-cracking was performed with the help of Dr Mostafavi at the University of Bristol, the rest of the testing was made at the University of Oxford with the help of Dr Dyson and Mr Cinar at the Department of Engineering.

The material was provided by Airbus Group as a 20 mm thickness plate in the T351 condition (i.e. solution heat treated and stress-relieved by stretching). The specimen dimensions, compliant with ASTM E399-09 [101], are specified on Figure 2.5a; the specimen thickness B is 20 mm and the orientation is LT. The Young's modulus, E, of the tested material was measured to be 72.5 ± 3 GPa

using a resonance method[4] [102] with a sample of dimensions 71.7 × 20.0 × 3.67 mm; the value quoted in the literature [103] for Al2024 is 73.1 GPa. The Vickers' hardness was determined at 146 ± 12 (standard deviation for 10 measurements); the literature value for the T351 heat treatment is 139 [103].

The specimen was fatigue pre-cracked at a frequency of 10 Hz at a load ratio (maximum/minimum load) of 0.1. Load shedding and optical observation on one surface maintained the maximum applied stress intensity factor below 15 MPa.m$^{0.5}$; this corresponds to 45% of the reported mode I plane strain fracture toughness, K_{Ic}, of 34 MPa.m$^{0.5}$ for this alloy in the T351 heat treatment [103]. The pre-crack was propagated to an average depth of 4.95 mm from the notch tip (a range of ±0.25 mm was measured on either side of the sample after pre-cracking) to obtain a ratio $a/W = 0.5$ (i.e. $a/W = 0.499 \pm 0.004$ mm), where a is the crack length and W is the specimen width (60 mm). The maximum load at the end of fatigue pre-cracking was 7.43 kN, which was applied over the final 1.5 mm of crack propagation. After pre-cracking, one surface of the sample was polished with grit-600 SiC paper and cleaned with ethanol. A non-reflective speckle pattern consisting of white and black spots was then applied using spray paint (Hammerite® smooth white & Rust-oleum® satin black) from a distance of ∼1 m. A clip-gauge displacement transducer (Instron 2620-604 Extensometer, precision better than 0.1%) measured the crack mouth opening with load. The clip gauge was attached to knife-edges (thickness 7 mm) that were mounted on the sample edge (Figure 2.5a). The crack mouth opening displacement (CMOD) at the specimen surface was calculated from the clip gauge, using a correction coefficient for the actual location of the gauge. The correction was obtained via a 3D linear elastic FE model of the test specimen for a crack depth a/W=0.5, and was determined from the calculated opening displacement at the location of the gauge for five different values of CMOD

[4]The sample used for the resonance method was excited in flexural resonance. The uncertainty in the obtained modulus comes mainly from measurement uncertainties in the plate dimensions of ± 10 μm.

in the 3D-FE model, a least-squares linear fit (R^2>0.99) was applied to the results to find the correction coefficient, which was 0.9752.

The stereo-DIC system comprised 2 CMOS Toshiba-Teli CSB4000CL-10A cameras, each capturing an image size of 2008 × 2047 pixels with a 10-bit depth. The cameras were positioned approximately 160 mm from the sample surface, on the same height with a 20° angle between cameras (Figure 2.5b). With this set-up, the achieved pixel size was 15 μm/pixel on the re-projected images, as determined from the calibration parameters. Image acquisition was performed using an in-house LabVIEW code with 2 PCI-1428 acquisition cards, which allowed synchronized capture with timing accuracy better than 1 ms. A 058-5 LaVision 3D calibration plate was placed on the surface of a test specimen that was positioned in the mechanical test frame (Instron 5982, with a 100 kN load cell). Lighting was achieved using two 36-LED spotlights, with one placed above each camera. The DIC calibration, using LaVision Davis 8.3.0 software, applied the polynomial calibration algorithm and the obtained re-projection error was less than 0.4 pixels for both cameras - the re-projection error is the mean difference between the positions of the calibration marks in the calibration image and their known positions, after correction.

The sample was loaded in a series of quasi-static cycles that progressively increased in magnitude up to 25 kN. An initial pre-load of 130 N was applied, and after each cycle the sample was unloaded to the same pre-load. Images were recorded at the maximum load and minimum load in each cycle. DIC analysis of images at the maximum and minimum loads was performed relative to both the initial pre-loaded reference state ("extra-cycle"), and also to the minimum loaded state at the end of the previous cycle ("intra-cycle"). In each case, the Step A analysis employed a square subset dimension of 32 pixels with an overlap between subsets of 75%. A threshold correlation coefficient of 0.85 was used to censor the displacement vector results; additionally, all vectors within 0.5 mm (equivalent to one subset size) of the crack path were censored. The step B analysis to detect the crack path

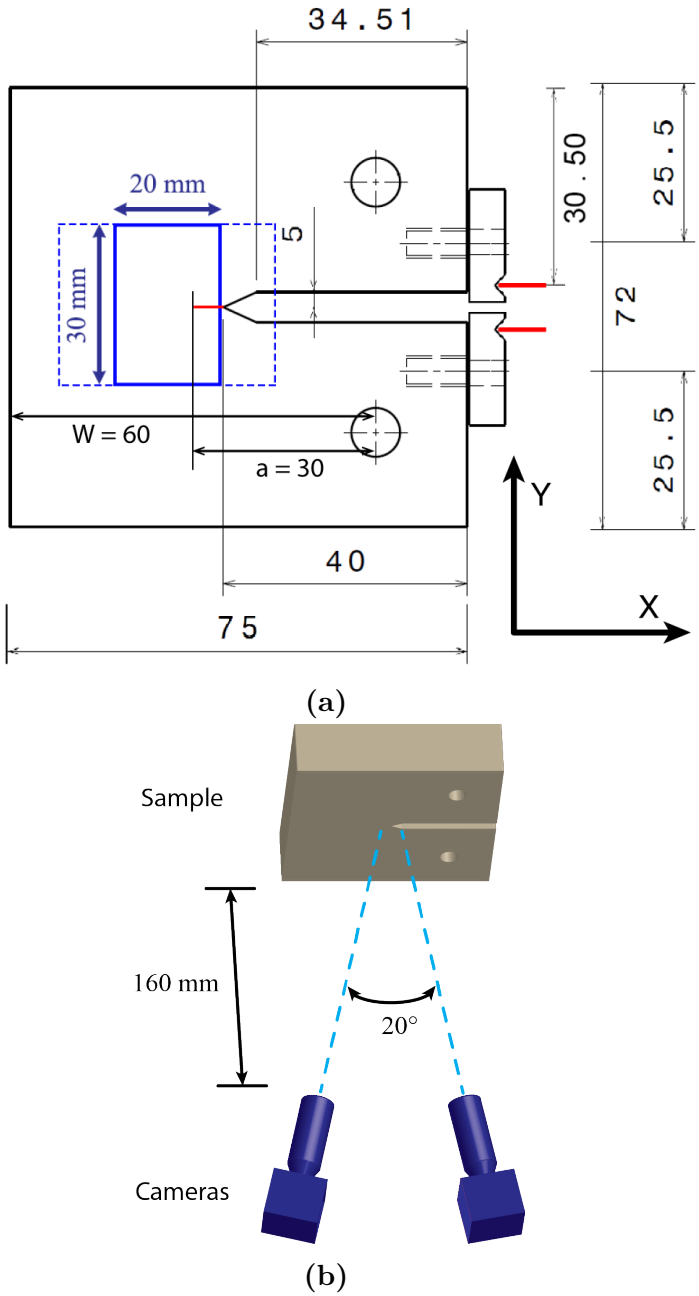

Figure 2.5: The experiment geometry: (a) CT specimen dimensions and clip-gauge position, the dotted box shows the area viewed only by one of the two cameras of the set-up, and the smaller solid box represents the calibrated area that was in common between the two cameras; the specimen thickness is 20 mm. (b) Schematic of the experimental set-up with a 20° angle between the two cameras.

used a square subset dimension of 9 pixels with 75% overlap. A straight crack was assumed and was fitted to the crack path, which was segmented from the strain data with a threshold that selected the top 1% of values of the maximum normal strain histogram. Example images of the obtained displacement fields and strain maps for crack segmentation are presented in the results section (Section 2.4.2). The surface crack path and crack tip positions were subsequently verified by optical microscopy, and the crack front straightness across the sample was verified by optical examination after breaking open the sample at ambient temperature.

2.3.4 Mixed mode crack in brittle PMMA experimental dataset

The mixed-mode decomposition via the interaction integral method was performed on an experimental dataset obtained by Molteno et al. and published in [51]. Arcan geometry [104] specimens, that allows mode I to mode II loading with a range of mixed-mode states via a simple tensile test, were used. The sample set-up is presented in Figure 2.6.

In the experiments that provided the dataset, the samples were machined in PMMA, which is a linear isotropic elastic material at room temperature; its nominal properties are E=3 GPa and ν=0.36. Sharp pre-cracks were cut using a razor blade from the tip of the notch. Two different specimen thickness were available, 6 and 12 mm. The critical values of K_I and K_{II} obtained from analytical solutions that were detailed in Molteno's paper are respectively of 1.7 MPa.m$^{0.5}$ and 1.31 MPa.m$^{0.5}$.

Molteno performed 7 different loading angles per sample thickness (i.e. 14 samples were tested), between 0° and 90° by steps of 15° increments. The loading was applied at a speed of 0.25 mm.min^{-1} and digital images of the sample surface were captured at a frequency of 1 Hz using a calibrated LaVision 3-D DIC system. Further details on the experimental set-up, camera calibration and acquisition system can be found in the original paper.

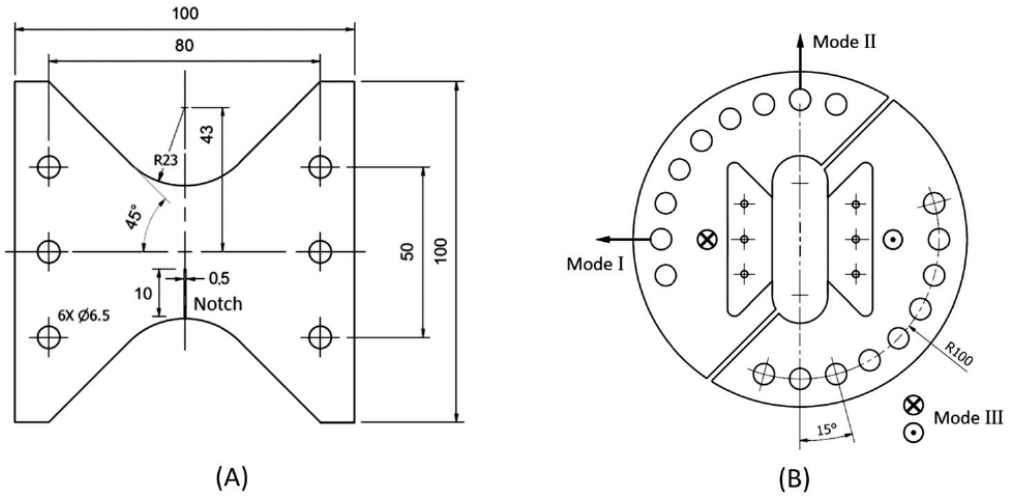

Figure 2.6: (a) Arcan specimen geometry, two different sample width were used, 6 mm and 12 mm. (b) Schematic of the Arcan fixtures, the position of the loading pins choses the amount of mode I and mode II loading. Picture from [51].

The last images obtained before any crack propagation occurred were used to perform the DIC analysis. For the 12 mm thick specimen at 0° and the 6 mm thick specimen at 45°, crack branching was observed in a propagation direction inconsistent with the expected one from the applied loading. This is illustrated on Figure 2.7 for the 12 mm thick specimen loaded at 0° where pure mode I is expected. The crack is propagating with an angle of ∼45° from the pre-crack; this should not be possible with mode I loading. Those data were discarded from the analysis as their occurrence was attributed to a probable data labelling error.

The DIC analysis was performed using a Least Square Matching algorithm in Davis 8.3.0 software with a square subset of size 45 pixels and an overlap of 75% for the Step A analysis. The obtained data was corrected for rigid body displacement and rigid body rotation using the approach described in [105], this was performed to remove parasitic movements that could have happened due to the rig compliance. The approach first determines the rigid body displacement as the average of displacement vectors then the rigid body rotation by solving for the rotation matrix. The Step B analysis, to detect crack path was not performed as the surface crack path and crack tip positions were determined by optical microscopy

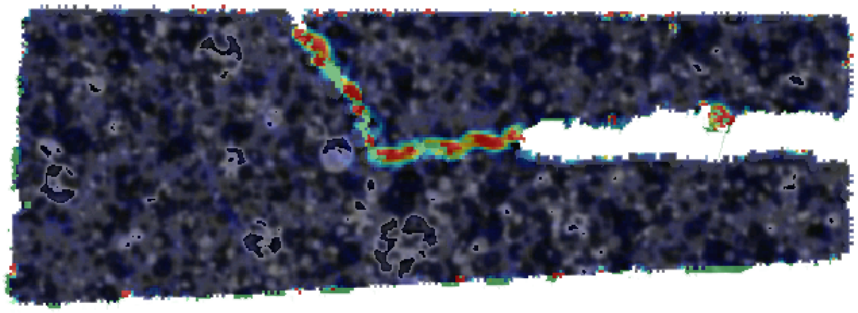

Figure 2.7: Maximum normal strains of the 12mm thick specimen loaded at 0° (pure mode I) at the image just after fracture occurred. The strain scale is quantitative and the only aim is to detect the crack path. Such a crack propagation path is not normal for a pure Mode I crack.

observations of the un-broken samples made by Molteno prior to the experiment, those observations are conservatively expected to have an accuracy of 0.1 mm.

2.4 Results and Discussion

2.4.1 Synthetic Datasets

For the linear elastic synthetic datasets, the relative error was evaluated between the J-integral obtained via the ODIN/OUR-OMA route and that calculated directly from the initial FE-model, which had provided the input to ODIN for the deformation of the images. As the position of the crack in the synthetic images is known precisely, the two-step DIC analysis was not required and it was sufficient to analyse the images with a single subset size to measure the displacement field. The effects on the J-integral of the image resolution, image noise and error in crack tip position were considered. In each case, the J-integral calculation was obtained for a set of different dimensions of the free region (P'Q'R'S') in both horizontal and vertical directions.

Effect of Free Region Size

A normalization of the free region size is done on the basis that in any elastic material, the same normalised free region should include the same strain field contributions, independently of the crack size, loading or elastic modulus. The normalized free region size in both directions (i.e. PQ parallel and PS perpendicular to crack propagation direction) is obtained using Equation (2.1), where L_{mn} is the normalized region size, l is the region dimension in mm, $CMOD_{ME}$ is the crack mouth opening displacement at edge of the region in mm, a_{ME} is the crack length within the free region (a_{ME}<l) in mm, E is the material's Young's modulus in GPa and B is a constant of 1 GPa.mm^{-1} used to make the normalized value dimensionless. This normalization factor scales the free region size by the crack tip opening displacement (ratio of the CMOD and crack length) and Young's modulus of the material - for an elastic material, the normalisation factor is proportional to K as CTOD $\propto K^2/E$ [106]. The normalization values used in the synthetic datasets are presented in Table 2.2.

$$L_{mn} = \frac{a_{ME}/CMOD_{ME}}{E} \times l \times B \tag{2.1}$$

Table 2.2: Parameters used in the free region normalization for each of the synthetic datasets. The mask length in mm is multiplied by $(B \times a_{ME})/(E \times CMOD_{ME})$ to obtain the normalized mask length.

	Elastic Datasets	Inelastic Datasets
a_{ME} (mm)	15	15
CMOD$_{ME}$ (mm)	2.44	0.17 (K=37.2 MPa.m$^{0.5}$) 0.25 (K=47.7 MPa.m$^{0.5}$)
E (GPa)	170	73
$(B \times a_{ME})/(E \times CMOD_{ME})$	0.036	1.21 & 0.82

A DIC analysis of the elastic 17 μm/pixel image dataset was made using a subset of 64 $\times$ 64 pixels, with 75% overlap. As the crack tip position was known precisely,

very good agreement was obtained with the J-integral that was calculated with OUR-OMA using the original FE simulation that provided the image-deforming displacement field; the relative error varies from 0.06% to 0.3% when the SNR is infinite (i.e. no noise added). Varying the dimension of the free region in the direction parallel to the crack has no significant effect on the J-integral error (normalized region dimensions from 7.4 to 23.8). For changes in the free region dimension in the direction perpendicular to the crack, slightly higher errors ($\sim$0.83%) are obtained for very small free region size (below 6.5) when uncertainties in the displacement field measured near the crack borders cause convergence issues.

There was no measurable effect of applied image noise up to 15 dB, while the addition of extreme image noise (-5 dB) gave an uncertainty in the J-integral between 0.8% and 2.7%. Varying the free region size in the direction parallel to the crack path had no influence on the J-integral error, nor could a trend be observed for an effect of the free region size in the direction perpendicular to the crack. This analysis is for a crack loaded in pure mode I, however a greater sensitivity would be expected with mixed mode loading, with both free region dimensions having an impact.

The J-integral analysis is found to be quite robust, so long as the contours remain within the free region. The free region is mechanically connected to the surrounding full displacement field, and using contours that directly sample the DIC data, rather than those using displacements within the free region that is bounded by data, results in a loss of convergence if noise is present in the DIC data. This is illustrated in Figure 2.8a, in which the distance of the outer contour from the crack tip is linearly proportional to the contour number. This example considers the same free region size (P'Q'R'S') with the 17 μm/pixel dataset, and makes a comparison of synthetic data with a SNR of 96 dB and with a SNR of 45 dB. The separation between successive contours is 400 μm, and those contours with number above 24 extend beyond the free region. The J-integral obtained for the contours beyond the free region for the 45 dB data does not converge, but for low levels of noise (96

dB), the method is shown to perform well even for contours within the DIC data. A comparison of the current FE based OUR-OMA method and the JMAN method [48] is also shown in Figure 2.8b for a data with a SNR of 45 dB. The free region in the FE method reduces the scatter significantly compared to the JMAN method.

When the integration contours are taken inside the free-region, and this is often necessary with experimental data, the approach is very noise robust as it uses indirect FE-calculated fields and allow quantification of the SIF where other approaches using direct measurements (such as JMAN) are affected by the noise in the data.

Effect of Image Resolution

The analysis of the 17 μm/pixel, 22 μm/pixel and 33 μm/pixel linear elastic datasets examined the sensitivity to image resolution, relative to the displacement field. The DIC analysis was performed with square subset sizes of 64, 96 and 128 pixels, with datasets that had no noise added to the images. To aid direct comparison, the subset sizes are expressed in mm in Figure 2.9. The effect of free region size at the lower resolutions was similar to that reported above for the elastic 17 μm/pixel data set, so each point in the figure is the average result for the full range of free region sizes (parallel to crack: 7.4-23.8; perpendicular to crack: 8.2-26.3); the error-bars are the standard deviation of each range of free region. There is a general trend for increasing error in the J-integral as the physical size of the subset increases, but the effect is not large and the error remains below 1% in all cases except for the largest pixel size dataset analysed with the largest subset size. The observed trend is attributable to two effects. First, the error increases with decreasing resolution as the number of features available within each subset to track the same portion of the displacement field decreases; this is related to the DIC analysis. Second, the mesh size of the FE model is dependent on the mesh size of the DIC analysis in order to reduce interpolation errors. However, even with a refined mesh in the

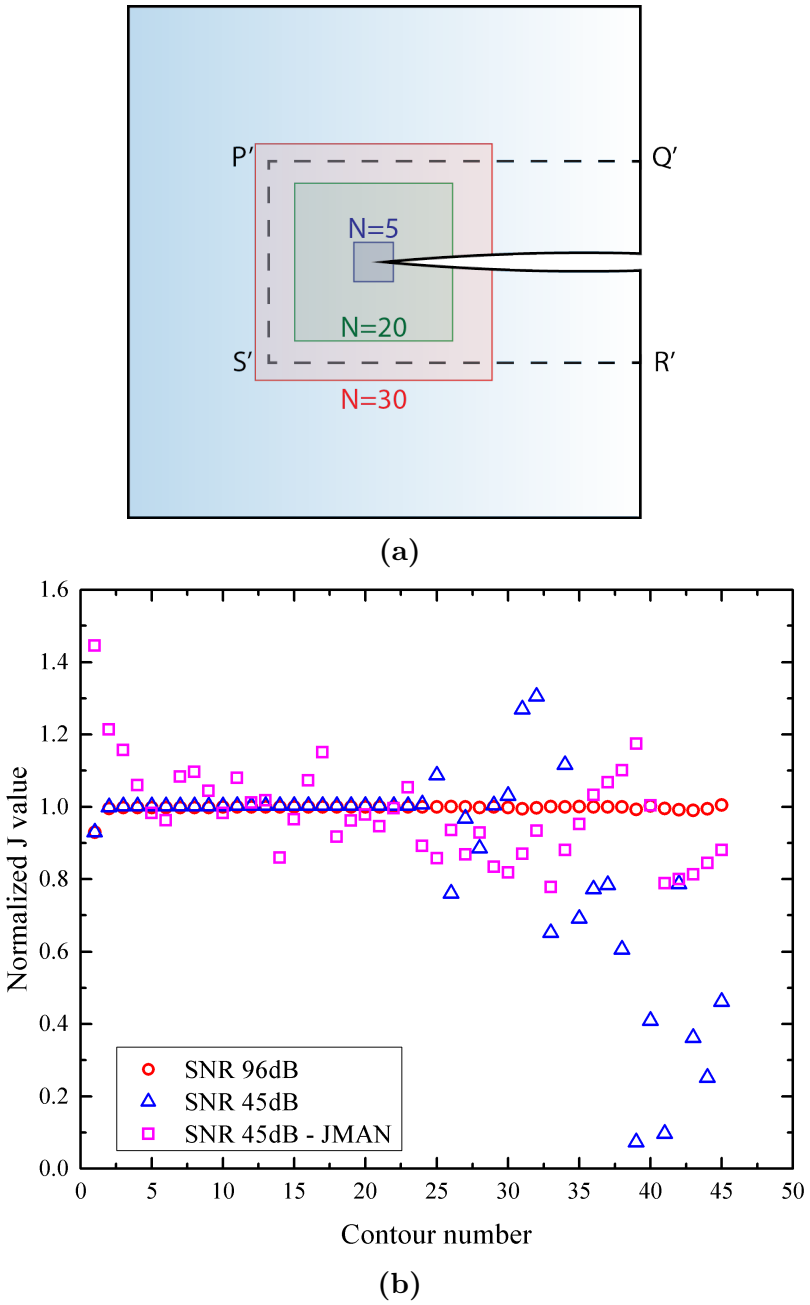

Figure 2.8: Illustration of the J-integral loss of contour independency that is caused by DIC noise when exiting the free region (around contour 25). The free region is included in the P'Q'R'S' box. (a) Schematic representation of the contour numbers – contours 5, 20, and 30 are shown; contours 5 and 20 are included in the free region and contour 30 includes data out of the free region. (b) Calculated J-integral value normalized by the theoretical value for different contours and different noise levels. Comparison is made between the OUR-OMA method and the JMAN method [48] for data with 45 dB SNR.

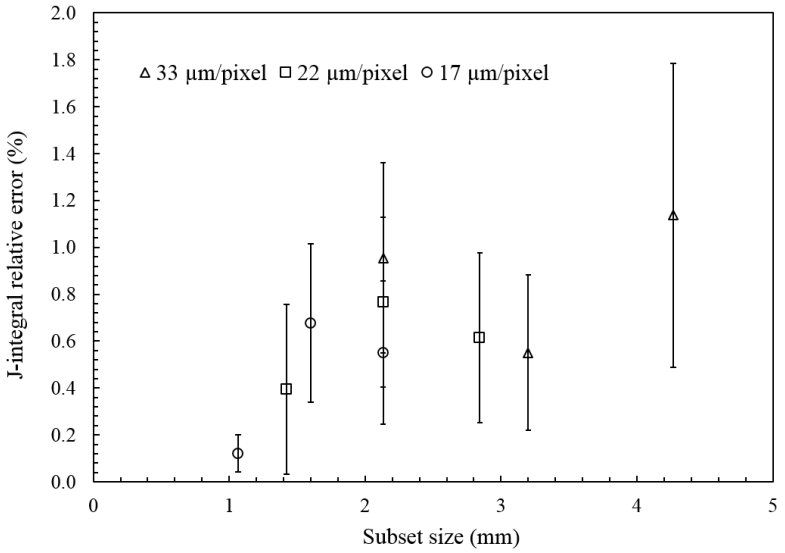

Figure 2.9: Effect of image pixel size and DIC subset size on the error in the calculated J-integral.

free region, for a coarse DIC subset size the FE mesh is insufficiently refined, so this error component is related to the FE analysis.

Effect of Crack Position Uncertainty

The effect of uncertainty in the crack tip position was examined using the linear elastic dataset at 17 μm/pixel, for a DIC analysis with a subset of 64 $\times$ 64 pixels and an overlap of 75% for step A. No noise was added. Free regions with normalized size between 10.7 and 23.8 in the direction parallel to the crack and 9.8 and 26.2 in the direction perpendicular to the crack were considered. Using OUR-OMA, the DIC results were injected into FE models in which the crack length was changed by up to $\pm$50 pixels from its known position, equivalent to $\pm$850 μm or an error in a/W of 1.4%. The obtained uncertainty is reported in Figure 2.10 as the average error for the full range of free region sizes. There is no specific trend in the effect of the free region size, and the error bars are the standard deviation for the range of region size. With a small uncertainty in crack tip position ($\pm$10 pixels) with noise-free data, the J-integral error is between 0.5 and 1.5%. With greater uncertainty in the crack tip position, the J-integral error becomes more significant, but it remains low

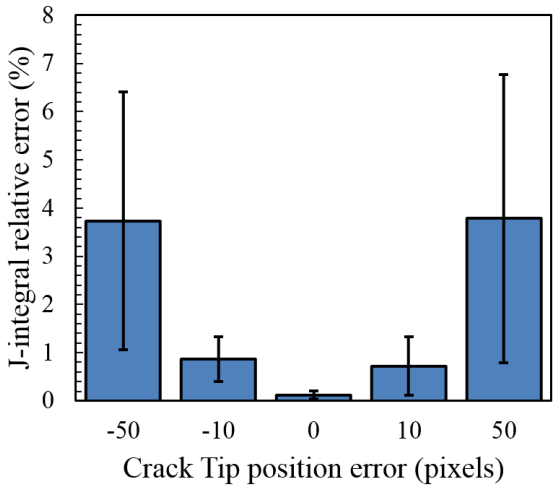

Figure 2.10: Effect of erroneous crack tip position on the J-integral error.

(4 ± 2%). In [43] the authors estimated a 7% uncertainty in the determination of the stress intensity factor by a field fitting method, for an uncertainty in crack tip position of 40 pixels, which is similar to the maximum uncertainty obtained here.

Effects of Inelastic Deformation

The inelastic cases are illustrated in Figure 2.11a, in which the crack tip plastic zone is represented by the elements in the initial FE model in which plastic strain predicted using the Ramberg-Osgood law develops during the last solver increment. The small plastic zone size, at an applied stress intensity factor of ∼37 MPa.m$^{0.5}$, is 3.2 mm measured in the crack plane, and represents a small scale yielding condition. The larger plastic zone size, at an applied stress intensity factor of ∼48 MPa.m$^{0.5}$ is 8.7 mm measured similarly, and exceeds the small scale yielding condition. The DIC analysis used a subset size 96 × 96 pixels for step A with a 75% overlap. The same Ramberg-Osgood material law was used in the evaluation of the J-integral from the injected displacement field, and the effect of the free region was examined as previously. The crack tip position was known precisely and no noise was added.

The average J-error was 0.48% (±0.14%) for the small scale yielding case and 0.49% (±0.22%) for the large scale yielding case. In each case, the range of normalised free region size investigated was from 20 to 60 in the X direction and

from 9 to 70 in the Y direction for the small plasticity dataset and from 13 to 41 in the X direction and from 6 to 46 in the Y direction for the large plasticity dataset. In the case of the small plastic zone size, the plasticity is essentially contained in the free region whereas in the larger plastic zone case, the plasticity always exceeds the free region. In both cases, very little effect of the free region size was observed in the J-integral error. Hence, in the case where the material law is well known, the strain energy release rate can be determined accurately from the displacement field, even for significant plasticity.

The displacement fields obtained for inelastic deformation were also analysed with the assumption of linear elastic properties (E=70 GPa, ν=0.3) (i.e. small scale yielding). The effect of the free region size was examined, as before. Examples are shown in Figure 2.11b and c for free regions of the same physical size with normalised dimensions of X = 37 for the small plasticity dataset and X = 27 for the large plasticity case. The J-integral error increases with the amount of plasticity, and tends to decrease when the free region is close to crack, and also when it was more remote. For a free region width that could reasonably be achieved in experiment (i.e. Y<10), the J-integral error is less than 5% with the assumption of small scale yielding, even for the large plasticity case. The observed behaviour may be rationalised by considering that when the free region is small, greater information on the deformation around the crack is available, which leads to lower uncertainty in the evaluation of the J-integral. However, the reason for the low error with a very large free zone is unclear.

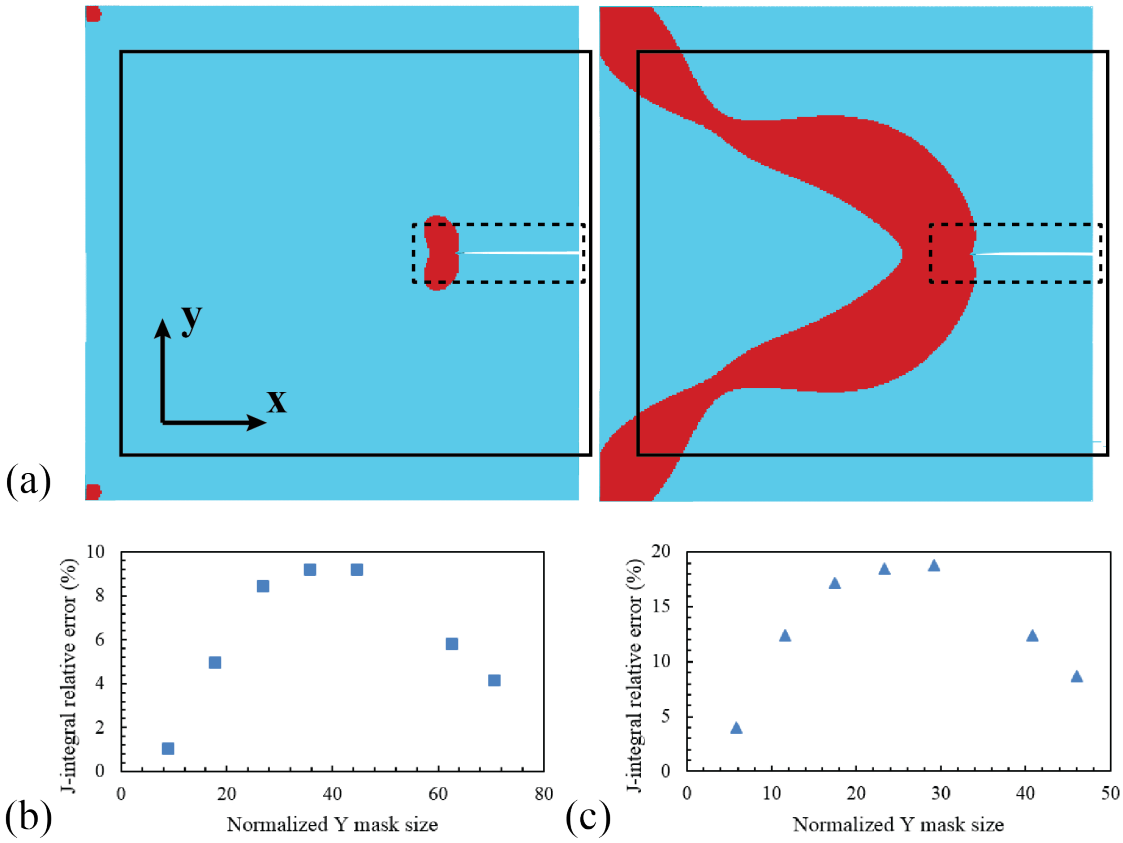

Figure 2.11: (a) The plastic zone sizes used for the inelastic Ramberg-Osgood material law analysis (left) small plastic region (right) large plastic region - the (black) rectangles show the minimum (dashed line) and maximum (solid line) free regions. Relative error in J-integral determination when small scale yielding condition is assumed. (b) Small plastic region (c) Large plastic region.

2.4.2 Mode I Fatigue crack in an Aluminium CT specimen

The fracture surface and the surface trace of the crack are shown in Figure 2.12a. The crack was straight and uniform within the ASTM E399-09 requirements [101]; the average crack surface length is 4.95 mm, measured on each side (±0.25 measurement precision) from the notch tip (a/W=0.499), and the average crack length across the specimen was 5.19 mm (a/W=0.503). The standard deviation of 5 evenly spaced measurements along the crack front was 0.12 mm, with a maximum length of 5.49 mm (a/W=0.508). The crack mouth opening displacement (CMOD) is shown in Figure 2.12b for the loaded and unloaded condition as a function of the maximum applied load. The clip gauge was zeroed with the initially unloaded

samples, before application of the pre-load. The CMOD under load increased linearly with load until 20 kN load (i.e. applied $K < 39$ MPa.m$^{0.5}$) and then rises more steeply. The unloaded CMOD, measured at 130 N, is approximately constant at 0.2 mm, and then rises as the peak applied load increases above approximately 15 kN (i.e. applied $K > 29$ MPa.m$^{0.5}$).

The literature value of K_{Ic} for this specimen is of 34 MPa.m$^{0.5}$ and is obtained for loads exceeding 18.5 kN. However, the sample was loaded up to 23 kN before failure. This behaviour is attributed to the specimen thickness, that is not large enough to impose the plane strain condition. Instead, the specimen is experiencing a combination of plane strain condition in its centre and plane stress condition closer to the surfaces. This can be confirmed by the observation of the fracture surface (Figure 2.13) that shows signs of the plane stress conditions by exhibiting shear lips of ∼5 mm long from each surface of the specimen. Fracture toughness increases in ductile materials under plane stress, so this mixed plane strain/plane stress behaviour is expected to produce the higher K_{Ic} value that is observed.

The specimen compliance data are shown in Figure 2.12c as a function of the maximum applied load. Several measures of compliance may be obtained from the data: the *maximum compliance* was calculated as the ratio of maximum CMOD to maximum applied load; the *intra-cycle loading compliance* is the ratio of the change in CMOD between the minimum and maximum load in each cycle to the applied load range; and the *intra-cycle unloading compliance* is the ratio of the change in CMOD between the maximum load of one cycle and the successive unload to the range in applied load. The theoretical compliance (V_m/P), calculated using Equation (2.2) [107] is 36.33 μm/kN (±0.25). The uncertainty in the theoretical compliance is due mostly to uncertainty in the measured Young's modulus; the measurement uncertainty in crack length make a negligible contribution.

The measured maximum compliance is very close to the ASTM E399-09 theoretical compliance. Initially slightly lower (e.g. 1% difference at 2.5 kN), the maximum

compliance increases gradually with increasing load up to about 15 kN, and then continues to rise at a rate that increases with increasing load. The intra-cycle loading and unloading compliances are almost identical and are initially lower than the maximum compliance. They approach the theoretical compliance as the maximum load increases, with the greatest changes occurring up to a maximum load of 7.5 kN and then above around 15 kN, where both increase significantly with applied load.

The displacement fields obtained from the DIC analysis at each load stages were corrected for rigid body displacement. An example of the corrected displacement field for a load of 15.5 kN is shown on Figure 2.13. The shape of the displacement field corresponds to what is expected for a crack loaded in mode I.

The DIC observations showed no measurable increase in crack length at the specimen surface, but plastic tearing and blunting both occurred sub-surface during the experiment, as indicated by the fracture surface (Figure 2.12a). An increasing in crack length by plastic tearing would increase both the intra-cycle unloading compliance and the maximum compliance, whereas crack blunting by plasticity would increase the loading compliance and the unloaded CMOD, with no significant effect on the intra-cycle unloading compliance. The reduced intra-cycle compliance below 7.5 kN may be attributed to plasticity-induced crack closure that was introduced by the fatigue pre-cracking. The effect of closure may also be apparent in the difference between the maximum compliance and the theoretical compliance at low loads. The increase in intra-cycle compliance above around 15 kN, accompanied by increased unloaded CMOD, can be attributed to crack tip plasticity. Above 24 kN, the difference between the unloading and loading intra-cycle compliance shows that plastic tearing to extend the average crack length has also occurred. Hence, the crack may be considered as fully open above approximately 7.5 kN, which was the maximum applied during fatigue-precracking. At loads above this, there is a progressive increase in the amount of crack tip plastic deformation, which becomes significant above 15 kN as greater crack tip plasticity develops.

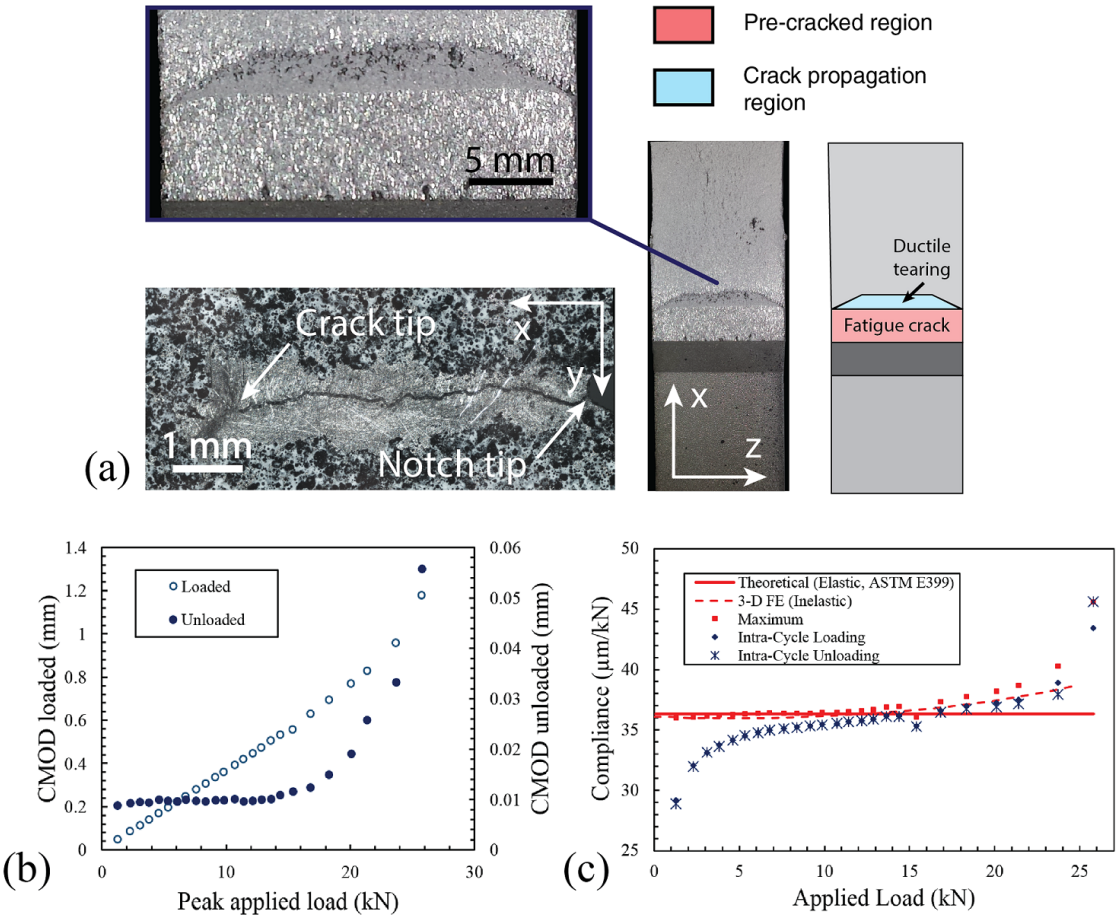

Figure 2.12: (a) Optical microscopy of the surface crack and the fracture surface. The specimen surface in vicinity of the cracked region was cleaned with ethanol prior to taking the picture in order to remove the paint pattern applied for the DIC analysis. (b) The crack mouth opening displacement (CMOD) measured in the loaded and unloaded states. (c) Specimen compliance measured as a function of maximum applied load, compared with the theoretical elastic compliance predicted using Equation (2.2). The CMOD uncertainty is 10 μm, and the compliance uncertainty is ± 0.1 μm/kN.

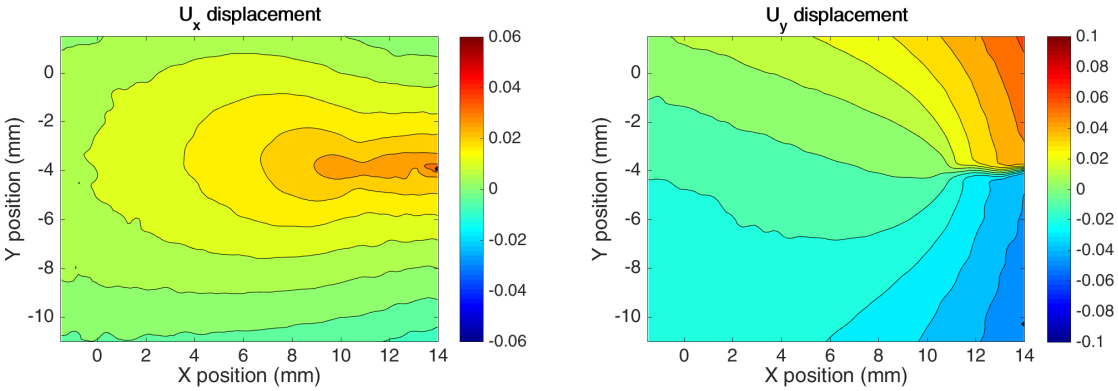

Figure 2.13: DIC calculated displacement field (at 15.5 kN) after rigid body displacement and rotation correction.

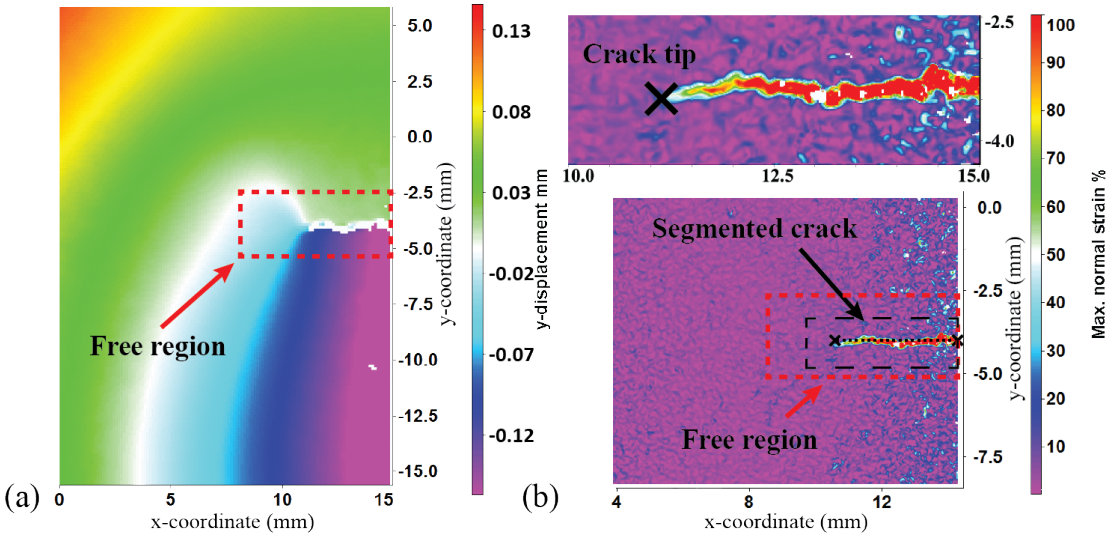

Figure 2.14: Example results of the DIC analysis (at 15.5 kN). The origin of the x-y coordinates is at an arbitrary position. (a) y-displacement change measured for a large subset (64 × 64 pixels, overlap 75%). (b) maximum normal strain obtained with small subsets (9 × 9 pixels, overlap 75%). The dashed boxes show the locations of the free region used in the J-integral analysis, and also the zoomed image of the crack. The position of the crack tip, obtained by segmentation of the strain data (small subset analysis) is also marked.

$$\frac{V_m}{P} = \frac{1}{E' B_e} \times q\left(\frac{a}{W}\right)$$
$$q\left(\frac{a}{W}\right) = \frac{19.75}{(1-\frac{a}{W})^2}\left[0.5 + 0.192\frac{a}{W} + 1.385(\frac{a}{W})^2 - 2.919(\frac{a}{W})^3 + 1.842(\frac{a}{W})^4\right]$$
$$\text{Plane strain} : E' = \frac{E}{1-\nu^2} \quad \text{Plane stress} : E' = E \tag{2.2}$$

The ASTM E399 standard [101] was used to calculate the applied stress intensity factor, K, from the measured specimen dimensions, surface crack length and applied load. This is compared with a 3-D FE simulation for the same specimen dimensions, obtained using the inelastic Ramberg-Osgood model for Al2024-T351. The FE simulation assumed hard frictionless contact between the loading pins and the sample, with displacement controlled boundary conditions at the loading pins to achieve the reaction forces equivalent to the applied load. The standard and FE simulation agree within 3% up to 15 kN applied load, above which the 3-D FE simulation increases non-linearly with increasing load due to plastic deformation.

The rise above 15 kN is also observed in the experimental data and is due to plasticity (Figure 2.12c). At higher loads, the measured maximum compliance is greater than the inelastic FE simulation. This may be due to uncertainties in the FE model definition and also the development of tearing in the experimental data.

The DIC-measured surface displacement fields were used to calculate J-integral values with the OUR-OMA method (Figure 2.14a). A small subset analysis (Figure 2.14b) was used to identify the crack position, the maximum normal strains values shown on the figure are unfiltered and their sole purpose is to determine the displacement discontinuity of the crack path by segmentation of the apparent strain field. These strains do not correctly define the crack tip strain field due to the inherent noise of displacements measured with small subsets, but the crack can be segmented easily using a strain threshold. The free region was fixed with dimensions of 6.4 $\times$ 3.1 mm; hence its normalized width ranged from 0.90 to 13.9 as the crack opening changed with load. The J-integral calculation was performed with contours that were only within the free region, as the experimental noise from the image acquisition and 3D-DIC analysis prevented calculation of the J-integral using the DIC data region. The experimental data could not be analysed using the JMAN code [48] due to this noise. For comparison with the standard calculation, the calculated J-integral values were converted to stress intensity factors using Equation (2.3), and are presented in Figure 2.15.

The *extra-cycle* analysis used the displacement fields relative to the initial reference 130 N preload, and the *intra-cycle* analysis used the relative displacement fields between the previous unload and the maximum load of each cycle. Each J-integral analysis was performed using linear elastic properties (plane stress, E = 73.1 GPa, ν=0.3) and also the inelastic Ramberg-Osgood model for the Al2024-T351 alloy. The crack tip position is known to within 15 pixels from the step B DIC analysis, and the maximum difference between surface and average crack length is similar at 240 μm, which is 16 pixels, hence from the benchmarking of synthetic

datasets, if the material law is correctly defined, the expected uncertainty in the evaluated J-integral is approximately 1.5%. When the small scale yielding condition is assumed (i.e. the elastic case), then an additional bias of 5% is expected. When combined with the 4% uncertainty in Young's modulus value, a propagation of error analysis gives an uncertainty in K of 2.2% when using the inelastic model and 3.2% when assuming small scale yielding. These uncertainties have been applied to the data in Figure 2.15. The relative difference between the stress intensity factors obtained by analysis of the measured displacement field, and that obtained using Equation (2.2), is shown in Figure 2.15b.

$$K = \sqrt{J \times E'} \tag{2.3}$$

Figure 2.15 shows that, with the assumption of small scale yielding (i.e. elastic behaviour), the extra-cycle DIC-based J-integral calculation obtains a higher stress intensity factor than the ASTM standard calculation. The standard analysis is relative to a zero load rather than the 130 N preload, but the effect of this is vanishingly small, so the difference is largely due to the neglect of crack tip plasticity. Crack tip plasticity increases the displacements around the crack and so causes the strain energy close to the crack tip to be overestimated when the J-integral is calculated with the assumption of linear elasticity. The error increases at loads above 7.5 kN, since there is no significant development of crack tip plasticity expected below the fatigue pre-cracking maximum load. The intra-cycle elastic analysis shows a similar but smaller difference, as it is affected only by the plasticity that develops in individual cycles, rather than the total plasticity.

Crack closure, or the residual stress field associated with this, also has an effect, but it appears to quite complex; the difference between the extra-cycle and intra-cycle elastic J-integral analyses below 7.5 kN indicates that the displacement field around the crack is not simply linear elastic, despite the stability of the minimum

CMOD that is observed in Figure 2.12b. Incorporating the correct elastic-plastic material law into the J-integral analysis provides a better agreement between the applied and measured stress intensity factor, particularly for the extra-cycle analysis that considers the total development of plasticity with increasing load; good agreement with the applied stress intensity factor is obtained, even when significant plasticity develops (i.e. above 15 kN load).

It is important to note that the J-integral analysis makes no use of the experimentally measured load, nor of the actual geometry of the test specimen. The analysis uses only the measured displacement field around the crack and an elastic or inelastic material law. The ASTM standard calculation is obtained with knowledge of the specimen geometry, crack length and the applied load, and the assumption of small scale yielding. In the specimen geometry used here, the effects of crack tip plasticity on the ASTM standard calculation are not significant except at high loads, as shown by the 3-D elastic plastic simulation of the test specimen (Figure 2.15a), since the crack tip plastic zone is small compared to the specimen geometry and crack length. The measured displacement field can be used to calculate the field applied to a crack, with good accuracy as a stress intensity factor or J-integral, without knowledge of the crack geometry and applied load, if the correct elastic-plastic material law is employed. Significant errors may arise when crack tip plasticity is neglected.

The image-based analysis uses the displacement field that is measured in the region surrounding the crack, but it is not immune to the effects of local effects close to the crack tip, such as the residual stresses from crack closure that can influence the development of the displacement field. In principal, these local effects might be extracted by using displacements measured very local to the crack tip. However, convergence problems will occur due to noise in these data. Direct measurements of the crack tip field, such as via diffraction methods that record elastic strains, are needed in this case. These can be analysed using the method presented in Chapter 3.

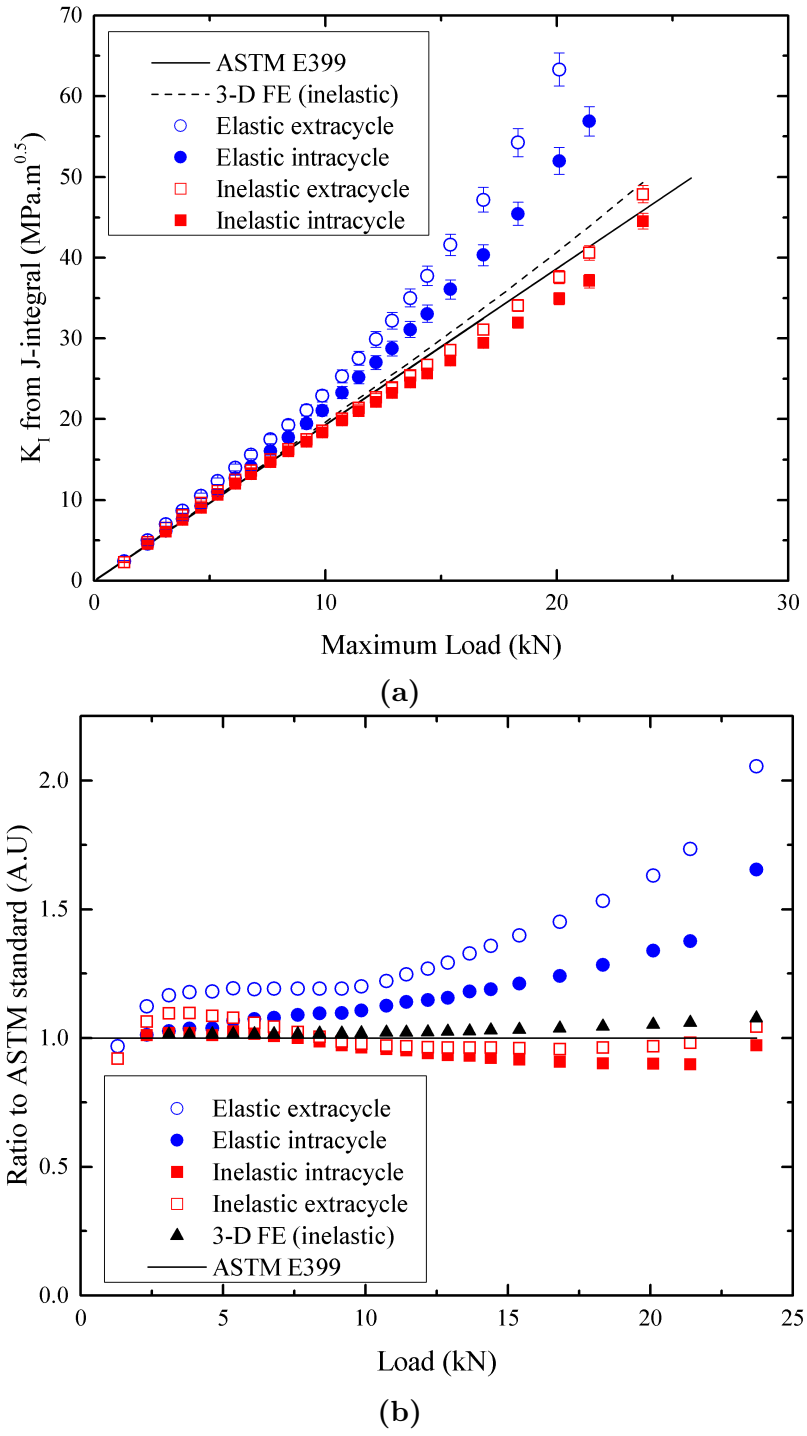

Figure 2.15: Comparison between K values from J-integral, FE modelling and theory. The error in the K values was determined from benchmark tests. (a) absolute values. (b) relative values.

2.4.3 Mixed-mode fracture in brittle PMMA

The DIC-measured surface displacement was used with the OUR-OMA method. The free region was fixed with dimensions of 6 × 6 mm centred on the crack tip. The J-integral calculation was performed over 20 contours; 10 contours were only within the free region while the 10 further contours included increasing area of the experimental data. Contours were centred on the crack tip with the largest contour probing data up to 6 mm away from the crack tip (Figure 2.16). The normalized size of the masked region is not relevant as the proposed normalising criteria is applicable for pure mode I crack only. The crack tip position is known within 0.1 mm from the optical microscopy observation.

The obtained K_I and K_{II} values are plotted on Figure 2.17, the error bars represent the standard deviation over the 20 integration contours. In this analysis, the SIF values are extracted and analysed; however, Abaqus software can also implement a maximum strain energy release rate criterion[5] to predict crack deflection angle. It could be of interest, in future work, to look at the validity of this prediction by comparing it with the available experimental data.

The Figure 2.17a exhibits the expected trend with the sample being loaded in pure mode I at 0° and pure mode II at 90°. Good agreement is obtained between the two different sample thicknesses. Figure 2.17b shows the same data as a 1-to-1 plot between mode I and mode II using the values normalized by the theoretical critical values in pure mode I or mode II loading, K_{Ic} and K_{IIc}. The dotted line is the best quadratic fit to the data and gives the evolution trend of the K_I to K_{II} ratio required for criticality. This curve shows that the linear assumption is erroneous and is of interest for modelling as it allows to define a multi-modal crack initiation criterion for this material.

[5] A maximum energy release rate criterion assumes that in an elastic solid, fracture occurs along the plane oriented at the angle to the plane of the existing crack that maximizes the energy release rate.

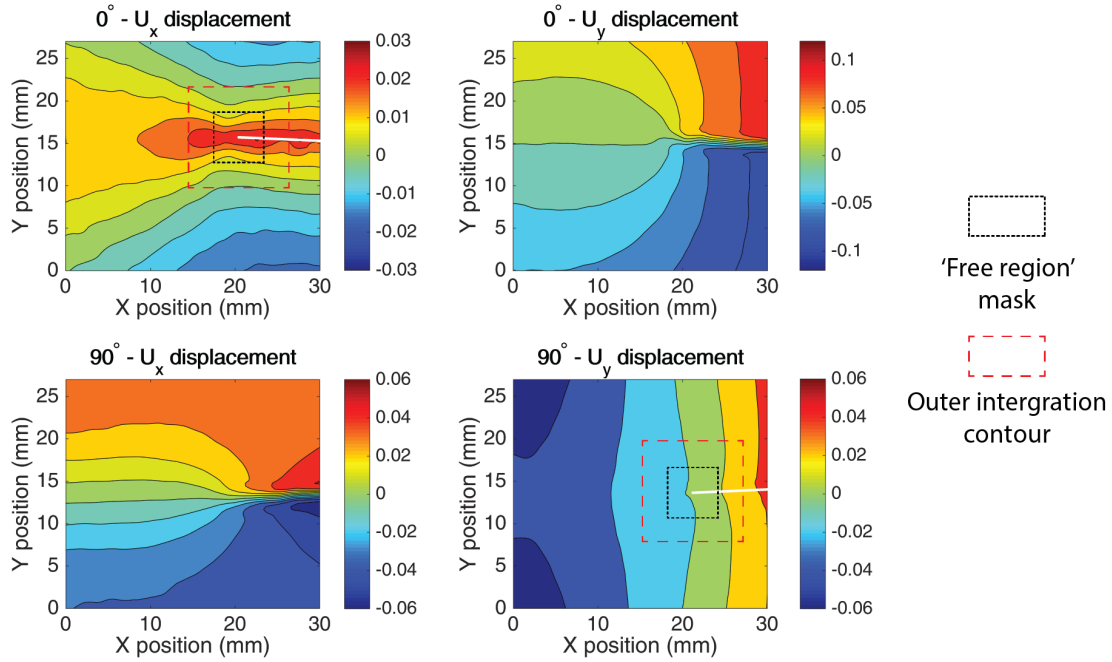

Figure 2.16: DIC determined displacement field for the 6 mm thick sample loaded at 0° and 90° (i.e. pure mode I and pure mode II). The crack path is shown as a white line. Black and red dashed rectangles respectively show the free region and the largest integration contour.

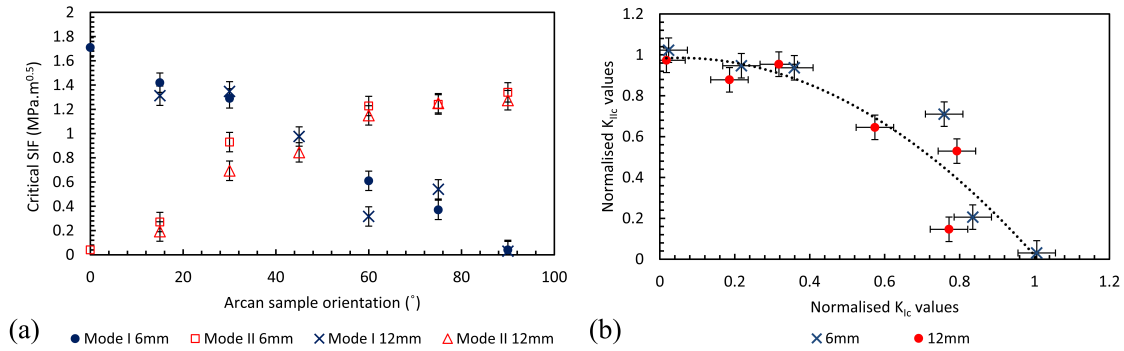

Figure 2.17: (a) Mode I and II stress intensity factors determined by the interaction integral for the different Arcan sample orientations. (b) 1-to-1 plot of the normalized SIF values. Normalisation was done by dividing the value by the analytical critical SIF. The dotted line is an order 2 polynomial fit of the data.

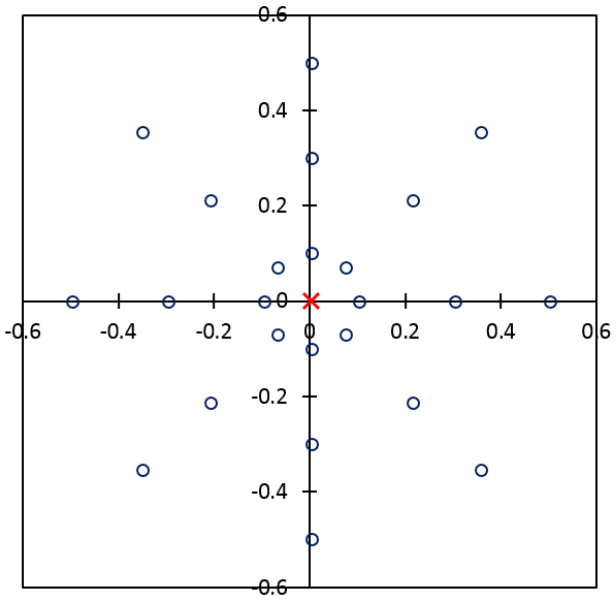

Figure 2.18: Crack tip positions used for the benchmark shown in blue circles, the original (detected) crack tip position is shown as a red cross. Axis show deviation from original crack tip in mm.

As no FE benchmarking on the interaction integral was made and that literature highlighted the fact that the method was sensible to crack tip uncertainty [61]; the sensitivity to crack tip position change was evaluated by looking at the change in the K_I and K_{II} value induced by a change in crack tip position definition. The 6 mm thick sample loaded at 15° was chosen as a test dataset and the analysis was run for 24 different positions of crack tip positioned radially at 0.1, 0.3 and 0.5 mm from the original crack tip (Figure 2.18). For each crack tip position, the deviation from the original SIF value was calculated in % of the original value and plotted on Figure 2.19.

From those data, the expected error for this experiment is conservatively estimated between 5-10% for both mode I and mode II values considering the accuracy in the crack tip position detected by optical microscopy by Molteno was judged to be of 0.1 mm. It is interesting to note how the mode I component is affected by error in the Y position whilst mode II component is affected by error in the X position. The error in the SIF value grows quickly with error in the crack tip position; confirming that the interaction integral method is to be used only

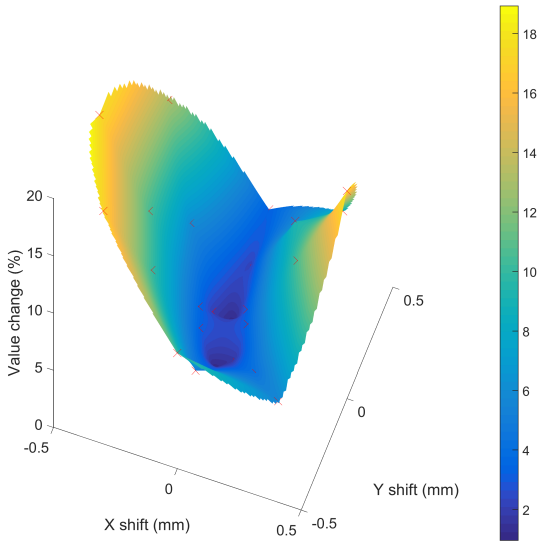

(a)

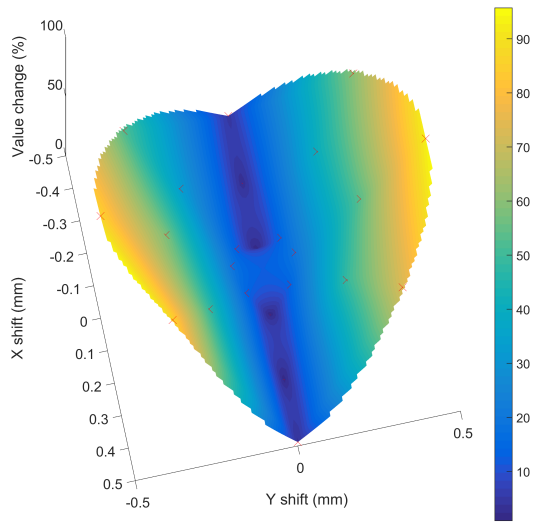

(b)

Figure 2.19: Mode I and Mode II relative change in % due to change in the crack tip position. (a) Mode I (b) Mode II.

in cases where the crack tip position in accurately determined. It is advised to combine DIC with another method for crack tip position identification like optical microscopy to gain enough confidence in the crack tip position. Due to the use of subsets and the loss of DIC quality next to crack faces, it is often difficult to achieve the same kind of accuracy in crack tip position determination via DIC techniques compared to human detection approaches. In many cases, visual detection of the crack in the camera image allow detection of the crack tip with an accuracy of a few

pixels, which, depending of the camera pixel size, is often sufficient to give good confidence in the use of the interaction integral approach. Also, as DIC is a surface measurement technique, it is important to verify that the crack tip position on the sample surface is representative of the crack tip position through the sample.

2.5 Conclusion

A method to determine the crack strain energy release rate from measured displacement fields has been presented, using digital image correlation (DIC) datasets. The method uses a Finite Element framework and is easy to implement. The full-field DIC measurements are used to apply boundary conditions for finite element calculation of the J-integral. The method is insensitive to the specimen geometry, does not require prior knowledge of the loading and may be applied when DIC measurements in the vicinity of the crack are not trustworthy. The method has been benchmarked on synthetic datasets to assess the errors arising from uncertainty in crack tip position, image noise and the incorrect assumption of small scale yielding. Like any full-field method, the choice of the material law must be considered carefully as it can be the major source of error. Application of the method to experimental data for an elastic-plastic material shows that the crack field (as a stress intensity factor) can be obtained with good accuracy, without knowledge of the specimen geometry and applied loads. Additionally, it was shown that for mixed-mode data, the interaction integral can be used to separate different modal contributions, however when using this method, extra care must be taken to insure the crack tip position is well determined.

Comment voulez-vous gouverner un pays où il existe 258 variétés de fromage ?

— Charles de Gaulle

3

J-integral calculation from diffraction mapping

Contents

3.1 Introduction

A recurrent fracture mechanics requirement is to quantify the field surrounding a crack that controls its propagation. With that aim, it is important to quantify the elastic strains around the crack, and various techniques exist that allow their point wise determination. In the previous chapter, the digital image correlation method has been presented, however image based methods cannot separate elastic and plastic strains (without the examination of image sequences that include unloading).

The analysis of diffraction patterns, obtained with monochromatic X-ray diffraction (XRD), Energy-Dispersive polychromatic X-ray diffraction (EDXRD) or neutron diffraction (ND) can achieve this goal [75, 76], where a set of point measurements can be used to map the elastic strain field.

Determining the surrounding elastic strain field is particularly important in cases where residual stresses are present and may modify the behaviour of the cracked material. This is the case with fatigue crack closure. In fatigue loading under LEFM conditions, Paris' law stipulates that the crack advance per fatigue cycle (da/dN) is linked to the range of applied stress intensity factor in the cycle (ΔK) by a power law; the law can also be influenced by the maximum stress intensity factor, K_{max}. However, this relation can break down with fatigue closure, particularly close to the fatigue propagation threshold, and the understanding of this phenomenon is paramount for engineering applications where crack closure can impact the fatigue life predictions from Paris' law.

The first observation of fatigue crack closure was made by Elber [25, 26] using microscopic observations; he showed that when progressively loading a fatigue propagated crack, some portion of the crack remains closed until a given load is reached. He proposed a modified formulation of Paris' law to account for crack closure by suggesting the use of an effective stress intensity factor range ΔK_{eff} to replace ΔK and take account for crack closure. ΔK_{eff} is defined in Equation (3.1) where K_{max} is the maximum applied SIF in the fatigue cycle and K_{op} is the value of the SIF at which the fatigue crack is fully opened.

$$\Delta K_{eff} = K_{max} - K_{op} \tag{3.1}$$

The mechanisms that can cause closure are multiple and can occur simultaneously. Plasticity induced closure is due to the crack leaving a wake of plastically deformed material, and as this is constrained within the elastically deformed bulk of the

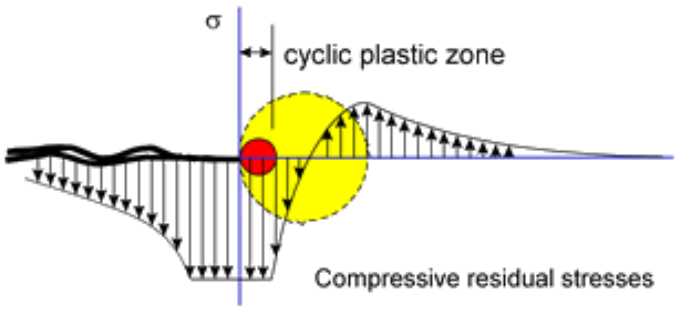

Figure 3.1: Mechanism of the plasticity induced closure. The compressive residual stresses from the previous loads close the crack. Picture from efatigue.com.

sample then residual stresses are developed whilst propagating (Figure 3.1). This phenomenon is most significant at the surface in ductile materials as the plastic zone is larger in the plane stress conditions at the surface where the out-of-plane flow of the material is not constrained. In a different manner, roughness induced closure is due to a rough crack surface causing the crack faces or lips (i.e. at the surface) to contact earlier than expected; this mechanism is more present under mode II or mode III loading of the crack due to the tortuosity of the crack [108].

Different approaches have been used to highlight the effects of crack closure. For example, Zhang [109] used SEM measurement of the crack opening displacement to highlight the crack closure point and closure stresses (Figure 3.2). The problem of this approach is the same as the one noted for DIC in Chapter 2; it only gives information on the specimen surface that could behave differently than the bulk material. Alternatively, the specimen's mechanical compliance [110] can be monitored to make similar measurements, this approach is less sensitive to differences between surface and bulk behaviour as it measures their combined effect and can be coupled with the COD measurement approach. It has been observed that closure is mostly dominated by surface effects and is only significant in plane stress conditions [111, 112], so surface observations may be sufficient. However, it would be ideal to be able to measure closure at surface and in the interior of the sample.

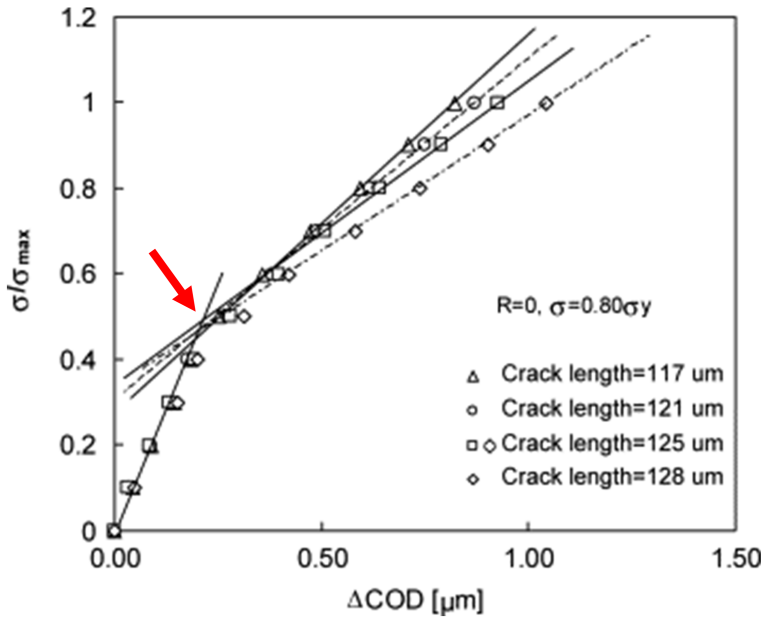

Figure 3.2: Crack closure point (identified by the red arrow) and closure stresses as determined by Zhang via in-situ SEM observation [109].

The possibility to create maps of the elastic strain field is particularly interesting to study residual stresses related issues. For instance, in [81] and [113] the authors use neutron and X-ray diffraction to map residual elastic strains in a TIG welded aluminium thin plate sample; because of the shape of the specimen, they probe strain values that are representative of the whole specimen thickness. Their observations allow them to validate a 3-D shell FE model (a shell element is a type of element suitable when thickness is small compared to other dimensions) that allows prediction of residual stresses caused by TIG welding of Al-2024. In [114] the mechanical shielding effect of crack bridging in stress corrosion cracking is observed via X-ray diffraction mapping to provide an explanation for the observed R-curve behaviour.

Elastic strain maps have also been used to study fatigue crack overloads and their effect on closure. In the early work from Allison [83], a calibration curve between XRD strains and bulk stresses was demonstrated (Figure 3.3a). Allison compared XRD determined residual stresses after overload with theoretical solutions for different types of steels and highlighted cases where theory did not explain

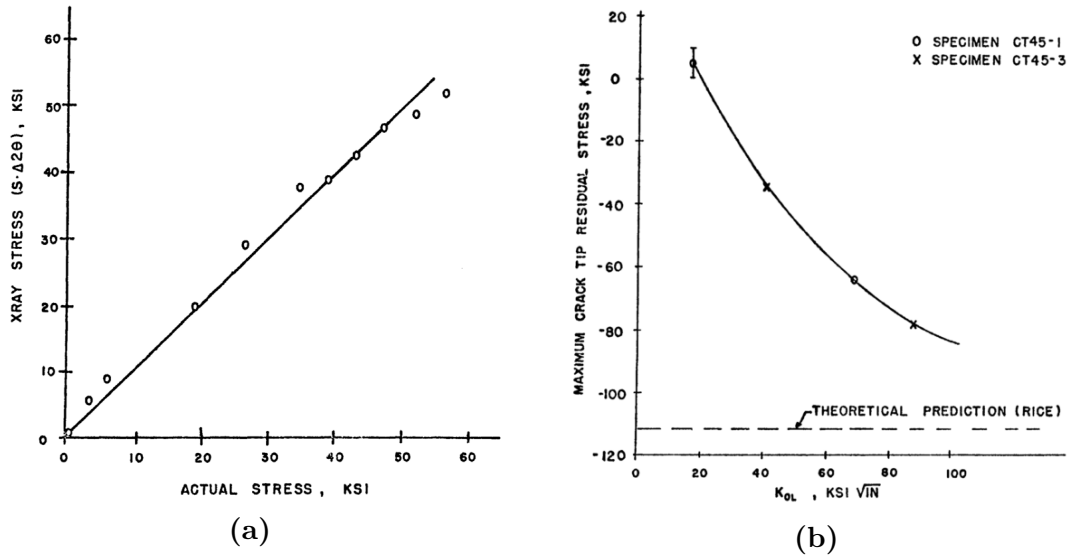

Figure 3.3: (a) XRD to bulk stress calibration curve as shown by Allison [83] for a 1020 Steel sample (b) Dependence of the crack tip residual stress on the applied SIF at overload for 1020 Steel samples.

experimental results. For example, theory predicts that the maximum crack tip residual stress will be equal to the material yield strength regardless the SIF of the overload; however, he observes a dependence of the crack tip residual stress on the overload SIF (Figure 3.3b). Allison encouraged the development of FE approaches that can capture those phenomena over the use of theory.

In [84], two full-field techniques, DIC and X-ray diffraction (EDXRD) were used conjointly. DIC provided the total strain measurement and was also used to measure the crack opening displacement profiles at the surface. Both EDXRD maps and COD profiles from DIC show shielding in the measurements made after the overload; this is illustrated in Figure 3.4 where the line profile of the crack opening stress at maximum load for different cycles, before and after overload, is shown. The effect of the compressive residual stresses induced by the overload are clear with a progressive recovery after 37k cycles. In [86], combined diffraction strain mapping and X-ray tomography were used to validate an FE model capable of determining the residual stresses after an overload and in the following crack

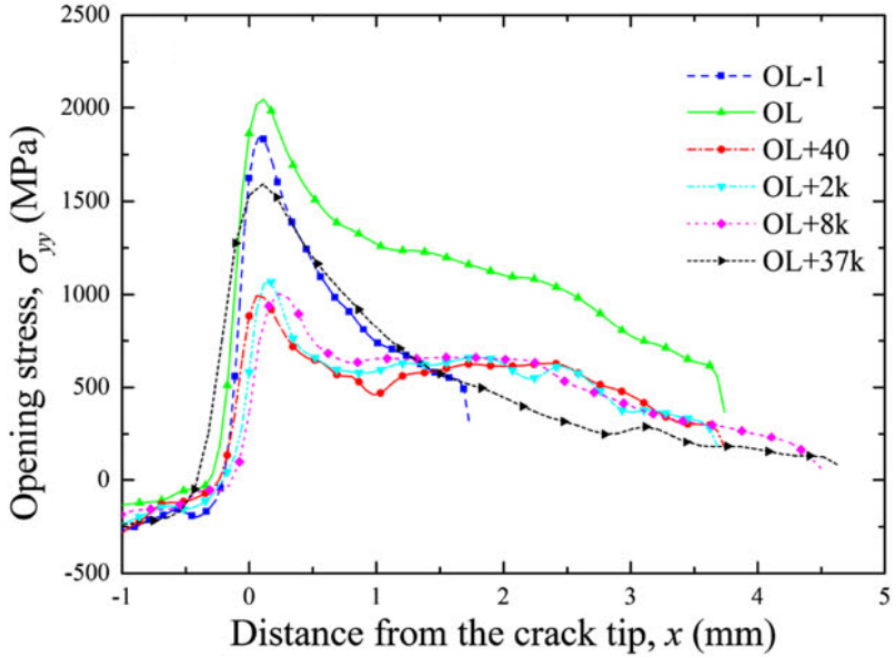

Figure 3.4: Effect of the overload and subsequent cycles on the loaded crack tip stress field [84].

propagation steps. Tomography was solely used for qualitative observations of the crack geometry and of the closed region at unloaded step.

Those different works could have benefited of a more quantitative analysis of the full-field data through the calculation of the SIF values via the techniques presented in this thesis or via field-fitting approaches. However, this is not widely applied in the literature. An example on determination of the SIF value using a least-square field fit to elastic strain maps obtained by synchrotron X-ray diffraction on a Ti-6Al-4V sample can be found in [89]. Even though it was noted that the classical LEFM equations do not apply in the plastic zone the authors did not discuss the sensitivity of the field-fitting approach to this issue. It can be observed from the fitted field that the LEFM equations are not able to fully capture the compressive wake of the crack (Figure 3.5).

The contour integral method based on the J-integral formulation is an alternative to field fitting methods, which have previously been applied to full-field displacement data to obtain stress intensity factors [115]. Following the work presented in Chapter

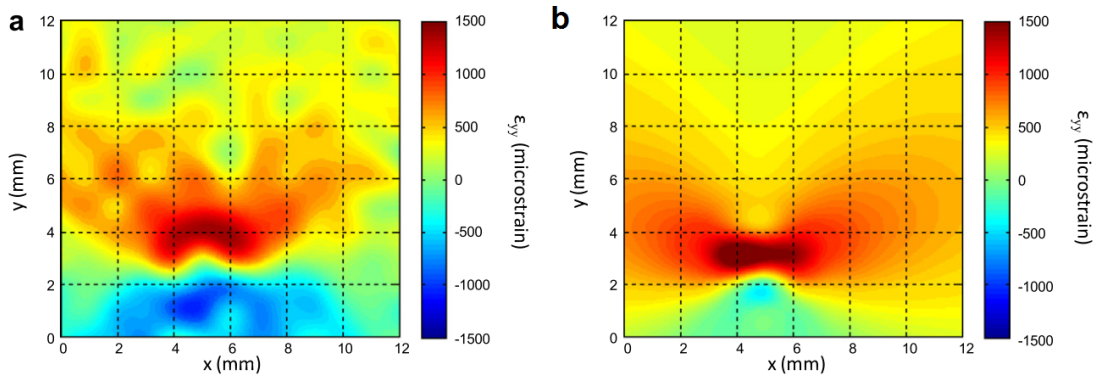

Figure 3.5: Comparison between the XRD measured strain field and the fitted LEFM field from [89]. The LEFM fit is good ahead of the crack, but is not able to capture the compressive wake.

2, where the J-integral was applied on full-field displacement data, it will here be applied to full-field strain measurements. A choice was made not to develop the method within the Abaqus framework as some of the steps could not be readily implemented within it. Instead, the MatLab code allowing direct evaluation of the J-integral from a measured crack displacement field and developed by Becker et al. [48], known as the JMAN method, was adopted and developed further. The original JMAN Matlab code takes as its input the full-field displacements from an image correlation analysis. It allows the user to define integration contours over which the J-integral is calculated, using the element-based virtual crack extension formulation [92].

A search of the literature finds no methods to determine the J-integral from strain-only datasets, such as those obtained by diffraction. However, there is a strong motivation to do this, as the J-integral method has some advantages over the field fitting methods. In particular, it is robust to uncertainties in the crack tip position and to poor definition of the field in the crack vicinity, and does not rely on theoretical assumptions of the field shape. This is particularly interesting where phenomena not explained by LEFM occur in the sample, such as observed on Figure 3.5. In this chapter, a method to determine the J-integral from elastic strain-only datasets is presented and benchmarked on a finite element

dataset. The effect of uncertainties in the measured strain data is also studied. The technique is then demonstrated on synchrotron EDXRD elastic strain maps around a crack tip in a bainitic steel compact tension (CT) specimen to study the effect of overload on a fatigue crack.

3.2 Numerical method

Firstly, it is necessary to go back to the mathematical formulation of the J-integral to identify the terms than can be determined directly from the diffraction analysis and the terms that could be at issue. The finite element formulation of the J-integral, as expressed by Rice and Cherepanov and modified for finite element formulations [14, 15], for a crack lying on the x axis is formalized by Equation (3.2), where σ_{ij} represents the 2-D stress tensor components; U_i the displacement components; W represents the strain energy density that for linear isotropic materials can be defined as $\frac{1}{2}\sum_{ij}\sigma_{ij}\varepsilon_{ij}$; and q is the virtual crack extension function whose value is 1 inside the inner integration contour and 0 outside the outer integration contour and is differentiable at all its points. The shape of the q-field is chosen to be linear here, as the shape of this field has been proven not to have an impact on the J-integral calculations [16]. The last term of the equation, A_{el}, expresses the element area.

$$J = \sum_{\text{elements}} \left[\left(\sigma_{xx}\frac{dU_x}{dx} + \sigma_{xy}\frac{dU_y}{dx} - W \right)\frac{dq}{dx} + \left(\sigma_{xy}\frac{dU_x}{dx} + \sigma_{yy}\frac{dU_y}{dx} \right)\frac{dq}{dy} \right] A_{el} \quad (3.2)$$

The full 2-D elastic strain tensor can be obtained from an adequate treatment of diffraction data with methods similar to the one presented in [116]. For example, for an XRD analysis, the original (i.e. reference state) interplanar spacing d_{0ini} and its change to reach the deformed stage Δd_0 can be obtained at all azimuthal angles, the normal strain at all these angles can be calculated as $\Delta d_0/d_{0ini}$. An ellipse (or another function, such as sine, depending on the authors) is then fitted to these strains and its principal axes are determined. The principal strains ε_I and

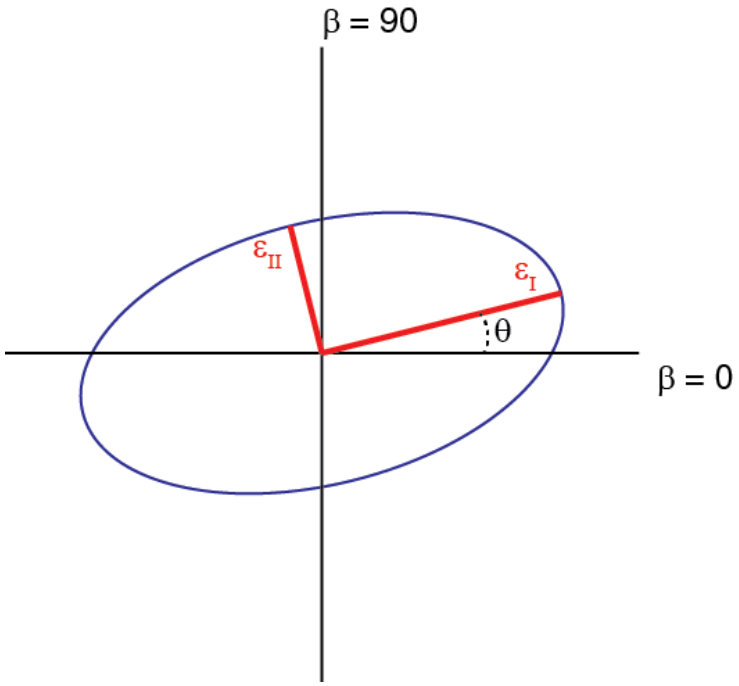

Figure 3.6: Diagram of the strain tensor calculation. The strain values are determined at each β azimuth position. Those value can be represented by the blue ellipse and its principal axis (red) are found. The rotation angle θ is used to retrieve the full tensor.

ε_{II} are read at the principal axis of the ellipse and the angle θ between the ellipse principal axis and horizontal axis is determined (Figure 3.6). The strain tensor can be calculated using Equation (3.3). In EDXRD mode, the use of several detectors positioned at different azimuthal angles permits the same type of processing.

$$R = \begin{bmatrix} \cos\theta & -\sin\theta \\ \sin\theta & \cos\theta \end{bmatrix} \qquad \begin{bmatrix} \varepsilon_{xx} & \varepsilon_{xy} \\ \varepsilon_{xy} & \varepsilon_{yy} \end{bmatrix} = R^T \begin{bmatrix} \varepsilon_I & 0 \\ 0 & \varepsilon_{II} \end{bmatrix} R \tag{3.3}$$

Despite the full strain tensor having been determined, not all the terms required in Equation (3.2) are known, so there is a missing value problem. In particular, dU_y/dx cannot be directly extracted from the shear strain, as $\varepsilon_{xy} = dU_y/dx + dU_x/dy$ and both terms of the sum cannot be considered as equal. All other values are either determined directly from the strain measurement technique, the finite element shapes or can be calculated using the elastic modulus (i.e. the stress terms). The case of complex stress/strain relationship, or challenges that can occur when working

with materials where the crystal specific modulus differs from the bulk modulus, will be tackled in the discussion of this thesis.

To address this missing value problem, the U_y displacement field must be obtained from the measured elastic strains, and then differentiated with respect to x. Integration of the strains in order to obtain the displacements was judged not suitable as the strain field include a discontinuity at the location of the crack, where the displacement field function is non-continuous (i.e. jump due to the crack) so cannot be integrated. Instead a finite element approach that does not require one to know precisely the position of the discontinuity (i.e. crack path and crack tip) has been applied.

The elastic strain map obtained by diffraction can be considered as equivalent to the elastic strains of a mesh of square quadrilateral elements where each element is centred on the measured ε_{xx}, ε_{yy} and ε_{xy} values (Figure 3.7a). The mesh elements can be defined as plane strain or plane stress depending on the region probed by diffraction. They have reduced integration formulation; this means that the elements only have one integration point (i.e. Gauss point) that is established at each element's centre, where the diffraction data has been collected.

In a conventional FE simulation, the elastic strains at the integration points are computed using the displacements of the element nodes. In the analysis developed here, the compatibility conditions for linear elastic materials are used to solve the displacement field from the input strain field. Thus, the diffraction-measured elastic strains are used to find the originating displacement field, which is required to obtain the J-integral.

Consider the case of a diffraction-measured elastic strain map that is represented by a FE mesh of N $\times$ N quadrilateral 4-node elements, the nodes are labelled as shown in Figure 3.7b; for each element a set of 3 equations can be defined that links the element node displacements to strains (one for each strain component), those are shown in Equations (3.4) to (3.6). This gives a total of $3N^2$ equations.

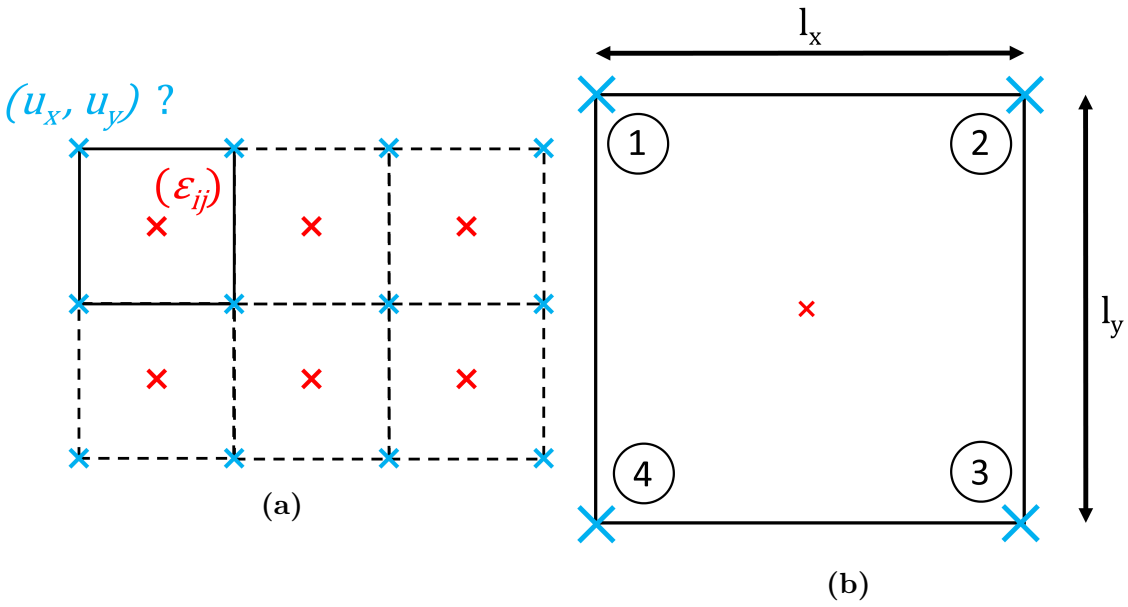

Figure 3.7: Definition of the problem for the determination of the displacement field. (a) Each strain measurement point is at the Gauss point of a reduced integration quadrilateral element. The aim is to retrieve the displacement at each element node. (b) Each element node is labelled and the undeformed element sizes are l_x and l_y.

$$\varepsilon_{xx} = \frac{[(u_{x2} + u_{x3}) - (u_{x1} + u_{x4})]}{2l_x} \tag{3.4}$$

$$\varepsilon_{yy} = \frac{[(u_{y4} + u_{y3}) - (u_{y1} + u_{y2})]}{2l_y} \tag{3.5}$$

$$\varepsilon_{xy} = \frac{[(u_{x3} + u_{x4}) - (u_{x1} + u_{x2})]}{2l_y} + \frac{[(u_{y2} + u_{y3}) - (u_{y1} + u_{y4})]}{2l_x} \tag{3.6}$$

There are 2 unknown orthogonal displacement values per node, so the total number of unknowns in the problem is $2(N+1)^2$. Therefore, any model with more than 5×5 elements will be over-constrained (the problem can be considered over-constrained when the number of equations is larger than the number of unknowns; in this case this occurs for $3N^2 > 2(N+1)^2$, i.e. $N>5$) and so can be solved and optimized to obtain the displacement field from the strain values. It is important to note that the elements next to the crack path are excluded from the analysis in order to avoid defining mesh connectivity where it is inappropriate. Neither

the crack path nor the crack tip does need to be known precisely so long as no physically unconnected elements are left connected (i.e. more elements can be set as unconnected than necessary).

The system of equations can be solved in MatLab when expressed in its matrix formulation such that MX=B (Equation (3.7)) where B contains the elements' strain values, X contains the elements' node displacements and M ensures the correct definition of the Equations (3.4) to (3.6). The matrix can be correctly populated as the element connectivity is known by the MatLab code (i.e. list of the nodes and element labels and list of the node labels for each element). The elements next to the crack path do not appear in the matrix equation; if a node is shared by four excluded elements, no displacement values will be calculated at this node. The size of the three matrices M, X and B are respectively ($3N^2$;$2(N+1)^2$), ($2(N+1)^2$;1) and ($3N^2$;1).

$$\mathrm{M} \begin{bmatrix} u_{x1} \\ u_{y1} \\ u_{x2} \\ u_{y2} \\ u_{x3} \\ u_{y3} \\ \cdots \end{bmatrix} = \begin{bmatrix} \varepsilon_{xx1} \\ \varepsilon_{yy1} \\ \varepsilon_{xy1} \\ \varepsilon_{xx2} \\ \varepsilon_{yy2} \\ \varepsilon_{xy2} \\ \cdots \end{bmatrix} \tag{3.7}$$

A linear least-square solver with a "trust-region-reflective" algorithm [117] that is implemented natively in MatLab was chosen. By default, the algorithm evaluates an approximate solution at each iteration via the method of preconditioned conjugate gradients (CG); in this case, the CG method was observed to induce noise in the results. It was therefore replaced by a direct Cholesky factorisation method that is computationally more expensive, but was found to provide better quality results.

It is interesting to note that theoretically the solution is not unique as different displacement fields with different amount of rigid body displacement (RBD) or rigid body rotation (RBR) are valid solutions to the problem. Because of this, the solved displacement field should be corrected for RBD and RBR using the approach presented in [105]. The RBD vector is determined as the average vector of the

displacement field and subtracted from the uncorrected field. The rotation matrix is then solved for, the Euler's rotation angles are calculated and the rotation is corrected. In practice, for all the observed cases, the solver converged on solutions with negligible quantities of RBD and RBR (less than $\times 10^{-3}$ degrees on rotation angles and $\times 10^{-6}$ mm RDB) thus making the correction unnecessary.

This method was incorporated within the JMAN Matlab code from Becker et al. [48] to create JMAN-S (i.e. "JMAN Strain"). The developed code allows one to use the elastic strain field from a diffraction experiment, without any displacement data, as an input to calculate the J-integral for a crack. In the calculation of the J-integral, stresses are obtained directly from the strains, using the crystal elastic modulus specific to the crystal planes of the diffraction analysis. The dU_y/dx term is obtained from the solved displacement field, and elastic strains are obtained from the diffraction data. This is acceptable when the material's bulk elastic modulus is close to the elastic modulus of the diffracting crystal planes. Cases where the crystal and bulk elastic moduli differ will be considered in the discussion.

In the case where the experimental procedure does not provide a strain map on a regular grid, an interpolation step could be used to format the data correctly. However, in most experiments data are acquired on a regular rectangular grid. A future development could be to accept non-rectangular elements, so that irregular maps could be analysed without an interpolation step; this approach then raises additional difficulty in the definition of the contours and has not been implemented. In the current form, rectangular (or square) elements of uniform dimension are used.

3.3 Synthetic and experimental datasets

3.3.1 Synthetic dataset

To benchmark the method, a 2-D finite element model of a pure mode I horizontal edge crack in a plate was created in the Abaqus FE software (version 6.13). Bi-linear,

four-node, plane stress quadrilateral elements with reduced integration were used with a linear elastic material model with a modulus representative of an austenitic stainless steel (E=190 GPa, ν=0.3). Each element was a square of 0.6 × 0.6 mm. The sample was loaded using displacement boundary conditions, the bottom of the plate was encastred whilst the top of the plate was uniformly pulled by 150 μm (Figure 3.8a). The resulting elastic strain field (ε_{xx}, ε_{yy} and ε_{xy}) determined by the FE solution (Figure 3.8b) at all integration points was exported and used as an input for JMAN-S. An area of 40 × 40 mm around the crack tip was considered, with the sampling points lying on a regular grid of step size 0.6 mm.

The accuracy of the method was evaluated by comparing the obtained elastic strain energy release rate with that calculated directly by the original FE solution. The quality of the solver result was also investigated.

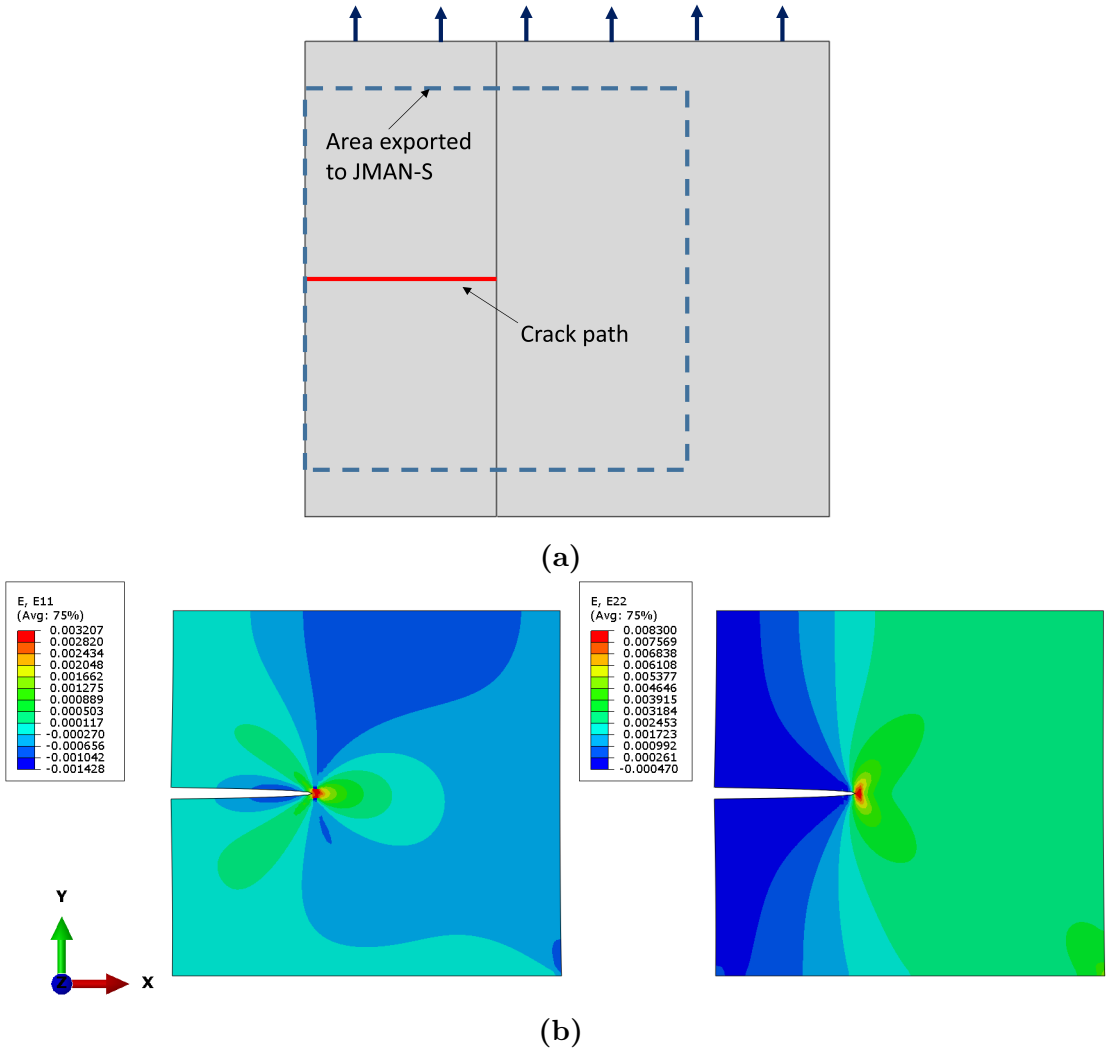

Figure 3.8: (a)FE model used for generating the synthetic strain dataset. The applied displacement is shown as blue arrows; crack path is shown as a red line. (b) ε_{xx} and ε_{yy} strain fields obtained from the FE model.

3.3.2 Experimental dataset

The experimental application was designed and realised by Dr Chris Simpson (University of Manchester), the data was made available to this study after the experiment. The author of this thesis takes no credit for producing the data.

In the experiment, EDXRD was used to obtain elastic strain maps of a 5 × 5 mm region centred on a fatigue crack tip in a bainitic steel Compact Tension specimen (W=50 mm, B=10 mm and a/W=0.45 as defined in ASTM standard geometry [107]; the fatigue crack was introduced prior to the experiment using

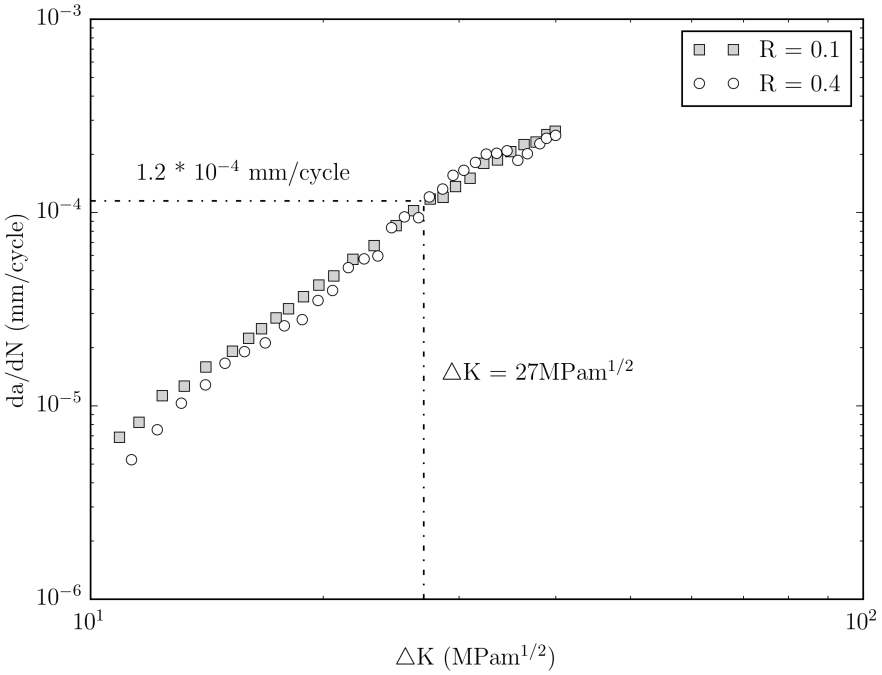

Figure 3.9: Crack growth rate as a function of ΔK obtained at two different R-ratios of 0.1 and 0.4 for bainitic steel. (C. Simpson, University of Manchester).

standard load shedding, to a maximum stress intensity factor 10.5 MPa.m$^{0.5}$; this correspond to 20% of K_{Ic} ($\sim$52 MPa.m$^{0.5}$) for this material.

A 3-D DIC system was concomitantly used to gather images of the specimen surface of a 7 $\times$ 7 mm region centred on the fatigue crack tip. The images had a resolution of 2048 $\times$ 2048 pixels and the camera calibration had a maximum reprojection error of 0.058 pixels.

Prior to the main experiment, the crack growth rate (da/dN) as a function of the applied ΔK for the used bainitic steel was determined by Dr Simpson in an experiment following the ASTM E647 standard [118]. This was done for R-ratios of 0.1 and 0.4. Little difference is observed between the two R-ratio data except at low ΔK values (Figure 3.9).

The strain data were obtained at the I12-JEEP (Joint Engineering, Environmental, and Processing) beamline at the UK Diamond Light Source as part of experiment EE12205. A 100 kN servo-hydraulic Instron machine was used to load the specimen in situ in the X-ray beam. The path length through the specimen

thickness was 10 mm and each strain map was a combination of 2 scans: a fine scan, used next to the crack tip, with a gauge measurement volume of 50 × 50 × 4000 μm; and a coarser scan used in the wider area with a gauge measurement volume of 100 × 100 × 4000 μm. All the results were interpolated onto a regular square grid of step size 100 μm using a bi-linear interpolator. The diffracting gauge volume was at the specimen mid-thickness; a plane strain condition could therefore be assumed.

The {110} Bragg diffraction peak was used and treatment of data from the 23-elements EDXRD detector allowed the creation of ε_{xx}, ε_{yy} and ε_{xy} maps using the pyXe python package[1] that uses a technique similar to the one described in Section 3.2 to retrieve the full strain tensor. The data analysis to produce all the strain maps was performed by Dr Simpson.

The experiment consisted in taking strain maps and surface images of the unloaded and loaded sample before applying an overload, after applying an overload and at different stages of crack propagation, by fatigue, through the overload affected region. At each step the average crack length was measured using an elastic resistivity method (ACPD - alternating current potential drop). Data were obtained from two different samples with two different R-ratio, the R-ratio being the ratio of maximum load over minimum load applied in one cycle. One sample was cycled at an R-ratio of 0.1 and the other at a ratio of R=0.4. In each case the monitored average crack length was used with the analytical solution of the SIF in a CT specimen in order to apply the same minimal and maximal K_I value on the sample. In the R=0.1 case, K_{min}=3 MPa.m$^{0.5}$ and K_{max}=30 MPa.m$^{0.5}$; in the R=0.4 case, K_{min}=18 MPa.m$^{0.5}$ and K_{max}=45 MPa.m$^{0.5}$, thus in both cases the ΔK is identical. This methodology was therefore designed to use different loads to achieve the same K values throughout the crack propagation steps. At overload, the applied K was 60 MPa.m$^{0.5}$ for both samples.

[1]PyXe is a software developed by Simpson, C. (2016). DOI. 10.5281/zenodo.50185

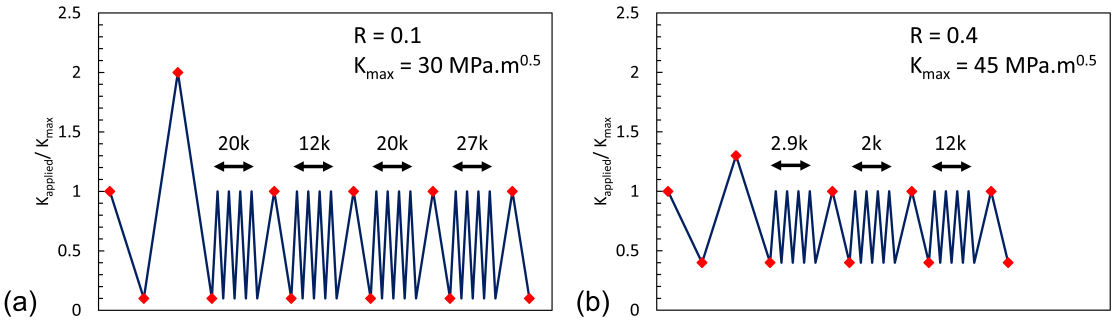

Figure 3.10: Loading applied to the two test specimens. The red symbols show the states where a diffraction map was taken. The number of cycles between each diffraction maps is indicated above the arrows. (a) Sample cycled at R=0.1. (b) Sample cycled at R=0.4.

Figure 3.10 displays the load cycles applied to the two samples. At each step, the fatigue crack was propagated to extend the crack by about 0.5 mm, and the fatigue cycling was stopped for the strain and 3D-DIC observation. For each of the diffraction maps, the load and crack length (Figure 3.11a) are known thus allowing calculation of the theoretical K value from the formula given in the ASTM standard [107]. The crack growth rate (da/dN) was also determined (Figure 3.11b). After the experiment, the samples were broken open via fatigue loading and fractography observations[2] confirmed that the crack front was straight.

[2]Performed by Dr C. Simpson

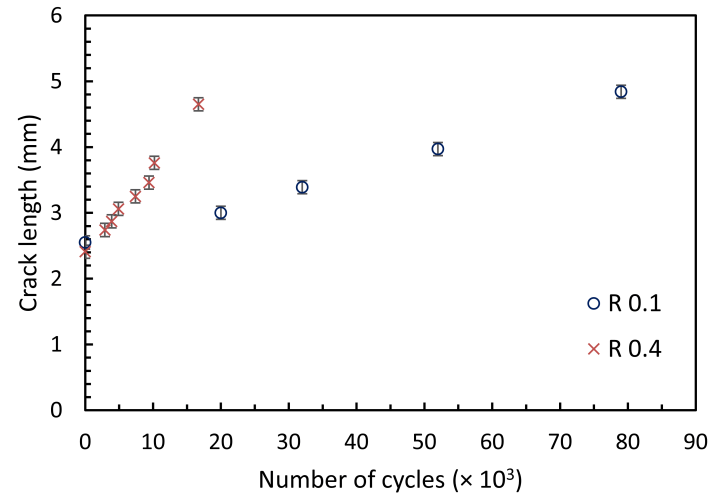

(a)

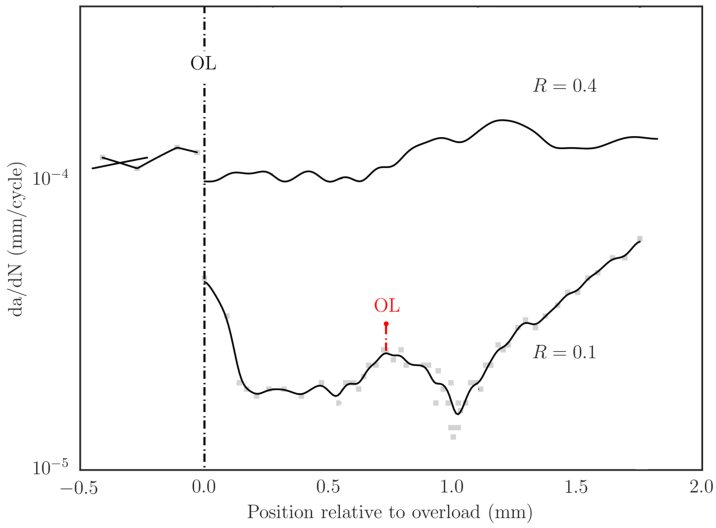

(b)

Figure 3.11: (a) Crack length from notch determined by ACPD for different number of cycles for the two samples cycled at different R-ratios. More crack length measurements than diffraction maps were made. (b) Crack growth rate measured via ACPD as a function of crack length from overload. The main overload (OL) is marked, and an accidental small overload (OL) is shown in red. Data from C.Simpson (University of Manchester).

3.4 Results and discussion

3.4.1 Synthetic benchmark results

The JMAN-S method was applied to the FE exported elastic strain field of the benchmark model. A mask of 4 elements width was applied on the crack path and extended 2 elements beyond the crack tip. The masked elements are excluded from the contour integral and the displacement solving step. The mask can be seen on Figure 3.12a as the white region. This is necessary to define both the start and end of the integration contour, and more importantly the unconnected regions in the displacement field solution. The known material properties, detailed previously, are used for the calculation of stresses from strains.

Solved displacement field quality

The Finite Element strain field with the applied mask was solved, using the method detailed in Section 3.2, to obtain the originating displacement field. The solver always converged on a solution; Figure 3.12a shows the U_y displacement field, which is the most significant displacement for a crack parallel to the x-axis and loaded in Mode I and the only field used in the later calculation of the J-integral to determine the dU_y/dx component. The FE displacements have been corrected for rigid body movement, so the displacement at the crack tip is zero.

Comparison of the displacement field that is obtained from the strains with original displacements in the FE model (Figure 3.12b) shows that the code accurately retrieved the original displacement values from the strain data at all positions in the sample. Numerically, the maximum deviation between the solved displacement and the original FE displacement is around 2 μm with an average error of 0.48 $\pm$ 0.31 μm. This degree of accuracy is of course due to the absence of experimental noise but proves the validity of the approach to solve the displacement fields.

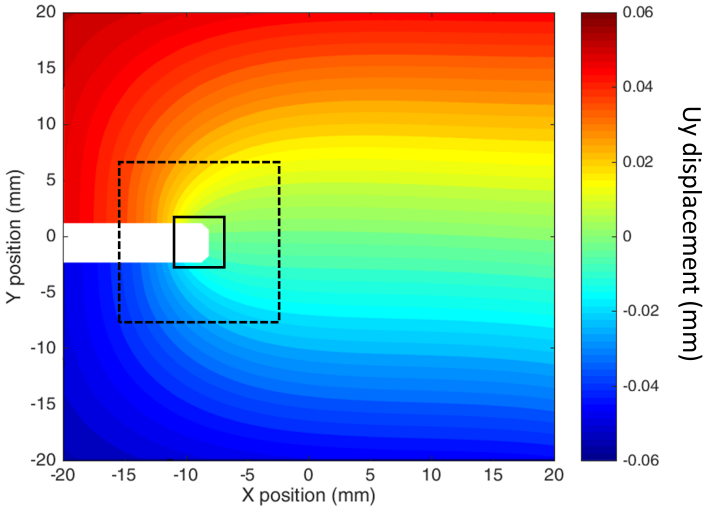

(a)

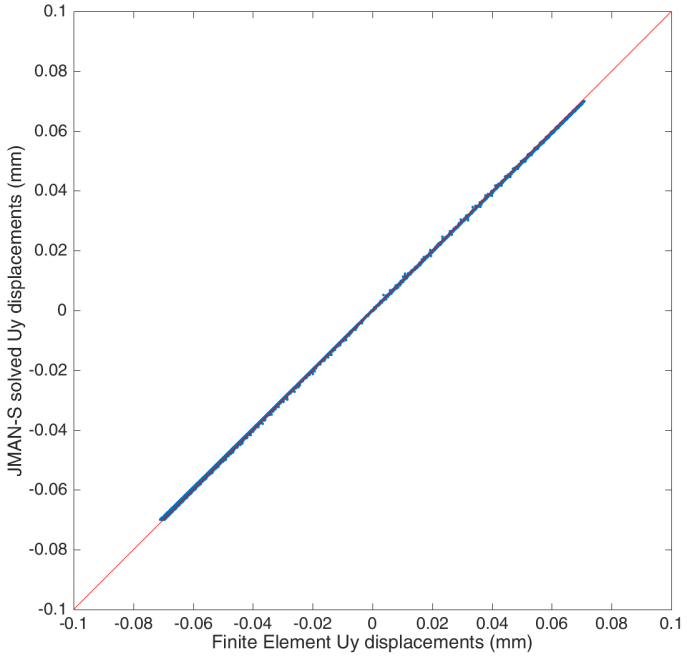

(b)

Figure 3.12: (a) Uy displacement field solved from the FE strain data, the white area is the applied masked used for the displacement solving step. The black rectangle is the fixed inner J-integral contour and the dotted rectangle is the outer integration contour. (b) Original FE displacements versus JMAN-S displacements, the red line corresponds to a 1 to 1 relationship, R^2=0.998.

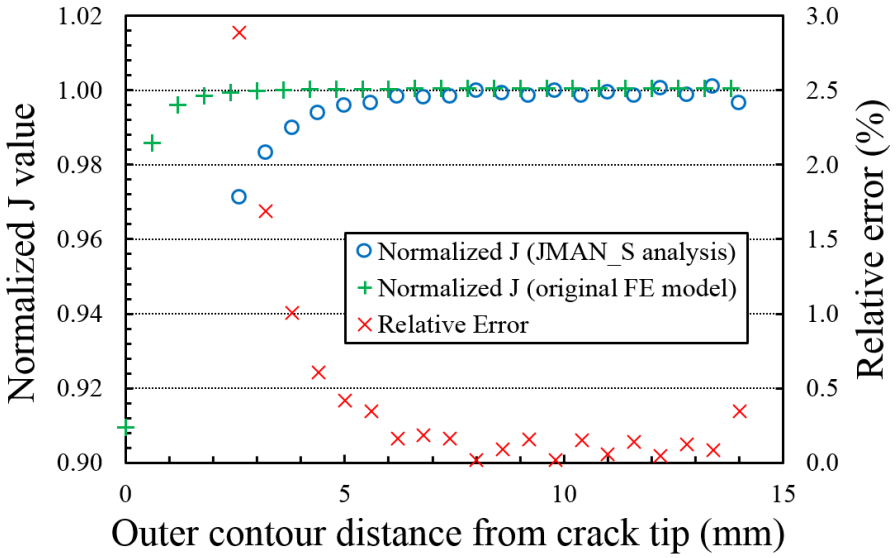

Figure 3.13: *J*-integral calculation from FE strain dataset using JMAN-S and original FE data. The *J*-integral value is normalized by the original FE *J*-integral value.

J-integral accuracy and contour independence

The *J*-integral was evaluated both using JMAN-S on the FE strain field with the solved displacements, and on the original FE model via Abaqus. Multiple contours were considered to check for path independency; the outer contours were centred on the crack tip and extended radially in all directions. In JMAN-S the inner contour had a fixed size of 4 × 4 mm, also centred on the crack tip (Figure 3.12a). In the Abaqus FE model, the inner contour is collapsed onto the crack tip.

It is important to note that the JMAN-S method, as with other contour integral methods, does not need to know the crack tip position precisely. The JMAN-S *J*-integral converged (Figure 3.13) within 4 contours with less than 0.5% relative error. The convergence of the original FE model within 2 contours is shown for comparison.

Effect of uncertainty and binning on *J*-integral calculation

The benchmark presented in the previous section considers a noise-free dataset where the strains were directly obtained from an FE model. In experimental strain measurement techniques, uncertainties are present in the determination of the strain tensor and are inherent to the strain analysis method. They are originated

by errors in the peak-fitting/correlation algorithms used and/or parasitic sample displacements during the experiment. An estimation of the errors in the strain measurements for X-ray and neutron diffraction data can be found in [88]. Those errors are estimated to 20 $\mu\varepsilon$ for X-ray diffraction [88] and 50 $\mu\varepsilon$ for neutron diffraction [119], those values can be compared to the strains shown on Figure 3.8b corresponding to an austenitic stainless steel specimen being loaded at its K_{Ic} value.

To study the effect of those errors on the J-integral calculation, the previous FE generated dataset was altered with additive zero mean white Gaussian noise of standard deviation 20 and 50 $\mu\varepsilon$, which are typical of X-ray and neutron diffraction respectively [88]. Each strain field (ε_{xx}, ε_{yy} and ε_{xy}) was added to a different random distribution. This approach is not strictly representative of a real case dataset as the noise distributions in the different strain fields cannot be considered independent but suffices to benchmark the effect of uncertainty on the method.

In both cases, the U_y displacement field was successfully solved and the J-integral converged on a solution. The error in the J-integral was calculated by comparing the determined value with the original FE value. Figure 3.14 shows the errors for the different datasets, the error bars are the standard deviation of the measurement on the contours where the J-integral calculation converged. Even in the most detrimental case (i.e. neutron diffraction) the achieved accuracy was better than 5%.

Another variable to consider when benchmarking the method is the XRD gauge area compared to the field of the SIF of the crack. The experimentalist determines the XRD gauge area to control the number of grains in the diffraction pattern. Whilst a small gauge area gives a better spatial resolution, it is not always possible to use it if the material is coarse grained or due to acquisition time constraints (if fewer grains diffract, the signal intensity is lower and the acquisition time must be increased). A large gauge area will average the strains over the gauge area and will impact the J-integral calculation.

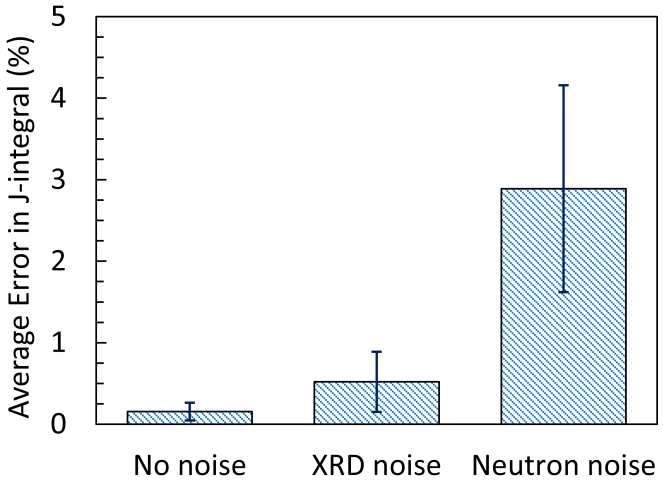

Figure 3.14: Average error in the J-integral for a dataset without noise and two datasets simulating the noise level present in typical XRD and neutron diffraction datasets (20 and 50 $\mu\varepsilon$ respectively).

In order to be able to relate the benchmark results with experimental results, different gauge area sizes were normalised. As diffraction techniques probe the elastic strains, it was considered that the measured strains were directly proportional to the stress intensity factor and the normalisation was achieved by dividing the gauge side length by the SIF. Although the normalisation uses the SIF that is to be determined by the technique, this does not pose a problem in most of the configurations where an estimate of the SIF can be determined prior to the experiment via analytical solutions or Finite Element modelling.

The J-integral value was determined on noiseless data for 5 different simulated gauge sizes. The increase in gauge area was simulated by averaging the data points included in one gauge element. The results are presented on Figure 3.15 where the error bars represent the standard deviation of the error over 13 different contours. Even for large gauge areas, the method performs well. This could be because the method relies on a contour integral that uses data from the far field where the gradient in strains is less important and it is therefore less impacted by large gauge areas than crack tip strains where the gradient is steep.

For the type of material used in this benchmark (austenitic stainless steel), the

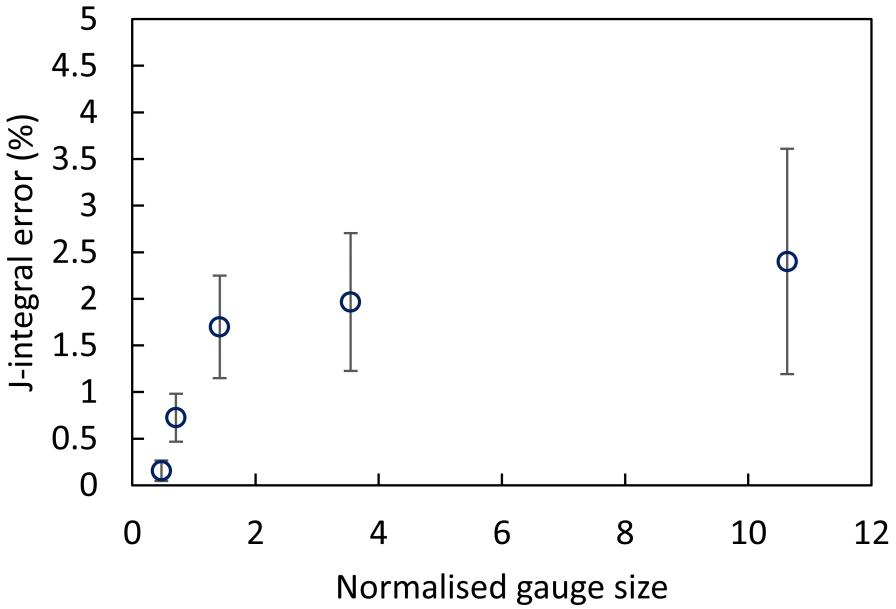

Figure 3.15: Effect of diffraction gauge area on the J-integral error. The gauge area side length (in μm) is normalised by the SIF (in MPa.m$^{0.5}$).

typical gauge area on specimen surface used for X-ray diffraction techniques would be between 50^2 and 100^2 μm^2. At the critical value of K_{Ic} ($\sim$52 MPa.m$^{0.5}$), the normalised gauge size is between 1-2 so the expected J-integral error (without noise) is lower than 0.5%.

3.4.2 Experimental results

Examples of the experimental diffraction map data, obtained at an applied stress intensity factor of 30 MPa.m$^{0.5}$ before overload (sample "R0.1" in its first cycle, c.f. Figure 3.10) and after overload and 20k cycles of fatigue are shown in Figure 3.16. Qualitatively speaking, the (a), (b) and (c) maps, obtained before the overload, follow the pattern expected for a horizontal crack loaded in mode I. The effect of the overload is clearly seen on maps (d), (e) and (f) as it leaves a wake of residual compressive strains, particularly important in the ε_{yy} (d) map as the crack is loaded in mode I.

Similar maps were obtained for all the steps shown in Figure 3.10 and processed through the JMAN-S method to calculate the J-integral. The {110} specific

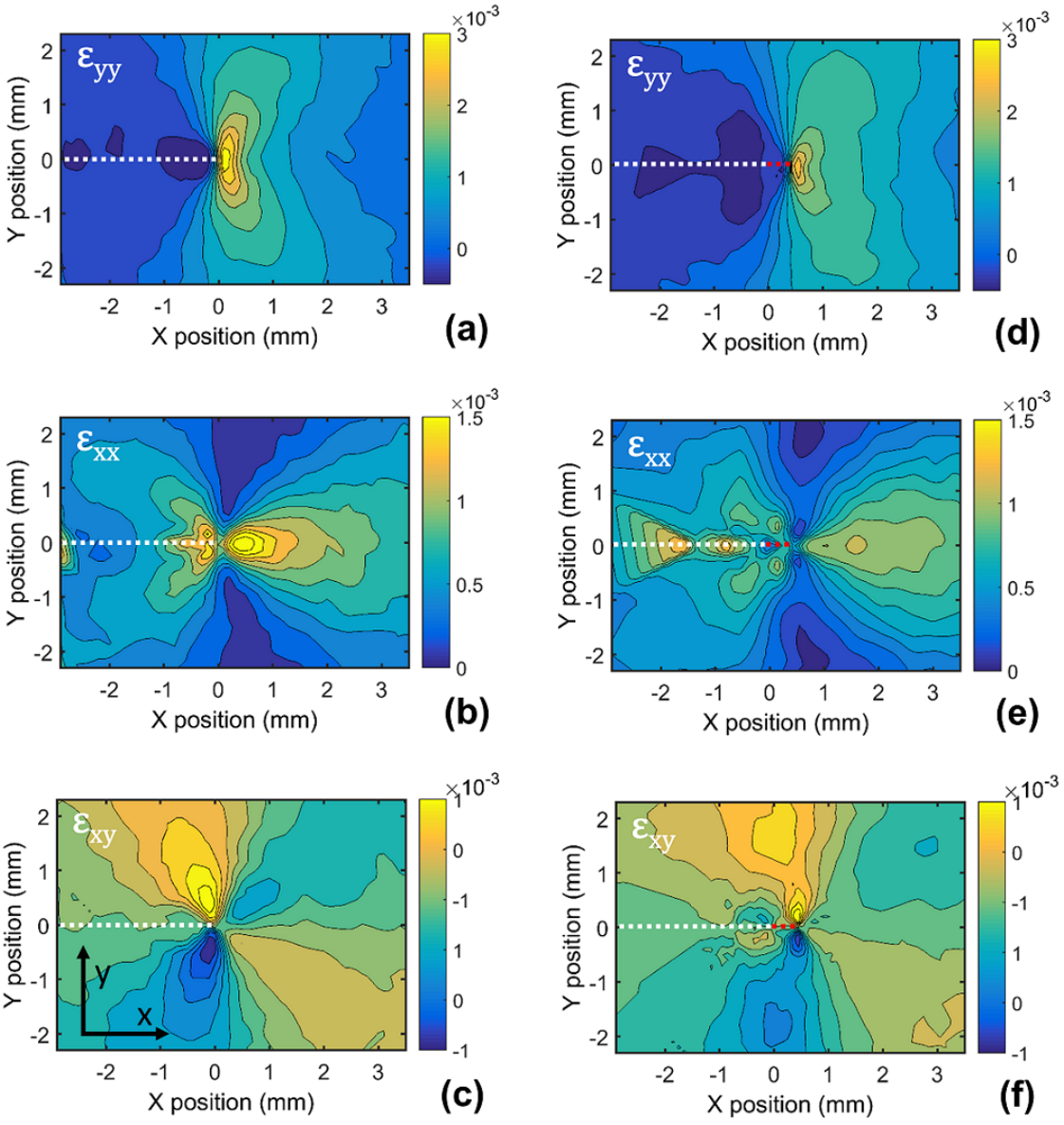

Figure 3.16: EDXRD strain maps for a theoretical applied K value of 30 MPa.m$^{0.5}$. (a)(b)(c) Before overload. (d)(e)(f) After overload and 20k cycles. The original crack path is shown in white. The crack propagated during fatiguing is shown in red. The overload was applied on the crack shown in white.

modulus of 210 GPa [120] was used in the computation of the stresses; the bulk tensile elastic modulus for bainitic steel is between 205-210 GPa. For comparison with the applied stress intensities in the experiments, the J-integral values have been converted to stress intensity factors using Equation (3.8), which is valid for plane strain condition and pure mode I loading, where the tensile elastic modulus is 210 GPa and Poisson's ratio is 0.3.

$$K_I = \sqrt{J\Big(\frac{E}{1-\nu^2}\Big)} \tag{3.8}$$

Pre-overload results

The case of the data obtained before the overload will first be treated as their interpretation is straight forward and provide a good estimate of the method accuracy. Four different maps are available for the data before overload; they are taken at K_{min} and K_{max} for the two samples "R0.1" and "R0.4". For those maps, the measured SIF value via the JMAN-S analysis is expected to be the same as the applied K as no significant crack closure should be present. In all the 4 cases, the calculated J-integral converged and was contour independent (Figure 3.17a). The results are summarised in Figure 3.17b, in comparison with the applied stress intensity values.

The SIF values determined with the JMAN-S method show good agreement with the applied stress intensity factors. The uncertainty in the applied value, mostly due to crack length determination errors, is estimated to be less than ± 0.5 MPa.m$^{0.5}$. The random error in the stress intensity factor obtained via JMAN-S is taken as the standard deviation over the last 10 contours, and is less than 2 MPa.m$^{0.5}$ in all cases.

Data from the benchmark allows evaluation of the expected calculation accuracy. In this case, the data comes from XRD that is expected to induce an error of $\sim$0.5% and the normalised gauge size for the experiment linearly varies between 30 and 2 for K_{applied} varying between 45 and 3; this should add an uncertainty between 1.5% and 3%. Considering that the uncertainty can be considered as

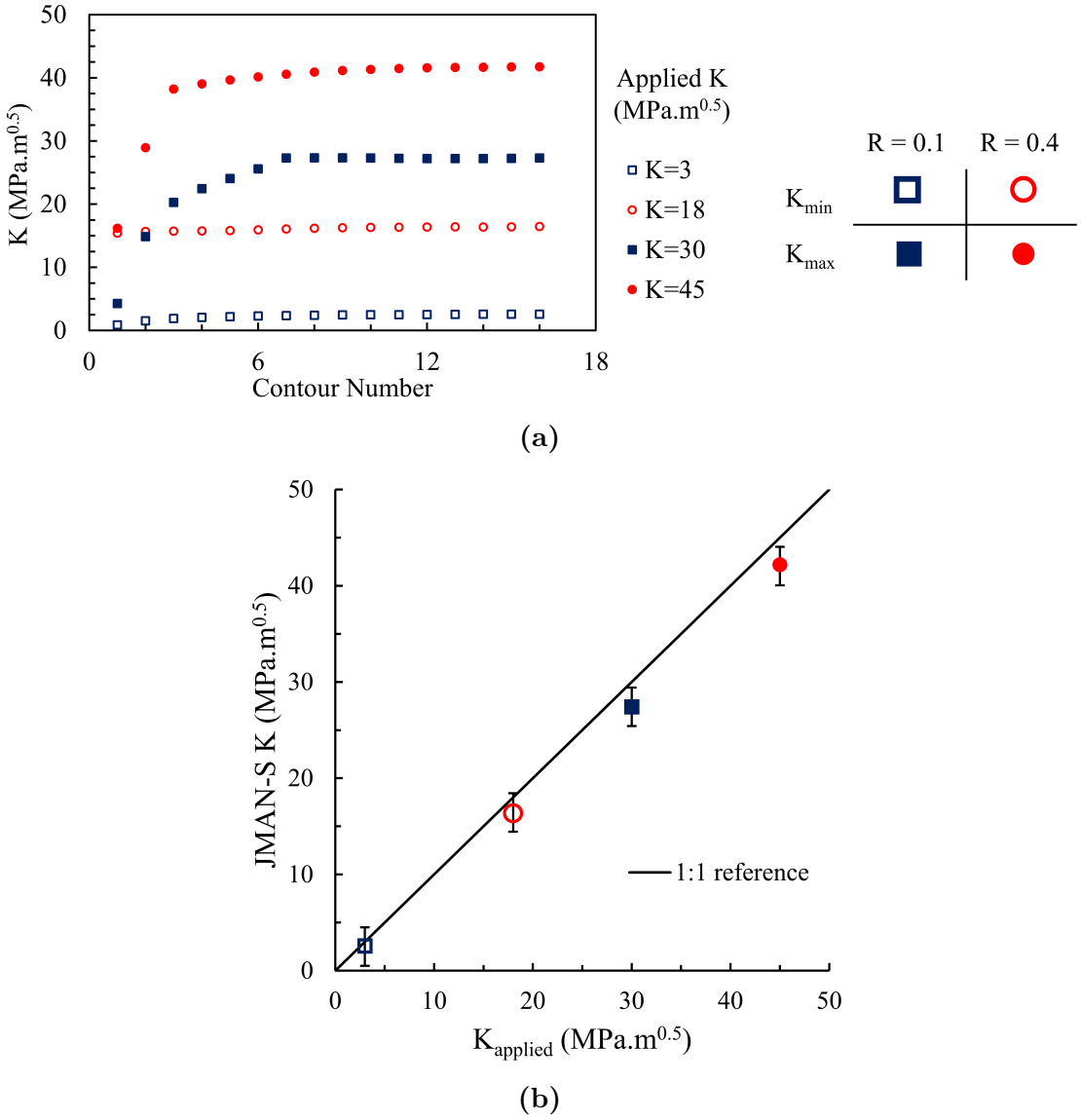

Figure 3.17: (a) J-integral contour independence and convergence at different applied stress intensity factors, the outer contour distance to crack tip increase linearly with each contour. (b) Comparison of the applied stress intensity factor K_{applied} with the JMAN-S calculated values. Experimental data gradient is 0.93 showing a systematic error of 7%. The same legend is used in both graphs to clarify which sample the data are from.

cumulative, the expected accuracy of the JMAN-S results in this experimental case is estimated between 0.5% and 2%. This is less than the 2 MPa.m$^{0.5}$ standard deviation over the different contours.

There is a systematic difference between the applied and calculated stress intensity factors. This systematic error is of 7% determined from Figure 3.17b as the difference between the experimental data gradient and the unit gradient. This may be due to extrinsic effects such as alignment errors in the loading of the crack, or the difference between the bulk and crystal elastic behaviour, and is the subject of further investigation and calibration studies. It is difficult to quantify the effect of error in the elastic modulus on the results as it not only changes the SIF value calculated from the J value but also changes the stress field calculated from the measured strains. Here the approximate error in the Young's modulus E is of 2.5%; by only considering the calculation of the SIF from Equation (3.8) and not the strain/stress error this can generate an additional uncertainty of 1.25% on the results. Nonetheless, the agreement between the expected and measured stress intensity factors is good.

Overload effect

All the acquired diffraction data were processed in the same way as presented in the previous section. The {110} specific modulus of 210 GPa was used and the calculated J-integral values were converted to stress intensity factors using Equation (3.8). In all cases, the J-integral converged on a solution, was contour independent and the solved displacement field looked as expected.

Figure 3.18 presents the calculated SIF values for the two samples ("R0.1" and "R0.4") determined from the strain measurement using the JMAN-S method. In all cases, apart for the overload, the applied load was aiming at generating SIF values of K_{min}=3 MPa.m$^{0.5}$, K_{max}=30 MPa.m$^{0.5}$ in the sample "R0.1" and K_{min}=18

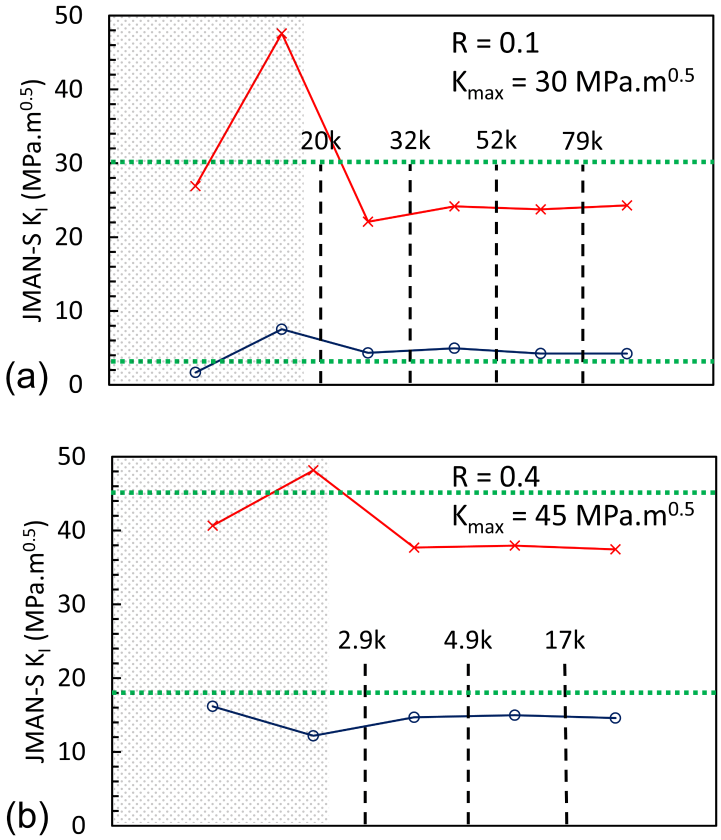

Figure 3.18: Stress intensity factor values determined with the JMAN-S method for the (a) "R0.1" sample and the (b) "R0.4" sample. The theoretically applied SIF value is shown as green dotted lines. The red crosses show the values at K_{max} and the blue circles the value at K_{min}. The dotted region contains measurements obtained before cycling. An effect of the crack overload is observed on the subsequent cycles.

MPa.m$^{0.5}$, K_{max}=45 MPa.m$^{0.5}$ in the sample "R0.4". At overload, the applied K was of 60 MPa.m$^{0.5}$ in both samples.

The size of the plastic zone produced by the overload is estimated by simple theory (Equation (3.9) considering $\sigma_{\text{yield}} = 570$ MPa) to have a radius r_y of 17.6 mm, which is quite substantial. At no point during the experiment has the crack propagated out of this region; this experiment is the case of a crack propagating through a changing stress field induced by residual stresses left by the overload. The effect of the overload on the elastic strain fields of the post-overload loaded cycles can be clearly observed with a significant reduction occurring on the K_{max} value (Figure 3.19c). In both specimens a reduction of 10 $\pm$ 3.5 % in K_{max} after

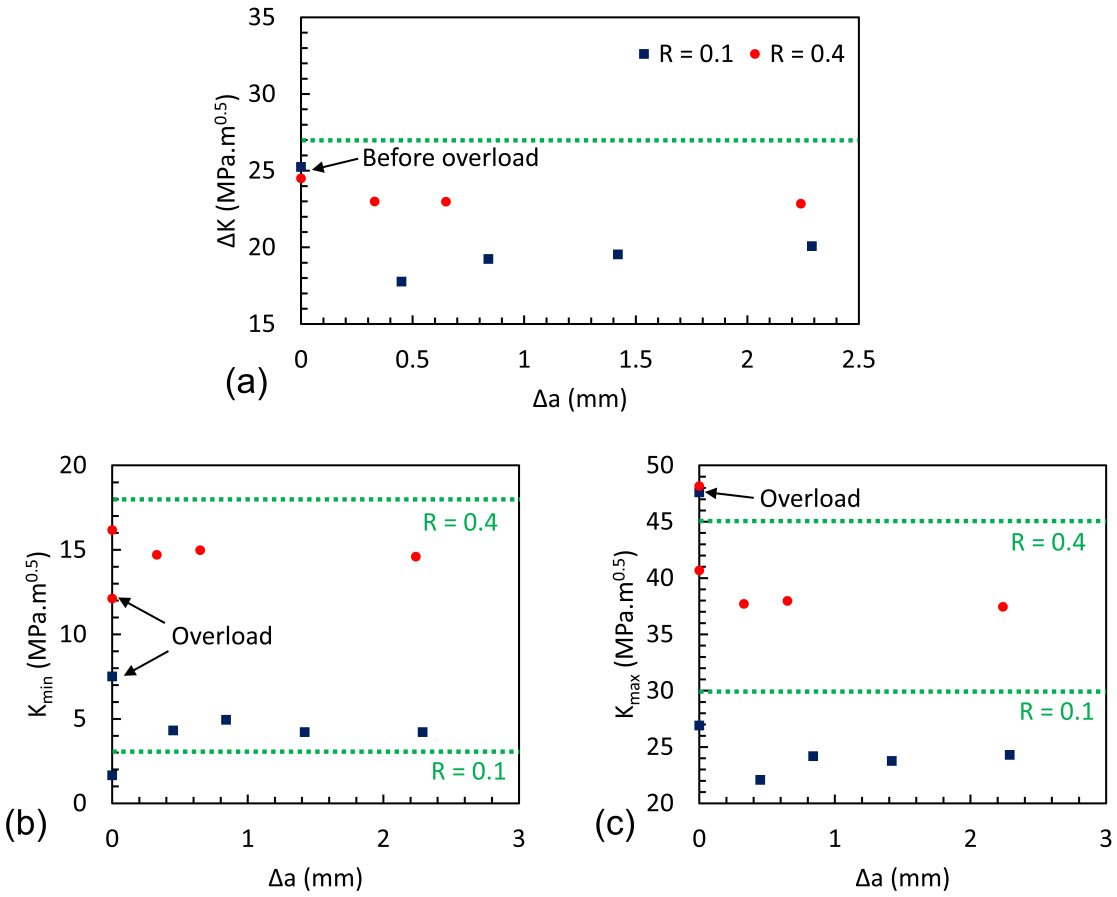

Figure 3.19: (a) ΔK measured for the two samples at different crack propagation increments. (b) K_{min} value at the different crack propagation steps. (c) K_{max} value at different crack propagation steps. The green dotted lines show the theoretically applied values.

overload is seen and this even after the crack has propagated by more than 2 mm.

$$r_y = \frac{1}{2\pi}\left(\frac{K}{\sigma_{\text{yield}}}\right)^2 \tag{3.9}$$

The 3-D DIC analysis of the surface images was performed by Mr Cinar (University of Sheffield) using LaVision's Davis software that implements a Least Square Matching (LSM) algorithm. The subset size was of 21 × 21 pixels and the step size between subsets of 5 pixels. For both samples, the image used as a reference was the sample, loaded at K_{min}, before overload. The resulting displacement field was then analysed by Mr Cinar using the codes and procedure developed in this thesis (Chapter 2) by considering the surface as plane stress and using bainitic

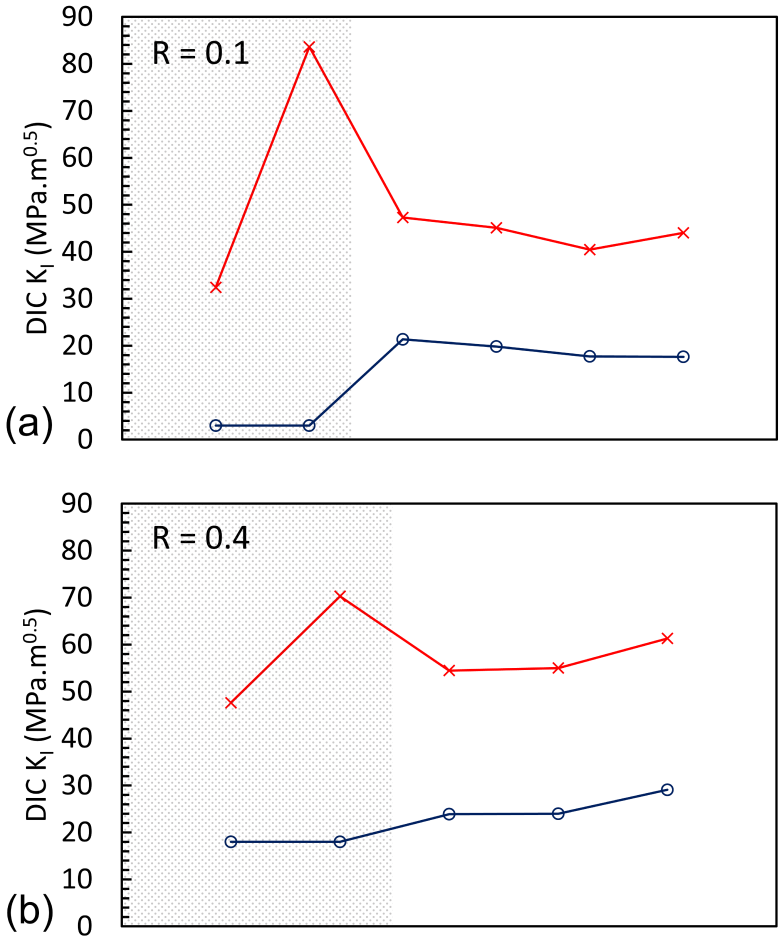

Figure 3.20: Stress intensity factor values determined, for the successive observations, using the method developed in Chapter 2 on the DIC data. (a) "R0.1" sample. (b) "R0.4" sample. The red crosses show the values at K_{max} and the blue circles the value at K_{min}. The dotted region contains measurements obtained before cycling. An effect of the crack overload is observed on the subsequent cycles.

steel elastic properties of $E = 210$ GPa and ν=0.3. Some of the results have been included in this thesis to aid the discussion of the diffraction data analysis.

The DIC determined K_{min} and K_{max} values at all propagation steps for both samples are presented in Figure 3.20. The calculated values at the loaded overload step are not trustworthy as plasticity occurred and the calculation is made using a linear elastic model. The effect of the plasticity induced by the overload can clearly be observed on the subsequent cycles; as the DIC reference image was taken before overload, the calculated K values include the non-recovered (plastic) deformation, thus shifting both the K_{min} and K_{max} values upwards. However, the

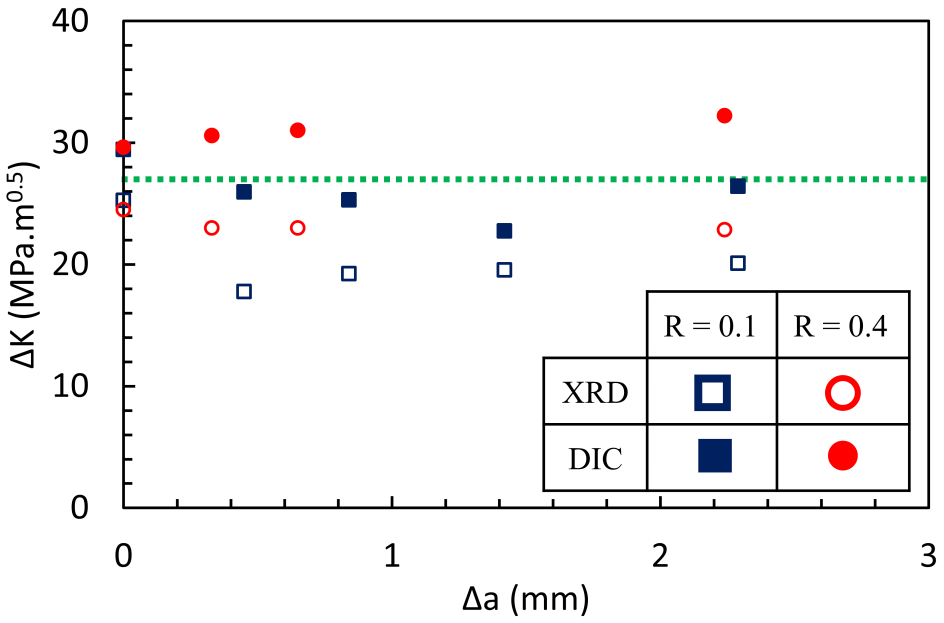

Figure 3.21: Comparison of the ΔK values obtained from the DIC data and the XRD data. The theoretically applied ΔK is shown as a green dotted line. Data at overload are not shown on the graph.

ΔK value remains in the expected range (Figure 3.21), showing that the elastic deformation applied during cycles is the expected one.

Comparison of XRD and DIC calculated ΔK (Figure 3.21) shows that surface DIC finds higher values than JMAN-S analysis from XRD. This can be attributed to the residual stresses within the body (i.e. see Figure 3.16), that must then interact in a non-linear manner with the applied loading to produce the ΔK experienced by the crack and measured by the XRD measurements. The DIC approach only captures the intra-cycle elastic deformation of the surface.

The crack grow rate (da/dN) directly measured by ACPD (Figure 3.11b) can be compared with the da/dN predicted from the JMAN-S and DIC determined ΔK (Figure 3.19a and Figure 3.21) using Paris' law constants extracted from Figure 3.9. This comparison is shown in Figure 3.22 for both R-ratios of 0.1 and 0.4.

The da/dN obtained via XRD and ACPD shows the same trends whilst the DIC data predicts a rather constant crack growth rate with no influence of the overload. For the "R0.1" sample, significant shielding is present in the measured

stresses after the overload and this progressively recovers when the crack has propagated more than 0.5 mm. In the "R0.4" sample, no shielding of the da/dN is observed after the overload.

From these results, one could draw the conclusions that crack closure is present in the "R0.1" sample and not in the "R0.4" sample and that DIC measurements are not sensitive enough to detect closure. This is the case if only K_{max} and K_{min} in the cycle are considered. However, DIC data was gathered throughout the load cycles and can be analysed by the same method to retrieve the SIF value at different loads within each cycles. The full data are not shown here (the SIF values were provided by Mr A. Cinar), but are summarised in Figure 3.23 as the rate change of the SIF with respect to load (i.e. dK/dL) for the cycles before and after the overload.

For an open, elastic crack, dK/dL is expected to be constant and is weakly sensitive to crack length in a compact tension specimen. For clarity, the data of all the post-overload cycles for each sample have been averaged and the overload cycle data have been omitted (they are similar to the pre-overload data over the same load range). The reported values are the average for both loading and unloading, which were similar. For the "R0.4" sample, there is no significant difference in dK/dL before and after overload. However, for the "R0.1" sample, dK/dL is significantly reduced at low load (< 4 kN) after the overload. This demonstrates that crack closure affects the specimen; at low loads the compressive residual stresses reduce the effect of the applied load on the crack opening and this is observed in the development of the displacement field around the crack, which is used to evaluate the SIF. Similar trends would be expected to be seen in the measurement of crack opening profile. The direct measurement of the SIF by diffraction is, however, more sensitive that its evaluation via the surface displacement field.

This analysis would have benefited of the acquisition of tomography data that would have allowed the precise determination of the crack shape. Calculation of the SIF values along the crack front from Digital Volume Correlation (DVC)

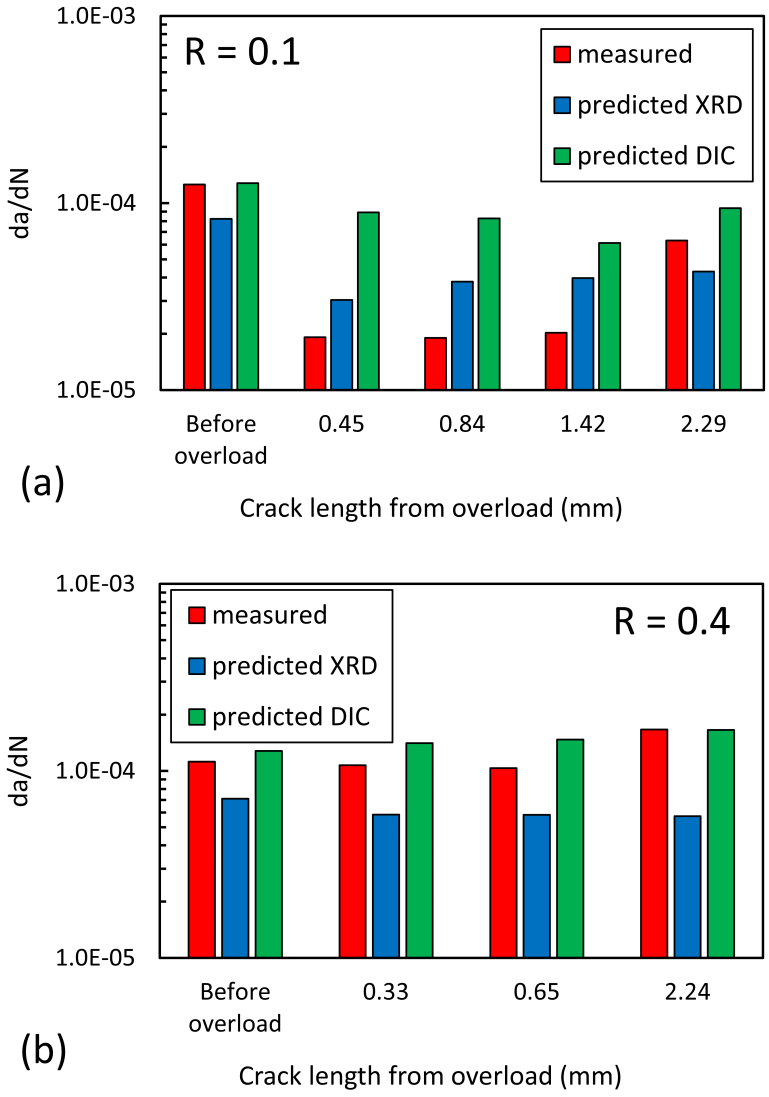

Figure 3.22: Comparison of the crack growth rate (da/dN) determined by direct ACPD measurement and predicted from the JMAN-S calculated ΔK (Figure 3.19), the DIC calculated ΔK (Figure 3.21) and Paris' law (Figure 3.9). Data for sample cycled at a R-ratio of (a) 0.1 and (b) 0.4.

results might be then also be possible, although it is likely that the bainitic steel microstructure would not provide sufficient tomography contrast.

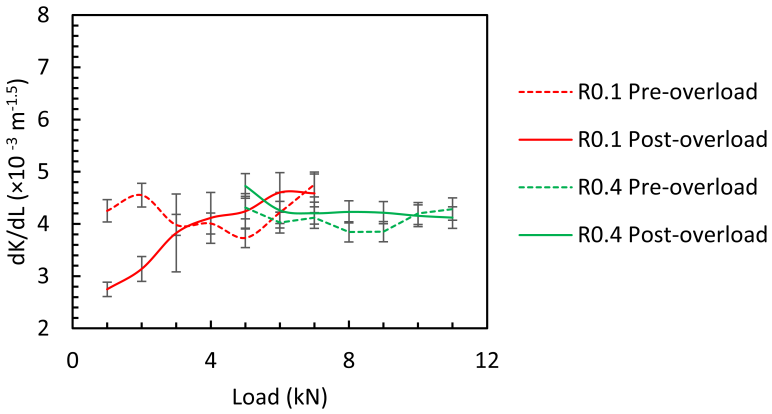

Figure 3.23: Rate of change of SIF with load during the load cycles for the two specimens before and after overload. The data of all cycles for each sample after overload have been averaged for clarity. The error bars are the larger of either the estimated 5% uncertainty in SIF or the standard deviation of the averaged values.

3.5 Conclusion

A novel technique is presented to characterize the crack driving force of a crack, as a J-integral elastic strain energy release rate, from diffraction-measured 2-D elastic strain datasets. In principle, it can be used with any experimental method that retrieves the full 2-D elastic strain tensor. The technique has been benchmarked on synthetic data for the effects of noise and spatial averaging and shown to calculate the J-integral with good accuracy. The data shown in this chapter should allow an experimentalist to carefully choose the experimental conditions to optimise the calculation of the J-integral.

The main interest of the approach is that it does not assume an analytical field. For diffraction techniques, the field is always elastic, but this can be affected by residual stresses and non-linear deformation that will impact field fitting techniques. The critical step is the solution of the equivalent displacement field, using a finite element approach and the compatibility conditions in linear elastic mechanics, the FE approach used is noise robust and computationally efficient.

Other integrals, such as the interaction integral or the decomposition method [51] could be implemented with little extra work to study mixed-mode datasets. The

analysis of data obtained via EBSD (electron backscatter diffraction) measurements (e.g. [121]) is also feasible.

самые же душевнобольные — это несомненно те, которые в других людях видят признаки сумасшествия, которых в себе не видят.

The most mentally deranged people are certainly those who see in others indications of insanity they do not notice in themselves.

— Lev Tolstoï *The Devil*

4

3-D J-integral Calculation from DVC Measurements

Contents

4.1 Introduction

The J-integral technique and its application on 2-D cases has been presented in the previous chapters. A strength of this method is that it can be readily transposed to 3-D cracks to determine the variation of the strain energy release rate along the crack front, which may not necessarily be straight. Coupled with the experimental

methods of X-ray tomography and Digital Volume Correlation, the 3-D J-integral can be evaluated on a 3-D experimental displacement field.

The calculation of J-integral values for 3D cracks is a well-established technique for FE modelling [16, 92, 94]. Calculation of the J-integral from measured displacement field removes the assumption of the stress/strain field shape that is required for field-fitting (e.g. [69]). Also it is interesting to note that in the literature, all cases of SIF measurement from 3-D cracks using field-fitting are actually made on a set of 2-D slice planes chosen along the crack front.

The method described here is derived from that previously applied to 2-D data (Chapter 2). It can deal with large datasets (e.g. several tomographs stitched together), is versatile in terms of sample geometry and material law and it is able to tackle complex crack paths. It uses standardised FE software to perform the calculation, to deal with missing data and to define the integration contours.

The technique itself is first presented followed by a benchmark analysis that is based on the use of synthetic datasets in order to assess the uncertainty in the calculated J-integral. An experiment to examine straight and corner fatigue cracks, under static loading, in nodular graphite cast iron is then analysed.

4.2 Method for the analysis of 3-D displacement fields

4.2.1 DVC analysis

General considerations

Digital Volume Correlation is a feature tracking method, presented in the Chapter 1, which determines the full-field displacement in a 3-D sample from two volume images of this sample at different load states. In this work, the volume images are obtained via X-ray tomography. The aim of the DVC analysis is to retrieve the displacement field with the best compromise between the noise present in the calculated displacement field and spatial resolution of the matrix of displacement

vectors; ultimately this is a function of the image quality (i.e. signal to noise ratio, presence of artefacts, image histogram, etc.) and the size of the trackable features. The LaVision Davis software (ver. 8.3.0) was used for this purpose. It uses a subset based approach where the volume is divided into cuboidal (typically cubic) subsets of known size whose movement and deformation is tracked between the original and deformed volume image.

Unlike 2-D experiments with DIC, for which it is possible to add a speckle pattern to the observed surface, the experimental parameters in DVC are harder, or indeed impossible, to control. Whilst the image quality can be optimised by the careful choice of imaging parameters (i.e. X-ray energy, pixel size, etc.) and reconstruction codes, some experimental set-ups can limit the number of projection angles, which then affects the tomograph quality [122]. Similarly, the sample chemistry and its distribution can drastically affect the tomograph quality (e.g. high-attenuation inserts within low-attenuation matrices [123]). Also artefacts known as ring artefacts [124] are common in synchrotron tomography, they are due to dead pixels on the scintillators and form large bright rings in the data. Despite methods existing to attenuate the problem [125], they are a major issue for volume correlation if present. It is important to note that the effect of artefacts on DVC is linked to their nature; if the artefact is attached to a feature of the material (e.g. case of metal artefacts), it could act as a trackable feature and the impact on DVC will be less. However, artefacts that don't displace with the material (e.g. ring artefacts) are particularly detrimental.

The size of the trackable features is also hard to control, some materials such as bone [65] or graphite [73] will present a microstructure that is well adapted to achieve good spatial resolution when other materials will not be suitable to provide good DVC results unless large DVC subsets are used where the size of the trackable pattern is large compare to the imaged area.

Because of those reasons and because of the increase in computational complexity due to the dimensionality of the data, DVC data often lie on a coarser grid than DIC results, though recently, analysis have been performed on $\sim 2000^3$ pixel data with a subset size of 32^3 pixel in a thermal barrier coating. Similarly, DVC typically achieves lower accuracy than its 2-D counterpart; for example, with trabecular bone, that provides a very good quality pattern for DVC, an accuracy of ~ 0.1 voxel was observed [126]. This is to compare with accuracy of DIC, that can be lower than 0.01 pixel, tested on computer generated optimal patterns [35]; the subset size used in [35] is of 31 pixel.

DVC Analysis Procedure

Prior to the DVC analysis, the raw data for the 3-D volumes typically has filters applied to it (e.g. median filter) to reduce noise [127] and empty regions around the sample are masked (i.e. padded with 0 values) using a thresholding approach so as to prevent the DVC software from attempting to achieve correlation within void. This reduction in the searchable area can also considerably speed-up the calculation, which is important for large 3-D datasets where the analysis can be lengthy ($\sim$a few hours). Compromise can also be made on the image bit depth. Typically, modern acquisition systems will gather images as 16-bit data (i.e. 65536 levels of grey); for faster processing time and because of RAM limitations, many authors downscale the data to 8-bit [128] (i.e. 256 levels of grey). The downscaling is realised after optimisation of the dynamic range of the original volume to limit the loss of information, however this procedure often uses bins of the order of 200 levels, so it is clear that a large amount of information is lost in the process. However, no thorough estimation of the effect of this parameter was found in the literature.

The DVC analysis in this work was performed in the LaVision Davis software, version 8.3.0. The use of a high-end workstation with multiple CPUs and a large quantity of RAM is generally required especially as the analysis is run on 16-bit

image volumes, as the available hardware allowed it. Two subset-based algorithms are implemented for DVC in this version of Davis; one using Fast Fourier Transform (FFT) [129] and the other using direct correlation [66]. Both were used, with the selected algorithm being the one that achieved the best accuracy in a rigid body displacement test for the data of interest. Additionally, the analysis of a rigid body displacement test was performed with different subsets sizes; the subset size that gave the better spatial resolution without failing to correlate in large areas or giving high errors in the displacement field was chosen. Once the correlation algorithm and the subset size have been selected, the analysis was run with an overlap between subsets chosen between 25% and 75% (values allowed by DaVis software) to improve the spatial resolution of the displacement field. Here again, a compromise between spatial resolution and computational time must be decided. Vectors with a low correlation coefficient are then removed in a post-processing step; typically, a threshold of 0.8 was applied. The censored vectors were not replaced using the neighbouring displacement field as the FE approach used to deal with the DVC results is able to tackle the case of incomplete data.

After these steps, the vectors of the displacements in the sample have been determined and the data lie on a regular 3-D grid which is not fully populated due to the masking in poorly correlated areas. A mask is also applied in the vicinity of the crack tip, the size of the mask is chosen by looking at the strain data and estimating the extent of the abnormally high strain region that signifies errors in the DVC results.

Crack surface determination

Determination of the crack surface in 3-D is more complicated than for 2-D cases. If the material microstructure allows the use of small subset sizes, a method similar to the one presented in Chapter 2 can be used. A region of interest of the data is selected around the cracked area and the DVC analysis is run on this volume using small

subsets. The outlier strain values in the results can then be use to threshold the data points belonging to the crack surface. It is important to note that for a 3-D dataset, this approach can generate a large quantity of data and requires a good hardware set-up, hence this approach was not used in the current work for 3-D datasets.

Another approach, developed by Cinar [**Cinar2015**], segments the crack surface from the 3D displacement field by using an edge detection algorithm based on the phase congruency method [**Cinar2015**]. It provides a quick way of evaluating the crack surface, the resolution of the technique also depends on the size of the DVC subsets.

Finally, segmentation of the crack directly from the tomographic data is possible [130]; depending on the material, the pixels containing the crack can be thresholded using a simple intensity threshold or using more complex methods like watershed segmentation [131]. For particularly complex materials or challenging data (i.e. interconnected pores or where intensity levels are affected by beam hardening artefacts), the crack can be manually segmented by iterating through the 2-D slices [132], although this process is particularly time consuming.

In all cases, those methods provide a definition of the crack surface as a 3-D cloud of points. In the current form of the 3-D analysis J-integral technique, only crack surfaces that are contained in a plane can be dealt with. A plane is therefore fitted through the cloud of points and the points are projected on this plane to define a crack surface that is suitable for the rest of the analysis (Figure 4.1).

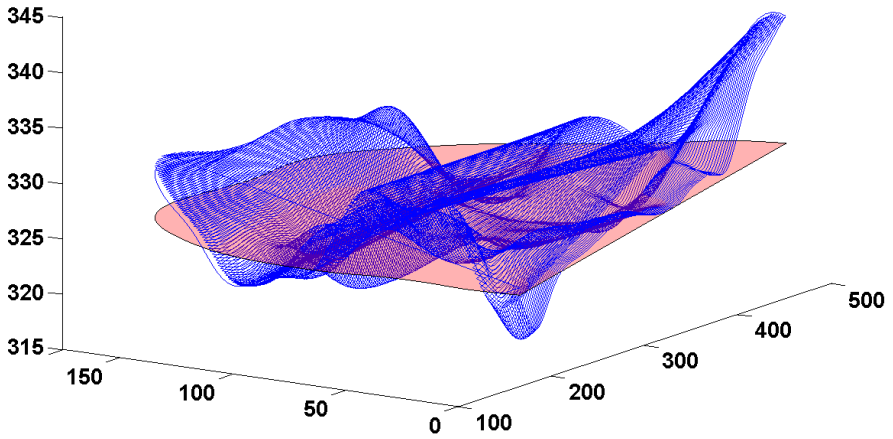

Figure 4.1: Qualitative example of the definition of a complex crack surface in 3-D. Axis units show the position in voxels. The original cloud of points is shown in blue, the crack projected on the best fit plane is shown in pink. Voxel size is 1.4 μm. Data obtained in a nodular graphite cast iron sample from Lachambre's work [133].

4.2.2 Finite Element (FE) treatment

In the original 2-D J-integral analysis method, the crack geometry is defined as a part of the mesh of DIC subsets. This avoids the need to interpolate the DIC results onto a different mesh, but there is cost of an increased complexity in the data processing flow due to the fact that the crack region must be remeshed in the FE model. In Abaqus, calculation of the J-integral requires a tetrahedron mesh in 2-D and a hexahedron mesh in 3-D; meshing algorithms for hexahedrons are much more complex than tetrahedron ones and therefore, in the 3-D case, the complexity cost would be too significant to proceed in a remeshing in a similar manner than for the 2-D case. The analysis method has been modified to overcome this problem.

In the first step, a finite element model of the tomographed volume of the specimen is created. This volume is not necessary a model of the full specimen geometry and only represents the area or interest. The model is registered in position and orientation with the tomograph (Figure 4.3); this can easily be done as the specimen dimensions are known and the coordinates of reference points can be extracted from the tomograph data to aid precise registration. Those reference points

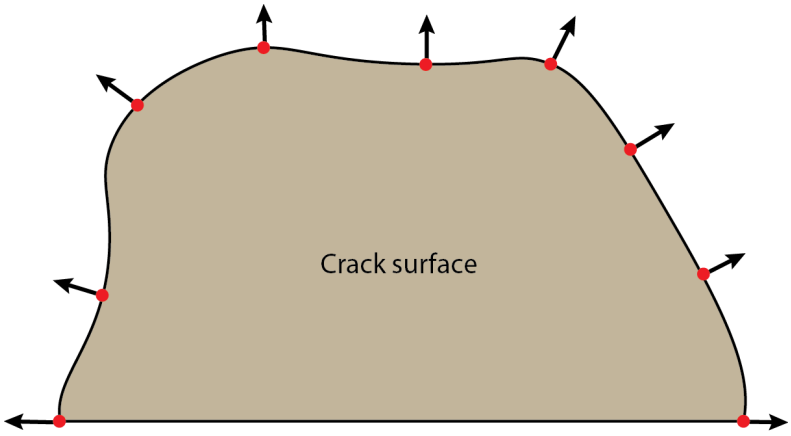

Figure 4.2: Example of q-vector definition at a few crack front nodes for the crack shown in Figure 4.1.

can be features of the sample design (e.g. a notch, a sharp corner, a hole, etc.) or fiducial markers that have been added to the specimen (e.g. metal or ceramic balls).

The planar crack surface determined previously is then added to the model to permit a faithful definition of the crack path. Although the crack surface, in the current stage of development, must be contained in one plane, the crack front does not have to be a straight line. In the case of a curved crack front, a simple Python script is used with the Abaqus Python engine to correctly define the q-vectors as perpendicular to the crack plane surface normal and with the crack front tangent at the point where the q-vector is defined (Figure 4.2).

Next, a 3-D hexahedron finite element mesh is generated on the model (Figure 4.3), the use of hexahedron mesh is mandatory as the J-integral is not formulated for other common element types in Abaqus. The mesh density is refined in the vicinity of the crack tip, aiming for a global mesh density that is close to the DVC mesh density whilst allowing a sufficiently good mesh quality for FE simulation. A set of "forbidden" nodes is then defined (Figure 4.3). They represent nodes where no boundary conditions from the DVC data will be applied (e.g. nodes in the vicinity of the crack where the correlation coefficient of the DVC data is low). As in the 2-D case, it is important not to leave free any surface that is not in the

experimental design; for example, when working with a region-of-interest model (i.e. model of a volume located inside the sample) all exterior surfaces should be constrained by DVC-measured displacements.

Finally, the DVC-measured displacement field datasets (stitched together in the case of multiple tomographs of a large volume) are interpolated onto the nodes of the finite element mesh. The choice of the interpolator can affect the quality of the results. In this work two different interpolators have been used depending on the data. The tri-linear interpolator natively implemented in MatLab is very computationally efficient and performs well as long as there is no steep gradients in the displacement field (i.e. with steep gradient the residuals are high). For other datasets, a neural-network type interpolator can be used; it may necessitate processing the data by chunks as it is computationally intensive. This applies Radial Basis Functions (RBF) as neurons and has been developed in MatLab to use multiquadric or polyharmonic splines as activation functions. It provides much better interpolation on fields containing steep displacement gradients and discontinuities. The downside is an increased computation time and memory consumption. If needed, this interpolation scheme can also be used on large datasets by dividing them into chunks, a MatLab code automates this process. The interpolation step is particularly time consuming and must be run on the 3 components of the displacement field. This step has been parallelised and the use of a high-end workstation can considerably accelerate this step.

Once the displacement field at the position of the Abaqus nodes has been obtained, this data must be fed into the Abaqus model as boundary conditions (BC) on the nodes. Because of the amount of BCs in a typical dataset, the Abaqus Python engine is not suitable to perform this task, instead the Abaqus Input File system is used. An Abaqus Input File (INP file) is a text file containing keywords that completely define an Abaqus model (nodes, elements, connectivity, etc.). For the application developed here, an INP file without the BCs is generated from

Abaqus and this file is parsed using a Python script to append the BC generated from the interpolation step in MatLab. The treatment chain is automated in MatLab from the reading of the DVC result file to the creation of the final INP file via calls to Python functions from the MatLab code.

The FE model is then run with the selected material properties and the J-integral values at each defined set of crack path nodes are extracted (Figure 4.3). For linear elastic materials, it is possible to use the interaction integral technique to retrieve Mode I, II and III stress intensity factors [94]. The extraction of the J-integral and/or stress intensity factors from the Abaqus output database file has been automated in Python.

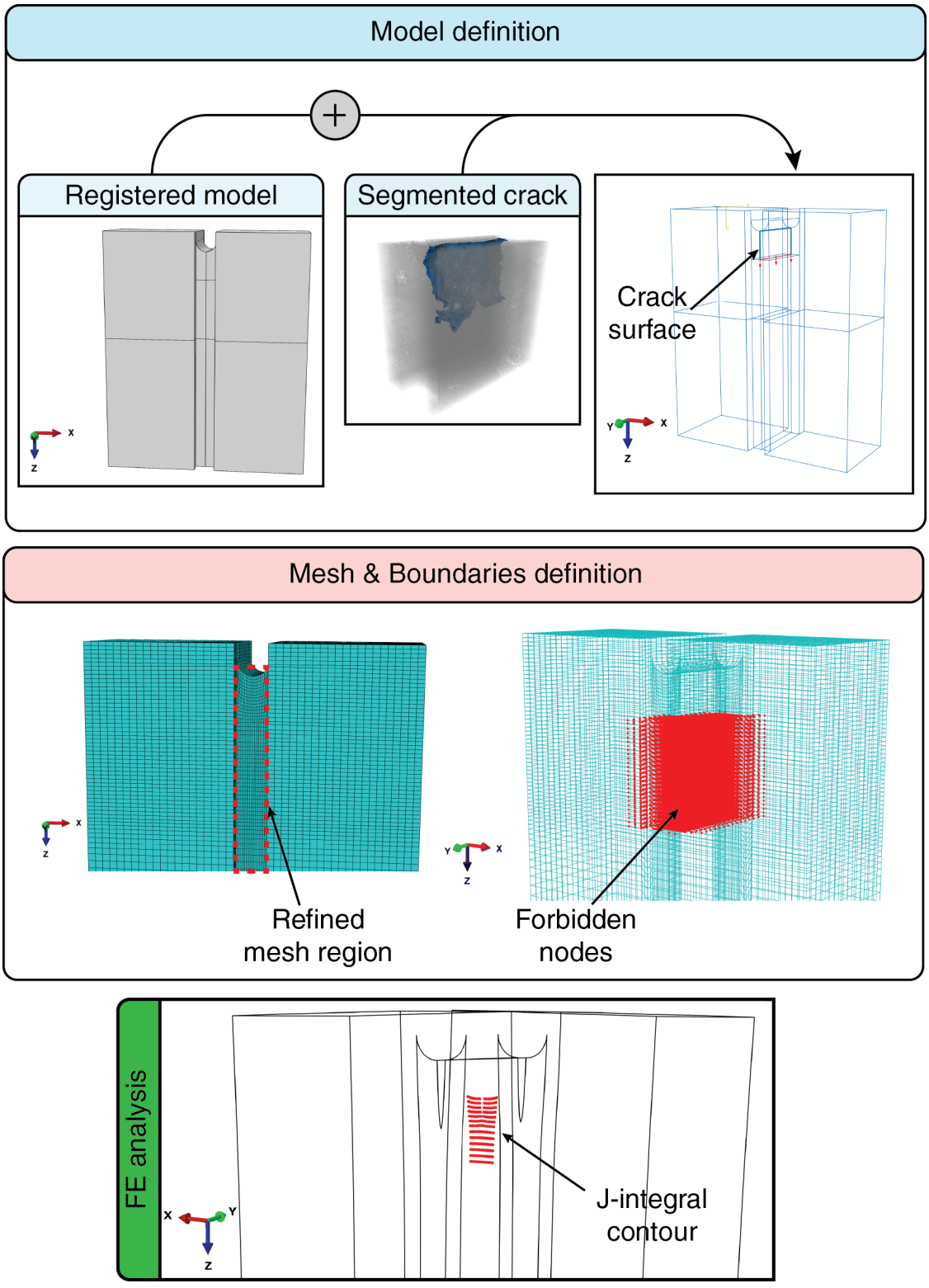

Figure 4.3: Analysis procedure of DVC results by Finite Element analysis.

4.2.3 Synthetic DVC data

Due to the large variety of 3-D datasets that could exist, the benchmarking approach used in Chapter 2 on 2-D data was not applicable to the 3-D case. Rather than trying to obtain the most exhaustive benchmark for all 3-D cases, it was decided to run a benchmark that was tailored to the analysed experimental cases. The methodology is based on post-treatment of FE data to simulate DVC data from the experiment and then proceed to their analysis. It is time efficient as the developed codes can readily be used for other models. It is of interest for the experimentalist to follow this procedure prior to an experiment so that the achievable precision in the determination of the J-integral is known.

The first step consists of the creation of a FE model of the tomographed region of the sample. In addition of the usual mesh refinement in the cracked region, the mesh should be sufficiently refined at all points to ensure creation of good synthetic DVC results. As a rule, to provide enough data points for the analysis, it was observed that the mesh size (i.e. average length of element's sides) should be at least half the subset size of the simulated DVC analysis.

In comparison with what was done in Chapter 2, a FE-simulated displacement field is adjusted to behave as if captured by DVC rather than adjusting an image using the FE displacement and running DVC on the image. Both approaches will capture the effect of issues such as steep displacement gradient relative to subset dimensions or presence of a crack in the material. However, the approach used in this chapter will not faithfully simulate the presence of noise in the image data.

The FE results are then exported and fed into a MatLab code ("DVC_generate") that takes as input a FE displacement field (in mm), a pixel size (in mm/pixel), a subset size (in pixels) and an overlap between subsets (in %). The MatLab code determines the position of each subset in the FE results and uses linear interpolation to determine the displacement vector value at each subset corner.

The displacement vector attributed to the subset is the average value of each of its 8 nodes displacements. With this approach, the averaging effect of large subsets and the effect of overlap is correctly simulated. Noise can also be added to the DVC displacement field as a post-processing if needed.

4.3 Synthetic and experimental datasets

4.3.1 Synthetic dataset

A FE model of a semi-circular corner crack of radius depth 2 mm in a rectangular volume of 5 × 5 × 7 mm was created in Abaqus 6.13 (Figure 4.4a). The crack plane was perpendicular to the Z-axis. The mesh size was imposed not to be larger than 100 μm, this should empirically allow accurate simulation of DVC results with subsets bigger than 200 μm; this correspond to ∼60 pixels with an experimental pixel size of 3.25 μm/pixel. The mesh was locally refined in the crack tip vicinity. A linear elastic material with the properties of nodular graphite cast iron was applied to the model, the Young's modulus E was 140 GPa and the Poisson's ratio ν was 0.27.

The loading was applied as displacement boundary conditions; the top surface of the model was pulled up on the Z axis by 25 μm whilst the bottom surface was pulled down on the Z axis by 25 μm (Figure 4.4a, a multiplier of ×5 is applied in the figure to allow a better visualisation of the crack opening). The stress intensity factor along the crack front, calculated using Abaqus, varies between 42 MPa.m$^{0.5}$ and 46 MPa.m$^{0.5}$ with those loading conditions.

The displacement field from the FE model was exported and used as an input for the DVC_generate MatLab code with a set pixel size of 3.25 μm/pixel, an overlap of 50% and subset sizes of 32, 64, 96 and 128 pixels. This treatment generated different pseudo-DVC results files that were used for the J-integral calculation. The effect of the MatLab code on the displacement field is illustrated

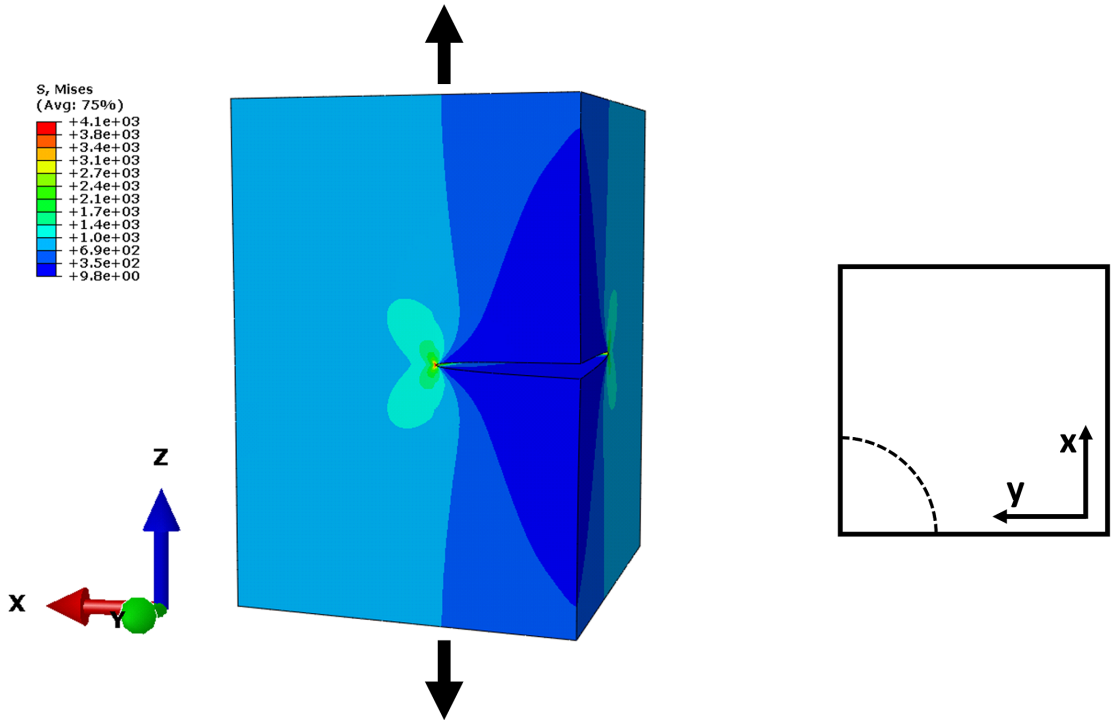

(a)

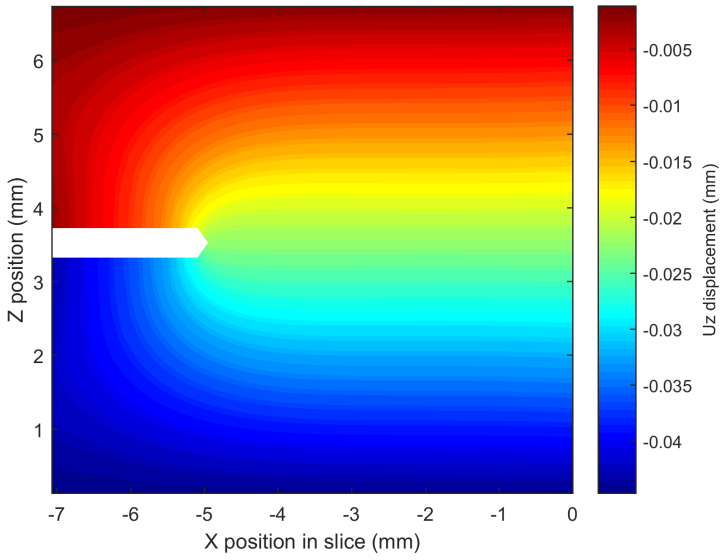

(b)

Figure 4.4: (a) Finite element model of the dataset used for the benchmark. The colormap shows the VonMisses stresses. The black arrows indicate the direction of the loading. The dashed line shows the crack front. (b) Section of the U_z displacement field at the 45° section plane.

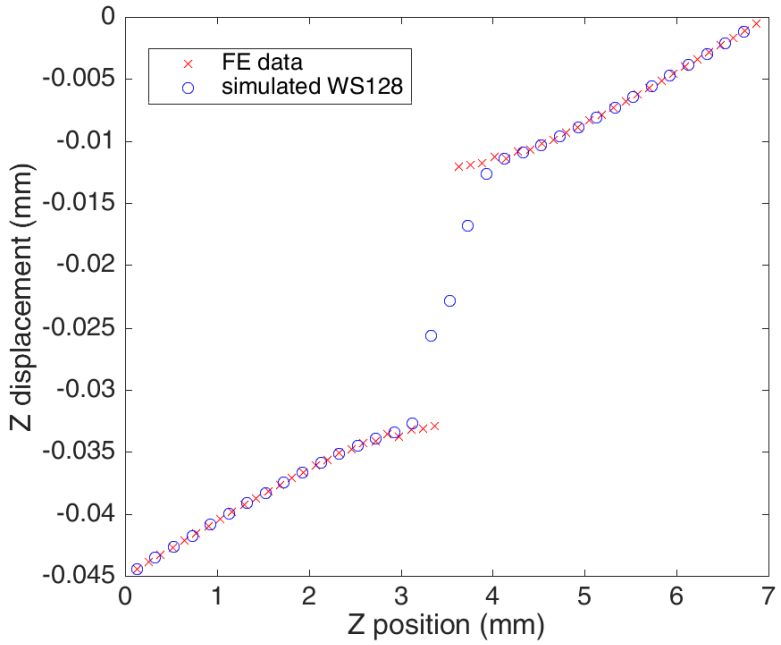

Figure 4.5: Example of the effect of the simulated DVC analysis on the original FE dataset. The loss of spatial resolution and averaging due to the subset size of 128^3 pixels is shown. This profile was obtained for a fixed (X,Y) position corresponding to a point on the 45° plan at 1 mm behind the crack tip position.

on Figure 4.5 where the loss of spatial resolution can be observed as well as the averaging effect in the crack tip vicinity.

The process described in Figure 4.3 was used to calculate the J-integral from the pseudo-DVC results. The crack front position was considered as known and all the nodes included in a radius of 0.75 mm from the crack front nodes were assigned to the "Forbidden Nodes" selection. This corresponds to ∼230 pixels with the used pixel size. The same FE model that produced the pseudo-DVC results was used as a base for DVC displacement injection. The mesh size was not modified.

4.3.2 Experimental dataset – Static loading of a fatigue crack in cast iron

Material

The experimental dataset was obtained on custom made nodular graphite cast iron samples, provided by Prof. Buffière (Mateis, INSA Lyon) and previously studied

using tomography by Buffière [69, 71]; a similar material was used by Marrow and Buffière in early studies of fatigue cracks using tomography [134]. The nodular graphite cast iron used is a ductile material with a Young's modulus of E=140 GPa, a yield strength σ_y=315 MPa and a Poisson's ration ν=0.27. The billet used to create the samples contains 3.4 wt% carbon and was ferritised at 880°C then air quenched. This material is particularly suitable for DVC analysis as it contains 14 vol% of graphite nodules of average diameter 45 μm that constitute good trackable features for the algorithm.

Sample geometry

The sample design is shown in Figure 4.6. The machining occurred in two parts; first the cylinder and thread were made using conventional machining then a CNC electro-discharge machining (EDM) tool was used to cut the central part of the sample. Due to the thickness of this part, milling was not an option as it would have resulted in sample failure.

Two types of samples were produced, one with an edge notch at one corner (EN) and one with a straight notch (SN), the dimensions of both are shown on Figure 4.6. The SN geometry was aimed at generating a straight crack and a uniform stress intensity factor at all position of the crack front whilst the EN geometry was aimed at generating a more complex, non-linear crack front to challenge the analysis. Four samples of each type were produced but not all of those were tested. All the notches were cut by EDM with a wire diameter of 300 μm thus generating a blunted notch with a tip diameter close to 300 μm.

Original plan & Pre-cracking

The original plan was to perform in-situ fatigue crack propagation at the synchrotron imaging facility on beam line I12 at the Diamond Light Source, adapters were machined to allow cycling of the samples on a hydraulic Instron tensile test machine,

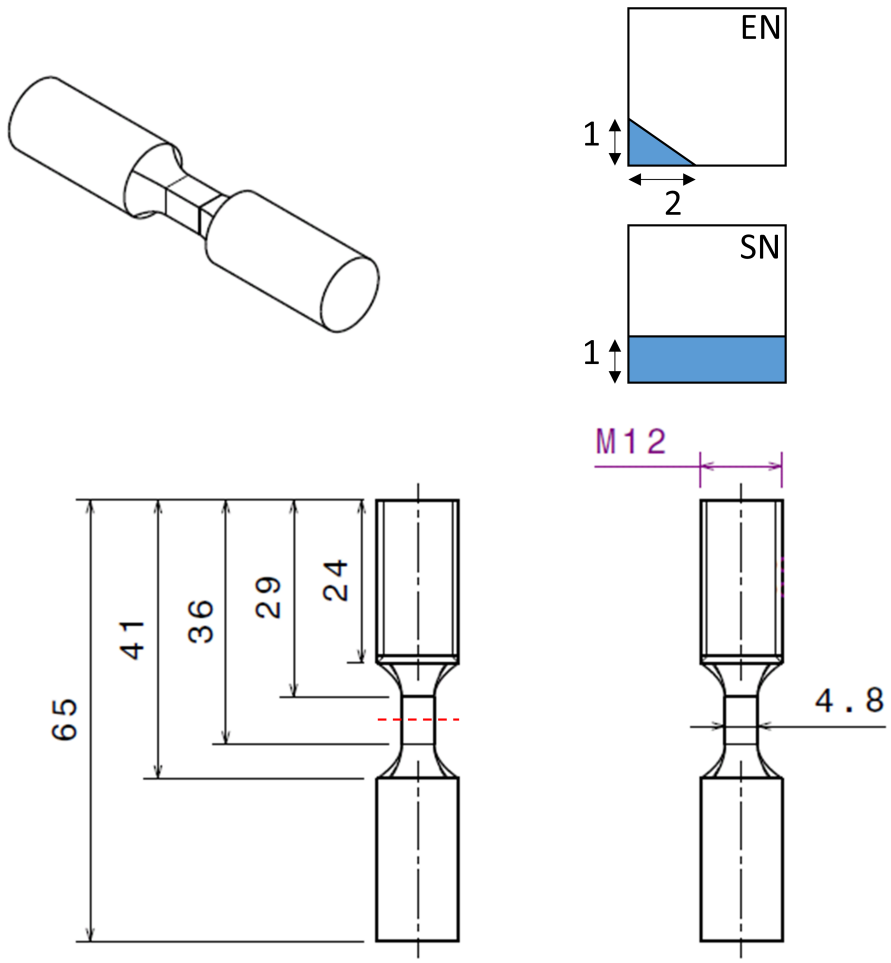

Figure 4.6: Sample geometry used for the experiment. The notch was cut in the region indicated by the red dashed line. Two types of notches were used: edge notch (EN) and straight notch (SN).

and preliminary tests were done before the allocated beam time to verify the conditions for crack initiation. Care was taken in the alignment and the design to ensure pure mode-I loading and reduced vibrations. Radiography and tomography was planned to be used to carefully monitor the crack initiation at small steps of fatigue cycling. However, due to a last minute major failure of the hydraulic pump for the servo-hydraulic loading rig a few days before the scheduled beam time, the experiment had to be redesigned within a tight schedule.

The samples were fatigue pre-cracked prior to the experiment then statically loaded. The fatigue pre-cracking was made on a hydraulic Instron 100 kN tensile

machine located at the ISIS neutron source (Engin_X beamline), which is at the same site as the Diamond Light Source. The samples were screwed into a metallic rod that was fixed in the bottom grip and secured with a lock nut. The top of the sample was clamped in V-shaped grips. No sliding of the sample in the top grip was observed during the fatiguing.

Due to their geometry, and the impossibility to monitor crack initiation via tomography as planned, the sample proved to be complex to fatigue pre-crack. The blunted notch forces the use of cycling at a relatively high K to obtain crack initiation in an acceptable number of cycles. As soon as the crack initiates, it propagates quickly due to the high applied K.

The fatigue cycles were performed at a frequency of 15 Hz in load control mode; displacement control mode would have been preferable to limit the risk of sample failure but the waveform controller at Engin_X proved to be capricious and would not respect the assigned values especially in displacement control mode. There was insufficient time to retune the PID controller to improve the feedback in displacement control for these specimens.

For the SN samples, the cycling was made with a R=0.1 and a K_{max} value equals to 65% of the critical SIF in mode I. For the EN sample, the aim was to obtain a K_{max} value of 60% K_{crit} at the deepest notch position (∼0.9 mm). The loads producing those settings were determined using the analytical solution for a straight edge crack and were input in the machine; the loads oscillate between 3.8 kN and 0.38 kN. The Instron waveform generator was then used to fatigue the sample in load control mode. Probably due to the age of the machine, the limit loads were triggered one or two times (depending on the samples) during the cycling but every time before crack initiation was visible. The limit load was set to 5.0 kN, therefore the maximum plastic zone size due to those overloads before crack initiation is 0.46 mm according to Irwin's theory. However, the predicted maximum plastic zone size of the propagated crack when loaded at 3.8 kN is 4 mm in the SN

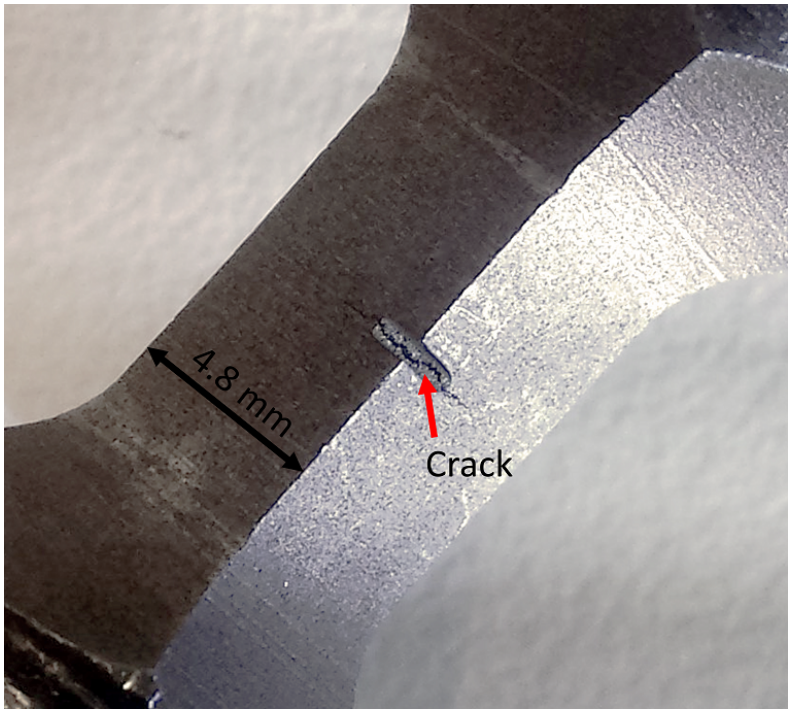

Figure 4.7: EN sample after fatigue loading, the crack is clearly visible at naked eye and indicated by a red arrow.

sample with the crack length of 2.7 mm and 2.3 mm in the EN sample with a crack length of 2.4 mm. Therefore, all the material ahead of the crack tip is expected to have some amount of plastic deformation in it, this could have been avoided in the original experimental design where crack initiation would have been picked up early and displacement control could have been used on the I12 Instron.

For both type of samples, pre-tests showed that failure with those loading parameters occurred after 50k-70k cycles. The samples were therefore fatigued for 30k cycles then by step of 5k cycles until a crack was spotted on the sample surface using optical observation with a magnifying glass. An example of a fatigue crack introduced in an EN sample is shown on Figure 4.7.

Due to the difficulty of controlling crack propagation, several samples were broken or overly deformed plastically during the pre-cracking stage. Two samples, one SN and one EN were prepared for the rest of the experiment.

Figure 4.8: Shimadzu machine in place on the I12 EH2 rotation stage.

Synchrotron X-ray tomography

A monochromatic beam of energy 80 keV was used and radiographs were recorded using a PCO.4000 CCD camera (2560 × 2160 pixels, 16-bit depth), with optics selected to image an area of 8.3 × 7.0 mm (i.e. 3.24 μm per pixel). Tomography was performed with 3000 projections over an angle range going from -75.1° to 72.7°, thus 32.2° were lost compared to a full 180° scan. The limited angle tomography was due to the presence on the rotation stage of a Shimadzu 10kN tensile machine used to load the sample[1] (Figure 4.8).

The reconstruction was performed using a standard back-filtered projection

[1]The Shimadzu was transported from Oxford to the Diamond Light Source for the experiment.

algorithm [124]. Additional treatment of the radiographs was needed due to the bad quality of the scintillator generating very large (10-20 pixels diameter) rings in the data that could not be corrected for using typical ring correction algorithms. The approach used here consisted of thresholding out the faulty scintillator pixels in the projections using an intensity threshold then replacing them using the median value of the neighbouring pixels. All of the reconstruction process was implemented in MatLab and parallelized on a 2-GPUs workstation (2 $\times$ NVidia Titan X) for improved computational speed. No specific correction was applied for the limited angle tomography as the data quality looked sufficient, the reconstruction algorithm was simply informed of the reduced angular range of the data.

Loading sequence

Prior to the loading, the fatigue precracked samples had to be re-machined to fit in the Shimadzu in-situ tensile machine used to replace the broken Instron machine. The 5 kN Shimadzu machine was only equipped with flat grips of maximum opening 7 mm so 15 mm on each end of the samples was machined down on the lathe to a diameter of 6.9 mm. The material was sufficiently ductile for the grips' teeth to bite in it and prevent any slipping during loading. However, gripping a cylindrical shape with flat grips does not guarantee a good sample to load axis alignment and despite care being taken when aligning the sample, misalignment was expected in the results.

The original plan was to study the relationship between the fatigue crack propagation rate and the local crack stress intensity factor values[2]. This was not possible due to the failure of the Instron hydraulic rig and so static loading of the pre-crack had to be used instead. A reference tomograph was obtained at the pre-load of 50 N followed by a rigid body displacement tomograph (movement of 30 μm) at the same load. The samples were then loaded by steps of 400 N until the peak load of 4000 N, at each load step a tomograph was recorded. The final

[2]Additional beam time has been allocated by Diamond in March 2017 to compensate for the experimental problems, and crack propagation will then be studied.

load of 4000 N was chosen to exceed the maximum load applied during cycling (excluding accidental overloads).

4.4 Results and discussion

4.4.1 Synthetic benchmark results

The J-integral results along the crack front for the 4 pseudo-DVC datasets were exported and compared to the J-integral values obtained in the original FE model at the same positions. The relative error in % for each of those positions was calculated and averaged for each data. The data is shown on Figure 4.9 where the error bars are the standard deviation of the error along the crack front. No relationship was observed between the error value and the position along the crack front.

An exponential relationship can be observed between the subset size and the relative error in the J-integral. Those results suggest that one should aim at using the smallest subset size result possible; this makes sense as small subset size induces less averaging of the underlying displacement field and therefore produces more accurate results, especially in the regions where the displacements gradients are high. In this case, the DVC results were synthetically produced using the "DVC_generate" MatLab code and the process described in the previous section. With this method, it is not detrimental to the data quality, in terms of noise, to produce DVC results with small subset sizes. However, in the case of a real DVC analysis, the use of small subsets, due to the lower quantity of data included in them, will increase the uncertainty in the determined field.

In DVC, the relationship between subset size and results uncertainty is also linked by an exponential relationship due to the loss of information with reducing subset size, so it is important to perform a rigid body displacement test on the sample to produce the subset size to uncertainty curve and compare this curve with the curve obtained in Figure 4.9 in order to determine the best compromise in term

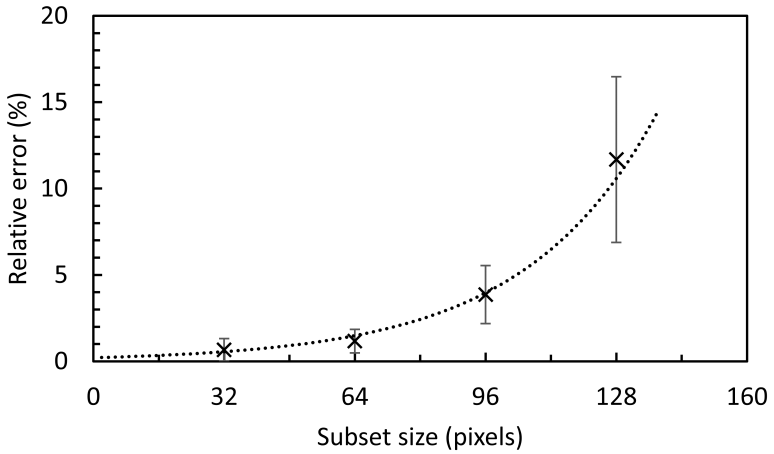

Figure 4.9: Relationship between DVC subset size and relative error in the J-integral. The overlap between subsets is fixed to 50% in this case.

of subset size. In the case of nodular graphite cast iron imaged with the pixel size considered here, a 32 pixels subset size will be chosen. The expected error in the J-integral will therefore be 1%. This constitutes a non-conservative estimate of the J-integral error as the displacement field noise has not been considered in the error analysis. However, as shown in Chapter 2 for 2-D datasets, the FE approach presented here is robust to image noise and only severe noise (i.e. SNR $<$ 15 dB) caused an increase in the error of up to 2%.

A similar procedure to the one described here can be used on any sample geometry and any material, prior to the experiment, to determine the expected error in the J-integral with the current set-up. This is particularly important when choosing the imaging parameters.

4.4.2 Static loading of a fatigue crack in cast iron - Results

Crack segmentation

For both the SN and EN samples, the crack was easily segmented from visual observation of the tomography slices (Figure 4.10). In the SN sample, the crack was well centred on the notch through all the sample thickness with an average deviation from centreline of 15 μm and a maximum deviation of 29 μm. The crack depth

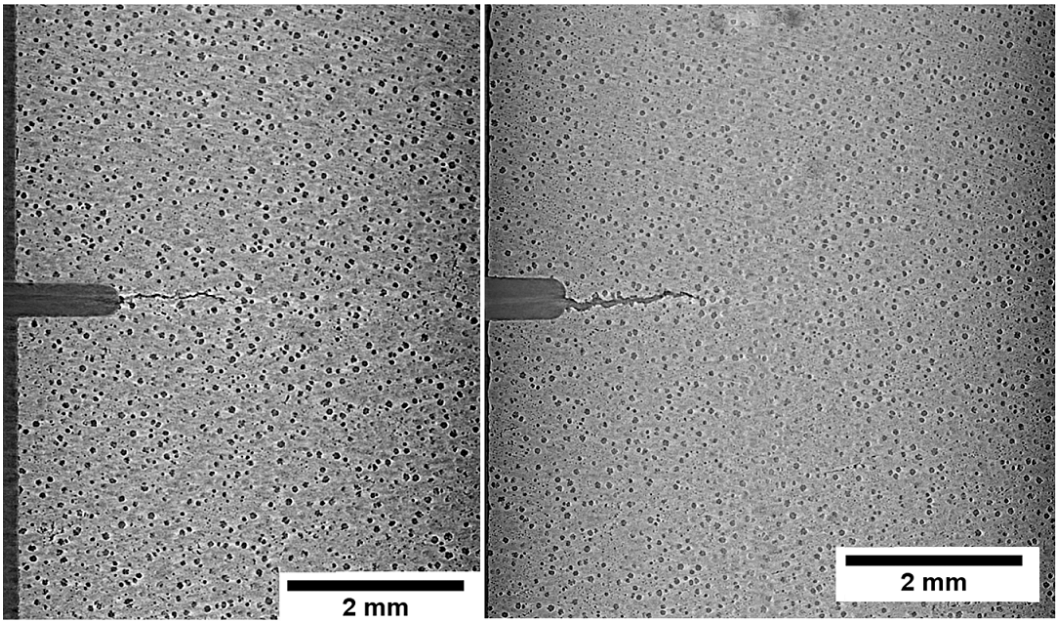

Figure 4.10: Example slice of the tomograph used for the visual crack segmentation. The radiographs are taken at unload state. (left) straight notch sample, yz-plane, x=2.5 (right) edge notch sample, slice at 45° at pre-load stage of 50 N. Slices position is indicated on Figure 4.11.

through the SN sample is shown on Figure 4.11a, the crack front is straight over ∼3 mm then deviates and is reduced by ∼40 %. In the EN sample, the crack also propagated from the centre of the notch with an average deviation from the centreline of 17 μm and a maximum deviation of 32 μm. The crack profile in the EN sample is shown in Figure 4.11b, the crack front lies on a circle of radius 2.4 mm ± 77 μm.

Those visual detection of the crack path, even if cumbersome to perform, is considered to be more accurate than crack paths obtained via other techniques, such a segmentation, and were used as input for the crack definition step when building the FE model for the J-integral calculation. It can be noted from the observation of Figure 4.10 that at unload, the SN specimen's crack appears more closed than the EN one that remains open.

When the flat surface of the specimen was positioned perpendicularly to the incident beam, artefacts linked to the limited angle tomography were more pronounced, generating a kind of "directional wind" in the reconstruction that

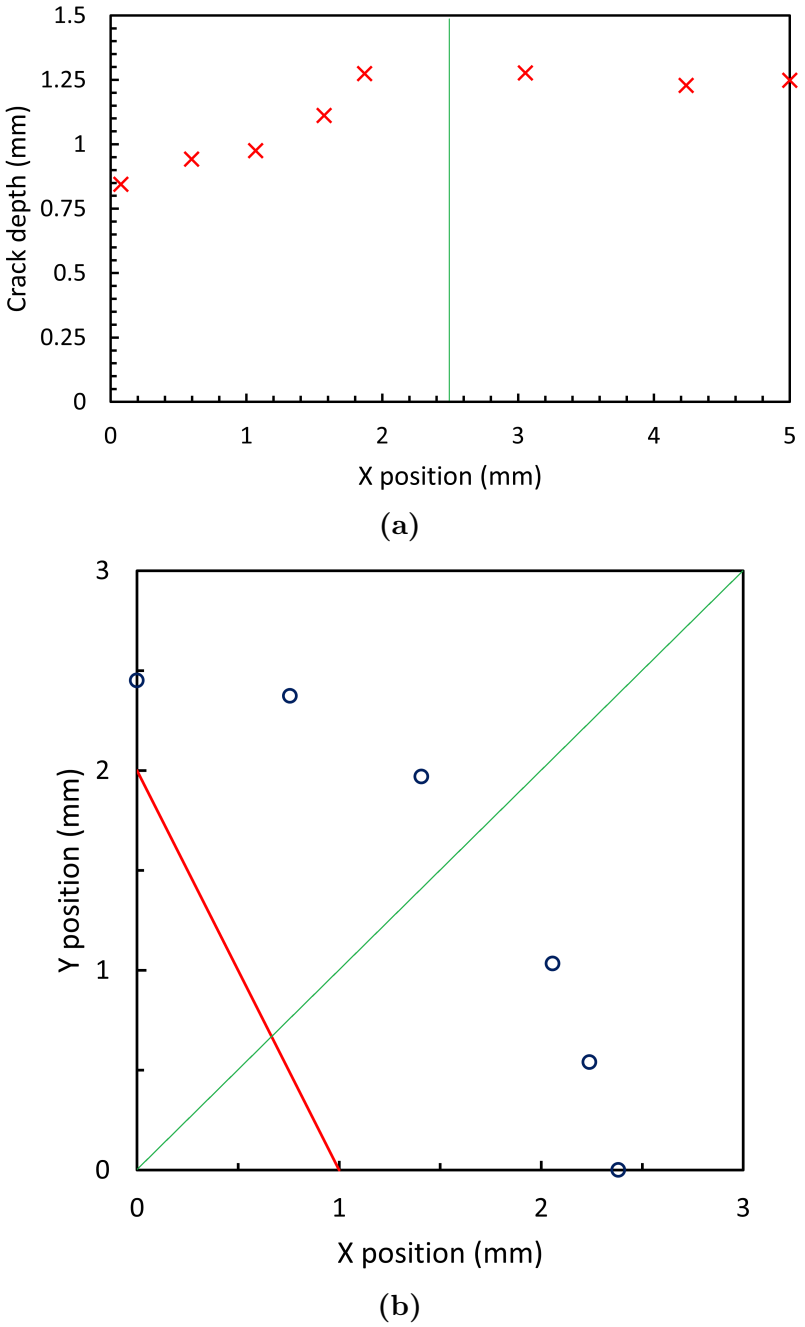

Figure 4.11: Crack depth identified by visual observation of the tomographs in (a) SN sample where the crack length is measured from the notch tip position. (b) EN sample, the red line represents the notch end position and the blue points represent the observed crack. Slices presented in Figure 4.10 are shown by a green line.

can be seen on Figure 4.10 left. However, when the sample was rotated 45deg from this position, less artefacts were observed (Figure 4.10 right). This is due to interactions between the sample geometry and the information included in the missing projection angles but the mechanisms are not fully understood. The use of an iterative reconstruction algorithm rather than the standard back-filtered projection approach could reduce the issue.

Digital volume correlation analysis

Digital volume correlation analysis was performed on the 16-bit datasets; a 3-D median filter of radius 1 pixels was applied on the volumes before correlation for noise reduction purposes. In all cases the pre-loaded 50 N tomograph was used as a reference. The exterior of the sample and the cut notch were masked in the reference tomograph using knowledge of the specimen geometry and MatLab post-treatment of the data.

The analysis was performed in LaVision's Davis using the FFT algorithm, with a final subset size of 32^3 pixel and an overlap between subsets of 50%. A multipass approach was used with 2 passes at 256^3 pixel then 2 passes at 96^3 pixel and 2 passes at 32^3 pixel. After each pass, the vectors with a correlation coefficient lower than 0.85 were discarded. The DVC results were exported as text files and post-treated in MatLab to correct for rigid body movement and rotation using the technique presented in [105] and previously used in this thesis.

A DVC analysis on a known rigid body displacement set was performed on the SN sample, it is representative of nodular graphite cast iron under the current imaging conditions and it was therefore not necessary to perform such a test for the EN sample. The applied displacement value was 30 μm and the retrieved displacement was of 29.51 μm with a standard deviation over the sample of 1.54 μm, this correspond to an accuracy of $\sim$0.15 pixel.

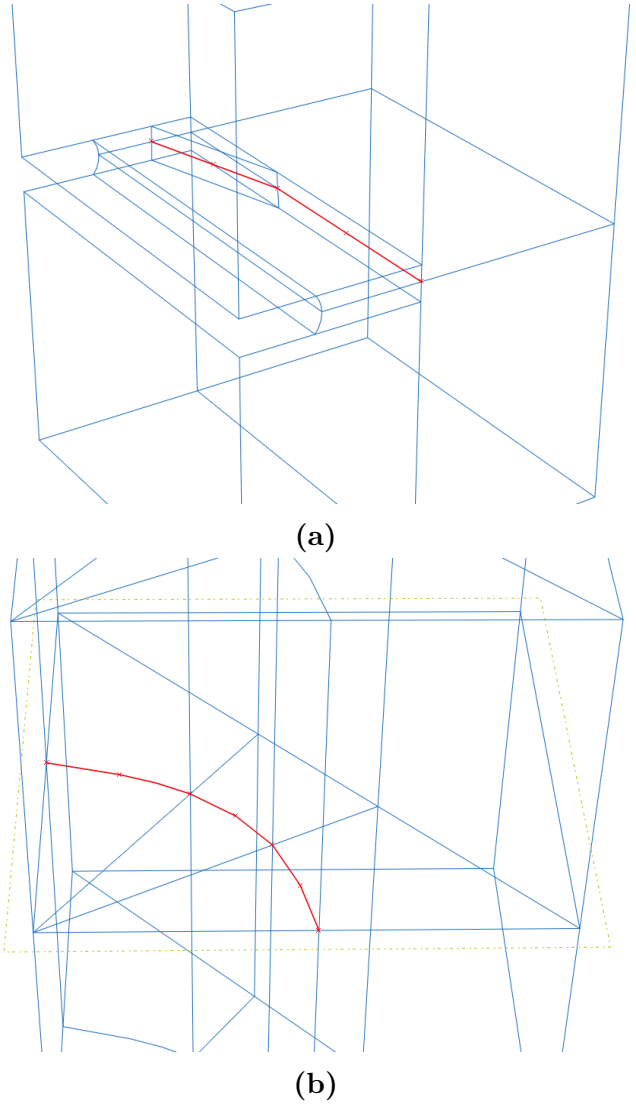

Figure 4.12: FE models with the crack definition from the tomographs. (a) SN sample (b) EN sample, the notch is not modelled and replaced by extending the crack in its plane; this is equivalent and simplifies the model definition.

For the SN sample, the analysis was performed for 5 different load steps of 800, 2000, 3200, 3600 and 4000 N. For the EN sample, the 3200, 3600 and 4000 N load steps were analysed.

Finite element models

Finite element models of the tomographed region of the samples were created in Abaqus 6.13. They were registered with the reference tomograph and the crack path determined from the tomograph was defined in the models (Figure 4.12).

The models were meshed using hexahedrons of average side length 200 μm, apart from in the crack path region where the mesh was refined to 25 μm to allow for better FE calculations and J-integral contour definitions. The material was defined as linear elastic with the properties identified for nodular graphite cast iron (E= 140 GPa, ν=0.27). The analysis was run a first time with the supposed well-aligned boundary condition from the experimental loading to obtain a reference value of the SIF along the crack front at max load (i.e. 4000 N) as the crack geometry was not standard. The loading was simulated by preventing the bottom face of the model from moving in the Z direction and by applying a pressure load of 160 MPa (this corresponds to 4000N over a 5 $\times$ 5 mm surface) on the top face of the sample.

The forbidden nodes were defined in the crack vicinity and in areas where the DVC results were not of sufficient quality. For both samples, this concerned all vectors within a region of 200 μm close to the sample edges and a region of 1 mm radius around the crack front. The J-integral contours used for the calculation of the results were taken in the "free-to-deform" region within the forbidden nodes of the crack vicinity.

DVC results were interpolated at the location of the FE nodes using a natural neighbour interpolation algorithm. This takes a weighting average of the natural neighbours of a point. The natural neighbours are found using Voronoi tessellation [135]. Natural neighbour interpolation is a good compromise between speed and accuracy and was judged sufficient here over the neural network technique as the DVC data was sufficiently smooth.

Abaqus input files with the experimental displacement applied were automatically created from the MatLab code and solved in Abaqus 6.13. The J-integral results as well as the stress intensity factor values from the interaction integral were exported at regular positions along the crack front.

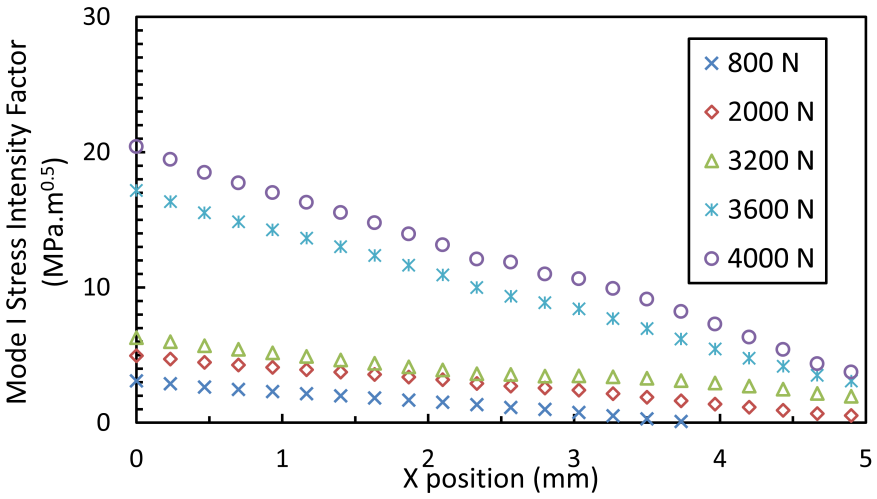

Figure 4.13: Mode I stress intensity factors along the crack front for the different loadings. A clear effect of the misaligned loading can be observed. For an aligned loading of 4000 N, the expected value is around 30 MPa.m$^{0.5}$

SIF measurements and discussion, SN sample

The SIF values for modes I, II and III were extracted along the crack front for the 5 analysed load steps of 800, 2000, 3200, 3600 and 4000 N. The values are plotted on Figure 4.13. The first observation is that the SIF value decreases along the crack front. This is attributed to misaligned loading, and can be confirmed by inspecting the FE model deformed by the DVC displacements. This is shown in Figure 4.14, for the load step of 4000 N, where a multiplier of 50× has been applied on the displacements to allow visualisation of the deformation, which is clearly misaligned.

To highlight the effect of misalignment, the stress intensity factor value at each side of the sample (i.e. X=0.2 and X=4.8 mm to avoid any surface effect) is plotted as a function of the mouth notch opening from the DVC results (Figure 4.15a); the full notch opening vs. K_I value is presented for the 4000 N dataset. The ratio of opening between left and right is constant through load steps and equal to 2.3 ± 0.19 (Figure 4.15b).

For the 4000 N datasets, the mode I SIF values obtained from the full-field DVC measurements were compared with FE simulations results (Figure 4.16). Two

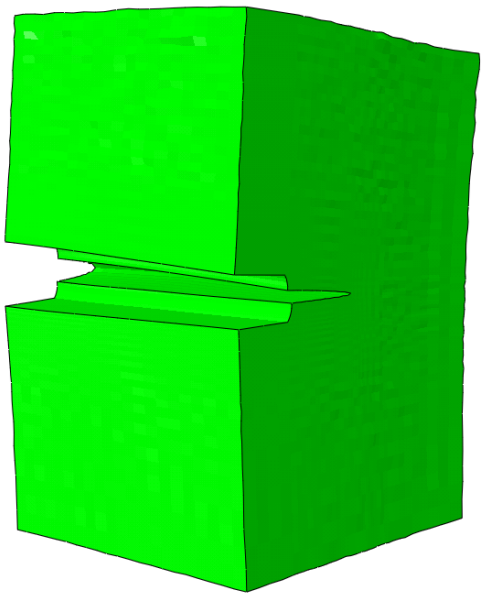

Figure 4.14: FE model deformed by the DVC measured displacements for a load of 4000 N, a multiplier of 50× is applied on the displacement field.

different FE models were used; one considering a perfectly aligned loading and the other one making use of the left/right misalignment ratio of 2.3 (Figure 4.15b) to apply a linear profile to the load distribution with total load of 4000 N. In both cases the predicted values are significantly higher than expected, the misaligned left/right FE load is however able to capture the same trend as the experimental data. A possible bending moment due to misaligned loading between the front and the back of the specimen was however not considered in the simulation and might reduce the SIF value and bring the FE results and experiment in agreement.

To investigate this further, an approach was used where only the far-field boundary conditions would be applied (i.e. case of a large "free-to-deform" area). This was done for the 3200 N and the 4000 N datasets, DVC displacements were applied only from measurements at a distance of 0.8 mm from the top and bottom of the tomographed region. No significant difference (∼1.2 MPa.m$^{0.5}$ in average for K_I values) between the two analyses was found. This suggests that the dominant effect here is the misalignment, since phenomena such as closure would be expected to mostly affect the displacements close to crack tip. This

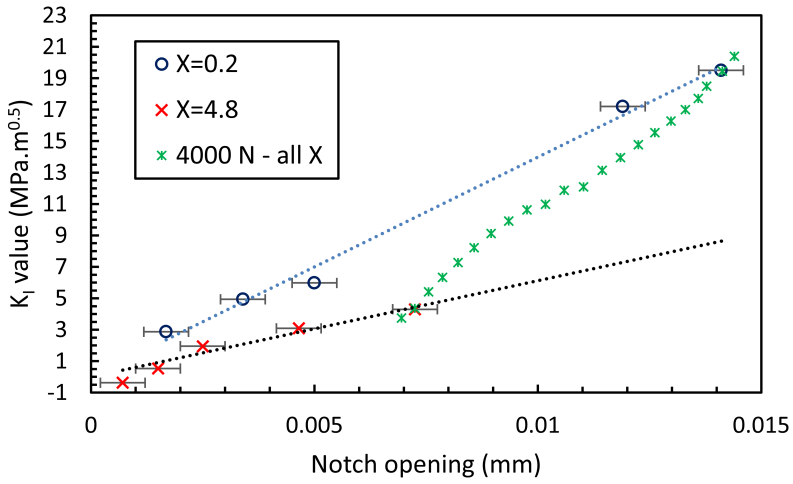

(a)

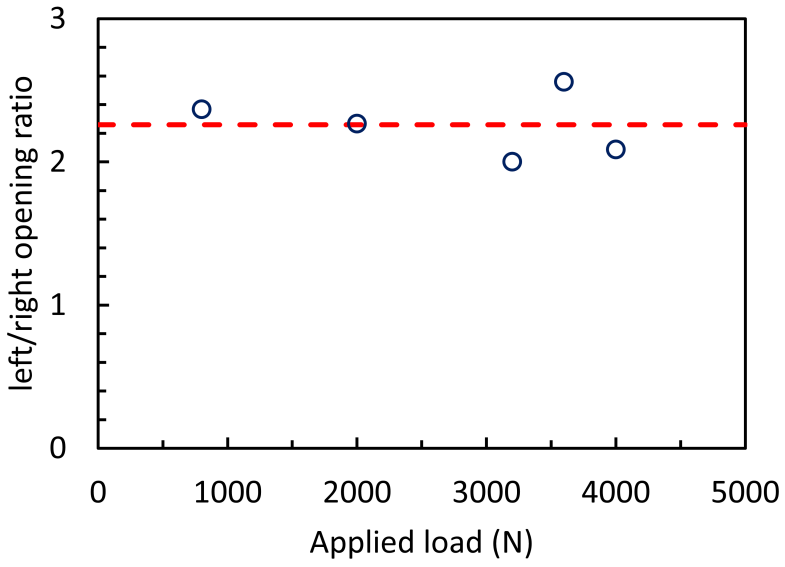

(b)

Figure 4.15: (a) Mode I SIF value on each side of the notch as a function of the notch opening. Two different regimes are observed but no closure can be highlighted. The complete SIF value vs. notch opening profile is presented for the 4000 N load step. (b) Left/right opening ratio, the average value is shown as a red dashed line.

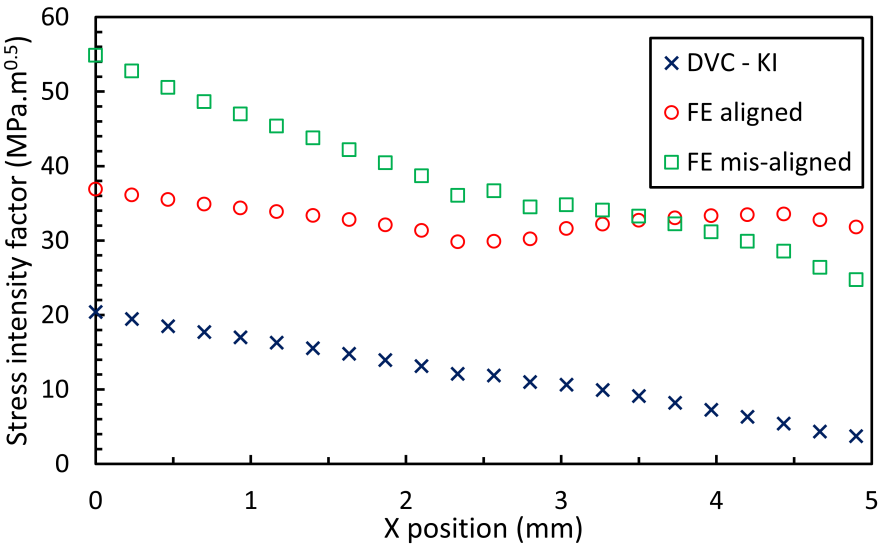

Figure 4.16: Comparison of the mode I SIF obtained for the 4000 N load step data from the DVC boundary conditions and from two FE models, one with aligned loading, one using the calculated ratio of 2.3 (Figure 4.15b) to simulate the misalignment. In both cases the predicted values are too high.

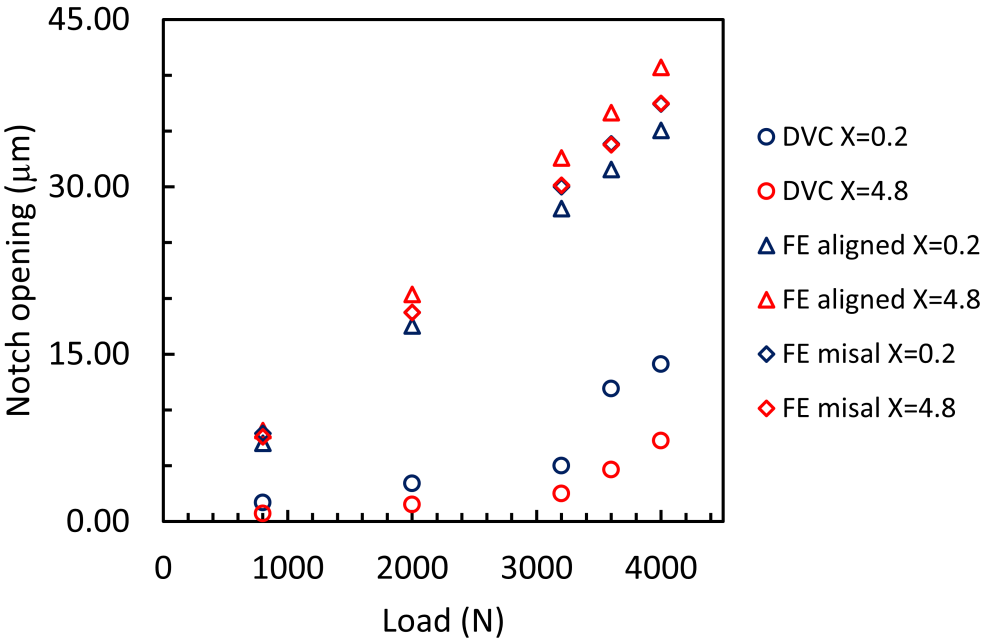

Figure 4.17: Notch opening versus load compared from the experimental data and the DVC simulations.

however does not explain the difference between the predicted FE result and DVC results; additionally, this cannot be attributed to yield as the load of 4000 N has already been exceeded during pre-cracking.

Figure 4.15a shows that the crack field is elastic and governed by the notch opening, this is consistent with the statement that the far-field is sufficient to correctly describe the crack field. The data presented in Figure 4.17 shows a disconnect between the applied loading and the notch opening. Neither of the FE models, aligned and misaligned can describe the experimental observation. There is no reason to question the reliability of the load measurements, and checks have since been performed to verify the linear response of the load cell. The implication is that the simple assumption of misaligned load is insufficient, and the DVC measured displacements provide the best description of the boundary conditions applied to the test specimen. The simple response of the load cell is an unreliable description of the loading applied to the misaligned test specimen. The steep change in the trend observed in the DVC notch opening results might be interpreted as crack closure, but the similar results using near and remote displacements suggests that closure is negligible. The change in gradient may reflect a change in specimen alignment with applied load, This, however, does not prevent the characterisation of the actual loading of crack by calculation of the J-integral from the measured displacement field.

When considering the 4000 N load step, it can be seen from the different modes of stress intensity factor that despite the non-centred loading, the main component is mode I (Figure 4.18a). Other modes exist but does not have a major contribution, except as the edge X=5 is approached. In order to validate the analysis method, the results obtained via the J-integral approach with the interaction integral were compared with results from Réthoré (Figure 4.18b) using a field fitting approach described in [46], the analysis was performed by Dr Réthoré, who then provided the results. This comparison is particularly interesting as the only data in common is the

original X-ray projections dataset. The reconstruction algorithm used by Réthoré is the one provided by the ESRF on their website[3], the DVC is performed with his own code, based on a different implementation of DVC than the one utilised in Davis; Réthoré's approach considers that all subsets are linked to each other. The SIF calculation is performed using field fitting of William's series using a technique that is fully documented in Lachambre's thesis [133]. Despite a totally different analysis chain, the agreement between the results produced by the two methods is clear.

This observation validates the method presented in this thesis. When using the interaction integral, the method is sensitive to changes in the crack tip position (as discussed in Chapter 2), this is also the case of the field fitting method and both methods are on equal grounds with regards to this problem. In terms of versatility, the FE approach presented here is interesting as it can handle any crack geometry as long as a model of it can be created. However, in Réthoré's approach, complex crack shapes require definition of cutting planes in the data on which the field fitting is performed, those are cumbersome to define. Also the FE method can use complex material models (see Chapter 5) that cannot be described using field-fitting approaches that assume the linear elastic Williams' series. The FE approach presented here also provide a good noise robustness as the J-integral contours are taken within the FE area, this reduces the effect of noise in the DVC data that would affect methods based on direct field measurements such as shown in Chapter 2 for 2-D examples.

SIF measurements and discussion, EN sample

The same type of analysis was performed on the EN sample data. Due to the lower compliance of the sample, the loading of the crack was better aligned, this was verified for the 4000 N load step by comparing the crack opening profile on the left and right surface (Figure 4.19). A slight misalignment can be observed

[3]PyHst2 software available at: https://forge.epn-campus.eu/html/pyhst2/

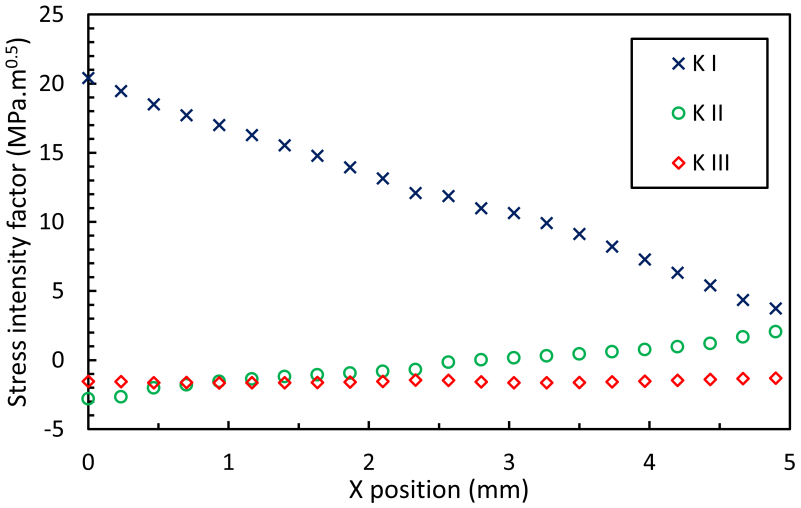

(a)

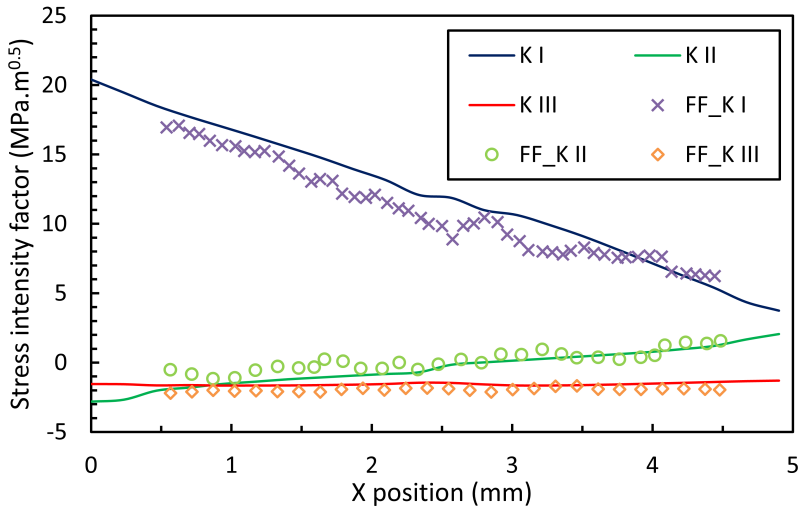

(b)

Figure 4.18: (a) SIF calculations for the different modes for the 4000 N load step. Data obtained using the interaction integral and the method presented in this thesis. (b) Comparison with the values obtained from the same tomography dataset, using Réthoré's DVC analysis and field fitting approach. Réthoré's data is plotted with symbols, J-integral data is plotted as lines.

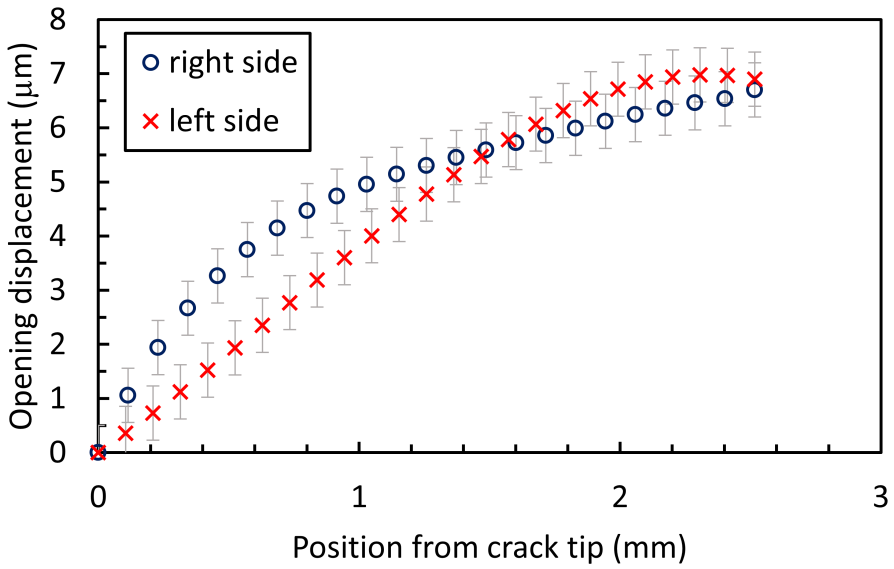

Figure 4.19: Left and right crack mouth opening displacement on the EN sample at a load of 4000 N.

with an average ratio between opening profiles of 1.3 ± 0.5, however the shape of the misalignment is not easily characterizable.

The crack is essentially loaded in mode I (Figure 4.20). The red line showed on Figure 4.20 is the mode I SIF value for the FE model with applied boundary load conditions to simulate a vertical loading of 4000 N (i.e. perfect alignment). The bottom surface of the FE model is not allowed to move in the Z direction and the top surface is applied a uniform pressure of 160 MPa. The hypothesis of perfect alignment is expected to give a reasonably good approximation due to the observations made in Figure 4.19. The mode I stress intensity factor obtained from the DVC displacement field is consistently ∼4 MPa.m$^{0.5}$ lower than the stress intensity for perfect alignment.

A comparison of the Mode I SIF values along the crack front for the three different analysed load steps is shown on Figure 4.21. Interestingly, very little difference is observed between the applied load of 3600 N and 4000 N. The significant change between the mode I SIF value at 3200 N and 3600 N is at this stage unexplained. The analysis of the DVC data using far field data (DVC displacement only applied

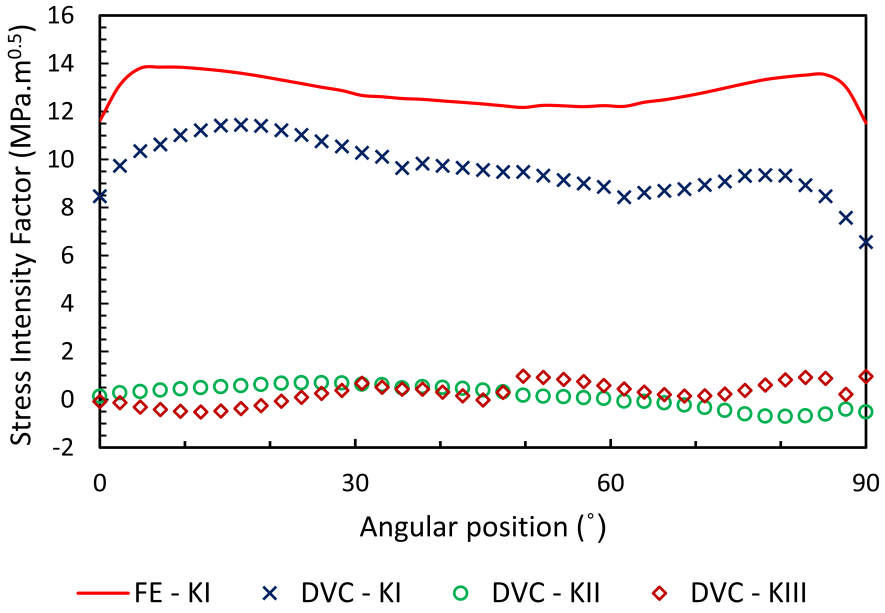

Figure 4.20: Stress intensity factor values for the different modes in the EN sample loaded at 4000 N. The red line shows the analytical result for a FE model with the corresponding load.

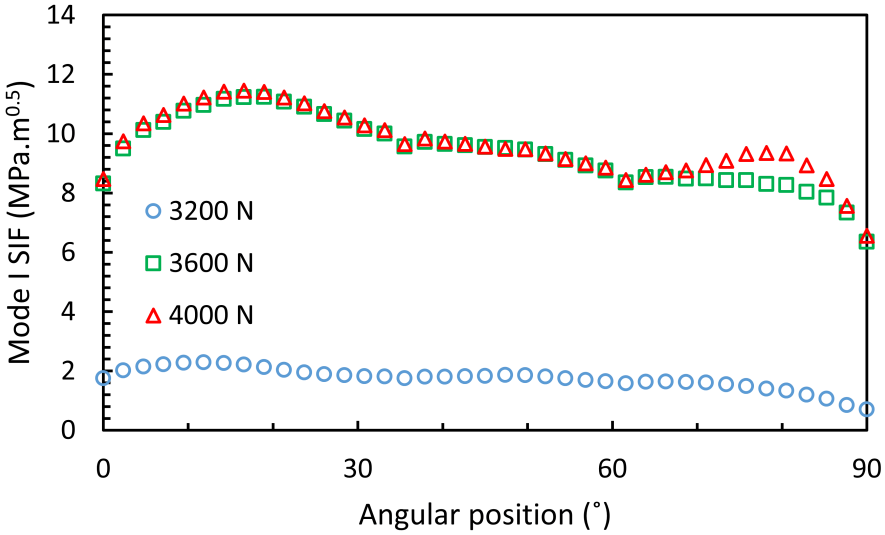

Figure 4.21: Mode I SIF for three different applied loads. The change between 3200 N and 3600 N is at this stage unexplained.

on 0.8 mm on the top and bottom of the specimen) produced no different results for the tested cases of 3200 N and 4000 N, the average difference in the mode I SIF values was of 0.3 MPa.m$^{0.5}$.

In both experimental samples, the same phenomenon of an unclear relationship between the measured applied load and the full-field DVC data can be observed. The change of behaviour for loads higher than 3200 N in both cases is hard to explain. The data do not show any significant effect of crack closure. An issue with the load cell measurements is to be considered. This will demonstrate the importance of full-field methods over analytical calculations. At present, the proposed method is shown to be able to determine what the crack is actually experiencing with no a priori knowledge of the applied loading or loading direction.

4.5 Conclusion

In this chapter, a method to calculate 3-D J-integral from DVC results has been presented. It is based on the processing of the DVC displacement fields using a FE approach. The different modal contributions can also be extracted using the 3-D interaction integral. The method was benchmarked and was found to be in good agreement with other approaches like field-fitting. The approach proposed here has the interest to be versatile in terms of crack shapes and materials models it can use. It is also noise robust thanks to the FE determination of the fields where the integral is calculated on.

The application of the method was demonstrated on two experimental datasets and highlighted the importance of using full-field data when the loading conditions are uncertain.

The golden rule of conduct is mutual toleration, seeing that we will never all think alike and we shall always see Truth in fragment and from different points of vision.

— Mahatma Gandhi

5

Characterisation of Crack Strain Fields in Polygranular Graphite

Contents

5.1 Introduction

Isotropic polygranular graphite is used in the UK's advanced gas cooled (AGR) nuclear fission reactors as a neutron moderator and reflector. These are load-bearing components, keyed in a structure that forms the reactor core [136, 137]. Their integrity is critical to the safe operation of the reactor. Some future high temperature nuclear fission reactor systems will also employ polygranular graphite in structural components [138]. Dimensional change of the graphite, caused by fast neutron irradiation and thermal gradients, can develop tensile stresses that have the potential to cause fracture [137]. An improved understanding and knowledge of the criteria for crack initiation and propagation in graphite under different stress states is important to support the structural integrity assessment of these graphite components [139].

Graphite is generally treated as a linear elastic material and its structural integrity is assessed using linear elastic fracture mechanics that assumes brittle fracture [140–143]. This leads to conservative design in non-irradiated graphite at least, as it is a quasi-brittle material that can exhibit non-linear mechanical behaviour [88, 144], development of permanent set after straining [145] and a rising fracture resistance (J-R curve) with crack propagation [88]. Reports of the latter are quite variable and appear to depend on the method of study. For instance, two studies in the same grade of coarse grained graphite used an analysis of the full-field displacements to obtain the J-integral [47] and direct measurement of the energy required to extend the crack length [146]; both found a rising R-curve behaviour (i.e. increase in fracture resistance with increasing crack length) that reached a plateau after significant crack growth (>50 mm), but differed by a factor of two. A recent study in a fine grained graphite compared compliance based methods to measure the critical strain energy release rate with a simple linear elastic fracture mechanics calculation of the stress intensity factor [147]. Rising fracture resistance was observed similarly by both analyses with no plateau, though the extent of crack

propagation was less than 10 mm in this case. Polygranular graphite also exhibits effects of size and stress state on strength [73], and these are not fully explained by Weibull-type approaches that consider the relative stressed volumes within a strain gradient [148, 149]. It has been proposed that some of these differences may arise from extrinsic factors, such as crack bridging, that may depend on specimen geometry; these would act to shield the crack tip and reduce the local stress and strain energy field [150]. Knowledge of the failure criterion in graphite is required to resolve these issues, as well as better observations of the stresses and strains that develop in graphite during mechanical loading.

Full-field displacement mapping is a powerful tool to measure deformation at surfaces. The strain field may be derived from the displacement field, and displacement field mapping by both DIC and the related technique of electronic speckle pattern interferometry (ESPI) has been employed for the early detection and study of fracture nuclei in polygranular graphite [151–154], to which the strain field is very sensitive. The surface length of observed cracks can be measured and their depth may be estimated from the opening displacements [151]. Full-field displacement data also allow characterization of the crack tip field, which describes the condition for crack propagation. This can be done via field-fitting or J-integral approaches as presented in the Chapters 1,2 and 4.

Elastic strains can be studied using diffraction to measure the interatomic planar spacing (see Chapters 1 and 3) and diffraction strain mapping can also be used to quantify the crack field as a stress intensity factor, and a least-square field fitting of the theoretical Williams' series to strain maps has been used to study the relationship between the SIF value and the growth rate (da/dN) for a fatigue crack [89]. In Chapter 3, the domain integral method to calculate the J-integral from a measured crack field [48] was extended to the analysis of diffraction data [155].

Diffraction of X-rays and neutrons has been used to study the tensile and flexural behaviour of a coarse grained polygranular graphite [88]. The study confirmed

that tensile strain produced permanent deformation, whilst the behaviour under compressive loading was essentially elastic. Significantly, the applied tensile strain reduced the bulk elastic modulus and relaxed the substantial thermally induced residual elastic strains within the graphite crystals. Both of these effects were attributed to microcrack development. Microcracking is commonly observed in quasi-brittle materials, such as graphite [156] and concretes [157], and a microcracked fracture process zone has been observed ahead of the crack tip in nuclear graphite [72, 73]. An analogy may be established between the fracture process zone and the plastic zone in ductile materials [158] as they both dissipate energy and lead to higher fracture resistance. Fracture process zones can be simulated in structural integrity calculations using cohesive models, which implement a traction-separation law, in materials such as concrete [157, 159, 160], graphite [161] and ceramic composites [162]. Such models are important to bridge the gap between specimen tests that provide property data, and the predictive simulation of the performance of larger engineering components.

The structural integrity assessment of nuclear graphite presents some complications, since its elastic modulus and strength increase with fast neutron irradiation [137] and decrease with radiolytic oxidation [163], but there are few data for the effects of irradiation on fracture resistance [164]. Better understanding of fracture behaviour may increase confidence in structural integrity assessments. However, if the fracture of irradiated graphite is to be understood, then non-irradiated graphite should first be addressed. Various fracture criteria for graphite have been proposed that may define a suitable cohesive model, including stress, strain and energy-based criteria [146, 165]. Energy-based criteria use thermodynamic principles, whilst strain and stress criteria have the advantage of being well suited to engineering design. To determine which criterion provides the most accurate description, detailed observations of the stress and strain states in the crack tip field are required.

Three-dimensional observations of deformation and damage through high-resolution X-ray computed synchrotron tomography and Digital Volume Correlation (DVC) in polygranular graphite are presented. Polygranular graphite is very well suited to this type of analysis, as it has significant porosity that is distributed over a wide range of length scales [73, 88, 137] that provide the necessary "speckle" contrast for DVC.

In this chapter, the progressive development of the deformation ahead of a quasi-static propagating crack in polygranular graphite is simultaneously characterised via synchrotron X-ray diffraction to measure the elastic strain field, and digital volume correlation of X-ray computed tomographs to measure the total strain field via the displacement field. The objective is to identify the fracture propagation criterion for non-irradiated graphite. This would allow more accurate simulation of fracture and damage nucleation in different specimen or component geometries. It may also guide the development of test techniques to extract the properties of irradiated nuclear graphites, which would need to be applied to small, non-standard, test specimens due to the practical difficulties of obtaining substantial specimens from operating reactors [166]. The experimental observations provide the crack's dimensions and its mode of opening under load in three-dimensions. These are implemented as boundary conditions in a finite element simulation with non-linear material properties to describe the microcracking behaviour of graphite, and the predicted stresses are verified by comparison with the experimental observations by diffraction. The calculated crack field is then used to obtain the strain energy release rate in equilibrium with the stable crack as a J-integral, which describes the criterion for mode I crack propagation.

5.2 Experimental Details

5.2.1 Material

The material is one of the graphites used in the UK Advanced Gas-cooled Reactor fleet. Manufactured by Graftech (formally UCAR) and supplied by EDF Energy Generation, the moulded IM1-24 Gilsocarbon (GCMB grade) polygranular nuclear graphite has weakly anisotropic properties. Depending on orientation, the reported Young modulus, E, is between 11.6 and 11.9 GPa, with a Poisson ratio, ν, of 0.2 and a tensile strength, σ_t, between 19 to 20 MPa at a strain of approximately 2.5×10^{-3} [167]. The same grade has been studied in previous works by Mostafavi et al. [72, 73, 88, 153]. The graphite in this work was from the same billet as the specimens of the previous study of Gilsocarbon graphite under tensile and flexural loading [88].

5.2.2 Specimen geometry

The test specimen (Figure 5.1a) was designed to facilitate tomography and diffraction observations whilst fracture was propagated quasi-statically from a stress concentrating notch. Conventional grinding was used to prepare the specimen, except for the notch that was cut with a tip radius of 0.5 mm by electro-discharge machining. Loading was applied by driving a vertical steel wedge (10° tip angle) into the notch under displacement control. The vertical side-grooves encouraged straight crack propagation from the notch tip in a region of near-uniform thickness, and the stiffness of the specimen was increased by the greater thickness towards the outer edges.

The digitally-controlled loading rig was equipped with a 1 kN load cell (± 1 N precision); the balancing tensile load was taken by an external polycarbonate tube (internal diameter 50 mm, external diameter 60 mm) that was X-ray and optically transparent. Previous studies [72, 73] had demonstrated the importance of wedge alignment for uniform loading of the notch, so a thrust bearing allowed free rotation of the wedge around the vertical axis. The specimen was also rigidly

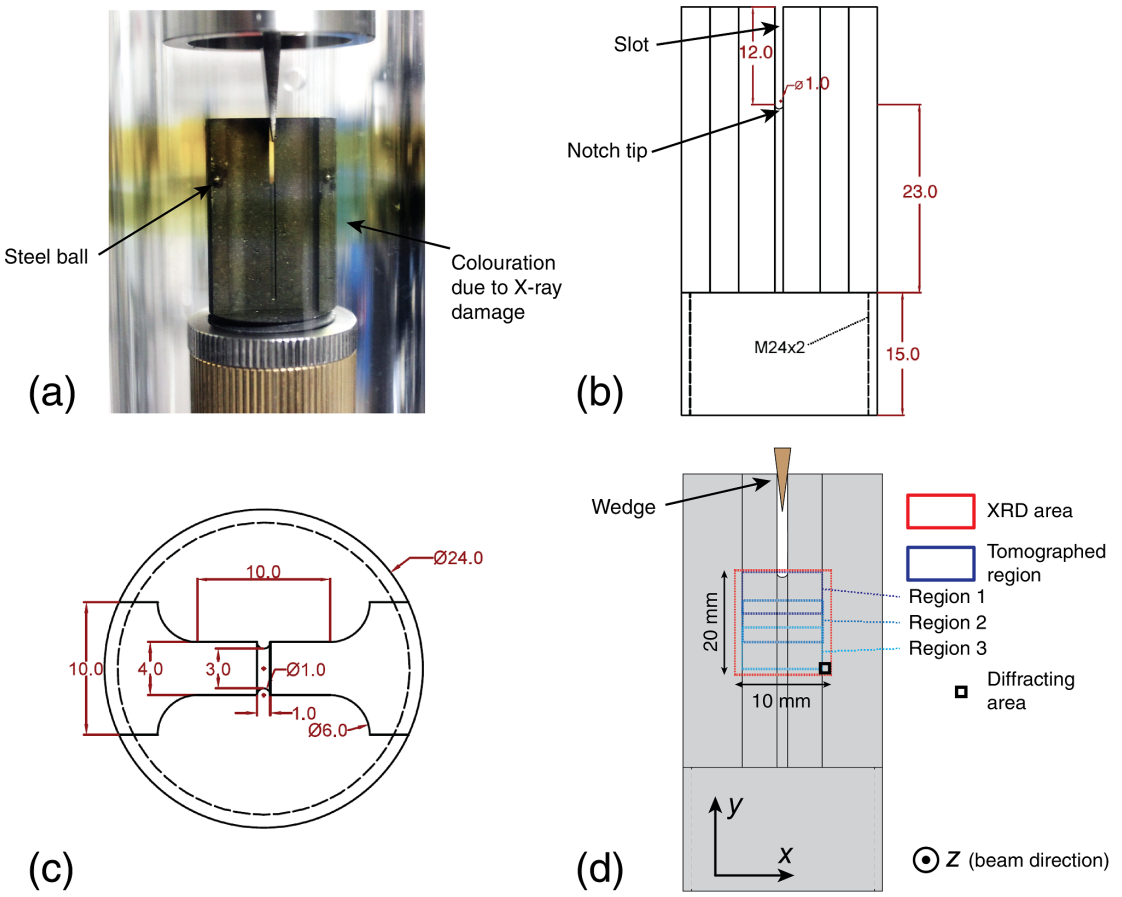

Figure 5.1: (a) The specimen, with wedge inserted, showing a pair of steel balls attached as fiducial points. The specimen is within the polycarbonate tube of the loading rig, which has been discoloured by exposure to high energy X-rays (b) Side-view drawing of the specimen (c) Top view drawing of the specimen (d) Regions of diffraction maps and tomography within the specimen. The dimensions of a single diffraction measurement point ("diffracting area"), within the mapped XRD area, are shown.

mounted via its screw thread (M24) to a single-axis horizontal slider. The wedge was centred in the slot at the start of the experiment, with the aid of radiographs. Preparatory tests determined the typical crack initiation load and verified that straight crack propagation was reproducible over distances in excess of 5 mm, which was satisfactory for the planned experiment. For crack lengths approaching 10 mm from the notch, there was a variable tendency for the crack plane to deviate.

5.2.3 Synchrotron X-ray diffraction and tomography

The experiment was conducted at the Joint Engineering, Environmental and Processing (JEEP – I12) beam line at the Diamond Light Source in the UK [168]. Radiographs were recorded using a PCO.4000 CCD camera (2560 × 2160 pixels, 16-bit depth), with optics selected to image an area of 8.3 × 7.0 mm (i.e. 3.24 μm/pixel). X-ray diffraction images were recorded using a Thales Pixium RF4343, 42 × 42 cm detector (2880 × 2881 pixels, 16-bit depth), located at a distance of 2.55 m from the specimen. At the chosen mono-chromatic X-ray beam energy (81.04 keV), this distance allowed the collection of Bragg diffraction rings up to a 2θ angle of about 5.5° (i.e. maximum {hkl} of {011} for graphite). Ceria powder diffraction observations were used to calibrate the detector distance from the vertical rotation axis of the specimen stage. Slits were used to reduce the incident X-ray beam to a size of 1.5 × 1.5 mm for the diffraction observations. They were removed for radiography and tomography. The exposures were 1 second for each diffraction pattern and 0.3 seconds for radiographs.

Tomographs were recorded with 3000 radiographs over a 180° rotation, and a standard back-filtered projection algorithm [124] was used for the image reconstructions. For noise reduction, a slice-by-slice 2-D median filter of 1 pixel radius was applied to the horizontal slices of the reconstructed 3-D volumes using the software ImageJ [169]. At each observation, three overlapping tomographs were acquired to record a total volume of 17.0 × 7.0 × 7.0 mm, the overlap between tomographs was 2 mm in the vertical axis (Figure 5.1d). The maximum path length of X-rays through the specimen was greater than the dimension of the tomographed volume, but due to the low X-ray attenuation of graphite, no corrections for the specimen geometry were applied in the reconstruction of these region-of-interest tomographs.

The diffraction maps were collected in the x-y plane, with the beam oriented in the z-direction (Figure 5.1d). The measurement points were positioned at 750 μm

intervals, by translation of the specimen, to map a rectangular region measuring 20 mm in the y direction and 10 mm in the x direction. Due to the beam slits, each diffracting gauge volume had a 50% overlap at the incident surface with adjacent measurements. The mapped region was centred horizontally on the notch tip, and positioned vertically to include the notch tip and the region beyond. Radiographs of the specimen with the steel fiducial balls attached to its surface were used to align the notch parallel to the beam.

Computer scripts were used to control the experiment, in particular automating the detector and specimen movements for the changeover between imaging and diffraction modes, the diffraction mapping and the collection of consecutive overlapping tomographs. A synchrotron X-ray beam interruption occurred near to the end of the allocation period of the experiment, and one diffraction map was acquired during a transient of the X-ray monochromator temperature. This slightly affected the beam energy, and these data were corrected using the procedure described in Section 5.4.3.

5.2.4 Loading sequence

A reference tomograph and a reference diffraction map were obtained with the wedge inserted at a pre-load of 8 N. The wedge was then inserted further in displacement control at a rate of 0.2 mm/min whilst the load was monitored. Visual inspection of radiographs was used to assess the approximate increment of the crack length, and the wedge insertion was arrested at constant displacement when the crack was judged to have propagated a sufficient distance. A set of tomographs and a diffraction map were obtained of the loaded specimen, which was then unloaded completely by removal of the wedge, and tomography and diffraction mapping were repeated. This procedure was cycled to obtain 5 sets of loaded and unloaded data of a progressively propagated crack, although the available beam time did not permit the collection of a final set of tomographs of the unloaded specimen in the 5^{th}cycle.

5.3 Analysis Methods

5.3.1 X-ray Tomography and Digital Volume Correlation

Image thresholding and segmentation methods that are commonly used to quantify the dimensions of cracks in X-ray tomographs are difficult to apply in nuclear graphite due to the high levels of connected porosity [73]. Hence, the tomographs of the loaded specimen were visually inspected, slice-by-slice, to identify the crack tip position at intervals of 50 pixels ($\sim$160 μm) across the specimen thickness. The uncertainty in the assessment of crack tip position at each point was conservatively estimated to be 32 μm (i.e. 10 pixels).

Digital Volume Correlation (DVC) analysis was applied to all tomographs to retrieve the displacement field relative to the reference tomograph. The 16-bit images were first converted to 8-bit; the extreme values of the 8-bit range (i.e. 0 and 255) were assigned to the same minimum and maximum grey level values that were observed in the 16-bit data for all the scans, with the objective of reducing the potential data loss in this process. Each tomograph was cropped to 2560 $\times$ 1536 $\times$ 2112 voxels to remove the majority of the empty volume outside of the specimen. The DVC analysis was performed using the LaVision DaVis (Version 8.1) software, employing a multipass FFT-based algorithm; the first pass used cubic subset sizes of 256^3 voxels with an overlap between subsets of 75% and the second pass 128^3 voxels with 75% overlap. All points with a correlation coefficient below 0.8 were discarded (i.e. set to NaN values). For each observation, the 3 overlapping tomographs were processed separately and the displacement vector data were stitched by averaging in the overlapped region. On comparison of the average vector representative of each tomograph in the overlap region, the magnitude of the difference between vectors was less than 2.0 μm (i.e. 0.6 voxel). This was regarded as a measure of the uncertainty in the DVC measurement of displacements. The combined dataset was then corrected for small rigid body displacements and rigid body rotations,

measured relative to the reference, using the method described in [73]. The final data have a coordinate system defined such that: the lowest point of the notch tip is at $y = 0$ and the y axis is positive towards the bottom of the specimen; the x axis is positive towards the right, with the notch tip at $x = 4.5$ mm; and the z axis is in the X-ray beam propagation direction, with centre of the notch at $z = 1.5$ mm.

5.3.2 Strain Mapping by Diffraction

The raw diffraction data are images of the Bragg diffraction rings, containing all reflections to a maximum Bragg angle of $\sim$5.5°. An example X-ray diffraction pattern is shown in Figure 5.2. A large slit size of 1.5 mm was chosen as the diffraction patterns from smaller slits can be affected by local texture in the coarse Gilsocarbon microstructure [137, 170]. The (002) ring located at 2.55° was of interest as it has the highest intensity and the anisotropic graphite crystal has its largest elastic compliance normal to this plane; the effect of tensile loading on this reflection has been studied previously by Marrow et al. [88] using a cross-correlation methodology to measure diffraction peak shifts with improved precision. Each ring centre was determined by ellipse fitting, and then data averaging was done by binning at 1° intervals of azimuth angle, so that for each sector a radial intensity profile was obtained by integration. The cross-correlation method was applied to measure the shift of the (002) peak (i.e. the change in ring radius) relative to the reference diffraction data at the same position on the specimen, so retrieving the principal strains and their azimuth orientation. A rotation matrix was applied to the principal strain diagonal tensor to retrieve the strains ε_{xx}, ε_{yy} and ε_{xy} in the coordinate system of the specimen. This was done for all of the 378 diffraction patterns that constituted each diffraction map, and the data were visualized using contour plot methods in MatLab. Strains calculated by this analysis method in polygranular graphite have a random measurement error of 1.2×10^{-5} [88].

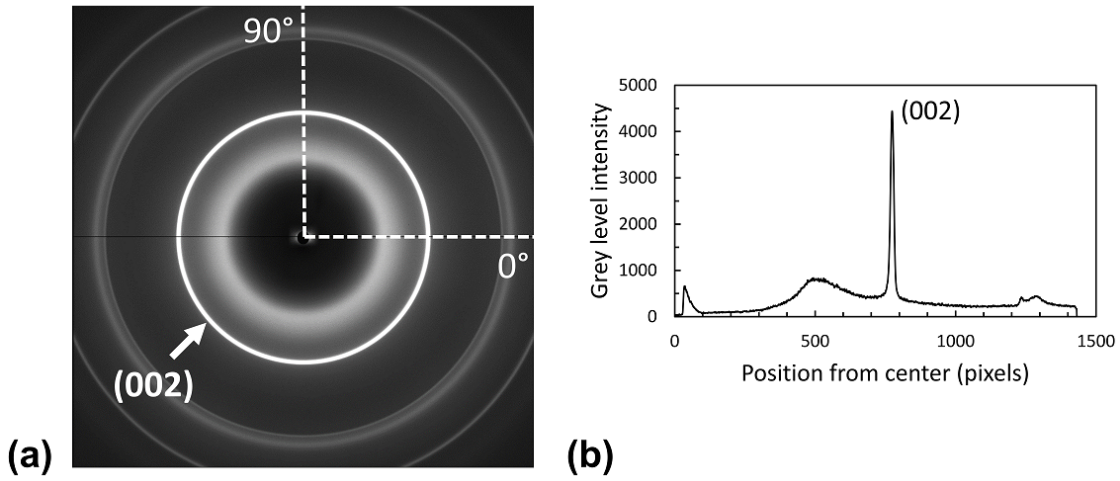

Figure 5.2: Example X-ray diffraction image for Gilsocarbon graphite, with a line profile of the measured intensity (16-bit) along the radius at 0° at a sample to detector distance of 2.55 m. The (002) Bragg reflection is marked. The pixel size is 148 μm.

Applied loads may cause movements of the specimen along the direction of the beam that will have a geometric magnifying or diminutive effect on the diffraction ring radius [88], which introduces artificial strains. The experiment set-up did not permit calibration of the specimen to detector distance (e.g. with a ceria reference) once loading has commenced, so the effects of specimen movements were corrected for each diffraction data point by direct measurement of the specimen position, relative to the calibrated rotation axis, using the raw tomography/DVC results. These had not been corrected for rigid body movements, and so measured the specimen position in the frame of reference of the synchrotron. The displacements along the beam were determined by first averaging the DVC-measured displacements through the specimen thickness in the beam direction. These had a spatial interval of $\sim$100 μm, so the obtained 2-D displacement field was interpolated to obtain the displacement at the exact position of each diffraction measurement. In the previous study of a tensile test of graphite [88], the corrections for specimen movement were quite significant due to the flexibility of the load train, but in this case, due to the high rigidity of the loading jig, the maximum movement was between 6 and 10 μm in the z direction and did not change significantly with applied load.

Without correction, this movement would introduce a strain bias of approximately 4×10^{-6}. There is no measurable error from the positioning reproducibility of the Pixium detector between diffraction observations; this was measured using image correlation of diffraction images to be better than 1 μm.

5.4 Results

5.4.1 Load versus crosshead displacement data

The raw data of the load vs. crosshead displacement for the 5 load cycles are presented in Figure 5.3, in which the red crosses identify the recording of diffraction maps and tomographs whilst the specimen was maintained under load at a fixed wedge displacement. The load at these observations was manually recorded, before and after each mapping and imaging sequence, and did not reduce by more than 12% over each period. Contact between the wedge and the test specimen above 10 N is apparent in the initial loading of each cycle – the wedge was removed completely between each cycle. The data are offset in displacement between cycles, which is attributed to damage that occurred at the contact between the wedge and the specimen. The reported displacements do not correctly represent the wedge position in the specimen's notch during unloading. This is due to friction that allowed slack movement in the thrust bearing to be taken up when the crosshead displacement was reversed, before the wedge itself was removed. A software issue affected data logging during cycles 2 and 3 and fewer load/displacement data points are available to show the loading curves, so the trend line has been fitted through the available data.

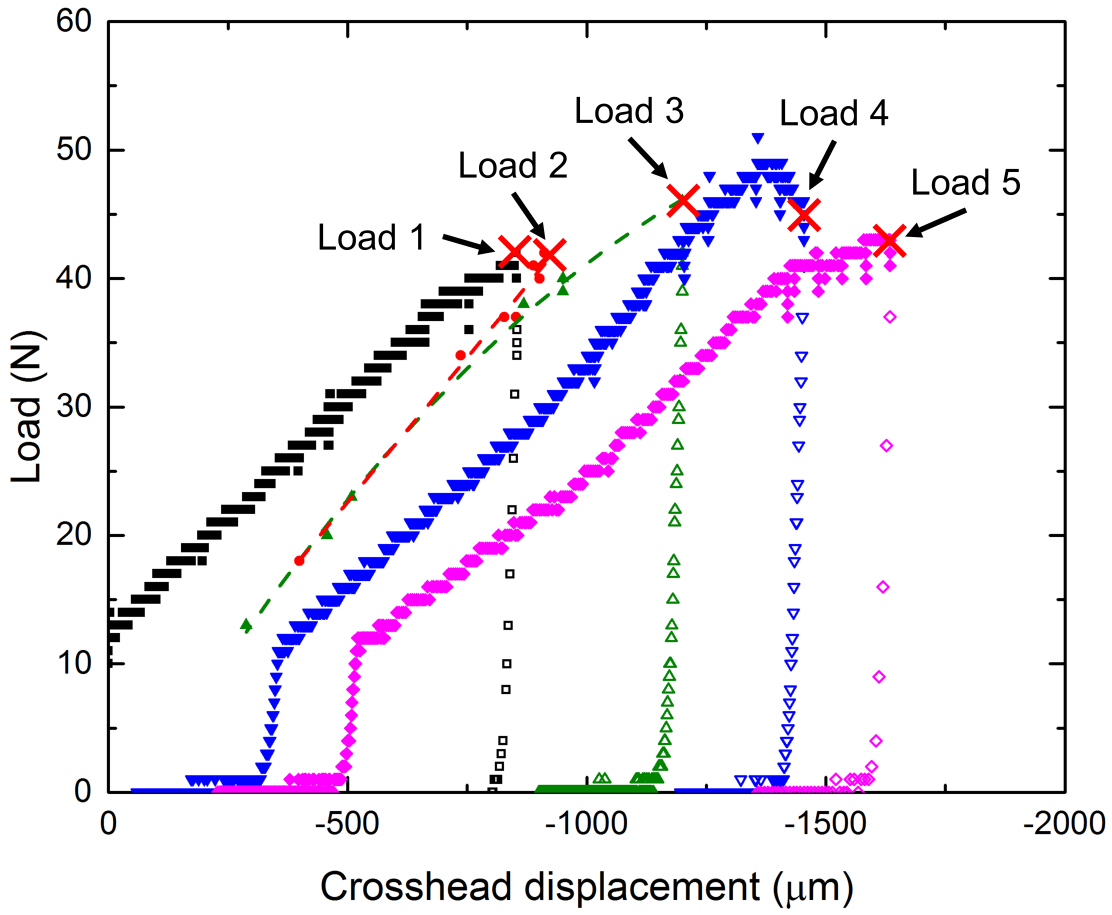

Figure 5.3: Load – crosshead displacement data for all cycles. Loading is shown with solid symbols, and unloading with open symbols. For cycle 2 and cycle 3, the loading curve is traced through the available data using a quadratic best-fit (both $R^2 > 0.99$). Tomographs and diffraction maps were collected at the points labelled "Load 1" etc.

5.4.2 Tomography and DVC analysis

The radiographs (e.g. Figure 5.4), were adequate to assess the approximate position of the crack tip during the experiment, but are not sufficiently sensitive for reliable measurements of the crack dimensions. This was done using the tomography data. Example sections of a tomograph of the specimen (cycle 3, loaded) are presented in Figure 5.5. Automatic segmentation of the crack is unreliable due to the high density of connected pores, so a manual slice-by-slice segmentation was done to provide a 3-D visualization of the crack. This confirms a straight crack has propagated parallel to the notch plane. The crack is continuous, with some bridged regions

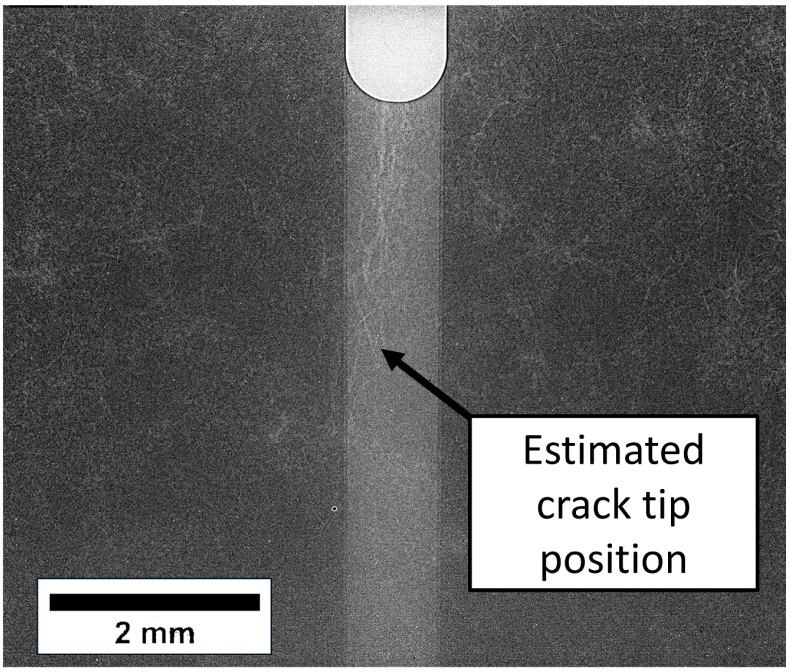

Figure 5.4: Radiograph taken at cycle 3 (Loaded), used for approximate monitoring of crack length during the experiment.

apparent as holes in the crack [150]. Some of the bridges near to the crack tip may be positions where the crack opening displacement is too small, compared to the voxel size, to provide sufficient contrast [153].

The crack's geometry was also measured using a 3-D edge detection analysis (E-D) that employs a method [**Cinar2015**] based on phase congruency. Applied to the displacement field, it is very sensitive to the discontinuity of the crack. The positional uncertainty depends on the interval between displacement vectors, which in this case is 100 μm. The crack opening displacements were obtained from the difference between the closest DVC displacement vectors on either side of the crack, with an uncertainty that depends on the DVC measurement precision (i.e. $\sim$2 μm). Applied to the DVC data (Figure 5.6a), this provides a direct 2-D measurement of the crack opening profile over the crack plane (Figure 5.6b), and shows that the crack does not fully close when the load is removed. The crack length was measured using both the visual analysis of the tomographs (loaded) and the edge detection analysis of the displacement field (loaded and unloaded).

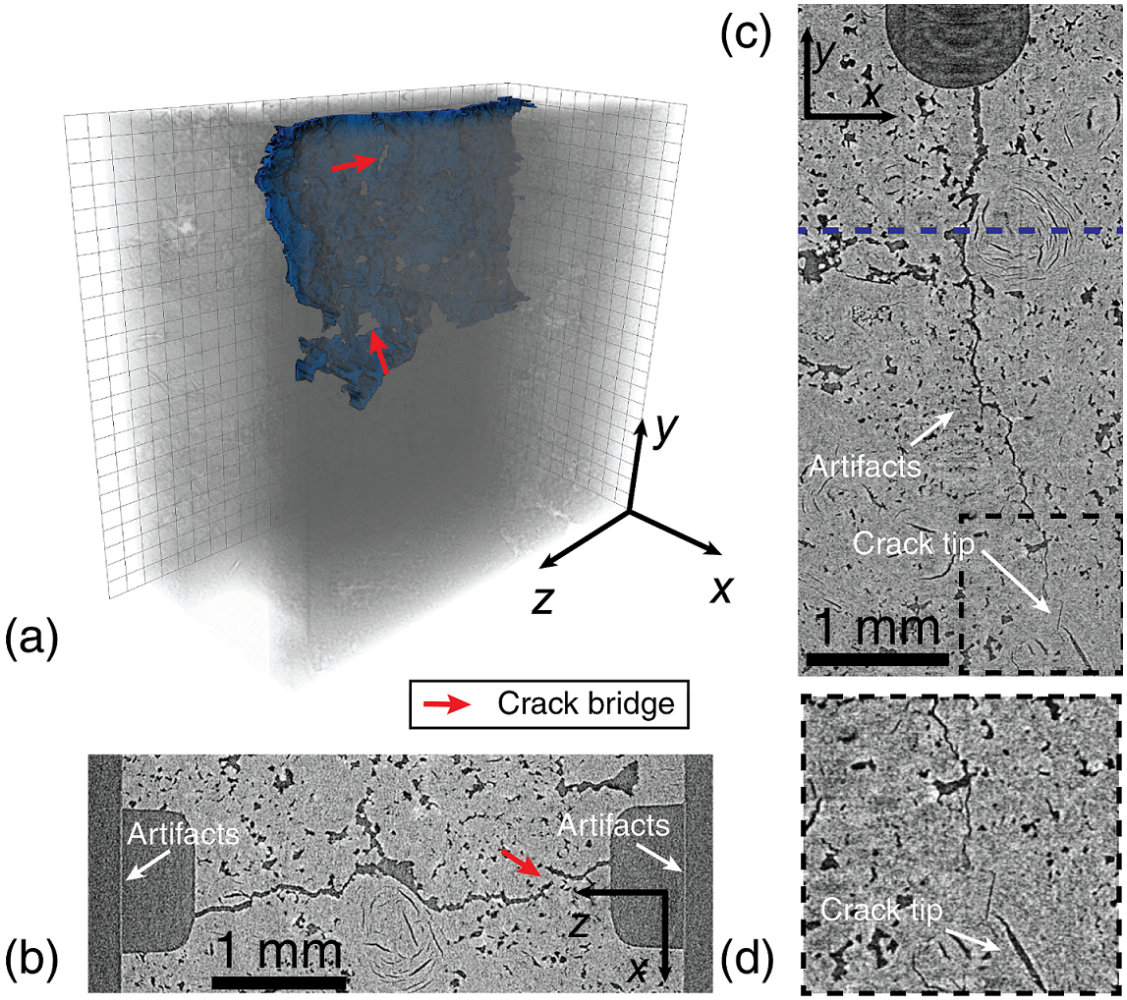

Figure 5.5: The crack at cycle 3, loaded. (a) 3-D visualization of the manual segmentation of the crack (each square on the grid is 320 μm). (b) xz-planar slice (c) yx-planar slice. The position of slice in (b) is shown as a dotted line in (c). Artifacts due to the "region of interest" tomography can be seen in the central section of (c), close to the rotation axis, and also at the mouths of the side-grooves in (b). (d) zoomed view of the crack tip region, which is outlined by a dashed box in (c). Some crack bridges are indicated in by arrows in (a) and (b).

Measurements were made of the crack depth from the notch across the specimen thickness (Figure 5.7a); the standard deviation of the observations provides the uncertainty in crack tip position, which was around 0.4 mm for both types of analysis. A good agreement is observed between the two methods for the loaded crack, but the edge-detection analysis of the unloaded displacements consistently shows a shorter crack length than the loaded data.

The observations for the loaded crack define its shape (Figure 5.7b). Crack

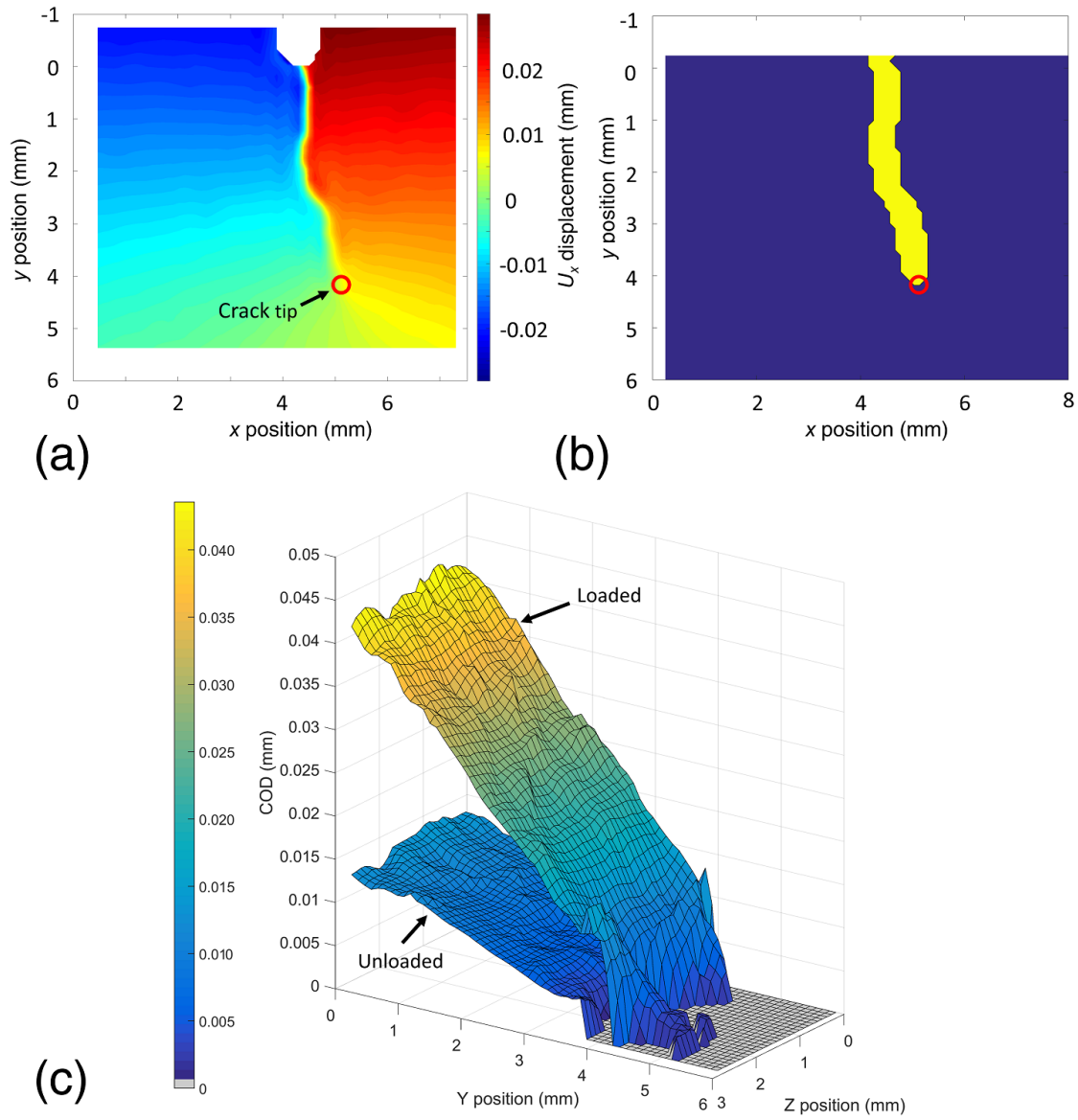

Figure 5.6: (a) Example map of the U_x displacement field obtained by DVC of tomographs (cycle 3, loaded), shown in the xy plane at z=1.5 mm, compared with (b) edge-detection (E-D) applied to the same displacement field by phase-congruency, the technique produces a binary image. Pixels detected as part of an edge (i.e. crack) are shown in yellow. The crack tip position, detected by E-D, is shown as a red circle; (c) 3-D measurement of the crack opening displacements for cycle 3 (Loaded and Unloaded) using the E-D method. The notch tip is at y=0.

initiation occurred in cycle 1, which is also indicated by the reduction in the load/displacement gradient observed above 40 N (Figure 5.3), but the crack did not propagate fully across the specimen thickness; in this cycle the maximum deviation of the observed crack front from the average crack length (including the notch depth) was ∼8%, measured using edge detection. There was no significant propagation of the crack front in the second cycle. This is consistent with the linear load/displacement trace measured during loading in cycle 2, although in this cycle the crack developed fully across the specimen thickness to achieve a more uniform crack length. The load peak in cycle 4 and the load plateau in cycle 5 indicate further crack extension, which is confirmed by the tomographs, and although the load/displacement data in cycle 3 are sparse, there is a clear decrease in the load/displacement gradient above 40 N that is consistent with crack propagation. In cycles 2 to 5, the maximum deviation of the crack front from the average crack length, measured by edge detection, was ∼5%, (average 1.7%). The visual analysis of the tomographs shows that the crack was always within 0.4 mm of the central plane of the specimen, except for cycle 5 where the crack deviated by up to 1 mm at some positions. In all cycles, the maximum deviation of the crack plane was less than 17°, measured over an arbitrary distance of 2 mm from the crack tip, thus in terms of the closest relevant standard (e.g. ASTM 647 [118]) the crack was essentially planar.

Two different analysis methods were used to assess the mode I crack openings (Figure 5.8). The first (DVC) had been applied in previous studies [72] and measures the difference between the U_x displacements on either side of the crack in the direction perpendicular to the notch plane. These were obtained at a fixed position of $z = 1.5$ mm that is close to the specimen's central axis, along two 0.4 mm wide bands running in the x direction that are located at approximately 0.4 mm on either side of the crack. The distance between each DVC data point is ~ 0.1 mm, so 4 points were averaged at each y position. Data points where the

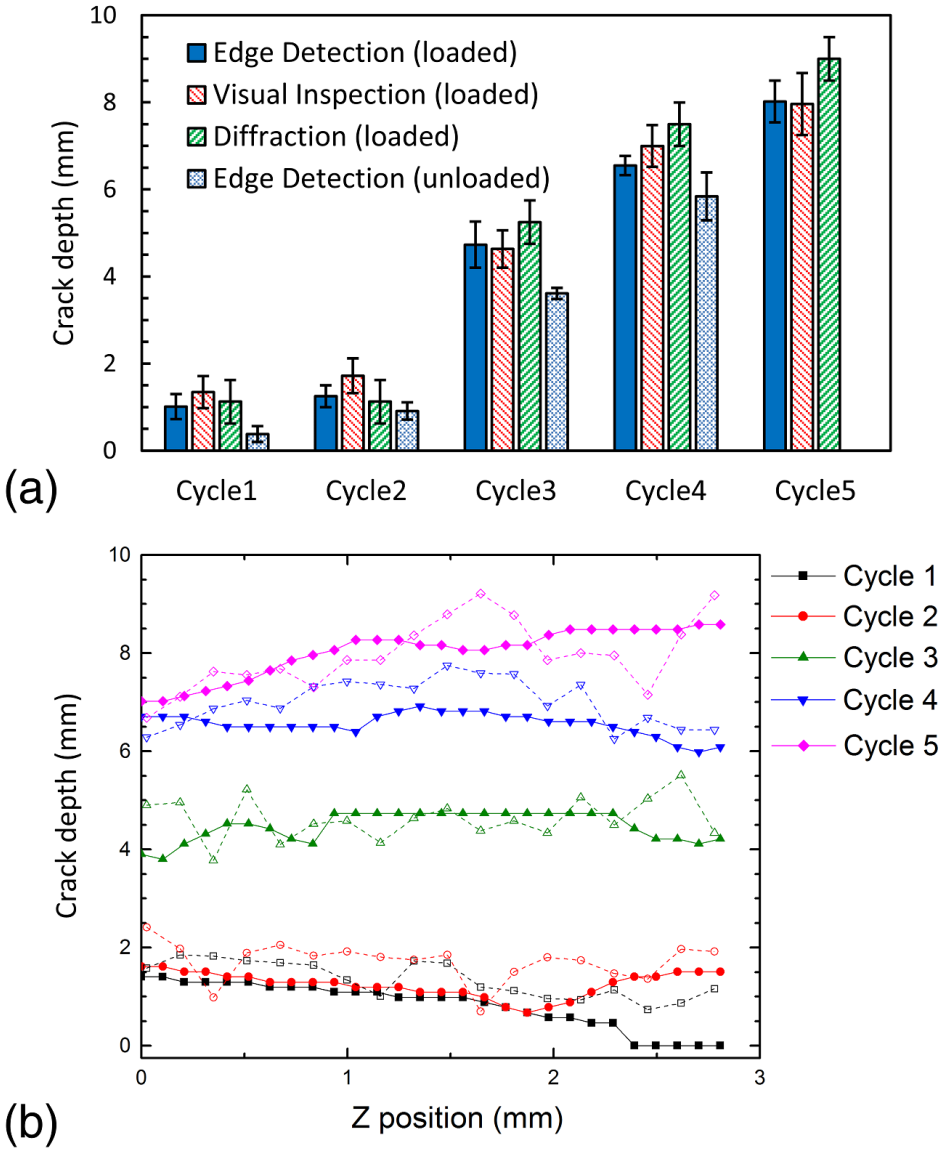

Figure 5.7: Measurement of the crack length. (a) Average crack depths (measured from notch tip at y=0), obtained by assessment of the crack tip position by visual inspection of tomographs and edge-detection analysis of the DVC displacement field. The crack tip position, assessed from the location of the strain peak measured by diffraction, is also shown; (b) Crack depth across the specimen thickness, measured under load – the full symbols show data obtained by edge-detection analysis (measurement error ∼100 μm) of the DVC displacement field, open symbols show data obtained by visual inspection of tomographs (measurement error ∼30 μm).

standard deviation of the averaged points was higher than their average value were censored. The censored points are less than 1% of the data and arise from poor DVC correlation; they were preferentially located at the bottom of the tomographs (probably due to the shape of the X-ray beam) and therefore affect regions where the tomographs overlapped (shown in light grey in Figure 5.8a and b). The second method (E-D) used the edge-detection method to identify the discontinuity of the crack [**Cinar2015**]; the crack opening displacement was obtained as the relative displacement between the displacement vectors closest to the discontinuity, so no data were extracted ahead of the crack tip. Here also, the position $z = 1.5$ mm was considered. Both crack opening profiles are quite similar, as shown by the examples in Figure 5.8a and b, and both show the residual opening of the crack after unloading that is visualised in Figure 5.6b. The crack tip position is sharply defined by the edge-detection method, but the DVC analysis shows a significant zone ahead of the loaded crack tip, several mm in length, with a measureable displacement difference across the crack plane. Observed previously [72], this has been attributed to the effect of microcracking in the fracture process zone. It is not found by the edge detection method, which is sensitive to steeper gradients in the displacement field. The full-field analysis of tomographs provides 3-D vector displacement data, so the relative displacements that create mode II and mode III shearing of the crack faces can also be examined. Measurements were extracted using the edge-detection analysis, at the crack mouth (i.e. at $y = 0$) at all z positions and were averaged (Figure 5.8c). The mode I displacement at this position increases with crack length. There is no significant mode II displacement in any observation, nor is there a significant mode III displacement until the final observation at the longest crack length. Hence the crack is loaded in mode I, except for the final observation (cycle 5), which has mixed mode loading.

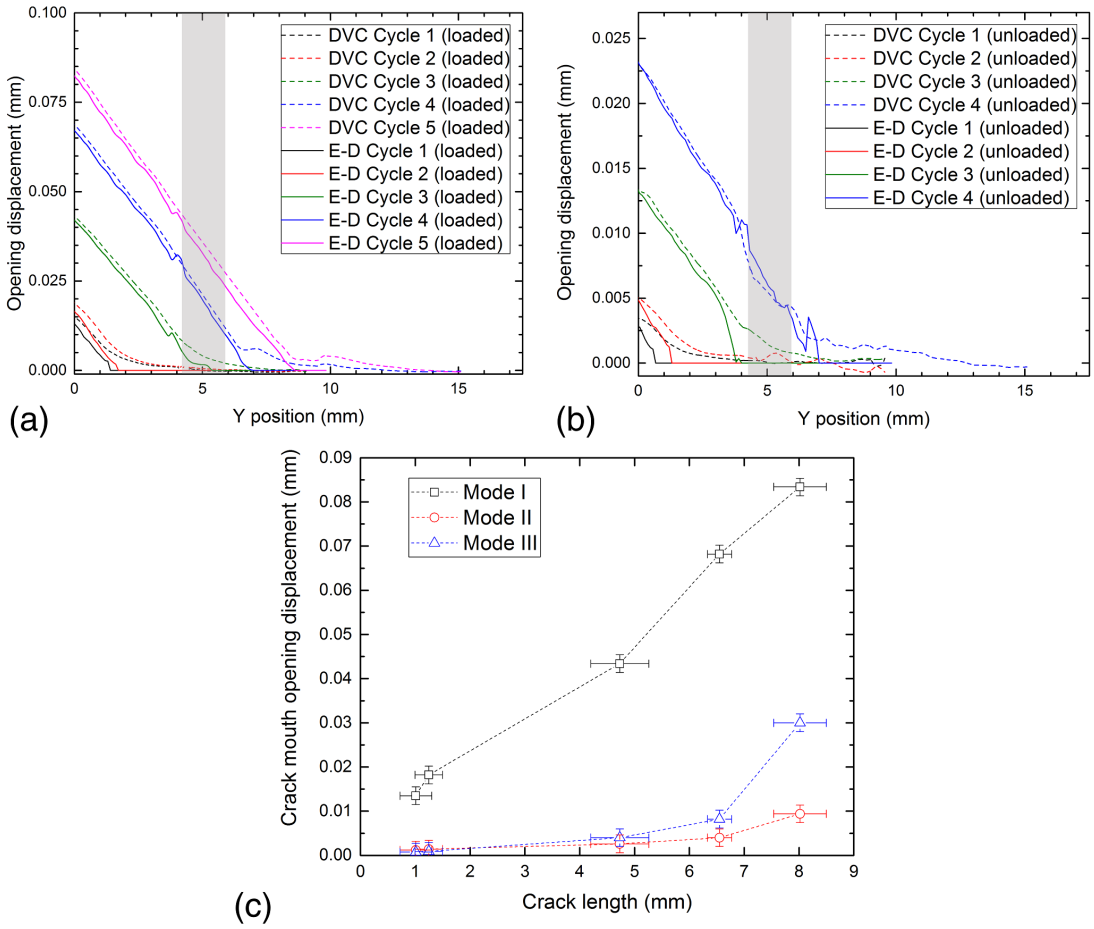

Figure 5.8: Measurements of the crack opening displacements. The mode I opening profile was obtained by both direct DVC analysis and edge detection (E-D) processing of the displacement field. The data are recorded at the centreline position, (z=1.5) in the (a) loaded and (b) unloaded states (the region where tomographs overlap is indicated in light grey). In (c) the mode I, mode II and mode III crack mouth displacements are shown for the loaded state. The data are taken at the notch position (i.e. y=0) averaged along the z direction.

5.4.3 Diffraction map analysis

XRD strain maps and profiles

The elastic strains ε_{xx}, ε_{yy} and ε_{xy}, measured by diffraction mapping of the change in the (002) interplanar spacing, are presented in Figure 5.9 for both the loaded and unloaded states for each of the loading cycles. In the loaded state, there is a tensile peak in the strain field ahead of the notch that moves further from the notch with successive load cycles. When unloaded, a region of compressive

strain extends to approximately the same position. This is shown in more detail in Figure 5.10, using the strain ε_{xx}. The data are the average, at the same distance, of the elastic strains in a band of 3 mm thickness that is parallel to the notch plane; this band is identified in Figure 5.10 (see ε_{xx} unloaded, cycle 1). The strains are presented as a function of distance from the crack tip, identified by the visual examination of the tomographs at that location (i.e. Figure 5.7), for which the positional uncertainty is approximately 30 μm. The peak strain is, on average, located at the crack tip position and there is a gradual increase in strain from cycles 1 to 5. There are tensile strains behind the crack tip when it is loaded, over a distance that increases to 5 mm as the crack propagates, and these strains become generally compressive when the load is removed.

Correction for the monochromator temperature transient

The cycle 5 (loaded) data presented in Figure 5.9 and Figure 5.10, was corrected for a transient of the X-ray monochromator temperature. The synchrotron produces a white X-ray beam with a range of energy, and a monochromator is used to select a single energy (i.e. wavelength), with a narrow energy spread. The design used at the I12 beamline is based on a bent Laue monochromator [171]; the X-ray beam passes through two silicon crystals which can be bent to change the energy bandwidth and flux. The monochromator temperature affects the thermal load on the silicon crystals and therefore the monochromatic X-ray beam energy. The monochromator is cooled by liquid nitrogen and its normal operation temperature is around -10°C. During the experiment a beam failure occurred before the start of cycle 5 (at 1:50 am), and the outage allowed the monochromator to cool. After the beam was restored (at 3:30 am), the experiment was resumed. A period of 15 minutes was allowed before data collection resumed, as it was assumed the monochromator temperature had stabilized sufficiently by this time. However, sensor data extracted after the experiment (Figure 5.11) reveals the monochromator temperature did not

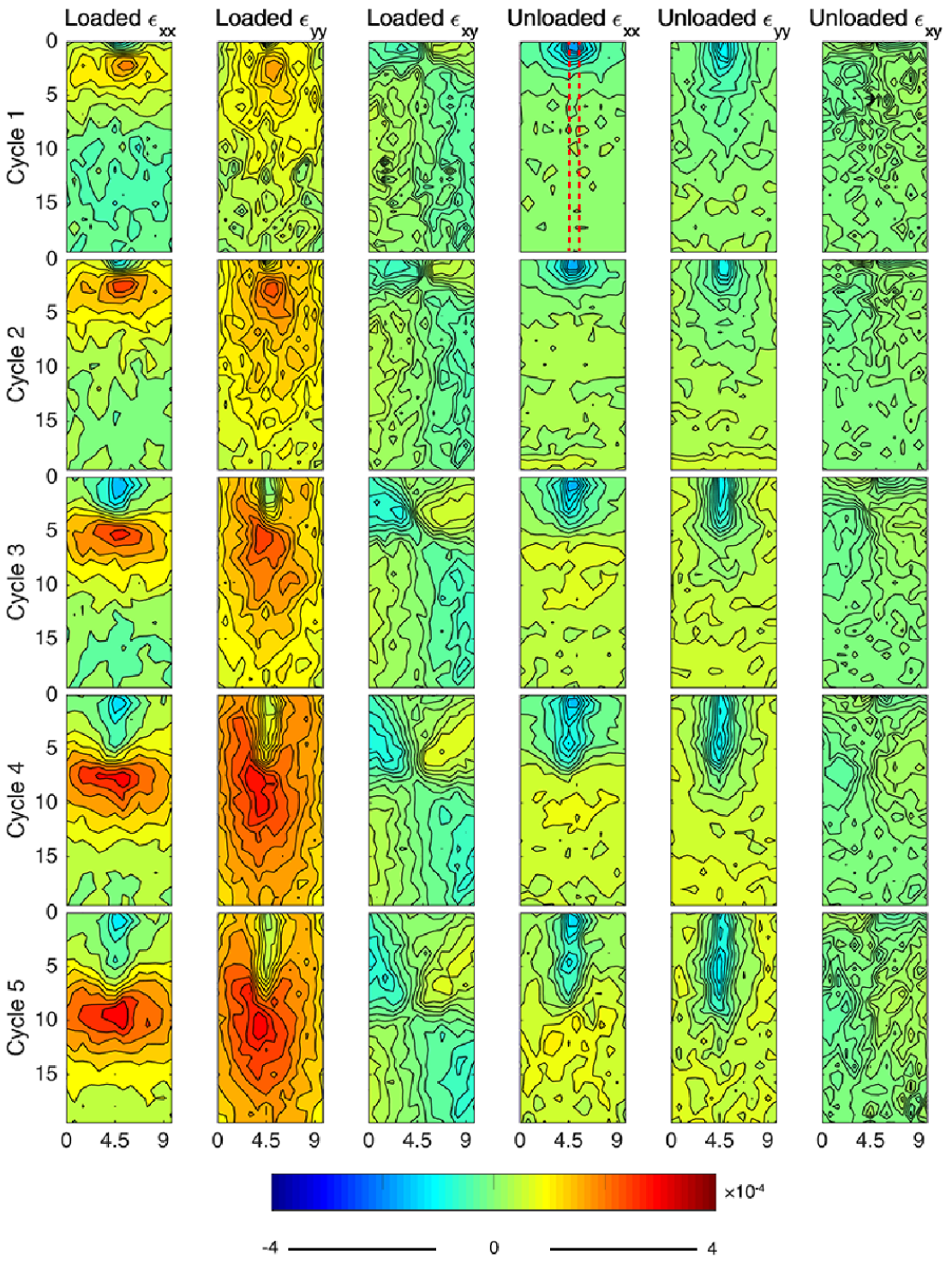

Figure 5.9: Diffraction maps for all load and unload states. The region used for the strain profiles that are presented in Figure 5.10 is defined on cycle1, Unloaded (ε_{xx}).

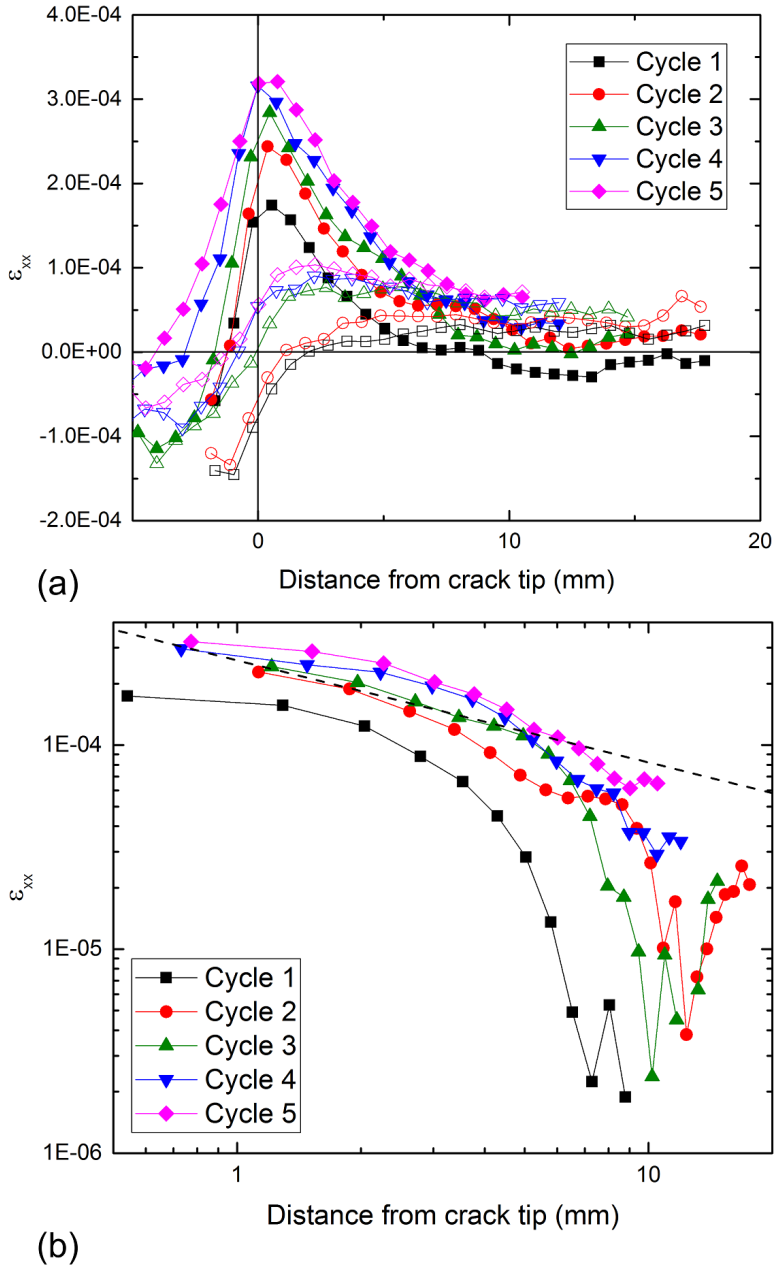

Figure 5.10: Elastic strain profiles measured by diffraction, presented as ε_{xx}, as a function of distance from the crack tip. Data for the loaded state are shown in full symbols, and the unloaded state in open symbols. The crack tip position was determined from the visual observation of tomographs. The expected uncertainty in strain measurement is 1.2×10^{-5}. (a) linear axis scale (b) log-log axis scale (loaded data ahead of the crack tip only, for clarity). The dashed line shows the gradient of the theoretical linear elastic singularity ($1/r^{0.5}$).

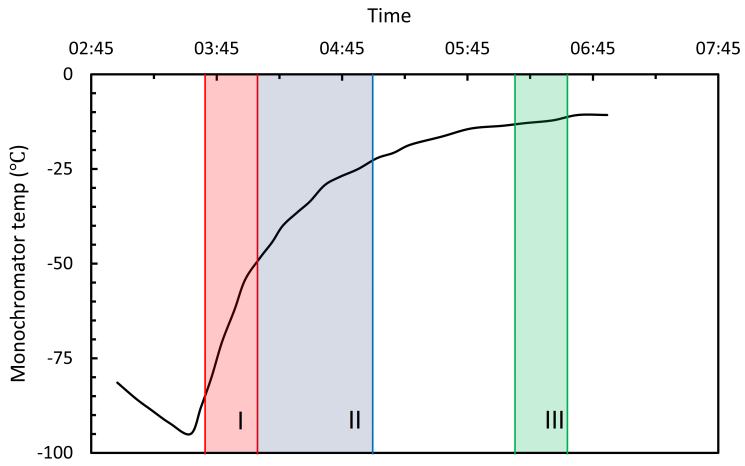

Figure 5.11: The variation in monochromator temperature with time after the beam outage. The beam was restored at 03:30. Cycle 5 (loaded) diffraction mapping was done in period I and tomography in period II. Cycle 5 (unloaded) diffraction mapping was performed in period III.

stabilize until at least 6:45 am. The period of diffraction mapping of cycle 5 (loaded) is indicated in Figure 5.11 by region I. Region II shows the collection of the cycle 5 loaded tomographs and region III is the period of cycle 5 (unloaded) diffraction mapping. During the cycle 5 (loaded) diffraction acquisition, the monochromator temperature rose by about 25°C, and its average was more than 50°C below the stable monochromator temperature of the previous scans.

The correction for the effect of the transient in the monochromator temperature on the cycle 5 (loaded) diffraction data, relative to cycles 1 to 4, was realized by considering that unstressed regions of the specimen should have constant properties throughout the experiment. Two regions were chosen, measuring 1.5 × 3.75 mm and located 0.75 mm above the notch tip on each side of the notch, and the 8 measurements in each were averaged to obtain a single value per diffraction map. The data are presented in Figure 5.12 as the change in d(002) relative to the reference diffraction map; the error bars are the standard deviation of the measurements. The data had already been corrected for rigid body movement, using the DVC of the tomographs, as described in the main text.

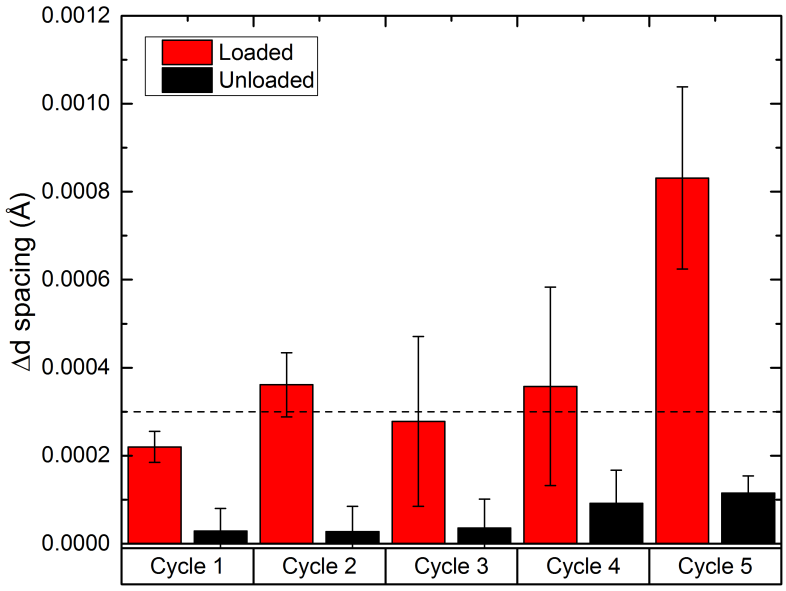

Figure 5.12: The apparent change in d(002) (i.e. Δd spacing) , relative to the reference measurement, calculated in unstressed regions for both loaded and unloaded states. The dashed line is the average for cycles 1 to 4 in the loaded condition.

For cycles 1 to 4 (loaded), the average change in d(002) relative to the unloaded reference is approximately 3.0×10^{-4} Å. The variations for the unloaded data in cycles 1 to 4 are negligible, and also for cycle 5 (unloaded) when the monochromator temperature had stabilised. This bias indicates a geometric effect, caused by a repeatable change of specimen to detector distance of 0.4 μm when the specimen is loaded. The movement of 0.4 μm is smaller than the precision of displacement measurement by DVC of tomographs, and its effect on d(002) is quite small, producing an equivalent strain of approximately 2.3×10^{-5}. The change in d(002) for cycle 5 (loaded), relative to the average of the previous loaded observations, is 5.3×10^{-4} Å, which is more significant and adds a further strain of approximately 4.0×10^{-5} to all the data. It represents an average monochromatic X-ray energy change of ∼0.2 eV. The cycle 5 (loaded) diffraction data were corrected uniformly by adjustment of the X-ray wavelength that was used to calculate d(002). Radiographs are insensitive to such small changes in beam energy, so no correction was needed for the tomographs that were recorded during the temperature transient.

5.5 Discussion

5.5.1 General Discussion

The crack is approximately planar with a reasonably straight crack front (Figure 5.7b) and it is loaded predominantly in mode I (Figure 5.8c), except for the final observation at the longest length that has a significant component of mode III shear. The average crack tip position is identified similarly by both visualisation and measurement of the crack opening displacements, to within approximately 0.5 mm (Figure 5.7a), so the crack is visualised well by X-ray tomography at 3.24 μm voxel resolution. The crack opening displacement data show the crack remains open when unloaded, with an opening that is approximately 20-30% of the crack opening displacement of the previous loading step (Figure 5.8). This is consistent with previous measurements [72], and may be attributed to the fracture surface roughness that prevents full closure of the crack.

The fracture process zone is apparent as a zone of increased displacement ahead of the loaded crack tip (Figure 5.8), which is shown by the difference between the edge-detection and the direct DVC measurements. The XRD maps in the unloaded state show significant compressive strains in the crack wake (Figure 5.9 and Figure 5.10a). The previous diffraction study of tensile loading in graphite [88] also found a compressive strain change relative to the as-received condition after the application of small tensile strains. This was proposed to be the result of relaxation, via microcracking, of the significant thermal residual stresses that exist in the microstructure after cooling from the high temperature graphitisation treatment. The observation of compressive strains in the crack wake is further evidence of a fracture process zone that is damaged by tensile strain. Its size remains approximately 2 mm as the crack extends. The tensile strain profiles (Figure 5.10b) for cycles 2 and 3 exhibit the classical inverse square root singularity of an elastic crack field. However, this cannot be affirmed for cycle 1, 4 and 5. It is expected

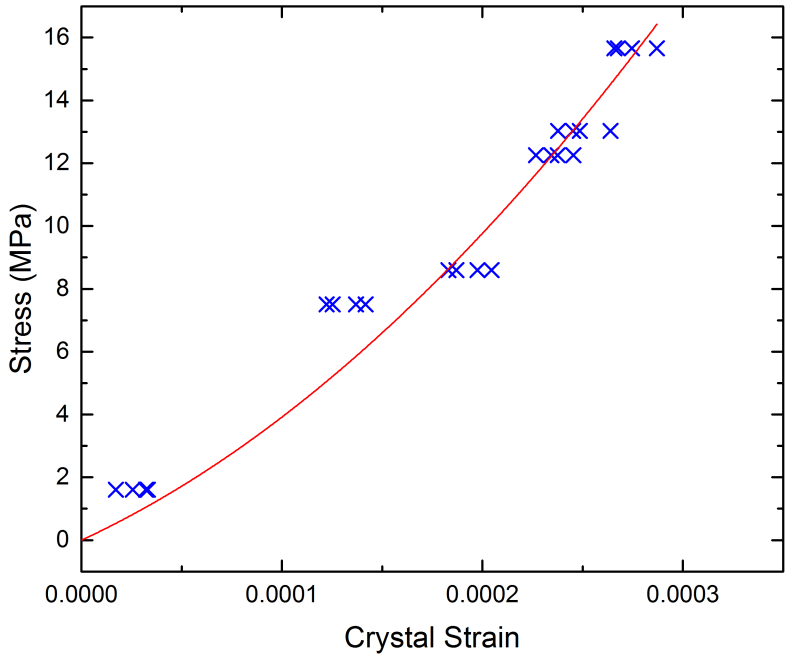

Figure 5.13: Tensile data for Gilsocarbon graphite from [88]. Relationship between tensile stress and crystal strain, measured for d(002). The red line shows the 2ndorder polynomial fit, the parameters are shown in Table 5.1.

that non-linear deformation and micro-cracking damage in the fracture process zone could affect the shape of the elastic crack field.

Table 5.1: Fitted parameters for the 2ndorder polynomial fit to Figure 5.13, the fitted equation is $y = B_1x^2 + B_2x$, where y is stress (MPa) and x is strain.

B_1	2.94×10^4
B_2	9.65×10^7

The objective of the work presented in this chapter is to determine the fracture criterion for graphite. As the observations of the loaded crack were obtained in static equilibrium with the applied deformation that caused it to propagate, it is assumed that the states of stress and strain ahead of the crack tip are representative of this criterion. The simplest fracture propagation criterion would be a critical strain or stress [143, 172, 173], which might be assessed at some characteristic distance from the crack tip. The magnitude of the total strain in the fracture process zone can be estimated using the mode I displacement difference measured by DVC across the

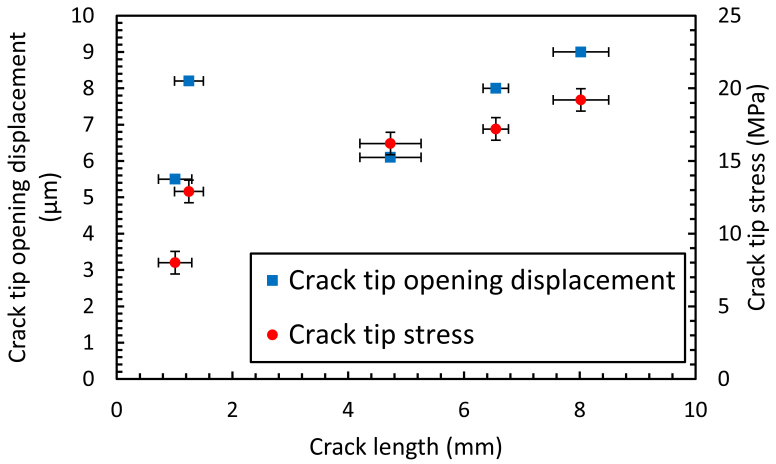

Figure 5.14: The crack tip opening displacement, measured by DVC at a distance of 0.5 mm ahead of the visually observed crack tip, as a function of the average crack length. The crack tip stress (i.e. the peak stress ahead of the crack tip), σ_{xx}, measured perpendicular to the crack plane is calculated from the XRD determined peak strain, ε_{xx}, using the empirical relationship measured in [88] (reproduced in Figure 5.13).

crack plane at an arbitrary distance of 0.5 mm ahead of the crack tip (Figure 5.14). The displacement difference has no significant trend with crack length, and it has an average value of 7.4 μm: measured over a gauge length of 0.8 mm, this represents an approximate strain of 9.25×10^{-3}. This might support a total strain criterion. However, the diffraction-measured elastic strains ahead of the crack tip increase in magnitude with crack extension (i.e. the peak strains in Figure 5.10), which suggests that a constant strain failure criterion is insufficient. A best fit to the relationship between applied stress and the elastic strain measured by diffraction, obtained in a tensile test [88] (Figure 5.13), was used to estimate the stress at the strain peak (Figure 5.14). Both the elastic strain and stress increase as the crack extends, so a stress criterion is also insufficient to describe the condition for crack propagation.

5.5.2 J-integral calculation of the strain energy release rate

The crack field governs the rate of release of elastic strain energy that is available for crack extension. It is necessary condition for crack propagation that this exceeds the energy required to extend the crack by surface creation and associated non-

reversible damage mechanisms. The elastic strain energy release rate of the strain field of a crack is described by its J-integral [15]. The displacement field data obtained by DVC were therefore analysed to calculate the J-integral in the loaded specimen as the crack was quasi-statically extended, to investigate whether this described the necessary fracture criteria. The analysis method, which injects the displacement field into a Finite Element (FE) simulation as the boundary conditions is presented in Chapter 4. It does not need to assume that the crack field follows a particular function, such as the singularity of a stress concentration in a linear elastic material. This is of particular utility for quasi-brittle materials such as graphite, which exhibits a non-linear stress-strain relationship and a change in elastic modulus with tensile strain [88].

FE model design

Three-dimensional finite element (FE) models (Abaqus 6.13) of the crack were meshed with eight-node linear brick elements that used full integration (i.e. 8 integration points per element). The element mesh size was 45 μm in the crack tip region, increasing to 250 μm at positions remote from the crack tip to reduce computational cost. Each FE model was registered in position and orientation with the reference tomograph, and so was also registered with the displacement field provided by the DVC analysis. A planar crack was defined with constant length across the specimen thickness, using the average crack lengths measured by the visual observation of the tomographs. A full model of the test specimen is not required in this analysis, and the model has the same dimensions as the DVC data (a figure of the model is shown in Figure 5.15a), which are on a regular 3-D grid of 96 μm intervals (32^3 voxels). This does not match the FE mesh, so the DVC data were interpolated onto the FE mesh using a Radial Basis Function (RBF) network interpolator, based on the techniques described in [174] and coded in MatLab.

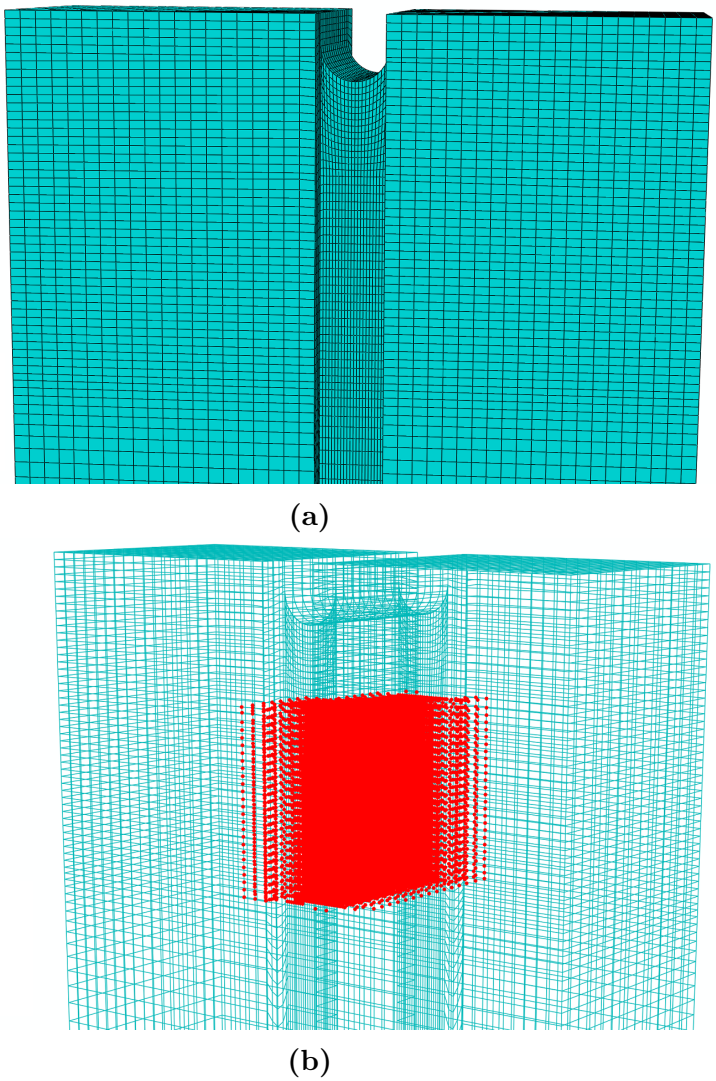

Figure 5.15: (a) View of the FE model used for the J-integral calculation. (b) Position of the forbidden nodes (in red) where no boundary conditions from DVC are applied.

The DVC data were censored (i.e. masked) close to the crack tip where DVC may give erroneous results due to steep strain gradients and the discontinuity of the crack [50]; the mask was applied to a volume of 1.5 mm width, centred on the notch and extending 3 mm beyond the crack tip (the arrangement of the mask is presented in Figure 5.15b). The FE model calculates the displacements within the masked region, since the displacements of the nodes at its boundary are provided by the DVC measurements. The J-integral integration contours are within the masked region, as the noise in the DVC data did not allow reliable calculation of

a contour-independent J-integral from the directly measured displacements. No experimental data from the fracture process zone were used, as it was within the masked region. The J-integral was calculated over 20 contours to verify contour independency and the volume integral approach natively implemented in Abaqus was used [92]. This provided a J-integral evaluation at all the nodes along the crack front. These were averaged, and the standard deviation, which was greater than the variation between contours, was used as a measure of the uncertainty of the J-integral. The analysis makes no use of the applied load-displacement data (i.e. Figure 5.3). Due to the computationally intensive aspect of the problem, each FE model was run on a high-end workstation using CPU parallelization over 8 cores.

The J-integral calculations were performed for the displacement fields obtained in the loaded condition of each cycle. Two material models were implemented: (i) an isotropic linear elastic model with typical bulk properties of Gilsocarbon graphite [167] (E=11600 MPa, ν=0.20); and (ii) an isotropic non-linear elastic model described with a custom UMAT (User-defined MATerial law) coded in Fortran, which determines the element's elastic modulus as a function of the maximal principal tensile strain in the element.

Definition of the UMAT (User-defined MATerial)

A previous study of Gilsocarbon graphite used X-ray tomography and diffraction [88] to study the non-linear tensile stress/strain relationship, and softening of Young's modulus with increasing tensile strain. The Young's modulus was measured from the total strain change during unloading via digital image correlation of radiographs, and crystal elastic strain via the change in interplanar spacing d(002). The relationships between (i) the tensile elastic modulus and total strain and (ii) tensile stress and elastic crystal strain are reproduced in Figure 5.16a and Figure 5.16b.

A further analysis of the raw data from that work finds that the crystal modulus for d(002), measured during unloading from the change in crystal strain with stress,

was constant and unaffected by the maximum applied stress (Figure 5.16b). Its average value was 61.2 GPa, with a standard deviation of 6.1 GPa. Single crystal graphite is most compliant perpendicular to the (002) plane, with an elastic modulus of 36 GPa [175]. Assuming a random arrangement of graphite crystals within the diffracting gauge volume, and integrating over all orientations to obtain the average strain in response to a uniaxial stress, the effective modulus is increased by a factor of $\pi/2$ (i.e. to 56.6 GPa). This approaches the experimental measurements of the crystal elastic modulus, which may be influenced by the local crystal texture of the filler particles and matrix. These data support the view that tensile damage in graphite is affected by the accumulation of micro-cracks that reduce the bulk elastic modulus [153, 157]. The stress is carried by the crystal lattice, which has constant elastic modulus.

The effect of strain on elastic modulus was extrapolated by assuming that microcracking has an equivalent effect as increased porosity, which can be simulated using the relationship for the change of elastic modulus with porous fraction of the material [176]. This is described by Equation (5.1) where E_0 is the elastic modulus of a non-porous material, P is the porosity fraction, a is a constant and n is the power law exponent. For interconnected pores of irregular shapes, such as observed in polygranular graphite, n=4.12 [176].

$$E = E_0(1 - aP)^n \tag{5.1}$$

Gilsocarbon graphite has an initial porosity P_0 of 0.18 [47, 73]. Assuming a linear relationship between the maximum principal tensile strain and the change in porosity; one can rewrite the relationship as Equation (5.2).

$$E = E_0(1 - a(P_0 + A\varepsilon + B))^n \tag{5.2}$$

The values of E_0, A and B are undetermined, so the relationship was fitted to the data obtained in [88] using a non-linear GRG solver (within Excel) and the assumption that $a = 1$. The fit is compared with the data in Figure 5.16a. The converged parameters are given in Table 5.2, which shows the parameter B has negligible magnitude and that the assumption of a linear relationship between strain and porosity is sufficient, within the data at least. The function was coded as a UMAT (User-defined MATerial law) for the finite element simulation of Gilsocarbon graphite, with limits that the modulus was constant at 11.9 GPa with compressive strain and also constant for tensile strains above 1%. The latter limit was introduced to avoid numerical instability.

Table 5.2: Fitted parameters (Equation (5.2)) for the effect of tensile applied strain on the elastic modulus of Gilsocarbon graphite.

E_0	28.3 GPa
A	36.34
B	6.8×10^{-7}
P_0	0.18
n	4.12
a	1

Model quality assessment versus experimental data

The results were assessed by comparison of the σ_{xx} stress profiles calculated by FE with stresses calculated from the diffraction measured strains (ε_{xx}) (Figure 5.10) using the tensile calibration curve obtained in [88] (Figure 5.13). Due to the diffraction slit size, each XRD data point represents the average stresses in a region measuring 1.5 × 1.5 mm, projected through the specimen thickness. To allow a direct comparison, the FE data were binned over a 1.5 mm gauge length with a moving average (Figure 5.17a), which has the effect of reducing the maximum stress reported close to the crack tip. The assumption of linear elasticity significantly

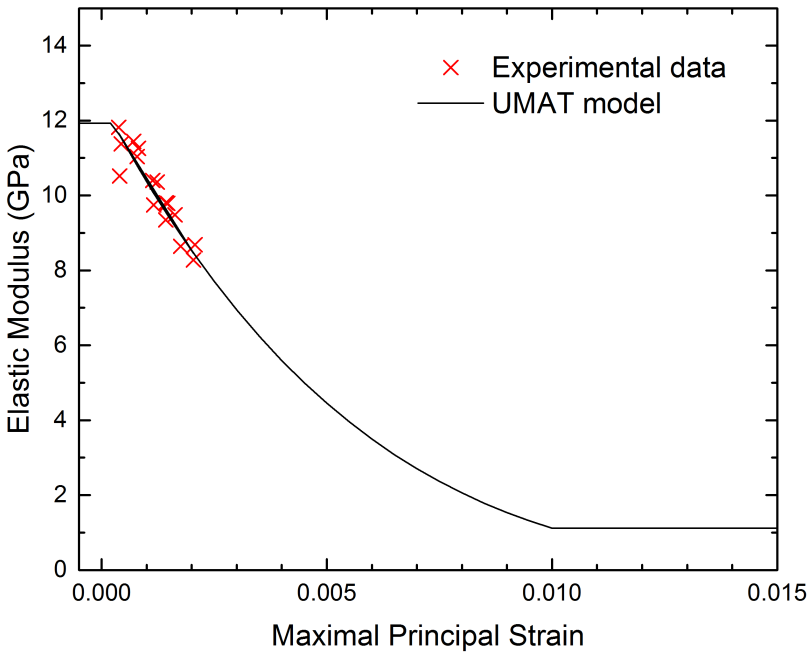

(a)

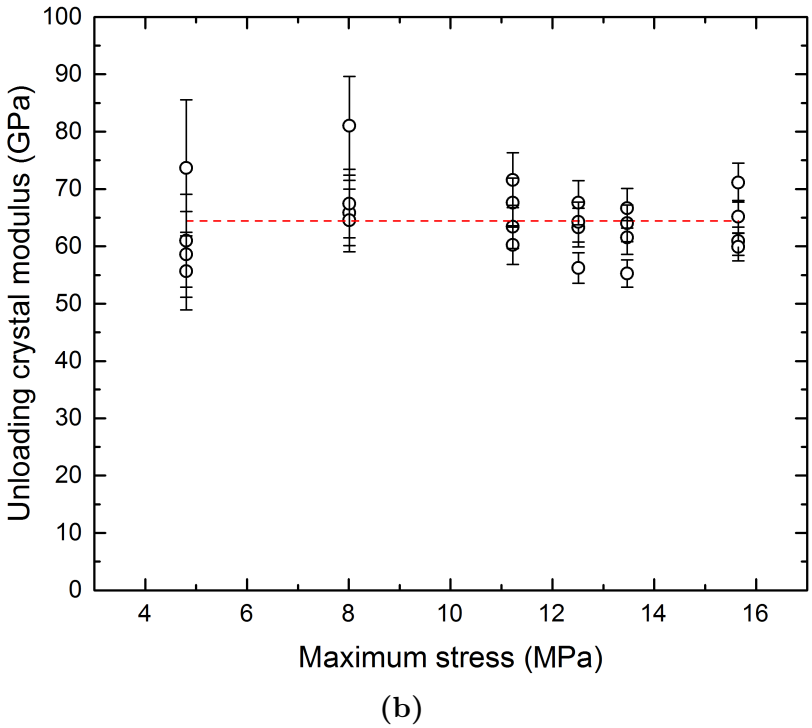

(b)

Figure 5.16: Tensile data for Gilsocarbon graphite from [88]: (a) Change of Young's modulus with applied strain, and the Graphite UMAT for this relationship implemented in Abaqus. (b) The crystal modulus for d(002) with maximum applied stress, measured during unloading. The red dashed line shows the average value for all points at 61.2 GPa.

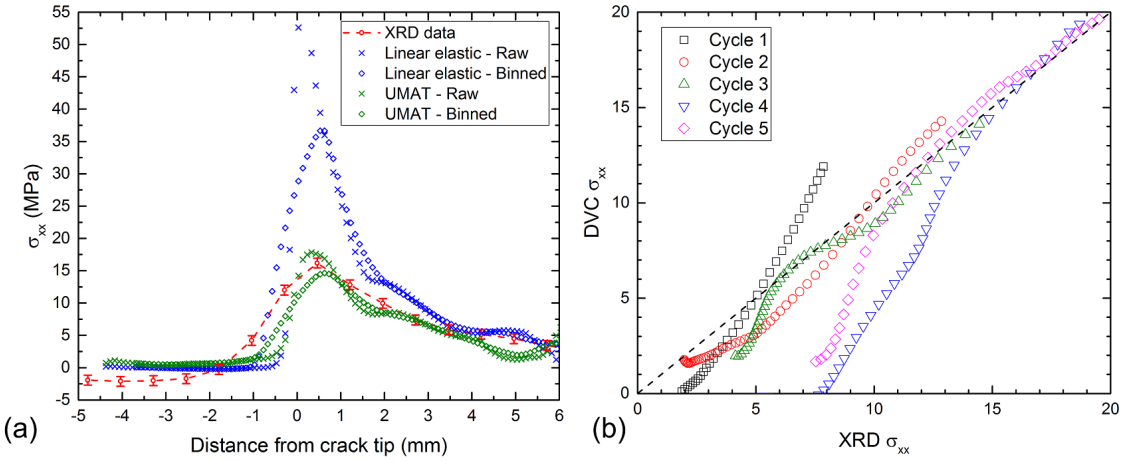

Figure 5.17: (a) Stress profiles (σ_{xx}) perpendicular to the crack plane for cycle 3 (Loaded), presenting a comparison between the XRD data and FE data with constant and UMAT-defined elastic properties. The positions of the XRD data are measured relative to the crack tip position defined by the visual observations of the tomographs. The "raw" data is binned in the x direction over 1.5 mm, this has little effect on the data. The "binned" data has an additional binning applied on the y axis, it reproduces the averaging effect of the XRD slit size. (b) A 1-to-1 comparison between the XRD and FE stress data for all points with a distance ahead of the crack tip. Error in the stresses is estimated around ±0.8 MPa.

increases the stresses, even with binning, whereas the UMAT provides a generally good agreement with the experimental data for all the load cycles (Figure 5.17b), particularly at high stress. The poor agreement at lower stresses in cycle 4 may be due to DVC errors arising from artifacts in the tomography data for this cycle. These are ring artifacts, caused by defects in the optical imaging system. They can come from different issues like dust on the scintillator, the optics and/or the detector or faulty pixels on the sensor. This generates artifacts at a fixed position on the radiographs that become rings in the reconstructed image and influence the DVC measured strains [124].

Strain energy release rates

The J-integral was calculated from the FE simulations, using both a constant elastic modulus and the UMAT properties (Figure 5.18). Higher values are obtained with constant elastic modulus due to the higher stresses close to the crack tip compared

to the UMAT, which reduces the elastic modulus with increasing tensile strain. The results from the first cycle (Load 1) are unlikely to be valid as the curved crack front (i.e. Figure 5.7) would reduce the deformation measured by DVC, and so reduce the calculated strain energy. The ring artefacts that influence the total strains in cycle 4 affect only the lower stressed regions (Figure 5.17b), and so do not significantly affect the J-integral calculation. For the last cycle (Load 5), the shear strains from the significant Mode III loading add to the J-integral, which does not separate the strain energy contributions of the different modes. To calculate the mode I strain energy release rate under mixed mode conditions would require the use of a 3-D interaction integral, which is beyond the scope of the current work. For cycles 2 to 4, the J-integral strain energy release rate calculated with the assumption of linear elasticity is substantially higher than the one calculated with the strain dependent UMAT. The respective average values are of 424 ± 47 J.m^{-2} and 190 ± 25 J.m^{-2} (i.e. Figure 5.10). However, with the strain dependent UMAT, predicted stresses are quite consistent with the diffraction measurements, thus giving higher confidence in the values determined via this route.

Previous studies of fracture propagation in Gilsocarbon graphite have reported a range of values of fracture propagation resistance. Direct measurements of the work of fracture, via the change in specimen compliance with crack length in compact tension specimens [150], obtained a fracture resistance that rose from 100 to 400 J.m^{-2} as the crack extended up to 30 mm in length. Computed tomographs showed the crack front was bowed and also bridged by substantial ligaments of material. Such significant bridging may introduce a mechanical shielding effect that can contribute significantly to the apparent fracture resistance [114]. Crack bowing could also lead to errors in the assessment of crack length, and the consequent work of fracture, and this may have affected some earlier studies of Gilsocarbon graphite [146, 177] that relied on surface observations. Significant crack bowing was avoided in studies of Gilsocarbon that used double-torsion specimens [47], in which

the fracture resistance to propagate the crack, measured over distances up to 50 mm, reached a plateau of 500 J.m^{-2}. Its separation into the elastic strain energy release rate and the non-linear inelastic work, by analysis of the load-displacement traces following the method of Sakai [178], showed the elastic energy component was constant at around 250 J.m^{-2}. More recently, direct measurements of the total work of fracture in chevron-notched specimens of Gilsocarbon graphite [179] , reported values of between 200-300 J.m^{-2}, with an increase with specimen size. Small chevron specimens do not develop significant inelastic deformation or crack bridging, so their total fracture energy would be expected to approach the intrinsic toughness of the microstructure. The elastic strain energy release rate was calculated directly from the crack field in this study (Figure 5.18), and its value of approximately 200 J.m^{-2} is quite consistent with the independent measurements obtained in the same material. It measures the intrinsic fracture resistance of the microstructure, as graphite is a quasi-brittle material that exhibits no significant plastic deformation. The total fracture resistance also includes the extrinsic contributions from the development of redundant microcracking in the specimen that does not contribute directly to crack propagation, and crack wake processes such as bridging. Both may depend on the specimen and crack geometry. Wake processes that depend on friction that may also be sensitive to the mode of crack loading [180].

In summary, the analysis of the experimental data presented in this paper shows that the mode I strain energy release rate in the crack tip field provides a satisfactory fracture propagation criterion for polygranular graphite. Direct analysis of the crack field, as done in this work, serves to measure the intrinsic fracture resistance of the microstructure. However, to predict unstable fracture propagation in engineering components, and also to analyse fracture tests to assess material properties, it would be important to take into account also the redundant damage in the microstructure and other extrinsic factors that can increase the apparent work of fracture.

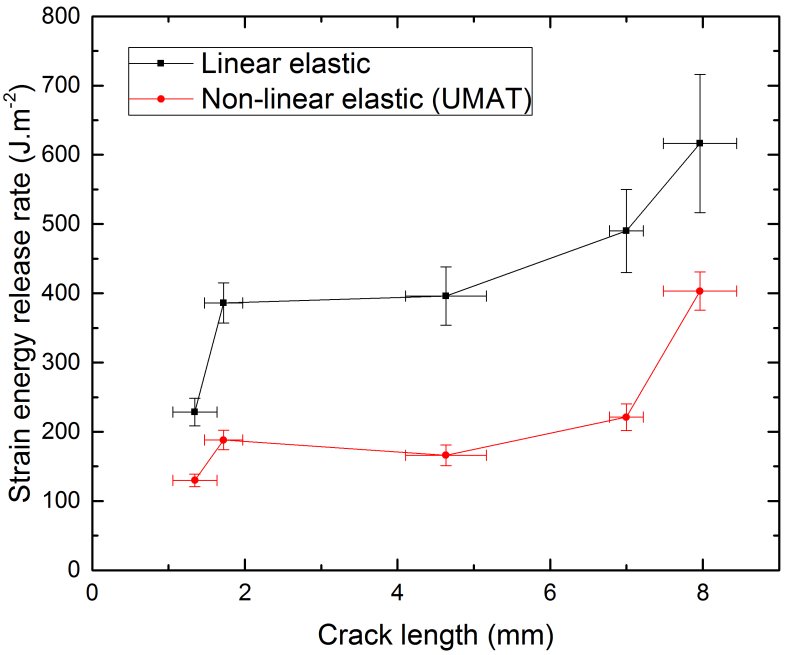

Figure 5.18: Strain energy release rate determined as a J-integral as a function of the crack length, which was determined via visual observation of the tomographs. The y-error bar is the standard deviation of the J-integral values along the crack front.

5.6 Conclusion

Tensile strain reduces the elastic properties of polygranular nuclear graphite, and this reduces the stress field at the crack tip. This has been demonstrated by synchrotron X-ray tomography, analysed by digital volume correlation, and synchrotron X-ray diffraction to map the total strain and elastic strain fields of a statically loaded crack.

Finite element simulation, with a suitable material law and directly measured boundary conditions of the deformation acting on the crack, can be used to calculate the elastic strain field, which can be expressed as a J-integral. The value obtained for a mode I crack that is in static equilibrium is the intrinsic fracture resistance of polygranular nuclear graphite.

Qu'est-ce qu'il y aurait à la fin si tout était au commencement ?

— Victor Hugo *Notre-Dame de Paris*

6 General Discussion

Contents

6.1 Direct vs. indirect analysis of 2-D and 3-D displacement fields

6.1.1 Precision and uncertainty in data and material properties

The techniques presented in this thesis to extract the J-integral from 2-D and 3-D displacement fields provide a means of obtaining the elastic strain energy release rate of a loaded crack either by direct calculation from the measured full-field displacement or indirect calculation from a FE-calculated field that is determined by using the measured full-field displacements as a boundary condition. Both approaches calculate fields of strain and stress, which can then be analysed by

field fitting to obtain the stress intensity factor (and hence the J-integral) or via calculation of the J-integral using the energy domain integral method.

The indirect-FE approach, which is described in Chapter 2 for 2-D cases and in Chapter 4 for 3-D cases, has the interest of being very robust to experimental noise, because the J-integral is calculated by the domain integral method over a FE-driven region where the fields are calculated by the FE solution and are therefore essentially noise free. This is illustrated in Figure 2.8b, for instance, which shows no effect of image noise on the indirect-FE method for an applied noise of SNR 45 dB. Direct field-fitting approaches, such as developed by McNeil or Roux [36, 43] are also interesting in their insensitivity to noise as they calculate a "best-fit" solution to the field (hence the name), thus averaging the effects of noise over the dataset. Roux's noise analysis of a field fitting approach [43] demonstrates that field fitting is very robust to noise. The dominant error is shown to come from the unknown geometry of the crack (i.e. uncertainty in crack tip position) and overpowers the noise error by a factor of 10.

The same trend has been observed for the indirect-FE approach in Chapter 2 where the error stays unchanged for image noise lower than 15 dB SNR (very high noise level) but the crack tip position uncertainty induces more significant errors (Figure 2.10). The indirect-FE approach seems however to perform slightly better than direct field fitting with, at comparable crack tip position uncertainties, an average error of 4 $\pm$2% vs. 7% for Roux's field fitting technique [43].

Direct-FE calculation of the J-integral, as exemplified by the Becker et al. JMAN approach [48] is per se theoretically insensitive to crack tip position as the integration contour does not need to contain the crack tip [15], but is quite sensitive to experimental noise (as shown in Figure 2.8), and so can only be successful with very good quality data. For instance, in Figure 2.8, the direct-FE evaluation is correct for an SNR of 96 dB but not feasible at 45 dB. A good image quality in an experiment would be expected to have SNR values between 40 dB and 60 dB.

Despite progress made in image/volume correlation algorithm development, such as use of the second-order displacement gradients or Newton-Raphson solvers [33, 34], in many cases the noise levels in experimental works are not acceptable for direct J-integral calculation (e.g. Figure 2.8).

It is possible to use smoothing on the data before field fitting in order to lower the field-fitting residuals [133], and a similar method could allow direct calculation of J-integral from smoothed experimental results, but this is less preferable than using an indirect-FE calculation. This is because in the indirect approach, the smoothing of the effects of displacement noise is, so to speak, performed by the FE layer and the calculation is informed by the material properties and continuum mechanics. Indirect field-fitting of the FE results is not of interest as it does not present advantages over the indirect-FE approach, it was not considered in this work. However, more complex hybrid cases are to be considered. For example, Réthoré and Lachambre's approach [133] that is used in Chapter 4 and later referred as a direct field-fitting approach makes use of a DVC algorithm that implements mechanical regularisation of the results [46] (i.e. the DVC "expects" the material to behave as linear elastic). This constitutes a form of smoothing and its implications are discussed in detail in Lachambre's thesis work [133].

Consequently, either direct field fitting or indirect-FE approaches have to be used with noisy data. For 2-D datasets, this noise can come from a range of factors such as the strain magnitude being small compared to image resolution, the illumination changing during the experiment or surface speckle variations as in the case of long corrosion tests [181] which have the effect of increasing uncertainty in the displacement field. In the case of 3-D datasets (e.g. tomographs), DVC currently presents a level of uncertainty that is an order of magnitude larger than DIC data (Section 4.2.1; estimated at similar subset sizes in [35, 126], DIC achieved an accuracy of $\sim$0.01 pixels and DVC of $\sim$0.1 voxel) and is unlikely to produce datasets that direct calculation of the J-integral is able to cope with.

However, analysis of the same DVC results via direct field-fitting [46, 133] and indirect-FE approaches have been demonstrated in Chapter 4 on cast iron samples and both methods give similar values (Figure 4.18b). Synthetic benchmark predicted an uncertainty of less than 5% for the indirect-FE approach whilst the uncertainty of the direct field-fitting technique was evaluated to 5-10% in the benchmarks presented by Lachambre [133].

In the case of uncertainty in the material law, for instance when the measurements are made within the plastic zone (Section 2.4.2, Figure 2.15 where the J-integral is evaluated in an Al sample deforming plastically at the crack tip) or when a microcracked fracture process zone is present ahead of the crack (Figure 5.17 where the stress field ahead of a crack is graphite is affected by the fracture process zone), both direct and indirect techniques experience issues. In the direct approach, measured strains are correct as they are derived from the displacement field but the calculated stresses are erroneous. Hence the direct approach will return incorrect values of the J-integral. This case was not explored in this thesis for the presented examples, as the direct approach was ruled out due to experimental noise. In the indirect-FE case, both strains and stresses in the FE regions are affected by uncertainty in the material law as they are determined from the displacement boundary conditions. However, they are self-consistent with the imposed material law and therefore allow calculation of a contour independent J-integral value. The sensitivity to errors in the material law can be qualitatively predicted; for example, when using an indirect-FE approach that assumes linear elasticity with a material that deforms plastically, one knows that the evaluated J-integral values will be artificially high.

It is therefore important to seek to correctly define the material law to obtain meaningful strain energy release rate values for the indirect-FE calculation of the J-integral. An example of the determination of a ductile metal properties via comparison of modelling and DVC results can be seen in [182] in which

Ramberg-Osgood parameters for an Al-SiC composite are determined by optimizing the residuals between experimental and simulated displacement fields from an indentation test. In this thesis, an approach is presented in Chapter 5 where FE calculated stresses are compared to XRD obtained stresses (Figure 5.17) to validate a non-linear model for the material law. Field fitting suffers the same problem as the indirect-FE method in terms of sensitivity to an erroneous material law with the additional drawback that analytic solutions only exist for a limited number of material laws, such as linear elastic and Ramberg-Osgood laws, so the field fitting technique cannot be implemented with complex laws. The indirect-FE method can utilise any material law than can be described in Abaqus including specific user defined materials (UMAT).

Approaches have been proposed to allow the experimentalist to assess the accuracy of the strain energy release rate calculation prior to the experiment based on synthetically deformed images in 2-D or modified FE displacement fields in 3-D; codes to automate this task have been developed. Those approaches are useful as they aid the experimental design, they produce displacement fields that can then be analysed using any of the pre-cited methods.

To sum-up, field fitting is comparable to indirect-FE calculation with linear elastic materials, since the FE region where the contours are taken from will reproduce the theoretical fields. However, field fitting implementation complexity increases when in problems with complex crack fronts, especially in 3-D. To address this with field fitting, slicing planes have to be defined in the data and the measured displacements have to be interpolated onto those [133]. The indirect-FE method utilises the well-established FE methods that have been developed to cope with complex crack geometries [16]. A major strength of the FE approach developed in this thesis is also that it can be extended to complex cases such as anisotropic materials, atypical material laws (e.g. hyper-elastic materials [55]) and presence of residual stress fields, without additional development costs.

6.1.2 Mixed-mode loading

The use of the interaction integral to separate modal contributions in 2-D and 3-D cracks is presented in this work (Figure 2.17 & Figure 4.18a). The effect of mixed mode loading on the crack propagation direction has not been tackled, but could be done for linear elastic materials using the maximum energy release rate criterion [10] for example. When looking at mixed-mode cases, the application of the indirect method presented in this work over the field-fitting approach is restricted as the interaction integral analysis is limited to linear elastic materials [94]. However, the indirect-FE approach can handle anisotropic strain/stress relations (not demonstrated here) which is particularly interesting for some industrial alloys/materials that have anisotropic properties due to texture (e.g. Inconel 718 [183], cfc-Pu [184] which has a Zener ratio of 7.03, or Ga-As with a maximum ratio of anisotropy of 1.6 [185], etc.).

6.1.3 Engineering application

The developed method is suitable for the analysis of cracks in real components as long as DIC (or possibly DVC) data can be obtained on the engineering part in response to a quantified load variation (e.g. pressure cycle or thermal transient). This has the potential to better inform structural integrity assessments [186]. Some industrial facilities are already equipped in DIC systems and perform tomographs for quality control purposes. Because the developed method uses software widely applied in industry (i.e. Abaqus and MatLab) its implementation as part of industrial processes is more straight forward. The versatility and the robustness of the solution makes this method a good candidate for analysis of real components. The already existing FE material models of components can be used, as is, but with full-field measurements rather than estimated boundary conditions thus increasing the confidence in the predictions of the SIF. The main difficulty of analysing 3-D datasets compared to 2-D datasets is the increase in computational cost. However,

the methods presented in this thesis do not require more computation power than the image or volume correlation analysis itself (respectively for 2-D and 3-D cases). The FE model calculation times increase with the complexity of the material model, but this would also be the case for a simple FE simulation.

6.2 Crack closure

Crack closure is a complex problem in the interpretation of fatigue test data and the prediction of fatigue crack growth rates in engineering components that are subjected to variable amplitude loading such as overloads. The phenomenon is due to residual stresses from plastic deformation in the vicinity of the crack [25, 26] (Figure 3.1). Those residual stresses should only affect the displacement field close to the crack. This was shown by Beretta et al. in [187] where they investigated crack closure in a Haynes 230 alloy after fatigue pre-cracking without overload. In Beretta's work, DIC was used to calculate the surface full-field displacements and field fitting was applied on two areas, one including only displacements close to the tip ("local field") and a larger area ("global field"). The fitted linear elastic SIF value using the local field exhibited effects of closure whilst the SIF value from the global field agreed with the analytical solution (Figure 6.1).

The same approach can be used with the indirect J-integral method by using either global field or local field boundary conditions to make the calculations. However, in Chapter 4 (Section 4.4.2) no difference could be found between the SIF values calculated using local and global field boundary conditions but nor could the presence of closure have been proven via observations of crack opening displacements.

The question to consider is then; how close to the crack tip do the local field needs to be assessed to allow the quantification of the effect of closure? In the study of Haynes 230 [187], an answer is partially given with the closure being highlighted by a significant difference between the SIF value evaluated from a region of 300

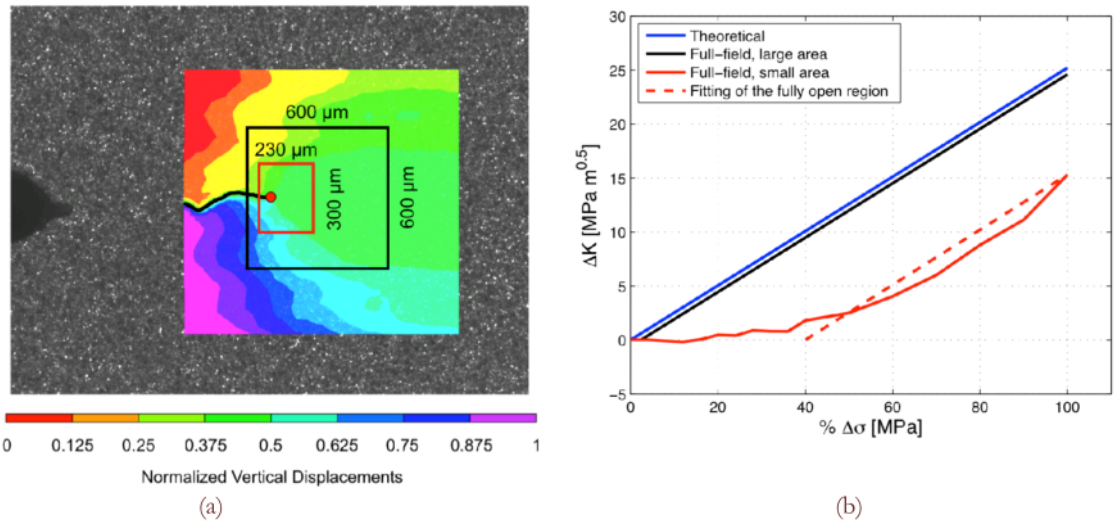

Figure 6.1: Data from Beretta's paper on crack closure in Haynes 230 [187]. (a) Two different area of the DIC displacement fields are used for the direct field fitting SIF calculation. The red and black regions respectively represent the local and global field case. (b) Calculated SIF values from the local and global regions at increasing applied loads and comparison with the analytical solution.

μm centred on the crack tip vs. a region of 600 μm for the global field calculation (Figure 6.1). In this case, the theoretical plastic zone radius calculated from Irwin's theory is of 600 μm. This is representative of Haynes 230 in the given loading conditions but will change with experimental conditions and materials. Work exists on simulating the residual stresses of crack closure [86], and the work presented in Chapter 3 of this thesis shows that these can be measured by diffraction. Further work is clearly needed to ensure that measurements are performed at length scales that are relevant to the length scale of the residual stress and deformation.

6.3 *J*-integral from diffraction strain mapping

The *J*-integral calculation from diffraction measurements is particularly interesting when it comes to studying residual stress effects, as the study of the bainitic steel in Chapter 3 demonstrates their measurement and effect on crack growth rates. The integration contours are taken on measured strain and stress data, so this is a "direct" method, a part of the fields used for the calculation are solved by

enforcing compatibility conditions, which is similar to the in-direct method. The method is less subject to noise than its displacement based counterpart as strains are measured directly and are less noisy than those obtained by differentiation of a DIC displacement field. The solved fields are also expected to bring some noise robustness in the calculation but this was not formally proved.

The J-integral calculation from diffraction data was demonstrated on materials undergoing linear elastic deformation when the bulk elastic modulus of the material and the specific modulus of the diffracting crystal plane are equivalent (Chapter 3, a bainitic steel where both bulk elastic modulus and {110} specific modulus are 210 GPa is used). This is not the case in all materials, for example in zirconium [188], the elastic modulus along (0001) is of 124.8 GPa, whilst the bulk elastic modulus is of 98 GPa. This poses a problem if the fracture behaviour or zirconium is to be studied by analysis of strain maps obtained from the (0001) diffraction ring for example. The same case can happen for materials like titanium, which has a bulk modulus of 110 GPa and crystal moduli that vary between 104 and 146 GPa [188], or graphite (Chapter 5) where in addition of anisotropy there is a large difference between crystal and bulk properties due to porosity.

For materials where E_{bulk} (elastic bulk modulus of the polygranular material) is very different to E_{Xtal} (elastic modulus along the diffracting crystal plane direction), but no non-linearity is observed between the crystal measured strains $\varepsilon_{\text{Xtal}}$ and bulk strains $\varepsilon_{\text{bulk}}$, the bulk strains can be obtained from measurements of the crystal strains (Equation (6.1)); hence the bulk elastic modulus can be used to determine the bulk stress field.

$$\left.\begin{aligned}\sigma_{\text{bulk}} &= E_{\text{bulk}}\varepsilon_{\text{bulk}} \\ \sigma_{\text{bulk}} &= E_{\text{Xtal}}\varepsilon_{\text{Xtal}}\end{aligned}\right\} \Leftrightarrow \varepsilon_{\text{bulk}} = \frac{E_{\text{Xtal}}\varepsilon_{\text{Xtal}}}{E_{\text{bulk}}} \tag{6.1}$$

The J-integral calculation of strain energy can then be performed on equivalent bulk data generated from crystal data. To this aim, the measured values of $\varepsilon_{\text{Xtal}}$ are

converted to $\varepsilon_{\text{bulk}}$ using Equation (6.1). This ensures consistency as the J-integral is calculated on equivalent bulk stresses and equivalent bulk strains.

In the cases where a non-linear behaviour exists between the bulk strain and the crystal strains, a more thorough calibration that covers all the strain levels observed in the diffraction maps is necessary to define the relationship between the crystal measured strains $\varepsilon_{\text{Xtal}}$ and bulk strains $\varepsilon_{\text{bulk}}$. Additionally, a material model must be available to determine the bulk stresses.

In Chapter 5, diffraction data from graphite is presented. It is a complex case where the bulk and crystal modulus are different but also the bulk modulus shows non-linearity with increasing strains due to damage (Figure 5.16a). However, the crystal modulus is not subject to damage (Figure 5.16b). Indeed, an increasing load causes microcracking that elastically "softens" the bulk but does not impact the crystal behaviour. The J-integral calculation from those diffraction map was not presented in this work as discussions on how to tackle this case are still ongoing.

One approach would be to convert the crystal strains to bulk strains using the calibration data obtained via a uniaxial tensile test [88]. Then to use the bulk material model to calculate the bulk stresses. One difficulty in this case is that the complex bulk material, which was defined in Abaqus via a UMAT (Section 5.5.2), is not readily implementable in JMAN-S. It is doable but require additional work. The calculated strain energy release rate should be equivalent to the one calculated from a method interested in the bulk data such as DVC results. If this is not observed, then the calibration might not be sufficiently refined. For example, in Chapter 5 a uniaxial tensile test is used to obtain the calibration data. It could however be interesting to have such data for biaxial loadings.

I go on working at science, and in fact I am turned into a sort of machine for observing facts and grinding out conclusions.

— Charles Darwin

7 Conclusion

Quantification of the crack fields is necessary to understand failure mechanisms. This can be achieved through the calculation of the crack strain energy release rate or stress intensity factor. A method based on finite element treatment of full-field measurement from image and volume correlation results was presented. The calculation of the strain energy release rate has been demonstrated for a 2-D (Chapter 2) and a 3-D (Chapters 4&5) crack via calculation of the J-integral of the elastic deformation field. The J-integral contours can be calculated in a FE governed region, driven by DIC/DVC measured boundary conditions to give the method great noise robustness compared to direct J-integral approaches and similar to field-fitting approaches. The achieved accuracy is of the same order of magnitude than field fitting techniques and seems slightly better.

In the case of mixed-mode loading in a linear elastic material, the different modal contributions can be separated by the use of the interaction integral, this was demonstrated in 2-D and 3-D cases. Complex strain/stress relationships and crack shapes can be analysed without increasing the complexity of the analysis, this constitutes a significant advantage over current field-fitting techniques.

A method has been developed to calculate the strain energy release rate from measurements of the elastic strains obtained by diffraction techniques. This is well suited to the analysis of strain fields that are affected by residual stresses or crack closure. In the case of materials that exhibit complex crystal strain to bulk stress relationships, a calibration procedure is needed but was not demonstrated in this work.

The combine use of image/volume correlation and diffraction methods on the same specimen has been demonstrated with an in-depth characterisation of the crack fields and permits the measurement of the failure criterion in complex materials.

I'm a great believer in luck, and I find the harder I work the more I have of it.

— Thomas Jefferson

8 Further Work

Contents

8.1 Crack propagating through a residual stress field

The FE package used in this thesis (i.e. Abaqus) offers the possibility to calculate the strain energy release rate of cracks that have a residual stress field acting on them. This is promising for the study of crack closure or could be used to study a crack in a welded joint for example. As mentioned in the discussion, the local/global approach can be used to quantify crack closure.

Alternatively, it could be interesting to acquire on one sample two datasets at different length scale with different optical systems. One would be optimized to retrieve the local field and the other one the global field. This could solve the problem that in most experiments, the set-up is optimised for the collection of the global field data and thus give a low spatial resolution of the local field. Another idea,

which will be explored in this section, would be to use the global field in conjunction with residual stress measurement from diffraction method. Such an approach could be implemented on the data presented in Chapter 3 as DIC data and EDXRD data are available. However, one believes that this experiment could be enriched notably by the use of tomography and by the collection of additional strain maps.

It would be of interest to design an experiment, similar to the one presented in Chapter 3, with diffraction being used to map the strain field and tomography to obtain full-field displacement data. This experiment that would require the use of synchrotron techniques would allow better understanding of the closure mechanisms in metals and would propose an approach to study it that could then be extended to other materials.

The diffraction technique can be chosen to either be EDXRD or XRD depending on the specimen thickness. XRD has a lower penetration depth than EDXRD (the monochromator used for XRD reduces the available X-ray intensity); for instance in stainless steel, XRD cannot penetrate more than 5-10 mm at 100 keV [189]. The diffraction map will only be representative of the residual stresses in a gauge volume region; this can be adjusted to acquire maps representative of the surface or mid-plane elastic strains in the sample. The acquisition of 3-D diffraction maps (3DXRD) [190] has recently been proven feasible for a Ni-Ti alloy with more than 15000 grains, this method is still limited to the study of a small number of grains as spotty diffraction patterns are needed. It is not yet suitable to relatively large scale fracture mechanics.

The analysed material would ideally have the same crystal and bulk modulus to alleviate the issues raised in the discussion. The chosen material needs to be of interest for engineering applications but should not present too much complex behaviour to start with (e.g. microcracking, fibre debonding, etc.). It also needs to have a naturally occurring good tomography contrast to allow the use of DVC

on it. A good candidate could be the cast magnesium alloy (WE43) already studied by tomography in [182].

The tomography analysis will allow characterisation of the crack path and crack tip position, thus giving information on its geometry, which can be simulated in a 3-D FE model. The DVC analysis of the tomography data will provide the displacement field that can be used both for the strain energy release rate calculations and for the measurement of the crack opening displacements. This could be done simply via the edge detection method developed by Mr Cinar [**Cinar2015**] and used in Chapter 5.

Limited angle tomography will be used due to the necessity to apply in-situ fatigue loading to the sample. This was proven to be feasible in Chapter 4 and to allow sufficient quality tomographs to be analysed by DVC. The hydraulic fatigue rig that was planned to be used in Chapter 4 can be used at Diamond synchrotron to perform the loading.

As in Chapter 3, the sample can be deliberately overloaded to induce residual stresses and diffraction maps and tomographs can be acquired before and after overload and with crack propagation. The residual stress map can be obtained by comparing the unloaded sample diffraction patterns at a given stage with the original unloaded sample.

To sum up, diffraction maps of the mid-plane and closer to the specimen surface will be obtained, as this is where residual stress differences are expected. Tomography data will provide full-field displacement via DVC analysis, and allow measurement of local crack growth rates. The SIF values can be calculated using the techniques presented in Chapters 2 to 4 from: diffraction maps (surface and middle-plane), DVC without considering the residual stresses obtained from diffraction (as this was done in Chapter 3), DVC informed of residual stresses (surface and middle-plane). For the DVC data, the effect of local vs. global boundary conditions can also be studied.

This experiment is more complete than the one presented in Chapter 3 as the tomography data allow to take into account the 3-D crack shape. Also it should

give information on whether crack closure only affects the surface and will allow better understanding of how those effects can be studied by full-field methods.

8.2 Tomography informed modelling

The area of tomography informed modelling is also worth exploring with for instance multi-phase materials. The case of cement [191] or plastic bonded explosives (PBX) [192] can be cited as examples where the material contains multiple phases of different mechanical properties. An example is shown for a cement paste and PBX in Figure 8.2.

To study a crack propagating in such a material, it is not correct to consider the material as homogenous. If the indirect J-integral calculation approach is applied to those materials, the free region need to be aware of the microstructure to yield correct results. In the case of PBX, a crack will not behave similarly if it is in the neighbourhood of a high stiffness or low stiffness.

The tomography data can be used with specific image processing software (e.g. ParaView) to create a FE model where the mesh faithfully defines the material microstructure and where different material models are affected to the segmented regions. The correct strain and stresses can then be determined by the FE solution in the "free to deform" region and the J-integral calculation will provide correct results. It is important to keep in mind that exact modelling of the microstructure is computationally expensive and that alternative methods exists to only consider the microstructure in the areas where it plays a role in the sample behaviour. Such an approach is presented by Saucedo-Mora with FEMME (multi-scale Finite Element Microstructure MEshfree fracture model) technique [193].

For such analysis to be possible it is important than the tomograph pixel size and resolution are sufficient to accurately define both the crack path and the microstructure. If the crack is very large compared to the microstructure (e.g.

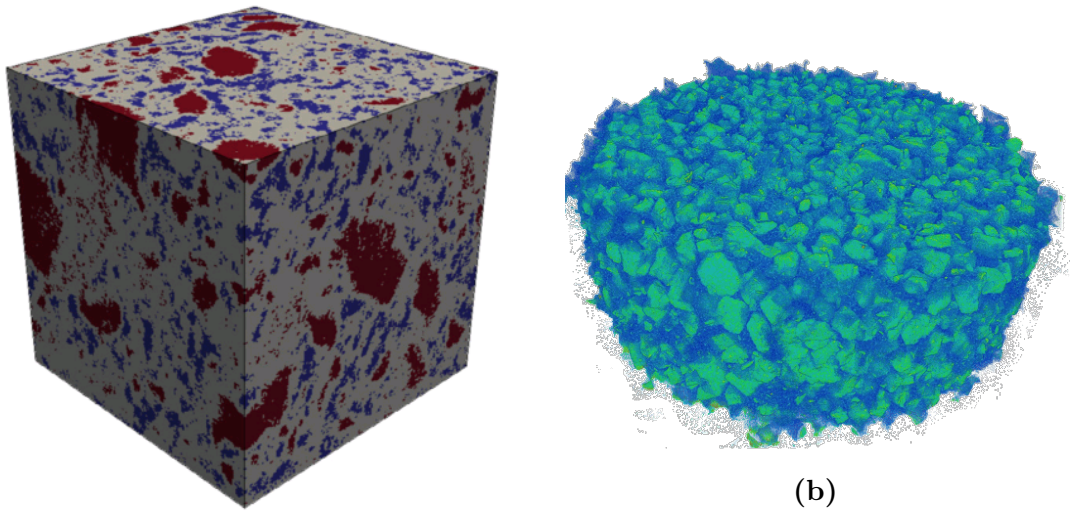

(a) (b)

Figure 8.1: (a) Example of the 3-D microstructure of a cement paste sample from [191]. The cube is 100 μm^3, the red regions represent anhydrous cement grains and the blue regions are pores. (b) 3-D microstructure of a reconstruction of a PBX sample. Unpublished work by the author in collaboration with Dr C. Siviour (University of Oxford). The crystals are shown in light green and the matrix in blue.

cast iron sample in Chapter 4), the effect of the microstructure on it will be reduced and it is not of interest to use a tomography informed modelling approach. This approach could also be interesting in the case of bio-materials such as bones where the porosity fraction is high. Here again it is important to understand what is measured by DVC at the used pixel size and resolution. If the speckle tracked by DVC is due to the modelled microstructure itself, the DVC results will inform on the bulk behaviour but will not be suitable to be applied on a fine microstructure FE model. However, if the DVC is able to track patterns in the phases themselves, the approach can be used.

Interestingly, the case of multi-materials seems not possible to tackle with field-fitting approaches as no analytical solution will exist.

8.3 Multi-axial diffraction calibration

To follow the problem raised in the discussion regarding calculation of J-integral from strain maps in materials where the bulk and crystal moduli are very different,

it would be worth running a model experiment where first time a calibration curve is obtained and then maps at known applied SIF values are acquired. This can be achieved by using a standard CT specimen geometry with a known crack length. The crack length can be accurately determined by tomography prior to the experiment.

A good candidate material could be Zirconium as is exhibits crystal elastic anisotropy and texture and is well characterized in literature [188]. The calibration presented in Chapter 5 for Gilsocarbon graphite is obtained using a uniaxial loading. However, it could be of interest to obtain a multiaxial calibration map to increase confidence in the stresses calculated ahead of a crack tip. Indeed, stresses in this region are multiaxial and the effect on this on the calibration is unclear.

An experimental design such as the bi-axial loading device (Figure 8.2a) developed by Erinosho [194] could be used for this purpose. They can be used with some specimen geometries (Figure 8.2b) that are meant to generate a range of multi-axis loadings that are identified from FE simulation and allow characterisation of the material with a limited number of tests. The obtained calibration than be used with the approach described in the discussion to convert measured crystal strains to bulk strains and calculate the bulk stresses. The SIF values obtained from those maps with the method presented in Chapter 3 can be compared with data from the analytical solution. It is important to note that this experiment, to be performed, requires the use of a synchrotron facility.

The experiment in itself (i.e. validation of the technique) will not provide novelty on the characterisation of zirconium but would pave the way for the application of the JMAN-S technique to a larger range of engineering alloys.

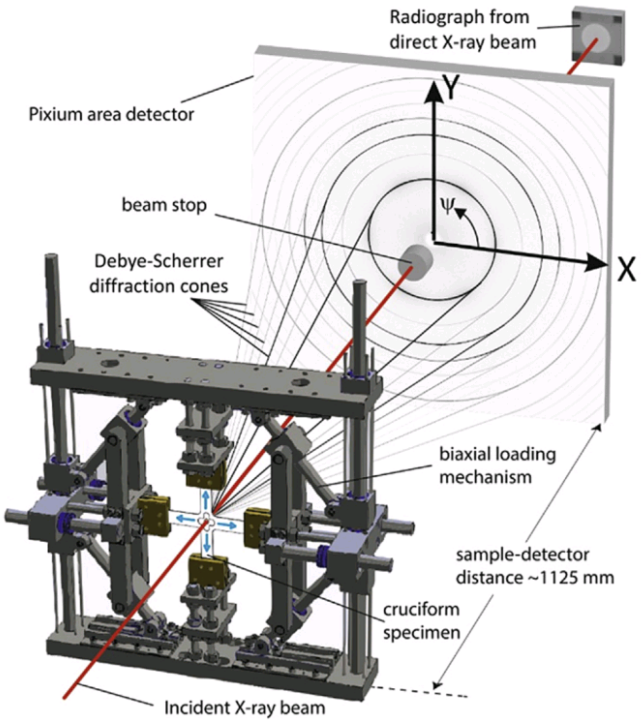

(a)

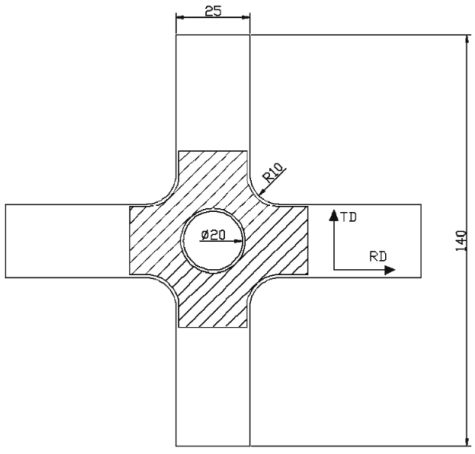

(b)

Figure 8.2: (a) Biaxial loading set-up as designed by Erinosho et al. in [194]. (b) Perforated cruciform specimen used by Cooreman [195]. The specimen allows generation of a range of strain states within the hachured region.

It wasn't my war!

— John Rambo

Bibliography

[1] C.E.Inglis. "Stresses in a Plate due to presence of Cracks and Sharp Corners". In: *Transactions of the Royal Institute of Naval Architectes* 60 (1913), pp. 219–241.

[2] A A Griffith. "The Phenomena of Rupture and Flow in Solids". In: *Philosophical Transactions of the Royal Society of London* 221 (1921).

[3] G.R. Irwin. "Fracture Dynamics". In: *Fracturing of Metals*. American Society for Metals, 1948, pp. 147–166.

[4] E. Orowan. "Fracture and strength of solids". In: *Reports on progress in Physics* XII (1948), p. 185.

[5] G.R Irwin. "Onset of Fast Crack Propagation in High Strength Steel and Aluminum Alloys". In: *Sagamore Research Conference Proceedings* May 1956 (1956), pp. 289–305.

[6] G Irwin. "Analysis of stresses and strains near the end of a crack traversing a plate". In: *Journal of Applied Mechanics* 24 (1957), pp. 361–364.

[7] I.N. Sneddon. "The Distribution of Stress in the Neighbourhood of a Crack in an Elastic Solid". In: *Proceedings of the Royal Society A: Mathematical, Physical and Engineering Sciences* 187.1009 (1946), pp. 229–260.

[8] M L Williams. "On the stress distribution at the base of a stationary crack". In: *ASME Journal of Applied Mechanics* 24 (1957), pp. 109–114.

[9] Rohola Hasanpour and Naghdali Choupani. "Rock fracture characterization using the modified Arcan test specimen". In: *International Journal of Rock Mechanics and Mining Sciences* 46.2 (Feb. 2009), pp. 346–354.

[10] G. C. Sih. "Strain-energy-density factor applied to mixed mode crack problems". In: *International Journal of Fracture* 10.3 (Sept. 1974), pp. 305–321.

[11] Jun Chang, Jin Quan Xu, and Yoshiharu Mutoh. "A general mixed-mode brittle fracture criterion for cracked materials". In: *Engineering Fracture Mechanics* 73.9 (2006), pp. 1249–1263.

[12] J W Hutchinson. "Singular behaviour at the end of a tensile crack in a hardening material". In: *Journal of the Mechanics and Physics of Solids* 16.1 (1968), pp. 13–31.

[13] J R Rice and G F Rosengren. "Plane Strain Deformation near a Crack Tip in a Power-law hardening material". In: *Journal of the Mechanics and Physics of Solids* 16 (1968), pp. 1–12.

[14] G P Cherepanov. "The propagation of cracks in a continuous medium". In: *Journal of Applied Mathematics and Mechanics* 31.3 (1967), pp. 503–512.

[15] J R Rice. “A Path Independent Integral and the Approximate Analysis of Strain Concentration by Notches and Cracks”. In: *Journal of Applied Mechanics* 35.2 (1968), pp. 379–386.

[16] C F Shih, B Moran, and T Nakamura. “Energy release rate along a three-dimensional crack front in a thermally stressed body”. In: *International Journal of Fracture* 30.2 (1986), pp. 79–102.

[17] Wilfred Kaplan. “Advanced calculus”. In: *Advanced calculus*. New York: Addison-Wesley, 2003. Chap. 5.5 Green’, p. 741.

[18] D M Parks. “A stiffness derivative finite element technique of crack tip stress intensity factors”. In: *International Journal of Fracture* 10.4 (1974), pp. 487–502.

[19] T Nishioka and S N Atluri. “Analytical solution for embedded elliptical cracks, and finite element alternating method for elliptical surface cracks, subjected to arbitrary loadings”. In: *Engineering Fracture Mechanics* 17.3 (1983), pp. 247–268.

[20] J C Newman and I S Raju. “Stress-intensity factor equations for cracks in three-dimensional finite bodies subjected to tension and bending loads”. In: *Computational Methods in the Mechanics of Fracture*. Ed. by S N Atluri. Elsevier Science Publisher, 1986. Chap. 9, pp. 312–334.

[21] A Luxmoore, M F Light, and W T Evans. “A comparison of energy release rates, the J-integral and crack tip displacements”. In: *International Journal of Fracture* 13 (1977), pp. 257–259.

[22] Xian Kui Zhu and James A. Joyce. “Review of fracture toughness (G, K, J, CTOD, CTOA) testing and standardization”. In: *Engineering Fracture Mechanics* 85 (2012), pp. 1–46.

[23] C F Shih. “Relationships between the J-integral and the crack opening displacement for stationary and extending cracks”. In: *Journal of the Mechanics and Physics of Solids* 29.4 (1981), pp. 305–326.

[24] S Suresh, G F Zamiski, and R O Ritchie. “Oxide-Induced Crack Closure: An Explanation for Near-Threshold Corrosion Fatigue Crack Growth Behavior”. In: *Metallurgical Transactions A* 12A (1981), pp. 1435–1443.

[25] W Elber. “The Significance of Fatigue Crack Closure”. In: *Damage Tolerance in Aircraft Structures ASTM STP 486* (1971), pp. 230–242.

[26] W Elber. “Fatigue crack closure under cyclic tension”. In: *Engineering Fracture Mechanics* 2 (1970), pp. 37–45.

[27] S Liu et al. “Measuring the fracture resistance of hard coatings”. In: *Applied Physics Letters* 102.17 (2013), p. 171907.

[28] F P Chiang and A Asundi. “A white light speckle method applied to the detemination of stress intensity factor and displacement field around a crack tip”. In: *Engineering Fracture Mechanics* 15.1-2 (1981), pp. 115–121.

[29] D B Barker and R J Sanford. “Determining K and related stress-field parameters from displacement fields”. In: *Experimental Mechanics* 25.4 (1985), pp. 399–407.

[30] J M Huntley and J E Field. “Measurement of crack tip displacement field using laser speckle photography”. In: *Engineering Fracture Mechanics* 30.6 (1988), pp. 779–790.

[31] W H Peters and W F Ranson. “Digital imaging techniques in experimental stress analysis”. In: *Optical Engineering* 21.3 (1982), p. 213427.

[32] T C Chu et al. “Applications of Digital Image-Correlation Techniques to Experimental Mechanics”. In: *Experimental Mechanics* 25.3 (1985), pp. 232–244.

[33] H Lu and P D Cary. “Deformation Measurements by Digital Image Correlation: Implementation of a Second-order Displacement Gradient”. In: *Experimental Mechanics* 40.4 (2000).

[34] Cofaru Corneliu, Philips Wilfried, and Van Paepegem Wim. “Improved Newton–Raphson digital image correlation method for full-field displacement and strain calculation”. In: *Applied Optics* 49.33 (2010).

[35] Pan Bing et al. “Performance of sub-pixel registration algorithms in digital image correlation”. In: *Measurement Science and Technology* 17.6 (2006), pp. 1615–1621.

[36] S R McNeill, W H Peters, and M A Sutton. “Estimation of stress intensity factor by Digital Image Correlation”. In: *Engineering Fracture Mechanics* 28.1 (1987).

[37] Jin Liu et al. “Experimental Characterization of Crack Tip Deformation Fields in Alloy 718 at High Temperatures”. In: *Journal of Engineering Materials and Technology* 120.1 (1998), pp. 71–78.

[38] J S Lyons, J Liu, and M A Sutton. “High-temperature Deformation Measurements Using Digital-image Correlation”. In: *Experimental Mechanics* 36.1 (1996).

[39] Sokhwan Choi and Surendra P Shah. “Fracture mechanism in cement-based materials subjected to compression”. In: *Journal of Engineering Mechanics* 124.1 (1998).

[40] Javier Gonzalez and W G Knauss. “Strain inhomogeneity and discontinuous crack growth in a particular composite”. In: *Journal of the Mechanics and Physics of Solids* 46.10 (1998).

[41] Audrey G Zink, Robert W Davidson, and Robert B Hanna. “Strain measurement in wood using a Digital Image Correlation technique”. In: *Wood and Fiber science* 27.4 (1995).

[42] Rui Zhang and Lingfeng He. “Measurement of mixed-mode stress intensity factors using digital image correlation method”. In: *Optics and Lasers in Engineering* 50.7 (2012), pp. 1001–1007.

[43] Stéphane Roux and François Hild. “Stress intensity factor measurements from digital image correlation: post-processing and integrated approaches”. In: *International Journal of Fracture* 140.1-4 (2006), pp. 141–157.

[44] S. Yoneyama, Y. Morimoto, and M. Takashi. “Automatic evaluation of mixed-mode stress intensity factors utilizing digital image correlation”. In: *Strain* 42.1 (2006), pp. 21–29.

[45] Julien Réthoré, François Hild, and Stéphane Roux. “Extended digital image correlation with crack shape optimization”. In: *International Journal for Numerical Methods in Engineering* 73.2 (2008), pp. 248–272.

[46] Julien Réthoré, Stéphane Roux, and François Hild. “Noise-robust stress intensity factor determination from kinematic field measurements”. In: *Engineering Fracture Mechanics* 75.13 (2008), pp. 3763–3781.

[47] T H Becker, T J Marrow, and R B Tait. “Damage, crack growth and fracture characteristics of nuclear grade graphite using the Double Torsion technique”. In: *Journal of Nuclear Materials* 414.1 (2011), pp. 32–43.

[48] T H Becker et al. “An approach to calculate the J-integral by digital image correlation displacement field measurement”. In: *Fatigue & Fracture of Engineering Materials & Structures* 35.10 (2012), pp. 971–984.

[49] Julien Réthoré, Stéphane Roux, and François Hild. “From pictures to extended finite elements: extended digital image correlation (X-DIC)”. In: *Comptes Rendus Mécanique* 335.3 (2007), pp. 131–137.

[50] J Poissant and F Barthelat. “A Novel ‘Subset Splitting’ Procedure for Digital Image Correlation on Discontinuous Displacement Fields”. In: *Experimental Mechanics* 50.3 (2009), pp. 353–364.

[51] M R Molteno and T H Becker. “Mode I-III Decomposition of the J-integral from DIC Displacement Data”. In: *Strain* 51.6 (2015), pp. 492–503.

[52] S. Yoneyama. “Smoothing measured displacements and computing strains utilising finite element method”. In: *Strain* 47.SUPPL. 2 (2011), pp. 258–266.

[53] J. Morton et al. “A localized hybrid method of stress analysis: A combination of moiré interferometry and FEM”. In: *Experimental Mechanics* 30.2 (June 1990), pp. 195–200.

[54] M. Y. Tsai and J. Morton. “New developments in the localized hybrid method of stress analysis”. In: *Experimental Mechanics* 31.4 (Dec. 1991), pp. 298–305.

[55] F Caimmi et al. “J-Integral from Full Field Kinematic Data for Natural Rubber Compounds”. In: *Strain* 51.5 (2015), pp. 343–356.

[56] G. Catalanotti et al. “Measurement of resistance curves in the longitudinal failure of composites using digital image correlation”. In: *Composites Science and Technology* 70.13 (2010), pp. 1986–1993.

[57] Jeong-Ho Kim and Glaucio H. Paulino. “Consistent Formulations of the Interaction Integral Method for Fracture of Functionally Graded Materials”. In: *Journal of Applied Mechanics* 72.3 (2005), p. 351.

[58] M. S. Kirugulige and H. V. Tippur. “Measurement of Fracture Parameters for a Mixed-Mode Crack Driven by Stress Waves using Image Correlation Technique and High-Speed Digital Photography”. In: *Strain* 45.2 (Apr. 2009), pp. 108–122.

[59] Perng-Fei Luo, Yuh J Chao, and Michael A Sutton. “Application of stereo vision to three-dimensional deformation analyses in fracture experiments”. In: *Optical Engineering* 33.3 (1994), pp. 981–990.

[60] Jeffrey D Helm, Stephen R McNeill, and Michael A Sutton. “Improved three-dimensional image correlation for surface displacement measurement”. In: *Optical Engineering* 35.7 (1996), pp. 1911–1920.

[61] J Réthoré et al. “Estimation of mixed-mode stress intensity factors using digital image correlation and an interaction integral”. In: *International Journal of Fracture* 132.1 (2005), pp. 65–79.

[62] Jiang Hsieh. *Computed Tomography, Second Edition*. Bellingham, WA 98227-0010 USA: SPIE Press, Oct. 2009.

[63] J.J. Young et al. “Magnetic resonance imaging of crack formation in hydrated cement paste materials”. In: *Cement and Concrete Research* 34.8 (2004), pp. 1459–1466.

[64] Jiliang Li et al. “Imaging bone microdamage in vivo with positron emission tomography”. In: *Bone* 37.6 (2005), pp. 819–824.

[65] B. K. Bay et al. “Digital volume correlation: Three-dimensional strain mapping using X-ray tomography”. In: *Experimental Mechanics* 39.3 (1999), pp. 217–226.

[66] T S Smith, B K Bay, and M M Rashid. “Digital volume correlation including rotational degrees of freedom during minimization”. In: *Experimental Mechanics* 42.3 (2002), pp. 272–278.

[67] M Gates, J Lambros, and M T Heath. “Towards High Performance Digital Volume Correlation”. In: *Experimental Mechanics* 51.4 (2010), pp. 491–507.

[68] Hugo Leclerc et al. “Digital volume correlation: what are the limits to the spatial resolution?” In: *Mechanics & Industry* 13.6 (2012), pp. 361–371.

[69] Nathalie Limodin et al. “Crack closure and stress intensity factor measurements in nodular graphite cast iron using three-dimensional correlation of laboratory X-ray microtomography images”. In: *Acta Materialia* 57.14 (2009), pp. 4090–4101.

[70] J Réthoré et al. “Digital volume correlation analyses of synchrotron tomographic images”. In: *The Journal of Strain Analysis for Engineering Design* 46.7 (2011), pp. 683–695.

[71] Nathalie Limodin et al. “Influence of closure on the 3D propagation of fatigue cracks in a nodular cast iron investigated by X-ray tomography and 3D volume correlation”. In: *Acta Materialia* 58.8 (2010), pp. 2957–2967.

[72] M. Mostafavi et al. “Three-dimensional crack observation, quantification and simulation in a quasi-brittle material”. In: *Acta Materialia* 61.16 (2013), pp. 6276–6289.

[73] M Mostafavi et al. “Observation and quantification of three-dimensional crack propagation in poly-granular graphite”. In: *Engineering Fracture Mechanics* 110 (2013), pp. 410–420.

[74] T J Marrow et al. “A quantitative three-dimensional in situ study of a short fatigue crack in a magnesium alloy”. In: *International Journal of Fatigue* 66 (2014), pp. 183–193.

[75] A J Allen et al. “Neutron diffraction methods for the study of residual stress fields”. In: *Advances in Physics* 34.4 (1985), pp. 445–473.

[76] P. J. Withers and P. J. Webster. “Neutron and Synchrotron X-ray Strain Scanning”. In: *Strain* 37.1 (2001), pp. 19–33.

[77] R. A. Young. *The Rietveld Method*. Ed. by R. A Young. Oxford: International Union of Crystallograhy/Oxford University Press, 1993, p. 308.

[78] Roger Pynn. “Neutron Scattering—A Non-destructive Microscope for Seeing Inside Matter”. In: *Neutron Applications in Earth, Energy and Environmental Sciences*. Ed. by Liyuan Liang, Romano Rinaldi, and Helmut Schober. Springer, 2009. Chap. 2, pp. 1–29.

[79] Stephen W. Lovesay. *Theory of Neutron scattering from Condensed Matter, Volume 1.* Oxford: Clarendon Press, 1984, p. 329.

[80] R. V. Preston et al. "Physically-based constitutive modelling of residual stress development in welding of aluminium alloy 2024". In: *Acta Materialia* 52.17 (2004), pp. 4973–4983.

[81] R A Owen et al. "Neutron and synchrotron measurements of residual strain in TIG welded aluminium alloy 2024". In: *Materials Science and Engineering: A* 346.1-2 (2003), pp. 159–167.

[82] A. J. Allen et al. "The analysis of internal strains measured by neutron diffraction in Al/SiC metal matrix composites". In: *Acta Metallurgica Et Materialia* 40.9 (1992), pp. 2361–2373.

[83] J E Allison. "Measurement of Crack-Tip Stress Distributions by X-Ray Diffraction". In: *ASTM STP677 Fracture Mechanics: Proceedings of the Eleventh National Symposium on Fracture Mechanics*. 1979.

[84] P Lopez-Crespo et al. "Characterisation of overloads in fatigue by 2D strain mapping at the surface and in the bulk". In: *Fatigue and Fracture of Engineering Materials and Structures* 39.8 (2016).

[85] T J Marrow et al. "Measurement of crack bridging stresses in environment-assisted cracking of duplex stainless by synchrotron diffraction". In: *Fracture of Engineering Materials and Structures* 29.6 (2006), pp. 464–471.

[86] A Steuwer et al. "In situ analysis of cracks in structural materials using synchrotron X-ray tomography and diffraction". In: *Nuclear Instruments and Methods in Physics Research Section B: Beam Interactions with Materials and Atoms* 246.1 (2006), pp. 217–225.

[87] R Sinclair et al. "The effect of fibre fractures in the bridging zone of fatigue cracked Ti-6Al-4V/SiC fibre composites". In: *Acta Materialia* 52.6 (2004), pp. 1423–1438.

[88] T. J. Marrow et al. "In situ measurement of the strains within a mechanically loaded polygranular graphite". In: *Carbon* 96 (2016), pp. 285–302.

[89] Jonathan P Belnoue et al. "Evaluation of the overload effect on fatigue crack growth with the help of synchrotron XRD strain mapping". In: *Engineering Fracture Mechanics* 77.16 (2010), pp. 3216–3226.

[90] Bing Pan et al. "Two-dimensional digital image correlation for in-plane displacement and strain measurement: a review". In: *Measurement Science and Technology* 20.6 (2009), p. 62001.

[91] M Bornert et al. "Assessment of Digital Image Correlation Measurement Errors: Methodology and Results". In: *Experimental Mechanics* 49.3 (2008), pp. 353–370.

[92] D M Parks. "The Virtual Crack Extension method for non linear material behavior". In: *Computer methods in applied mechanics and engineering* 12 (1977), pp. 353–364.

[93] C. F. Shih and R. J. Asaro. "Elastic-Plastic Analysis of Cracks on Bimaterial Interfaces: Part I—Small Scale Yielding". In: *Journal of Applied Mechanics* 55.2 (1988), p. 299.

[94] Matthew C Walters, Glaucio H Paulino, and Robert H Dodds. "Interaction integral procedures for 3-D curved cracks including surface tractions". In: *Engineering Fracture Mechanics* 72.11 (2005), pp. 1635–1663.

[95] M L Williams. "Stress singularities resulting from various boundary conditions in angular corners of plates in extension". In: *Journal of Applied Mechanics* 19 (1952), pp. 526–528.

[96] R G Keys. "Cubic Convolution Interpolation for Digital Image Processing". In: *IEEE Transactions on Acoustics, Speech, and Signal Processing* ASSP-29.6 (1981).

[97] R C Rice et al. *Metallic Materials Properties Development and Standardization (MMPDS)*. U.S. Department of Transportation.

[98] D P Rooke and D J Cartwright. *Compendium of stress intensity factors*. Procurement Executive, Ministry of Defence. H. M. S. O., 1976.

[99] Lin Hsin-Chih, Wang Ling-Ling, and Yang Shi-Nine. "Extracting periodicity of a regular texture based on autocorrelation functions". In: *Pattern Recognition Letters* 18.5 (1997), pp. 433–443.

[100] John C. Russ. *The Image Processing Handbook, Sixth Edition*. Boca Raton FL: CRC Press, 2011, p. 885.

[101] American Society for Testing and Materials. *Standard Test Method for Linear-Elastic Plane-Strain Fracture Toughness of Metallic Materials*. 1997.

[102] BSI. *Advanced technical ceramics — Mechanical properties of monolithic ceramics at room temperature*. 2007.

[103] Michael Bauccio. *ASM metals reference book*. Ed. by Michael Bauccio. ASM International, 1993, p. 614.

[104] Leslie Banks-Sills and Mircea Arcan. "A compact Mode II fracture specimen". In: *ASTM special technical publication* 905 (1986), pp. 347–363.

[105] Mahmoud Mostafavi et al. "3D studies of indentation by combined X-ray tomography and digital volume correlation". In: *13th European Conference on Fracture - Key Engineering Materials*. Brno, Czech Republic, 2013.

[106] T. L. Anderson. *Fracture Mechanics: Fundamentals and Applications*. Taylor & Francis, 2012.

[107] ASTM Standard E1820 and ASTM. *Standard Test Method for Measurement of Fracture Toughness*. 2013.

[108] A. K. Vasudeven, K. Sadananda, and N. Louat. "A review of crack closure, fatigue crack threshold and related phenomena". In: *Materials Science and Engineering A* 188.1-2 (1994), pp. 1–22.

[109] X.P. Zhang et al. "A study of the crack wake closure/opening behaviour of short fatigue cracks and its influence on crack growth". In: *Materials Science and Engineering: A* 406.1 (2005), pp. 195–204.

[110] C K Clarke and G C Cassatt. "A Study of fatigue crack closure using electric potential and compliance techniques". In: *Engineering Fracture Mechanics* 9.3 (1977), pp. 529–751.

[111] K. Minakawa, G. Levan, and A. J. McEvily. "The influence of load ratio on fatigue crack growth in 7090-t6 and in9021-t4 p/m aluminum alloys". In: *Metallurgical Transactions A* 17.10 (Oct. 1986), p. 1787.

[112] A.J. McEvily. "Discussion". In: *Fatigue & Fracture of Engineering Materials and Structures* 12.1 (Jan. 1989), pp. 71–72.

[113] R V Preston et al. "Finite element modelling of tungsten inert gas welding of aluminium alloy 2024". In: *Science and Technology of Welding and Joining* 8.1 (2003), pp. 10–18.

[114] T J Marrow et al. "Three dimensional observations and modelling of intergranular stress corrosion cracking in austenitic stainless steel". In: *Journal of Nuclear Materials* 352.1-3 (2006), pp. 62–74.

[115] P Lopez-Crespo et al. "The stress intensity of mixed mode cracks determined by digital image correlation". In: *The Journal of Strain Analysis for Engineering Design* 43.8 (2008), pp. 769–780.

[116] A M Korsunsky, Karen E Wells, and P J Withers. "Mapping Two Dimensional State of Strain Using Synchrotron X-Ray Diffraction". In: *Scripta Materialia* 39.12 (1998).

[117] Thomas F Coleman and Li Yuying. "An Interior, Trust Region Approach for Nonlinear Minimization Subject to Bounds." In: *SIAM Journal on Optimization* 6.2 (1996), pp. 418–445.

[118] ASTM International. *ASTM E647-15e1 Standard Test Method for Measurement of Fatigue Crack Growth Rates*. 2015.

[119] M R Daymond, M W Johnson, and D S Sivia. "Analysis of neutron diffraction strain measurement data from a round robin sample". In: *The Journal of Strain Analysis for Engineering Design* 37.1 (Jan. 2002), pp. 73–85.

[120] M T Hutchings et al. "Interpretation and Analysis of Lattice Strain Data". In: *Introduction to the Characterization of Residual Stress by Neutron Diffraction*. Ed. by CRC Press. London, 2005. Chap. 5.

[121] Angus J. Wilkinson, Graham Meaden, and David J. Dingley. "High-resolution elastic strain measurement from electron backscatter diffraction patterns: New levels of sensitivity". In: *Ultramicroscopy* 106.4 (2006), pp. 307–313.

[122] Jürgen Frikel and Eric Todd Quinto. "Characterization and reduction of artifacts in limited angle tomography". In: *Inverse Problems* 29.12 (Dec. 2013), p. 125007.

[123] Ge Wang, Troy Frei, and Michael W. Vannier. "Fast iterative algorithm for metal artifact reduction in X-ray CT". In: *Academic Radiology* 7.8 (2000), pp. 607–614.

[124] Sofya Titarenko, Philip J. Withers, and Anatoly Yagola. "An analytical formula for ring artefact suppression in X-ray tomography". In: *Applied Mathematics Letters* 23.12 (2010), pp. 1489–1495.

[125] Daniel Prell, Yiannis Kyriakou, and Willi A Kalender. "Comparison of ring artifact correction methods for flat-detector CT". In: *Phys Med Biol* 54.12 (June 2009), pp. 3881–3895.

[126] Li Liu and Elise F Morgan. "Accuracy and precision of digital volume correlation in quantifying displacements and strains in trabecular bone". In: *Journal of Biomechanics* 40.15 (2007), pp. 3516–3520.

[127] Juan C Ramirez Giraldo et al. "Comparative Study of Two Image Space Noise Reduction Methods for Computed Tomography: Bilateral Filter and Nonlocal Means". In: *31st Annual International Conference of the IEEE Engineering in Medicine and Biology Society*. Minneapolis, USA: IEEE, Sept. 2009, pp. 3529–3532.

[128] F. Gillard et al. "The application of digital volume correlation (DVC) to study the microstructural behaviour of trabecular bone during compression". In: *Journal of the Mechanical Behavior of Biomedical Materials* 29 (2014), pp. 480–499.

[129] C. Franck et al. "Three-dimensional full-field measurements of large deformations in soft materials using confocal microscopy and digital volume correlation". In: *Experimental Mechanics* 47.3 (May 2007), pp. 427–438.

[130] W Ludwig et al. "Study of the interaction of a short fatigue crack with grain boundaries in a cast Al alloy using X-ray microtomography". In: *Acta Materialia* 51.3 (2003), pp. 585–598.

[131] Adrian P. Sheppard, Robert M. Sok, and Holger Averdunk. "Techniques for image enhancement and segmentation of tomographic images of porous materials". In: *Physica A* 339 (2004), pp. 145–151.

[132] Karsten Ehrig et al. "Comparison of Crack Detection Methods for Analyzing Damage Processes in Concrete with Computed Tomography". In: *International Symposium on Digital Industrial Radiology and Computed Tomography*. Berlin, 2009.

[133] Joël Lachambre. "Développement d'une Méthode de Caractérisation 3D des Fissures de Fatigue à l'aide de la Corrélation d'Images Numériques obtenues par Tomographie X". PhD thesis. 2014.

[134] T. J. Marrow et al. "High resolution X-ray tomography of short fatigue crack nucleation in austempered ductile cast iron". In: *International Journal of Fatigue* 26.7 (2004), pp. 717–725.

[135] Hugo Ledoux and Christopher Gold. "An efficient natural neighbour interpolation algorithm for geoscientific modelling". In: *Developments in Spatial Data Handling* (2004), pp. 97–108.

[136] B.T. Kelly. "Graphite—the most fascinating nuclear material". In: *Carbon* 20.1 (1982), pp. 3–11.

[137] B. J. Marsden and G. N. Hall. "Graphite in gas-cooled reactors". In: *Comprehensive Nuclear Materials*. Ed. by R.J.M. Konings. Vol. 4. Elsevier Ltd, 2012, pp. 325–390.

[138] Jean-Pierre Bonal et al. "Graphite, Ceramics, and Ceramic Composites for High-Temperature Nuclear Power Systems". In: *MRS Bulletin* 34.01 (Jan. 2009), pp. 28–34.

[139] Michael P. Hindley et al. "Failure prediction of full-size reactor components from tensile specimen data on NBG-18 nuclear graphite". In: *Nuclear Engineering and Design* 284 (2015), pp. 1–9.

[140] M.R. Ayatollahi, F. Berto, and P. Lazzarin. "Mixed mode brittle fracture of sharp and blunt V-notches in polycrystalline graphite". In: *Carbon* 49.7 (2011), pp. 2465–2474.

[141] M. R. Ayatollahi and A. R. Torabi. "Tensile fracture in notched polycrystalline graphite specimens". In: *Carbon* 48.8 (2010), pp. 2255–2265.

[142] Timothy D. Burchell. "A microstructurally based fracture model for polygranular graphites". In: *Carbon* 34.3 (1996), pp. 297–316.

[143] M O Tucker and N McLachlan. "Fracture and microstructure of graphites". In: *Journal of Physics D: Applied Physics* 26.6 (June 1993), pp. 893–907.

[144] Gareth B. Neighbour, Brian McEnaney, and Mike Phillips. "Acoustic emission responses from cyclic loading of a nuclear graphite". In: *Carbon* 30.3 (1992), pp. 359–363.

[145] R Taylor et al. "The mechanical properties of reactor graphite". In: *Carbon* 5 (1967), pp. 519–531.

[146] Pierre Ouagne, Gareth B Neighbour, and Brian McEnaney. "Crack growth resistance in nuclear graphites". In: *Journal of Physics D: Applied Physics* 35.9 (May 2002), p. 927.

[147] A. R. Shahani and M. M. Nejadi. "Investigation on the mechanical properties and fracture toughness of graphite". In: *Fatigue & Fracture of Engineering Materials & Structures* 38.10 (Oct. 2015), pp. 1209–1218.

[148] J. E. Brocklehurst and M. I. Darby. "Concerning the fracture of graphite under different test conditions". In: *Materials Science and Engineering* 16.1-2 (1974), pp. 91–106.

[149] Po-Yun Tang. "Interpretation of bend strength increase of graphite by the couple-stress theory". In: *Computers & Structures* 16.1 (1983), pp. 45–49.

[150] A Hodgkins et al. "X-ray tomography observation of crack propagation in nuclear graphite". In: *Materials Science and Technology* 22.9 (2006), pp. 1045–1051.

[151] Haiyan Li, Jonathan Duff, and Thomas James Marrow. "In-Situ Observation of Crack Nucleation in Nuclear Graphite by Digital Image Correlation". In: *Materials and Fabrication* 6.PARTS A AND B (2008), pp. 813–820.

[152] M. Mostafavi and T. J. Marrow. "In situ observation of crack nuclei in poly-granular graphite under ring-on-ring equi-biaxial and flexural loading". In: *Engineering Fracture Mechanics* 78.8 (2011), pp. 1756–1770.

[153] M. Mostafavi and T.J. Marrow. "Quantitative in situ study of short crack propagation in polygranular graphite by digital image correlation". In: *Fatigue & Fracture of Engineering Materials & Structures* 35.8 (Aug. 2012), pp. 695–707.

[154] M R Joyce and T J Marrow. "Microstructural scale strain localisation in nuclear graphite". In: *Journal of Nuclear Materials* 381.1-2 (2008), pp. 171–176.

[155] S M Barhli et al. "Obtaining the J-integral by diffraction-based crack-field strain mapping". In: *Procedia Structural Integrity*. Vol. 2. 21 st European Conference on Fracture, ECF21. Catania, Italy, 2016, pp. 2519–2526.

[156] A Hodgkins et al. "Fracture behaviour of radiolytically oxidised reactor core graphites: a view". In: *Materials Science and Technology* 26.8 (2010), pp. 899–907.

[157] B. L. Karihaloo, H. M. Abdalla, and Q. Z. Xiao. "Deterministic size effect in the strength of cracked concrete structures". In: *Cement and Concrete Research* 36.1 (2006), pp. 171–188.

[158] V. Veselý and P. Frantík. "An application for the fracture characterisation of quasi-brittle materials taking into account fracture process zone influence". In: *Advances in Engineering Software* 72 (2014), pp. 66–76.

[159] A. L. Rosa et al. "A loading rate dependent cohesive model for concrete fracture". In: *Engineering Fracture Mechanics* 82 (2012), pp. 195–208.

[160] A. R. Ingraffea and V. Saouma. "Numerical modeling of discrete crack propagation in reinforced and plain concrete". In: *Fracture mechanics of concrete: Structural application and numerical calculation*. Dordrecht: Springer Netherlands, 1985, pp. 171–225.

[161] Z. Zou et al. "Numerical simulation of strength test on graphite moderator bricks using a continuum damage mechanics model". In: *Engineering Fracture Mechanics* 73.3 (2006), pp. 318–330.

[162] L. Saucedo-Mora et al. "Three-dimensional measurement and cohesive element modelling of deformation and damage in a 2.5-dimensional woven ceramic matrix composite". In: *Fatigue and Fracture of Engineering Materials and Structures* (2016).

[163] R. Moskovic. "Degradation of graphite in gas cooled reactors due to radiolytic oxidation". In: *Nuclear Engineering and Design* 269 (2014), pp. 83–87.

[164] S. Sato et al. "Neutron irradiation effects on thermal shock resistance and fracture toughness of graphites as plasma-facing first wall components for fusion reactor devices". In: *Carbon* 27.4 (1989), pp. 507–516.

[165] M. M. Mirsayar et al. "Strain-based criteria for mixed-mode fracture of polycrystalline graphite". In: *Engineering Fracture Mechanics* 156 (2016), pp. 114–123.

[166] M.S.L. Jordan et al. "Measurements of Stress Concentration Behaviour in AGR Nuclear Graphite". In: *23 rd Conference on Structural Mechanics in Reactor Technology*. Manchester, UK, 2015.

[167] S. D. Preston and B. J. Marsden. "Changes in the coefficient of thermal expansion in stressed Gilsocarbon graphite". In: *Carbon* 44.7 (2006), pp. 1250–1257.

[168] Michael Drakopoulos et al. "I12: The Joint Engineering, Environment and Processing (JEEP) beamline at Diamond Light Source". In: *Journal of Synchrotron Radiation* 22.3 (May 2015), pp. 828–838.

[169] Caroline A Schneider, Wayne S Rasband, and Kevin W Eliceiri. "NIH Image to ImageJ: 25 years of image analysis". In: *Nature Methods* 9.7 (June 2012), pp. 671–675.

[170] Keyun Wen, James Marrow, and Barry Marsden. "Microcracks in nuclear graphite and highly oriented pyrolytic graphite (HOPG)". In: *Journal of Nuclear Materials* 381.1-2 (2008), pp. 199–203.

[171] S D Shastri et al. "Cryogenically cooled bent double-Laue monochromator for high-energy undulator X-rays (50-200 keV)". In: *Journal of Synchrotron Radiation* 9.5 (2002), pp. 317–322.

[172] M. O. Tucker, A. P G Rose, and T. D. Burchell. "The fracture of polygranular graphites". In: *Carbon* 24.5 (1986), pp. 581–602.

[173] A.P.G. Rose and M.O. Tucker. "A fracture criterion for nuclear graphite". In: *Journal of Nuclear Materials* 110.2 (1982), pp. 186–195.

[174] Holger Wendland. *Scattered data approximation*. Cambridge: Cambridge University Press, 2005, p. 348.

[175] O. L. Blakslee et al. "Elastic constants of compression-annealed pyrolytic graphite". In: *Journal of Applied Physics* 41.8 (July 1970), pp. 3373–3382.

[176] K. K. Phani and S. K. Niyogi. "Young's modulus of porous brittle solids". In: *Journal of Materials Science* 22.1 (Jan. 1987), pp. 257–263.

[177] Shahed Fazluddin. "Crack growth resistance in nuclear graphite". PhD thesis. University of Leeds, 2002.

[178] Mototsugu Sakai et al. "R-Curve Behavior of a Polycrystalline Graphite: Microcracking and Grain Bridging in the Wake Region". In: *Journal of the American Ceramic Society* 71.8 (Aug. 1988), pp. 609–616.

[179] Nassia Tzelepi and P Ramsay. "Development of New Techniques for AGR Graphite". In: *The 4th EDF Energy Nuclear Graphite Symposium. Engineering Challenges Associated with the Life of Graphite Reactor Cores*. Nottingham, UK, 2015, pp. 397–412.

[180] H.M. Jensen. "Mixed mode interface fracture criteria". In: *Acta Metallurgica et Materialia* 38.12 (1990), pp. 2637–2644.

[181] S Rahimi et al. "In situ observation of intergranular crack nucleation in a grain boundary controlled austenitic stainless steel". In: *Journal of Microscopy* 233 (2009), pp. 423–431.

[182] M Mostafavi et al. "Yield behavior beneath hardness indentations in ductile metals, measured by three-dimensional computed X-ray tomography and digital volume correlation". In: *Acta Materialia* 82 (2015), pp. 468–482.

[183] J. P. Pédron and A. Pineau. "The effect of microstructure and environment on the crack growth behaviour of Inconel 718 alloy at 650 °C under fatigue, creep and combined loading". In: *Materials Science and Engineering* 56.2 (1982), pp. 143–156.

[184] H. M. Ledbetter and R. L. Moment. "Elastic properties of face-centered-cubic plutonium". In: *Acta Metallurgica* 24.10 (Oct. 1976), pp. 891–899.

[185] W. A. Brantley. "Calculated elastic constants for stress problems associated with semiconductor devices". In: *Journal of Applied Physics* 44.1 (Jan. 1973), pp. 534–535.

[186] Basil Housari and Lian X. Yang. "Experimental Techniques for Strain Measurement and Validation of CAE Model". In: *Strain* 724 (Apr. 2005).

[187] Stefano Beretta, Silvio Rabbolini, and A Di-Bello. "Multi-scale crack closure measurements with digital image correlation on Haynes 230". In: *Frattura ed Integrità Strutturale* 33.33 (2015), pp. 174–182.

[188] Desmond Tromans. "Elastic Anisotropy of HCP Metal Crystals and Polycrystals". In: *International Journal of Recent Research and Applied Studies* 6 (2011), pp. 462–483.

[189] M. Mostafavi et al. “Quantifying yield behaviour in metals by X-ray nanotomography”. In: *Scientific Reports* 6 (Oct. 2016), p. 34346.

[190] P. Sedmak et al. “Grain-resolved analysis of localized deformation in nickel-titanium wire under tensile load”. In: *Science* 353.6299 (2016), p. 559.

[191] Mingzhong Zhang and Andrey P. Jivkov. “Microstructure-informed modelling of damage evolution in cement paste”. In: *Construction and Building Materials* 66 (2014), pp. 731–742.

[192] Scott Gary Bardenhagen et al. “Detailed characterization of PBX morphology for mesoscale simulations”. In: *17th Biennial Conference of the American Physical Society Topical Group on Shock Compression of Condensed Matter*. Vol. 1426. Chicago, IL: American Institute of Physics, 2012, pp. 637–640.

[193] Luis Saucedo-Mora and T. James Marrow. “FEMME: A multi-scale Finite Element Microstructure MEshfree fracture model for quasi-brittle materials with complex microstructures”. In: *Engineering Fracture Mechanics* 147 (2015), pp. 355–372.

[194] T. O. Erinosho et al. “Assessment of X-ray diffraction and crystal plasticity lattice strain evolutions under biaxial loading”. In: *International Journal of Plasticity* 83 (2015), pp. 1–18.

[195] Steven Cooreman et al. “Identification of mechanical material behavior through inverse modeling and DIC”. In: *Experimental Mechanics* 48.4 (2008), pp. 421–433.